

Selective Catalytic Reduction of Nitrogen Oxides with Ammonia over Transition Metal Exchanged Zeolites

Jamal Abdul Nasir

A dissertation submitted in partial fulfilment of the requirements for the degree of

Doctor of Philosophy of University College London.

Department of Chemistry
University College London

08th August 2023

Declaration

I, Jamal Abdul Nasir, confirm that the work presented in this thesis is my own. Where information has been derived from other sources, I confirm that this has been indicated in the thesis.

Abstract

Metal-exchanged zeolites have received considerable attention in recent years, owing to their wide range of catalytic activity, especially their application in the selective catalytic reduction (SCR) of NOx species. In this thesis, we study the NH₃-SCR reaction over transition metals (Cu and Fe) exchanged zeolites (CHA and BEA) using the hybrid quantum mechanical/molecular mechanical (QM/MM) technique and where needed with input from the experiment. First, we investigate the NH₃-SCR reaction mechanism on Cu-CHA zeolite and compare the reaction energies of water- and ammonia-solvated and bare Cu species. Our results indicate that physisorbed solvent coordinated to the Cu-active sites has a promoting effect on the oxidation component of the NH₃-SCR cycle. In particular, we find that the formation of important nitrate species is energetically more favourable on solvated Cu sites than in the absence of solvent molecules. However, both water and ammonia molecules inhibit the reduction component of the NH₃-SCR cycle. Next, we study the NH₃-SCR of NOx reaction over various Fe-BEA active sites including systems with both framework and extra-framework Fe cations. The catalytically active sites are found to include Fe-Fe_F-BEA, Fe-Al_F-BEA, and Cu-Fe_F-BEA, (where the subscript F indicates framework species) on which the formation and consumption of key intermediates, including nitrosamine and nitrate species were analyzed. The results obtained from this study are further compared with other zeolites including ZSM-5 and Chabazite. Finally, we study the formation of Cu-dimer species which are considered to be one of the possible species in the NH₃-SCR of the NOx reaction. We find that the isolated Cu species can form dimer species in the presence of a solvent. This thesis contributes to the understanding of the reactivity of transition metals containing zeolites and offers insights for improving the efficiency of the existing zeolitic system in the NH₃-SCR reaction.

Impact Statement

The use of transition metal-based zeolites in NH₃-assisted NOx SCR is rapidly expanding, but understanding the reactivity of these metal ions in zeolites is critical for their practical usage. The NH₃-SCR of NOx reactions requires a thorough knowledge of the structure and mechanism in transition metal ion (TMI) exchanged zeolites, as well as identifying TMI speciations and their redox mediation behaviour. To expose the dynamic character of metal-ions active species at the molecular level, different pathways for Cu and Fe must be investigated and explored by understanding the parallel between theoretical simulations and experimental spectroscopic techniques. The hydrothermal stability of zeolite-based SCR reactions is also a challenge; however, recent research has shown the efficacy of small-pore zeolites containing metal ions such as Cu-CHA, which are used commercially. Therefore, gaining mechanistic insight into the NH₃-SCR reaction and developing innovative low-NH₃-SCR catalysts will need a thorough understanding of TMI as a catalytic site in zeolites. Another significant challenge in the development of zeolite-based SCR catalysts is balancing high activity at low temperatures with high-temperature stability. This equilibrium is essential for the practical implementation of these catalysts in real-world contexts. As a result, more research and development are required to optimise the design and composition of TMI-exchanged zeolites for increased catalytic performance and durability, which could entail employing new synthesis processes and characterization technologies, as well as including various metal ions and other additives to improve the activity and stability of these catalysts. Finally, the successful development of high-performance TMI-based zeolites for NH₃-SCR of NOx reactions could have a significant impact on further reducing harmful emissions from various sources, such as vehicles and industrial processes, as well as improving air quality for human health and the environment.

Acknowledgements

All praises for the **Almighty Allah**, Who guides us in darkness and helps us in difficulties, who has bestowed man with intelligence, wisdom and knowledge, and all respects to **Holy Prophet Hazrat Muhammad** (Peace be upon him) who exhorted his followers to seek for knowledge from cradle to grave and who enable us to recognize our creator.

First and foremost, I want to thank my supervisor, Professor Sir Richard Catlow for providing me with the opportunity to undertake this PhD. His wisdom, guidance, and reassurance have been invaluable to me, and I am forever grateful for their support.

I would like to extend my sincere thanks to Dr Alexey Sokols -- his enthusiasm and patience were instrumental and provided invaluable assistance in all facets of setup and analysis during this whole period of my PhD journey. Dr Jingcheng Guan offered insightful inputs into the problems faced along the way, while Dr Thomas Keal and You Lu's help with running large numbers of calculations and the initial stages of the Zeolite setup in both Tcl-Chemshell and Py-Chemshell is greatly appreciated. I'd like to recognize the assistance I received from Prof. Scott Woodley (Secondary supervisor), Alec Desmoutier, Dr Lei Zhu, Dr Qing Hou, Xingfan Zhang, and Erze Gao. I would like to thank my other Colleagues especially, Isa Tristan Lough, Dong-Gi Kang, and Woongkyu Jee. It would not be the same without you people. In addition, other members of Richard's groups especially Mohammad Alotaibi (Master's student, who later became my best friend). Special thanks to Dr Naveed Ahmad (from King College London) and Zaibunisa Khan (University College London) who provided many insightful inputs into the problems faced along the way and I am extremely appreciative of the help they provided.

I would like to acknowledge the financial support for my study from the Project Management Unit (PMU) Higher Education Department of KPK, Pakistan. Furthermore, I am grateful to UCL, and the EPSRC for providing funding for my research. I also want to acknowledge the Materials Chemistry Consortium for granting access to the THOMAS, YOUNG and ARCHER2 supercomputing clusters, which were essential to my work. I acknowledge the work of those who studied TMI zeolite before me, as their research paved the way for my own discoveries. Without their detailed studies, the findings presented in this thesis would not have been possible.

Finally, I am deeply grateful to my friends, family, and especially my **Parents, Siblings, & Cousins** for their unwavering support throughout my research journey. Their presence provided me with normality, laughter, and much-needed fun, which helped me maintain my sanity during a demanding and challenging environment. I cannot thank them enough for their support.

UCL Research Paper Declaration Form

referencing the doctoral candidate's own published work(s)

1. For a research manuscript that has already been published

a) What is the title of the manuscript?

Influence of Solvent on Selective Catalytic Reduction of Nitrogen Oxides with Ammonia over Cu-CHA Zeolite

b) Please include a link to or doi for the work

doi.org/10.1021/jacs.2c09823

c) Where was the work published?

Journal of the American Chemical Society

d) Who published the work? (e.g. OUP)

American Chemical Society (ACS)

e) When was the work published?

December 22, 2022

f) List the manuscript's authors in the order they appear on the publication

Jamal Abdul Nasir*, Jingcheng Guan, Thomas W. Keal, Alec W. Desmoutier, You Lu, Andrew M. Beale, C. Richard A. Catlow*, Alexey A. Sokol

g) Was the work peer reviewed?

Yes

h) Have you retained the copyright?

Yes (openly available under the terms of the CCBY4_0 license)

i) Was an earlier form of the manuscript uploaded to a preprint server?

No

If 'No', please seek permission from the relevant publisher and check the box next to the below statement:

X

I acknowledge permission of the publisher named under **1d** to include in this thesis portions of the publication named as included in **1c**.

Table of Contents

1.	. Chapter 1	1
	1.1 Introduction	1
	1.2 Zeolites: Fundamentals and Challenges	3
	1.3 TMI Chemistry in Zeolite	7
	1.3.1 Location and Distribution of TMI in Zeolite	8
	1.3.2 Coordination of TMI to the Lattice and Activation of Oxygen	12
	1.3.3 Spectroscopic Analysis of TMI in Zeolite Frameworks	15
	1.3.4 TMI Location: Perspective	18
	1.4 NH ₃ -SCR of NOx on TMI-Zeolites	19
	1.4.1 Reactivity and Structural Complexity of TMI in Activated Materials	24
	1.4.2 Modelling Mobility and Restructuring of TMI in NH₃-SCR	29
	1.4.3 TMI Stability in Zeolites	33
	1.4.4 Reaction Mechanism and Kinetics of NH ₃ -SCR	35
	1.4.5 Industrial Importance of NH₃-SCR Process	40
	1.5 Objectives	42
2.	. Chapter 2	43
	2.1 Introduction	43
	2.2 Quantum Mechanics	44
	2.2.1 Hartree-Fock Theory	46
	2.2.2 Density Functional Theory	47
	2.3 Implementations	47
	2.3.1 Basis Sets	48
	2.3.2 Effective Core Potentials	49
	2.4 Molecular Mechanics	50
	2.5 QM/MM Embedding Techniques	52
	2.5.1 ChemShell QM/MM Coupling	55
	2.5.2 QM/MM Implementation	56
	2.5.3 Choice of Model Clusters	57
	2.6 Geometry Optimisation	60
	2.7 Lattice Parameter Test	61
	2.8 Energy Barrier and Transition State Search	63
	2.9 Vibrational Calculations	64

	2.9.1 Validational Scaling Factor	66
	2.10 Resources	69
	2.10.1 Justification of the Choice of Software	69
	2.11 Benchmarking	69
3.	Chapter 3	71
	3.1 Introduction	71
	3.2 Computational and Experimental Methodologies	72
	3.2.1 QM/MM Methodologies	72
	3.2.2 Choice of Model Cluster	73
	3.2.3 Vibrational Calculations	74
	3.3 Result and Discussions	75
	3.3.1 Vibrational Study	76
	3.3.2 Adsorption Properties of the Cu-CHA	86
	3.3.3 Comparison of Reaction Energetics with Experiment	89
	3.3.4 Catalytic Cycle	91
	3.3.5 H ₂ NNO Decomposition	96
	3.3.6 Reactivity of HONO	98
	3.4 Summary and Conclusion	99
4.	Chapter 4	. 101
	4.1 Introduction	. 101
	4.2 Computational Approach	. 102
	4.2.1 QM/MM Methodologies	. 102
	4.3 Result and Discussion	. 104
	4.3.1 Vibrational Study on Solvated Sites	. 104
	4.3.2 Cu Displacement on Solvation	. 112
	4.3.3 Catalytic Cycle	. 115
	4.3.4 Solvent Effect on H₂NNO Decomposition	. 121
	4.4 Summary and Conclusion	. 123
5.	Chapter 5	. 124
	5.1 Introduction	.124
	5.2 Computational Approach	.127
	5.2.1 QM/MM Methodologies	. 127
	5.2.2 Choice of Model Cluster	.128
	5.3 Result and Discussions	.129

	5.3.1 Reduction of Intra-framework Fe-BEA	130
	5.3.2 Adsorption Properties of the Fe-BEA	132
	5.3.3 NH ₃ Binding Study	137
	5.3.4 Catalytic Cycle	139
	5.3.5 Reaction Pathway	144
	5.4 Summary and Conclusion	147
6.	Chapter 6	149
	6.1 Introduction	149
	6.2 Computational Approach	151
	6.2.1 QM/MM Methodologies	151
	6.3 Results and Discussions	152
	6.3.1 Mobility and Restructuring of Cu-species	153
	6.3.2 Oxidation Half-cycle	154
	6.4 Summary	160
7.	Chapter 7	161
	7.1 Summary, Conclusions and Future Perspective	161
	7.1.1 Future Perspective	164
8.	References	167

List of Figures

Figure 1.1. a) The representative rings (8-MR, 6-MR, and 4-MR) of CHA zeolite, and b) examples allowed Al distributions in β -6MR sites, where qualitative rules on Al distributions in zeolites allow from, two, or three Al T-sites. Colour code: O, red; Si, grey; Al, green. Adopted with permission from ref. 28 .	
Figure 1.2. a) Schemes of four possible Fe species in Fe-zeolites and b) Co siting in ZSM-5 structure, according to ref. 55 . Local framework structures of the a -, b -, and c -sites9	
Figure 1.3. a) Cu-SSZ-13 location and coordination b) the distribution of active sites in Cu(II)-SSZ-13 at different ELs obtained from total energy calculations. At an EL of 0.2, only the most stable sites (a) (blue), (b) (yellow), and (f) (green) will be occupied. With increased EL, the occupation of the site (f) increases, and only at the end site (c) will it be exchanged. Comparison with experiment 63 indicates that the most stable sites (a) and/or (b) are the active centres in the self-catalytic reduction of NOx. Reproduced from Ref. ⁵⁹	
Figure 1.4. Characterization techniques for the isolated Cu ²⁺ active sites (a) XRD patterns with observed (crosses) and calculated (line) with the relative difference curve (bottom line) of the refinements of Cu-SSZ-13 patterns, ⁸³ (b) Normalized Cu K-edge XANES spectra for Cu-SAPO-44 catalysts and the reference samples, ¹⁰² (c) EPR spectra of hydrated Cu-SSZ-13 samples measured at 155 K, ¹⁰³ (d) H ₂ consumption profiles during H ₂ -TPR on Cu-SSZ-13. Cu ion exchange level: 20 % (red), 40 % (green), 60 % (blue), 80 % (purple), and 100 % (black)-bottom to top ⁹⁰	
Figure 1.5. Comparing Cu and Fe-SSZ-13 in standard, wet SCR before (fresh) and after hydrothermal ageing. Conditions in the inset. Adapted with permission from ref (118). Copyright 2015 Elsevier22	
Figure 1.6. Proposed local sites of the copper species in the cage of the CHA at high temperature and under oxygen treatment. a) [CuOH] ⁺ b) [Cu(II)O ₂ ·] ⁺ superoxide species c) [Cu(trans-μ-1,2-O ₂)Cu] ²⁺ . Adapted from ¹⁵⁹	
Figure 1.7. Cu-SSZ-13 H ₂ -TPR results with varying Cu dosage and Si/Al ratio; Top panel represents hydrated samples while the bottom panels report hydrated samples ¹⁶¹	
Figure 1.8. a) Free energy profile as a function of the Cu-Al distance; the mobile $[Cu(I)(NH_3)_2]^+$ species and Al atoms of CHA framework for charge balancing; (1) reactant $[Cu(I)(NH_3)_2]^+$ (2) transition state $[Cu(I)(NH_3)_2]^+$ (3) Product state $[Cu(NH_3)_2]^+$. For comparison, the computed point-charge model has also been reported as a red line 9 . b) $[Cu(I)(NH_3)_2]^+$ configuration. Cu; grey, N; blue, Al; green and H; white	
Figure 1.9. The proposed reduction process on isolated Cu (II) ions (residing near one (left) or two (right) framework Al centres). The transportation of Cu(I) ions into the cage and the subsequent oxidation by O ₂ (inner step). NH ₄ ⁺ ion is generated in the right-hand cycle to balance the charge and maintain the stoichiometry. Si; yellow, O; red, Cu; grey, N; blue and H; white ¹²⁰	
Figure 2.1. QM/MM embedding setup used within both Py and Tcl Chemshell: Progressing from top to bottom; the quantum mechanical region (treated with ab initio calculations), the relaxed MM region (treated with a force field), and the frozen MM ions. The outermost region (not displayed) contains point charges to ensure the Madelung potential in the centre of the cluster is accurately reproduced	
Figure 2.2. The QM/MM embedding setup ; a) the CHA cluster (above) and b) the BEA (below) with QM regions for three different active sites; Fe(III)-Fe _F -BEA, Fe-Al _F -BEA, and Cu-Fe _F -BEA. The outermost region contains point charges to ensure the Madelung potential in the centre of the cluster is accurately reproduced. Atom colour codes: Cu (brown), Al (green), Si (yellow), O (red), N (blue), and H (white)	

Figure 2.3. The representative Cu ²⁺ -OH ⁻ CHA Al-tetrahedra shows various possible locations of Cu DH ⁻ within the CHA framework. Color code: Al, purple; Si, yellow; O, red; Cu, gray; N, blue; and white;		
Figure 2.4. Schematic representation of the transition state theory (TST)		
Figure 2.5. Resonating structure of nitrosamine species		
Figure 2.6. Benchmarking of Gamess-UK calculations by varying nodes on Archer2 machine7		
Figure 3.1. Schematic representation of NH ₃ -SCR of NO _x catalytic cycle		
Figure 3.2. The QMMM embedding setup ; the CHA cluster (left) with a quantum mechanical regio containing nitrate species (right). The outermost region contains point charges to ensure the Madelun potential in the centre of the cluster is accurately reproduced. Atom colour codes: Cu (brown), A (green), Si (yellow), O (red), N (blue), and H (white)		
Figure 3.3. The NH ₃ -SCR reaction cycle highlights the identified species in the DRIFTS spectra 7		
Figure 3.4. Spectroscopic Signatures; (a) Concentration modulation ME DRIFTS experiment with corresponding phase-resolved spectra for bidentate Cu nitrate (Cu–NO ₃) and Cu-nitrosamine (Cu N(=O)–NH ₂) species		
Figure 3.5. Spectroscopic Signatures; data yielded from QM/MM calculations for Cu-nitrosamin (Cu-N(=O)-NH ₂) species. Atom color codes : Cu (brown), Al (green), O (red), N (blue), and H (white The framework SiO ₂ is shown using a wire framework motif		
Figure 3.6. Spectroscopic Signatures; (a) Concentration modulation ME DRIFTS experiment wit corresponding phase-resolved spectra, and (b) data yielded from QM/MM calculations for bidentate C nitrate (Cu–NO ₃) and Cu-nitrosamine (Cu–N(=O)–NH ₂) species. Atom colour codes : Cu (brown), A (green), O (red), N (blue), and H (white). The framework SiO ₂ is shown using a wire framework moti		
Figure 3.7. Vibrational spectroscopic analysis of the Cu-(N(=O)-OH)-NH ₃ species		
Figure 3.8. Vibrational spectroscopic analysis of the N=O _{str} vibrational mode of bidentate-nitrite (Cu NO ₂) species for all three sites		
Figure 3.9. Vibrational spectroscopic analysis of the N=O _{str} vibrational mode of bidentate-nitrite (Cu (NO ₂)–NH ₃) species for all three sites.		
Figure 3.10. DRIFTS spectra showing various species that are collected during the NO concentratio modulation experiment. The experiment is conducted by Andrew Beale's group		
Figure 3.11. The reaction adsorption energies of NH ₃ , NO (with both O and N end-down), H ₂ O, an O ₂ on Cu(I)-CHA and Cu(II)-OH/CHA sites. The model used is shown as an extra framework. Colo codes: Cu (brown), Al (green), O (red), N (blue), and H (white). The framework SiO ₂ is shown using wire framework motif.		
Figure 3.12. The relative potential energy landscape of NO-activated NH ₃ -SCR of NOx catalytic cycl on bare Cu-CHA site		
Figure 3.13. The structures of each corresponding intermediate species reside on bare Cu-CHA. The model used is shown as an extra framework. Atom color codes : Cu (brown), Al (green), O (red), I (blue), and H (white). The framework SiO ₂ is shown using a wire framework motif		
Figure 3.14. NEB calculations ; the NEB images showing the formation pathway of nitrate species and their relative energies landscape.		
Figure 3.15. The optimized structure of Cu-nitrosamine (Cu–N(=O)–NH ₂)9		

Figure 3.16. Calculated potential energy surfaces for H ₂ NNO isomerization The model used is shown as an extra framework. Atom color codes : Cu (brown), Al (green), O (red), N (blue), and H (white The framework SiO ₂ is shown using a wire framework motif		
Figure 3.17. The binding of HONO species with NH ₃ , H ₂ O, O ₂ , and NO. Color code: Al, green; Si yellow; O, red; Cu, brown; N, blue; and H, white;		
Figure 4.1. Solvated active sites i) H ₂ O coordinated Cu-CHA, and ii) NH ₃ coordinated Cu-CHA 102		
Figure 4.2. The QMMM embedding setup ; the CHA cluster (left) with a quantum mechanical region ontaining solvated-nitrate species (right). The outermost region contains point charges to ensure the Madelung potential in the centre of the cluster is accurately reproduced. Atom colour codes: Cubrown), Al (green), Si (yellow), O (red), N (blue), and H (white)		
Figure 4.3. Spectroscopic Signatures of solvated nitrosamine; a) physisorbed water and b physisorbed ammonia Cu-nitrosamine (Cu–N(=O)–NH ₂) species. Atom colour codes : Cu (brown), A (green), O (red), N (blue), and H (white). The framework SiO ₂ is shown using a wire framework motif		
Figure 4.4. Spectroscopic signatures of solvated nitrate; a) physisorbed water and b) physisorbed ammonia Cu-nitrate (Cu-NO ₃) species. Atom colour codes : Cu (brown), Al (green), O (red), N (blue) and H (white). The framework SiO ₂ is shown using a wire framework motif		
Figure 4.5. Spectroscopic Signatures of nitrosamine; a) protonated and b) deprotonated Cunitrosamine (Cu–N(=O)–NH ₂) species. Atom colour codes : Cu (brown), Al (green), O (red), N (blue) and H (white). The framework SiO ₂ is shown using a wire framework motif		
Figure 4.6. Spectroscopic signatures of solvated nitrite; a) physisorbed water and b) physisorbed ammonia Cu-nitrite (Cu-NO ₂) species. Atom colour codes : Cu (brown), Al (green), O (red), N (blue) and H (white). The framework SiO ₂ is shown using a wire framework motif		
Figure 4.7. Spectroscopic Signatures; data yielded from QM/MM calculations for protonated and deprotonated Cu-nitrosamine (Cu-N(=O)-NH ₂) species. Atom colour codes : Cu (brown), Al (green) O (red), N (blue), and H (white). The framework SiO ₂ is shown using a wire framework motif111		
Figure 4.8. The interaction of physisorbed a) water and ammonia, and b) the behaviour of NO or solvated Cu(I)-CHA site. The model used is shown as an extra framework. Atom colour codes : Cu (brown), Al (green), O (red), N (blue), and H (white)		
Figure 4.9. The behaviour of NO on solvated Cu(I)-CHA site. The model used is shown as an extra framework. Atom colour codes : Cu (brown), Al (green), O (red), N (blue), and H (white). The framework SiO ₂ is shown using a wire framework motif		
Figure 4.10. The structures of each corresponding intermediate species residing on solvated (H ₂ O) Cu CHA. Atom colour codes : Cu (brown), Al (green), O (red), N (blue), and H (white). The framework SiO ₂ is shown using a wire framework motif.		
Figure 4.11. The relative potential energy landscape of the NO-activated NH ₃ -SCR of NOx catalytic cycle on the physisorbed water Cu-CHA site is presented in the lower panel. The model used is shown as an extra framework.		
Figure 4.12. The structures of each corresponding intermediate species residing on solvated (H ₂ O) Cu-CHA. Atom colour codes : Cu (brown), Al (green), O (red), N (blue), and H (white). The framework SiO ₂ is shown using a wire framework motif.		
Figure 4.13. The relative potential energy landscape of NO-activated NH ₃ -SCR of NOx catalytic cycle on the physisorbed water Cu-CHA site is presented in the lower panel. The model used is shown as an extra framework.		

Figure 4.14. The relative potential reaction-energy landscape at room temperature for NH ₃ -SCR or activated Cu-CHA site; (black) on bare-site, (green) with physisorbed ammonia, and (red) with physisorbed water. Inset right: No-activated NH ₃ -SCR of NOx catalytic cycle
Figure 4.15. The schematic illustrations of isomeric decompositions of H ₂ NNO intermediates 121
Figure 4.16. Calculated potential energy surfaces for H ₂ NNO isomerization (a) without water and (b) in the presence of physisorbed water on the Cu-CHA sites. The model used is shown as an extra framework. Colour codes : Cu (brown), Al (green), O (red), N (blue), and H (white)
Figure 4.17. Solvent-occupied (water) active sites H ₂ NNO (nitrosamine) intermediates
Figure 5.1. Fe-BEA : framework and extra framework cations in BEA zeolite a) Fe(III)-Al, b) Cu(II)-Fe, c) Fe(III)-Fe
Figure 5.2. The QMMM embedding setup ; is the BEA cluster (centre) with a quantum mechanical region of Fe(III)-Fe _F -BEA, Fe-Al-BEA, and Cu-Fe _F -BEA. The outermost region contains point charges to ensure the Madelung potential in the centre of the cluster is accurately reproduced. Atom colour codes: Fe (yellow), Cu (brown), Al (green), Si (yellow), O (red), and H (white)
Figure 5.3. Illustrate the Fe(II) species surrounded by the QM atoms, and the reduction of Fe(III) to Fe(II).
Figure 5.4. The adsorption energies of NH ₃ , NO, and H ₂ O on Fe(II)-Al/BEA and Fe(IIII)-Al/BEA sites The model used is shown as an extra framework. Atom colour codes: Cu (brown), Al (green), O (red), N (blue), and H (white). The framework SiO ₂ is shown using a wire framework motif
Figure 5.5. The adsorption energies of NH ₃ , NO, and H ₂ O on Cu(I)-Fe _F /BEA and Cu(II)-Fe _F /BEA sites The model used is shown as an extra framework. Atom colour codes: Cu (brown), Al (green), O (red), N (blue), and H (white). The framework SiO ₂ is shown using a wire framework motif
Figure 5.6. The adsorption energies of NH ₃ , NO, and H ₂ O on Fe(II)-Fe _F /BEA and Fe(III)-Fe _F /BEA sites. The model used is shown as an extra framework. Note, Fe _F act as a framework cation and Fe as an extra framework. Atom colour codes: Cu (brown), Al (green), O (red), N (blue), and H (white). The framework SiO ₂ is shown using a wire framework motif
Figure 5.7. The reaction adsorption energies of NH ₃ on different active sites in BEA zeolite including the Brønsted acid site.
Figure 5.8. The mechanistic representation of NH ₃ -SCR cycle on Fe-BEA catalyst; yellow represents the reduction cycle and blue - the oxidation cycle
Figure 5.9. (a) The reduction half cycle of the NH ₃ -SCR cycle and its corresponding landscape energy representation on three active sites - [Fe(III)-Al _F -BEA, Cu(II)-Fe _F -BEA, and Fe(III)-Fe _F -BEA]. Where M in the above diagram represents the metal site. Atom colour codes: Fe (yellow), Cu (brown), Al (green), O (red), N (blue), and H (white). The framework SiO ₂ is shown using a wire framework motif
Figure 5.10. Formation of nitrate ; (a) the corresponding landscape energy description and (b) the schematic representation of nitrate species formation on three active sites [Fe(III)-Al _F -BEA, Cu(II)-Fe _F -BEA, and Fe(III)-Fe _F -BEA]. Atom colour codes : Cu (brown), Al (green), O (red), N (blue), and H (white). The framework SiO ₂ is shown using a wire framework motif
Figure 5.11. The structures of each corresponding intermediate species reside on bare Cu-CHA. The model used is shown as an extra framework. Atom colour codes : Cu (brown), Al (green), O (red), N (blue), and H (white). The framework SiO ₂ is shown using a wire framework motif

Figure 5.12. The structures of each corresponding intermediate species reside on bare Cu-CHA. The model used is shown as an extra framework. Atom colour codes : Cu (brown), Al (green), O (red), blue), and H (white). The framework SiO ₂ is shown using a wire framework motif		
Figure 5.13. The structures of each corresponding intermediate species reside on bare Cu-CHA. The model used is shown as an extra framework. Atom colour codes : Cu (brown), Al (green), O (red), N (blue), and H (white). The framework SiO ₂ is shown using a wire framework motif		
Figure 6.1. Schematic representation of low-temperature NH ₃ -SCR of NO _x over binuclear Cu(II) sites.		
Figure 6.2. The QM/MM embedding setup ; is the CHA cluster with a quantum mechanical region containing Cu-dimer species. The outermost region contains point charges to ensure the Madelung potential in the Centre of the cluster is accurately reproduced. Atom colour codes: Fe (yellow), Cu (brown), Al (green), Si (yellow), O (red), N (blue), and H (white)		
Figure 6.3. Effect of solvation on the mobility of Cu cations a) water solvation b) ammonia solvation as shown in chapter 4		
Figure 6.4. The proposed catalytic NH ₃ -SCR cycle contains dimeric Cu-species		
Figure 6.5. CHA cluster of QM region showing two Al compensating two CuI(NH ₃) ₂ species 156		
Figure 6.6. O ₂ activation on pair of [Cu(NH ₃) ₂] ⁺ and the corresponding optimized structures 158		
Figure 6.7. Energy landscape of O ₂ adsorption and oxidation of two Cu(I)(NH ₃) ₂ equivalents. The different elements are represented by distinct colours: green for Al, grey for Cu, red for O, blue for N, and white for H.		

List of Tables

Table 1.1. Transition metals exchanged Zeolite for various catalytic reactions. 2
Table 1.2. Comparing Various Methods for Identifying Metal Species in Zeolites: Strengths and Limitations of Different Characterization Techniques 16
Table 1.3. List of the TMI-Zeolites tested in SCR of NOx with NH3. 21
Table 2.1. Selected calculated parameters of the optimized silica CHA chabazite, using two different DFT functional, and their comparison with the experimental data
Table 2.2. The calculated bond lengths of the Al-O (Å) Cu ²⁺ -OH ⁻ CHA chabazite for the possible three configurations.
Table 2.3. Calculated scaling factor value based on the theoretical and experimental values for N-O _{str} of HNO ₃ as a reference molecule
Table 2.4. Calculated scaling factor value based on the theoretical and experimental values for N-O _{str} of NO ₂ as reference molecules
Table 2.5. Calculated scaling factor value based on the theoretical and experimental values for N-O _{str} of N ₂ O as reference molecules. 68
Table 2.6. Calculated scaling factor value based on the theoretical and experimental values for N-N $_{str}$ of N $_2$ O as reference molecules.68
Table 2.7. Calculated scaling factor value based on the theoretical and experimental values for N-N _{str} of N_2H_2 as reference molecules
Table 3.1. Scaled vibrational frequencies for the nitrosamine species. 79
Table 3.2. Scaled vibrational frequencies for the bare nitrate species. 81
Table 3.3. Features observed in a concentration ME DRIFTS experiment's time-resolved spectrum under SCR conditions (NO gas switch pulse sequence). Assignment is based on an analysis of literature and calculated vibrational spectra of reactant intermediates shown in Figure 3b
Table 3.4. Calculated vibrational bands of key intermediate species presented in the NH ₃ -SCR catalytic cycle – see Figure 3.3
Table 3.5. The calculated reaction energies (eV) for NO-activation reaction (Eqn 3.2); both theoretical and experimental values. All theoretical calculations are performed using def2 basis sets ²⁷⁶ 89
Table 3.6. The standard enthalpy of formation values of the species at temperatures 298°C and 0°C . 90
Table 3.7. The calculated reaction energies for reaction (Eqn 3.2) are based on the standard enthalpy of formation of the species involved
Table 3.8. The calculated N_2 association energies (eV); both theoretical and experimental values. All theoretical calculations are performed using def2 basis sets 276
Table 4.1. Scaled vibrational frequencies for the physisorbed water nitrosamine species
Table 4.2. Scaled vibrational frequencies for the physisorbed ammonia nitrosamine species 106
Table 4.3. Scaled vibrational frequencies for the physisorbed water nitrate
Table 4.4. Scaled vibrational frequencies for the physisorbed ammonia nitrate
Table 4.5. Calculated vibrational bands of key intermediate species presented in the NH ₃ -SCR catalytic cycle – see Figure 3.4, chapter 3

Table 5.1. Fe-Al _F - BEA system ; the reaction adsorption energies (eV) of NH ₃ , NO (with both the and N-end down), H ₂ O, N ₂ and O ₂ on Fe(II)-(OH)-BEA and Fe(III)-(OH) ₂ -BEA sites		
Table 5.2. Cu-Fe _F -BEA system; the reaction adsorption energies of NH ₃ , NO (with both the O-and down), H ₂ O, and O ₂ on Cu(I)-BEA and Cu(II)-(OH)-BEA sites		
Table 5.3. Fe-Fe_F-BEA system ; the reaction adsorption energies of NH ₃ , NO (with both the O- and end down), H ₂ O, and O ₂ on Fe(II)-(OH)-BEA and Fe(III)-(OH) ₂ -BEA sites		

In this thesis, we discuss various zeolite structures, which are widely utilized in catalysis and materials science. To aid readers in understanding the classification of these zeolites, the following table presents the Zeolite Codes along with their respective Zeolite Names. This information will serve as a helpful reference throughout the thesis, providing insight into the diverse structural characteristics and applications of each zeolite family.

Zeolite Code	Zeolite Name
SSZ-13	CHA
ZSM-5	MFI
Beta	BEA
Υ	FAU
ZSM-11	MTW
Mordenite	MOR
Ferrierite	FER
ZSM-23	EUO
ZSM-22	TON
ZSM-48	MEI
SSZ-16	AFX
SSZ-39	AEI
Sigma-1	DDR
LEV	ERI

This table presents a comprehensive list of abbreviations used throughout the thesis, along with their corresponding full names. These abbreviations are frequently referenced in the text and figures to provide concise representations of various concepts, methodologies, and materials studied in the research. The table aims to facilitate the reader's understanding by providing a quick reference guide to the key abbreviations employed in the thesis.

Abbreviation	Full Term
AIMD	Ab Initio Molecular Dynamics
ВО	Born-Oppenheimer
DFT	Density Functional Theory
DRIFTS	Diffuse Reflectance Fourier Transform Spectroscopy
EDS	Energy-Dispersive X-ray Spectroscopy
ECP	Effective Core Potentials
ESR	Electron Spin Resonance
EXAFS	Extended X-ray Absorption Fine Structure
FTIR	Fourier Transform Infrared Spectroscopy
GTO	Gaussian-type Orbitals
GULP	General Utility Lattice Program
HF	Hartree-Fock
HRTEM	High-Resolution Transmission Electron Microscopy
LBFGS	Limited-memory Broyden-Fletcher-Goldfarb-Shanno
MM	Molecular Mechanics
MR	Member Ring
N_2O	Nitrous Oxide
NH ₃ -SCR	Selective Catalytic Reduction of NOx with NH3
NMR	Nuclear Magnetic Resonance Spectroscopy
NOx	Nitrogen Oxides
PBCs	Periodic Boundary Conditions
Ру	Python
QM	Quantum Mechanics
QM/MM	Quantum Mechanics/Molecular Mechanics
Raman	Raman Spectroscopy
SCR	Selective Catalytic Reduction
SEM	Scanning Electron Microscopy
TEM	Transmission Electron Microscopy
Tcl	Tool Command Language
TST	Transition State Theory
UV-Vis	Ultraviolet-Visible Spectroscopy
XANES	X-ray Absorption Near Edge Structure
XPS	X-ray Photoelectron Spectroscopy
XRD	X-ray Diffraction

Chapter 1

Transition metal-based Zeolite in NH₃-SCR

1.1 Introduction

Zeolites are porous aluminosilicate materials, with pores of molecular dimensions; they are members of the class of microporous materials which also includes microporous aluminophosphates (ALPOs). They possess unique and outstanding chemical and physical properties that are useful in a wide range of key applications including ion exchange, gas separation, and catalysis¹. To modify their adsorption ability and to incorporate new catalytic functionality into zeolites, ion-exchange with transition metal ions (TMI) is a widely used strategy ^{2,3}. TMIs, which may also be introduced into framework sites, play a key role in zeolite catalytic chemistry because of their variable oxidation states, which are pivotal in many catalytic reactions. Their study is facilitated by widely available spectroscopic techniques including electron paramagnetic resonance (EPR), UV-visible, and near-infrared (NIR) spectroscopy. For example, Cu(I) due to the characteristic luminescence spectra, can be characterized by photoluminescence spectroscopy.

TMI-zeolites are highly active in a variety of key redox reactions (Table 1.1) including deNOx catalysis⁴, and hydroxylation of benzene⁵ and methane⁶ to phenol and methanol, respectively. The use of TMI-containing zeolites for the remediation of NOx from combustion engines and the mild partial oxidation of unreacted hydrocarbons has attracted particular attention. The selective catalytic reduction (SCR) of NOx to N₂ in the presence of ammonia plays an important role in mitigating the emission of NOx from power plants and combustion engines⁷. The reactions in the NH₃-SCR either involve oxygen (standard SCR) or NO₂ (Fast SCR) to

generate nitrogen and water from NH_3 and NO 9 . Several other reactions can occur in this mixture of NOx, NH_3 , O_2 , and H_2O such as the oxidation of ammonia or the formation of N_2O . The conversion of NH_3 and NO to N_2 may not be directly affected by these side reactions, but they do affect the selectivity of N_2 , and therefore, can control the catalytic performance.

In this chapter, we first discuss the basics of zeolite science, and then attempt to describe the TMI chemistry; their distribution and location within the zeolite framework, the possible coordination to the lattice, and especially the formation of oxo-complexes. Next, we discuss in depth the structural complexity of TMI-based-zeolite and its reactivity in activated materials in NH₃-SCR. In addition, we highlight some of the state-of-the-art characterization techniques employed to investigate the structural and chemical identity of metals in the zeolite framework. In the subsequent section, we focus on the role of TMI in the NH₃-SCR reaction, where we provide a summary of the mobility and restructuring of TMI-active sites and their ultimate effect on the NH₃-SCR reactivity. To this end, we discuss the chemistry of the intermediate species and their formation. Finally, we briefly discuss the stability of TMI-zeolites, in particular the ageing impact of materials in the NH₃-SCR activity, and the potentially interesting possibilities of designing ideal zeolite-based heterogeneous catalysts along with the future perspectives. Our account provides the background to the detailed study of de-NOx catalytic reaction mechanism which is presented in later chapters of the thesis.

Table 1.1. Transition metals exchanged Zeolite for various catalytic reactions.

Catalyst	Reactants	Main Products	Reference
Ni/H-USY	CO ₂ , H ₂ O	CH ₄	10
Cu-ZnO/H-MFI	CO_2, H_2	CH ₃ OH	11
Cu/CHA	NO, NH_3, O_2	N_2, H_2O	12
Fe/BEA	NO, NH_3, O_2	N_2, H_2O	13
Ni/Zeolite-Y	Triolein	Biofuel (green diesel)	14
Fe/MFI	H_2O_2	OH ⁻ , ·OH	15
Co/Mo-Beta(25) zeolite	Methyl palmitate	Bio jet fuel	16

1.2 Zeolites: Fundamentals and Challenges

Zeolites are a type of crystalline alumino-silicate or silica nanoporous material with large specific surface areas, well-defined and variable microporous channels, and adjustable acidity and basicity that are widely used in a variety of industrial applications owing to their excellent catalytic activities and product selectivities 17, 18. The materials occur naturally as minerals, but there is also an extensive range of synthesised systems. Their production, topologies, and behaviours raise fascinating basic questions, and their extensive industrial usage has sparked both the improvement of current zeolitic structures and the search for new materials with novel capabilities. In addition to zeolites, other classes of nano-porous materials including ALPOs (Aluminophosphates) and SAPOs (Silicoaluminophosphate) offer distinctive characteristics and properties¹⁹. ALPOs, synthesized using aluminium and phosphorus precursors, exhibit thermal stability (although generally less than that of zeolites) and acid-catalytic activity due to the presence of framework aluminium. SAPOs, incorporating silicon, aluminium, and phosphorus, possess enhanced structural flexibility, enabling a broader range of pore sizes and shapes. The range of nano-porous materials has also in recent decades been greatly extended by the development of nano-porous metal-organic framework (MOF) materials which have been very extensively studied ²⁰.

A key, basic feature of zeolite chemistry is the isomorphous replacement of Si⁴⁺ with Al³⁺ which has two consequences. First, as the distance between Al-O bonds is longer than Si-O bonds, the tetrahedrally coordinated Al³⁺ with four lattice oxygen influences the shape and free diameter of the rings within the framework. Second, the incorporation of Al³⁺ creates a locally negative charge as Si⁴⁺ carries one positive charge more than Al³⁺, which must be compensated by the introduction of cation species which can include protons, as discussed further below. As

these cations are not part of the framework, they can be exchanged with the other cations such as TMI. The location of these exchanged cations depends on several factors such as the charge of the TMI, Si/Al ratio, amount of TMI, the method, and conditions ²¹. Moreover, Al³⁺ tetrahedra are not located in direct neighbouring sites in the framework (no Al-O-Al linkage) according to Lowenstein's rule ^{22, 23}, which appears to be strictly obeyed in zeolites. Our previous computational investigations have discovered that small clusters of zeolites have lower energy for "Lowensteinian" aluminium distributions ²². The upper limit of isomorphous substitution of Si with Al, thus, corresponds to a Si/Al ratio = 1. Also, there are different rules to describe the distribution of Al³⁺ including Takaishi and Kato rules ²⁴, which state that within 5-MR only one Al³⁺ substitution is allowed, but, Dempsey's rule proposes that the Al³⁺ substitution follows, as far as possible, for an even Al distribution ²⁵. However, deviations from Dempsey's rule occur in synthetic zeolites ²⁶. The experimental analysis shows that Al³⁺ substituents may be in close proximity rather than in a dispersed distribution, but Lowenstein's rule still holds ²⁷. The possible aluminium configurations in different ring structures with 5 > Si/Al > 1 for the 6-MR of zeolite are shown in Figure 1.1 ²⁸.

Many experimental results have found that the distribution of Al in the Si-rich zeolites lattice is not random and does not obey simple statistical rules ²⁹⁻³¹. Daniel *et al.* quantitatively determine the spatial distribution of Al using atomic-scale analysis (known as Atom Probe Tomography) ³¹. They observed a very non-random distribution of Al within highly crystalline zeolites which is very important for zeolite-based catalysis. Upon steaming the non-random, Al distribution promotes clustering and further develops a long-range redistribution of Al. This pronounced clustering appears to occur at the regions near diffusion barriers supposed to separate the zeolite subunits and hence, behave as a highway for the transportation of Al towards the outer surface of zeolites.

More than 200 frameworks of zeolites have been reported so far with a one-, two- or three-dimensional pore system. Examples are shown in Figure 1C. The access of species to the cage through the window of O atoms relies on the channel system, which connects the cage to the pore system. The number of O atoms determines the structural feature and free diameter of the window and channels ³². Different rings are symbolized with the notation *n*MR (8-MR, 6-MR, and 4-MRs where *n* represents the number of oxygen atoms). The molecules can enter through the window if the diameter of the rings is equal to/or exceeds the size of the molecules, although zeolites are flexible frameworks and molecules may be able to "squeeze" through windows at higher temperatures. Indeed the actual free diameter is a dynamic property owing to the breathing motion of the framework.

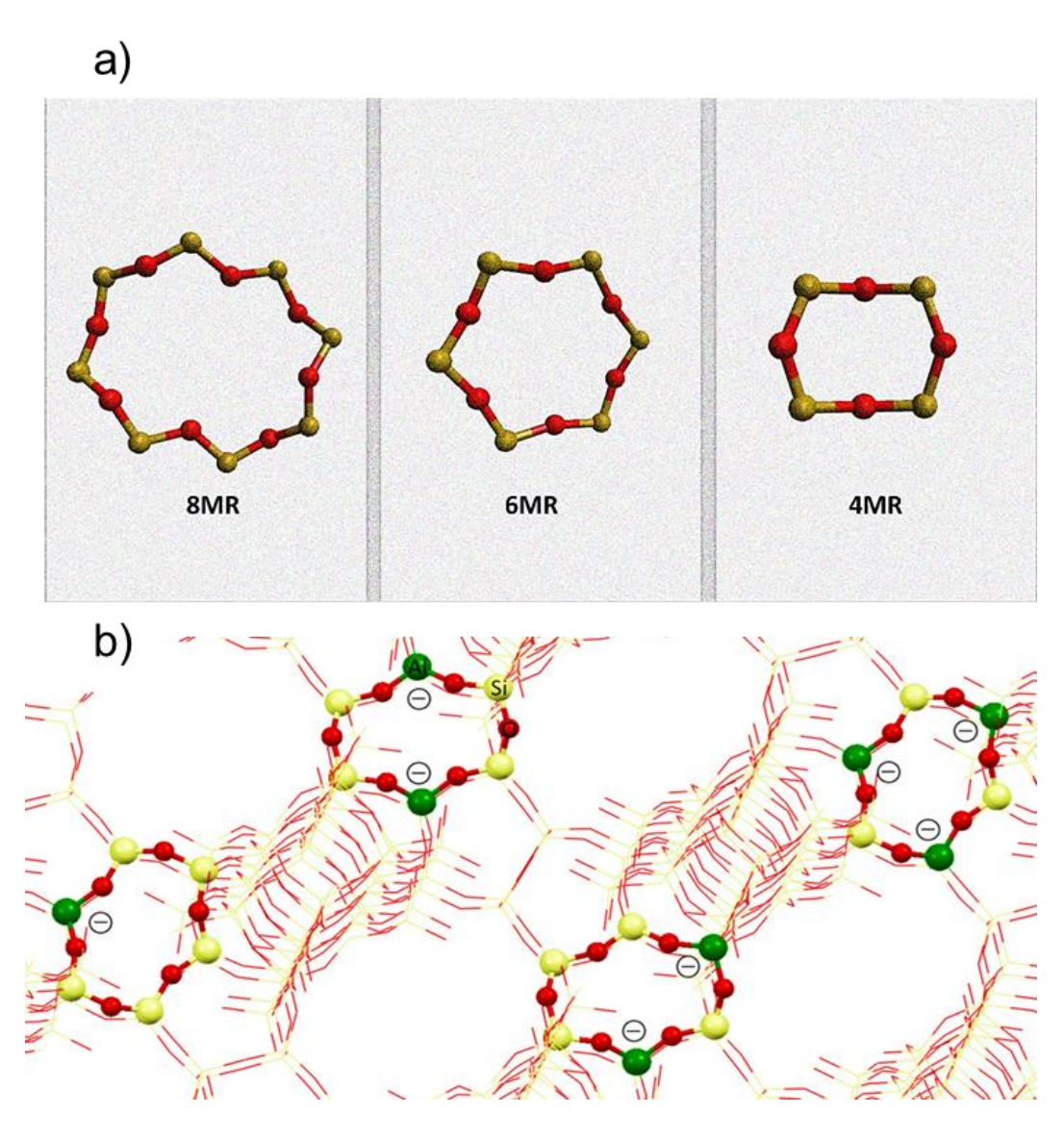


Figure 1.1. a) The representative rings (8-MR, 6-MR, and 4-MR) of CHA zeolite, and b) examples of allowed Al distributions in β -6MR sites, where qualitative rules on Al distributions in zeolites allow for one, two, or three Al T-sites. **Colour code**: O, red; Si, grey; Al, green. Adopted with permission from ref. ²⁸.

The siting and distribution of Al are also closely coupled with the location of charge compensating cations. The Si/Al ratio and the distribution of Al in the zeolite framework are key factors in influencing catalytic reactions. However, the nature and siting of the charge-compensating cation have a major influence on zeolite catalytic activity. Differences in coordination surrounding the cations in extraframework sites may result in cation-zeolite combinations with distinctive acid-base characteristics and/or enhanced redox chemistry ³³.

The framework Si/Al ratio controls cation exchange density inside zeolites, providing additional dimension for active site selection. All of these special characteristics suggest the possibility of designing molecular catalysts with enzyme-like selectivity and activity. In addition, Brønsted acid sites are formed when protons are used to balance the negative charge in aluminosilicate zeolites ³⁴. The protons bind to the lone pairs of the bridging oxygen atoms. The term Brønsted acidity is commonly used to refer to both acid strength and acid density. The acid density is straightforward; however, the acid strength is more widely discussed. The intrinsic acid strength is determined in principle by the electronic cloud density of a single acid site, which is influenced by charge dispersion within the zeolite framework and is directly related to the local electric field. The strength of well-isolated Brønsted acids in high-silica zeolites might be expected to be similar; yet, Brønsted acid sites of different zeolites have significantly different strengths. In the next section, we will discuss the metal-exchanged zeolite, especially relating to TMI distribution and location in the zeolite framework.

1.3 TMI Chemistry in Zeolite

The proper description of metal ions especially TMI is essential for an understanding of zeolite-based catalytic processes. Here we will survey the literature highlighting the most prominent work on the mode of attachment and coordination of TMI in zeolites. In addition, we will emphasise that a better description of the activation of O₂ and oxo complexes of TMI in zeolites can establish important concepts in the applications of NH₃-SCR.

1.3.1 Location and Distribution of TMI in Zeolite

The structural and coordination chemistry of TMI-exchanged zeolites has been extensively studied. Here we focus on Cu, Co and Fe exchanged systems which are of greatest relevance to catalysis.

Considering the Fe systems first, It is evident from the experimental findings that the NH₃-SCR reaction occurs on several Fe-sites with distinct energetics, hence leading to different turnover frequencies ³⁵. Liu *et al.* reviewed different active sites of Fe, including monomeric, dimeric, and oligomeric type species as shown in Figure 1.2a ³⁶. They investigated Fe complexes in ZSM-5 and concluded that the distribution of mononuclear sites of Fe species (FeO)⁺ is not sensitive to the local environment while binuclear sites preferentially reside in the 8-MR.

Considering monomeric species (FeO)⁺ as an active site, a series of reaction pathways were explored and the energy for various species was stated by Li *et al.* ³⁷ and Bruggeman *et al.* ³⁸ to envisage the N₂O decomposition in the NH₃-SCR process. It is straightforward to propose that when two exchanged Fe species are in close proximity, the dimer of Fe species is readily generated which is evident from the previous reports ^{39, 40, 41}. These dimer species are extensively studied by DFT and are suggested to be active species in NH₃-SCR reaction for N₂O and NO decomposition ⁴²⁻⁴⁵. Brandenberger *et al.* performed a Poisson distribution, a method used for the prediction of rare but significant events in a fixed interval to estimate the fraction of content of different Fe species in zeolites ⁴⁶. Notably, the results obtained through this method have a satisfactory accuracy which is unveiling the correlation of the degree of Fe exchange species with active sites. Consistent with the observation, there is a consensus that

more than one site can be present in the zeolite, and the monomeric Fe ions will predominate only for low levels of exchange ⁴⁶.

The diffuse reflectance spectra of Co^{2+} ions in the Co-zeolites, including BEA and ZSM-5 indicate the presence of three sites denoted as α , β , and γ^{47-49} . The positions and the structure of these sites in the local framework of ZSM-5 are shown in Figure 1.2b. From the synchrotron-XRD analysis, these sites (α , β , and γ) are also confirmed for other TMI divalent cations such as Cu^{2+} 50 and Ni^{2+} 51 in zeolites. These sites are coordinated to 6-MR, created by the pentasil rings of this framework. However, the case study in Cu-zeolites is quite similar to Fe-zeolites, and there is considerable debate, focusing on the location of cations as active sites. Izquierdo *et al.* 52 and Morpurgo *et al.* 53 employed DFT-ONIOM and Cluster methods to calculate the isolated as well as the dimer species of Cu in Cu-ZSM-5 as case examples, Their study revealed that both species can catalyze NO decomposition but the process needs extra energy to overcome the energy barrier in the case of dimeric Cu⁺54.

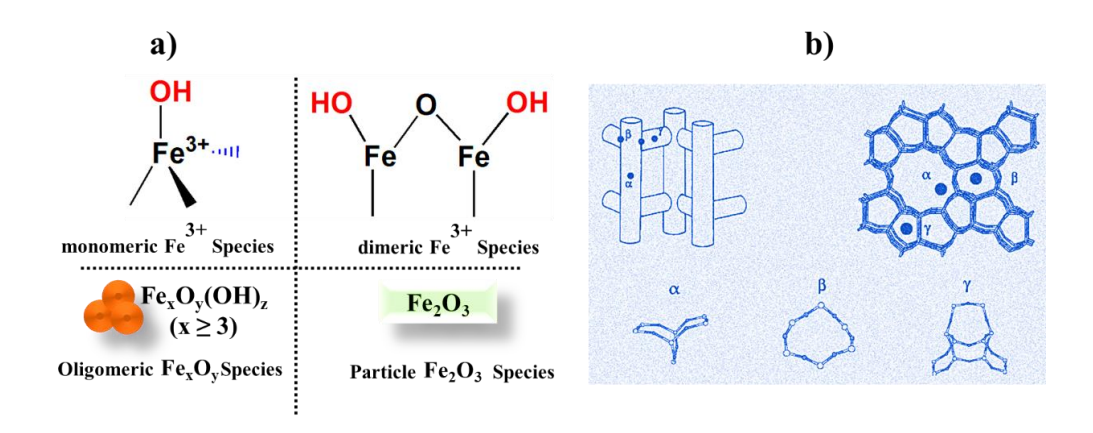


Figure 1.2. a) Schemes of four possible Fe species in Fe-zeolites and b) Co siting in ZSM-5 structure, according to ref. 55 . Local framework structures of the a-, b-, and c-sites.

The zeolite, chabazite (CHA) stands as an exception in this scenario because of its unique structure and relatively small pore size $(0.37 \times 0.42 \text{ nm}^2)^{56}$. The isolated Cu⁺ species is generally believed to be an active site which is located in the 6-MR of CHA. This observation was proved

by Mcewen *et al.* studied Cu-SSZ-13 and Cu-SAPO-34. They performed periodic DFT calculations and confirmed that it is the 6-MR of CHA that hosts the isolated Cu⁺ species ⁵⁷. A similar statement was made by Uzunova *et al.* performing extensive calculations *via* virtue of DFT in periodic models ⁶¹. However, Cu²⁺ species are considered to be more stable in the 8-MR of CHA. Work reported later in this thesis will show that extraframework Cu²⁺ ions are more stable when they are present in 8-MR as compared to 6-MR by a margin of 0.3 eV. This finding is similar to that reported in reference ⁵⁸. In addition, Goltl *et al.* established a new theoretical approach to combine DFT calculation and statistical approaches to predict the position of isolated Cu²⁺ species in Cu-SSZ-13 while varying the exchange level of Cu ⁵⁹. The allocation of the cations amongst the various active sites for a range of exchange levels is shown in Figure 1.3. Experimentally, the presence of isolated Cu²⁺ species in Cu-CHA during NH₃-SCR has been demonstrated by Korhonen *et al.* employing the UV/Vis technique ⁶⁰.

The contribution of Rice and coworkers in this regard deserves attention ^{61, 62}. They examined several divalent transition metal cations including Zn, Pt, Cu, Ni, and Co in ZSM-5, and investigated the coordination, location, stability, and structural properties using the gradient-corrected DFT technique. The coordination of these ions at both isolated charge-exchange sites and pairs at adjacent exchange sites was modelled. The data obtained indicate that Fe²⁺, Cu²⁺, Ni²⁺ and Co²⁺ are coordinated to 5-MR containing 2Al, whereas Rh²⁺, Pd²⁺, Pt²⁺, Zn²⁺ and Ru²⁺ are preferentially coordinated to 6-MR of ZSM-5.

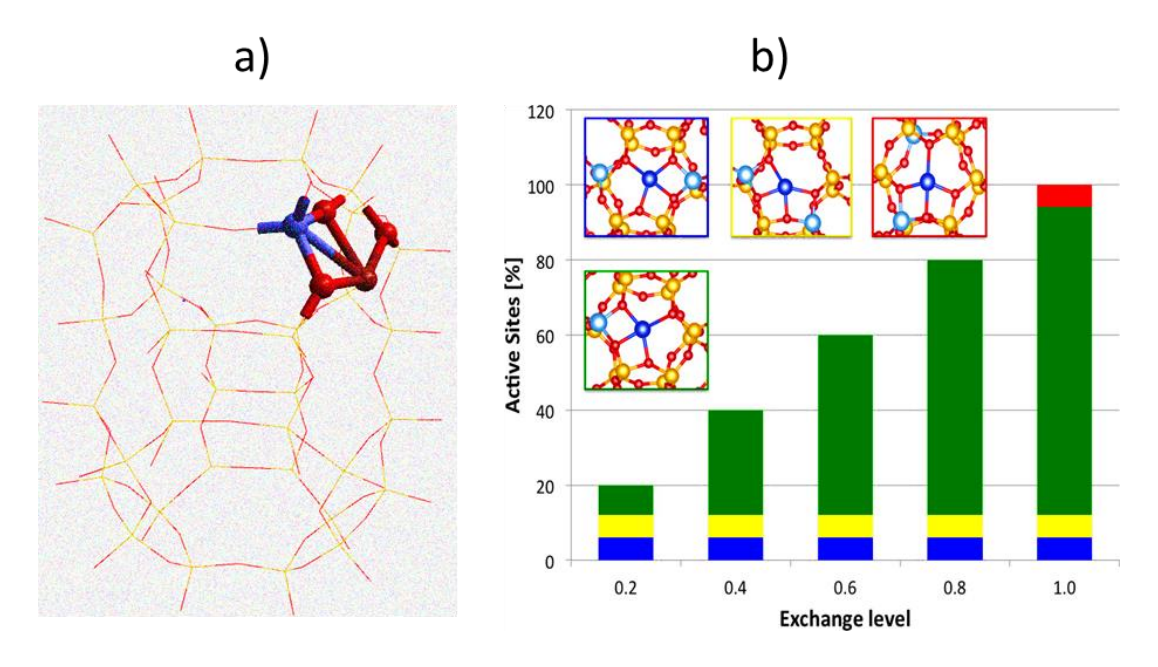


Figure 1.3. a) Cu-SSZ-13 location and coordination b) the distribution of active sites in Cu(II)-SSZ-13 at different ELs obtained from total energy calculations. At an EL of 0.2, only the most stable sites (a) (blue), (b) (yellow), and (f) (green) will be occupied. With increased EL, the occupation of the site (f) increases, and only at the end site (c) will it be exchanged. Comparison with experiment 63 indicates that the most stable sites (a) and/or (b) are the active centres in the self-catalytic reduction of NOx. Reproduced from Ref. ⁵⁹.

The nature of the metal species which dominates in the NH₃-SCR process remains a challenge for both experimentalists and theorists. The rearrangement of the zeolite framework after the incorporation of cation was studied by Skenak *et al. via* periodic DFT molecular dynamics ⁶⁴. A similar study conducted by Uzunova *et al.* ^{65,66}, examined the location of Cu(I), Cu(II), and Co(II) at the extra framework sites *via* periodic DFT calculations and demonstrated the adsorption of NO species on these sites. We note that the rearrangement and the location of cations are also affected by other factors such as temperature. The performance and reactivity of metal-exchanged zeolites presumably depend on the local structure of the metal ions. Indeed, the understanding of the coordination and location of metal ions in the framework of zeolite is vital to explore the structure-relationship which is a key topic in theoretical and experimental studies.

1.3.2 Coordination of TMI to the Lattice and Activation of Oxygen

Transition metals, such as cobalt, copper, iron, and nickel, can be incorporated into zeolite structures through several synthesis methods. The coordination of these transition metals within the zeolite structure is dependent on factors such as the size and charge of the metal ion, the nature of the zeolite framework, and the synthesis conditions. The coordination of transition metals in zeolites is of great interest due to its potential applications in catalysis, gas separation, and ion exchange. The presence of transition metals in zeolites can modify their chemical and physical properties, leading to enhanced reactivity and selectivity in catalytic reactions. The coordination of transition metals in zeolites can be studied via a range of analytical techniques, including X-ray diffraction, X-ray absorption Near Edge structure (XANES), and Extended Xray absorption fine structure (EXAFS). Coordination of TMI to specific exchange sites leads to a strong distortion in the framework of zeolites, as revealed by detailed ab initio quantumchemical analysis ⁶⁷⁻⁶⁹. Dooryhee et al. studied nickel ion exchanged Y zeolite (Si/Al=2.25) by X-ray absorption and diffraction at room temperature and suggests that there is a significant distortion in the shape of the sites, indicating that the framework of the zeolite adjusts in response to the migration of nickel during the process of dehydration ⁷⁰. There are several reasons i) first, are the strong electrostatic interactions between the cations and the framework; and second, TMIs where possible expand their coordination number to get a stable configuration within the zeolite framework. Initially, the exchanged ions occupy the lowest energy positions and maximize their coordination number. The loading of the metal, which is only partially determined by the Al content can also affect the coordination of TMI to the lattice O. At low loading, the majority of Fe ions are present at the ion-exchange positions as a monomer while at higher loading, oligomers of Fe are formed which are mostly reside inside the micro-pores of zeolites ⁷¹.

From the perturbation of T-O bonds, it was observed that NO and CO are too weak to coordinate with Co ions as compared to framework O 72 . However, H₂O and NO₂ are comparatively made a strong bond to the cation, which opens a door for the TMI as a catalytic centre that can drive a reaction if the coordination site is flexibly open with a window that can accommodate the guest molecule. Similarly, in MFI the sites which contribute to the catalytic reactions are the 10-MR rings with a diameter of ~ 0.55 nm where TMI is located either in straight or zigzag channels, which means that a smaller pore size makes it difficult for the reacting molecules to access the active sites. Noting the importance of the pore size, the same approach can be made for other zeolites. The advantage of larger pore sizes is that they not only allow rapid diffusion of reactants to gain access to the active sites but also make the desorption process more favourable. Moreover, they have several other advantages such as i) liberating the active site for the next reaction and ii) avoiding the chances of side reactions that affect the selectivity of the process. However, on the other hand, SSZ-13 is a small-pore zeolite that exhibits excellent activity (when doped with Cu) in the selective catalytic reduction (SCR) of nitrogen oxides (NOx) with ammonia (NH₃).

The self-reduction of metal ions during the reaction has a key impact on the coordination of the metal to the zeolite framework. As evidenced in the literature, under high temperatures and an inert atmosphere, TMI-Zeolites (Co³⁺, Fe³⁺, Cu²⁺) can undergo auto reduction. The auto reduction of Fe³⁺ to Fe²⁺ under He treatment is characterized by X-ray absorption spectroscopy ^{73,74}. The switching behaviour of Fe³⁺ to Fe²⁺ is attributed to the desorption and dehydration of Fe³⁺(OH)₂ to liberate O₂ and form two Fe²⁺(OH) species ⁷⁵. Another assumption regarding such exchange is that bare Fe³⁺ only coordinates with oxygen and can be hardly mediated in high silica zeolites due to the inadequate negative charge within the zeolite lattice to counterbalance the trivalent ions ⁷⁶. The characterization of such trivalent ions especially Fe³⁺ is quite

challenging. The identification and the chemistry of the Fe ions in an aqueous solution are, of course, well defined from the existence of various mono-, di, and poly- complexes bearing different species such as oxygen, water molecules, and OH groups (depending on the reaction media, especially. pH) ^{77, 78}. For example, Fe³⁺ exists only in the acidic solution (pH < 3), where proton exchange easily occurs. Furthermore, Fe ions (Fe²⁺ and Fe³⁺ ions) can be incorporated into the high silica zeolites; however, the steaming of ferrisilicates induced the abstraction of Fe from the framework and introduced it into the extra-framework sites ⁷⁹.

Pierloot et al. investigated the local environment of Cu²⁺ in zeolites Y (FAU), A (LTA), and ZK-4 (LTA) and showed that Cu is coordinated to the four framework oxygen atoms 80. For the low Si/Al ratio, the distance of Cu to the four neighbouring oxygen atoms was reported as 1.9 Å, 2 Å, and 2.2 Å for the first two, third, and fourth respectively. However, with increasing Si/Al ratio the interactions of Cu with neighbouring oxygen also changed with three oxygen atoms at ~1.95-2.0 Å and with the fourth distant one at ~2.4 Å. Owing to the need for hydrothermal stability in the NH₃-SCR reaction, zeolites with higher Si/Al are needed, and as such, the latter model is more appropriate. Commensurate with this study, the single-crystal study conducted on Cu- Y also supported this observation showing that Cu (at site II) coordinated with three oxygens at 1.85-2.0 Å and the fourth one at 2.5 Å 81. The resulting geometry of Cu, in this case, corresponds to the distorted square-planar Cu²⁺ located at one side of the 6-MR. In FAU, the TMI preferably resides in the hexagonal prisms after dehydration. At higher dosages, TMI occupies the most accessible sites (sites II and III). In this case, sites I' and II are important as both belong to 6-MR. In MFI, the TMI is either located in 10-MR or at the intersections of the channels. In contrast, TMI coordinated in other member rings occupied different T sites 82.

1.3.3 Spectroscopic Analysis of TMI in Zeolite Frameworks

The techniques used to probe the detailed textural and structural properties of TMI species in zeolite frameworks are summarized in Table 1.2. The location and interactions of these TMI in zeolites have a considerable impact on the stability and activity of the zeolite. Powder X-ray Diffraction (PXRD), and XAS spectroscopy are the most widely used techniques to characterize TMI species in zeolites. The phase study and the location of TMI ions are mainly identified through the XRD technique. For example, Fickel et al. explored the Cu²⁺ speciation in the SSZ-13 framework using the Rietveld refinement of synchrotron-based XRD 83 (Figure 1.4a) and suggested that Cu²⁺ ions mainly occupied the 6-MR. XAS is widely used to locate the coordination environment of the Cu ions in CHA (Figure 1.4b). Using XAS, Deka et al. found that Cu²⁺ ions are coordinated to three oxygens atoms in the 6-MR of SSZ-13 ⁸⁴. Further to Deka's study, Korhonen et al. through XAS techniques confirmed that in the Cu-SSZ-13 the isolated Cu-species coordinated with the three oxygen atoms of the 6-MR in the cage of CHA ⁶⁰. Through operando XAS techniques, they showed that there is a mixture of Cu²⁺ and Cu⁺ ions following steady-state standard NH₃-SCR conditions ^{60, 85}. Deka et al. performed XAFS analysis on Cu-SAPO-34 and correlated the excellent SCR activity to the active sites of isolated Cu²⁺ species located in the 6-MR of Cu-SAPO-34 ⁸⁶.

Table 1.2. Comparing Various Methods for Identifying Metal Species in Zeolites: Strengths and Limitations of Different Characterization Techniques

Acquired Information	Method	Advantages	
Morphology	Cs-STEM	Atomic resolution	
Particle size	Cs-STEM	High spatial resolution	
Metal location	Cs-STEM	Direct observation of metal single sites and clusters	
Coordination number	EXAFS or XANES	Atomic resolution	
Bond distances	EXAFS or XANES	Sensitive to the coordination environment of the metal	
		species	
Oxidation state	EXAFS or XANES	Measurement of the whole sample	
Coordination env.	SSNMR spectroscopy	Feasible to be performed under in situ/operando conditions	
Identification of Functional	Infrared spectroscopy	Study the surface properties of materials are linked to the us	
Groups		of probe molecules	

UV/Vis. and IR spectroscopies can be used to gain further insight into the structural properties of cations, hydroxyl groups as well as other extra framework species under operando or in situ conditions ⁸⁷. The existence of isolated Cu²⁺ species in Cu-CHA during NH₃-SCR has been demonstrated by Korhonen et al. employing the UV/Vis technique 60. Vibrational frequencies of adsorbed probe molecules (e.g. NO, CO, and NH₃) are used to confirm the chemical environment of cation sites in zeolites ^{88, 89}. The nature of Cu ions present in the Cu-SSZ-13 zeolite at different ion exchange levels was characterized using H₂-TPR and FTIR techniques by Kwak et al. 90. They collected results from both H2-TPR and FT-IR data to determine the position of Cu²⁺ ions under different ion exchange levels; their data suggested that Cu²⁺ ions located in 6-MR of CHA at the low exchange level and occupied the large cage when the level of exchange increases. Further, DRIFTS is extensively used to explore the reaction mechanism ^{91, 92}. For example, Wang et al. performed DRIFTS and revealed that under low-temperature SCR reaction first NH₄NO₃ intermediates are generated followed by their subsequent reduction by NO 93. To probe the surrounding environment and the existence of cations, the EPR is one of the powerful techniques used to determine the concentration, location, oxidation state, symmetry, and coordination number of TMI ^{87, 94, 95} (Figure 1.4c). Gao et al. reported a detailed study quantifying the isolated Cu²⁺ ions using Cu(II) imidazole solution employing the EPR technique ^{94, 96}. Following the *in situ* EPR analysis, Yu et al. identified the oxidation state of Cu species during the SCR reaction using Cu-SAPO-34 as a catalyst ⁹⁷. They showed using EPR that during NH₃-SCR catalysis, Cu(II) ions are reduced to Cu(I) when exposed to NH₃, and then reoxidized to Cu(II) when the adsorbed NH₃ is consumed by the purging NOx environment.

The comparative study of SAPO-34 and SSZ-13 was performed by Sue *et al.* who found that SAPO-34 was much more stable than SSZ-13, although, under hydrothermal ageing, both samples undergo desilication (in SAPO-34) and dealumination (in SSZ-13) ⁹⁸. To determine the acidity and redox properties of TMI-Zeolites, temperature-programmed (TP) techniques are normally used. NH₃-bonded to the zeolite was investigated by Giordanino *et al.* ⁹⁹ using NH₃-TPD. They identified three types of adsorbed ammonia species, which can participate in SCR reactions. At low temperatures (T<400°C), the NH₃ linked to Cu-site appears to be more stable, whereas, at a higher temperature (T>400°C), the NH₃ bonded to Brønsted sites predominates. Moreover, NH₃-TPD can also determine the poisoning of acidity by metals such as Pt, Zn, and the effect of hydrothermal ageing on acidity ^{92,100}. H₂-TPR study revealed that Cu²⁺ ions with different ion exchange levels can occupy various cationic positions as studied by Kwak *et al.* ⁹⁰. In the case of a low ion -exchange (IE) level, the Cu²⁺ ions occupy the 6-MR while for a high ion exchange level, they occupy the large cage of CHA¹⁰¹ (Figure 1.4d).

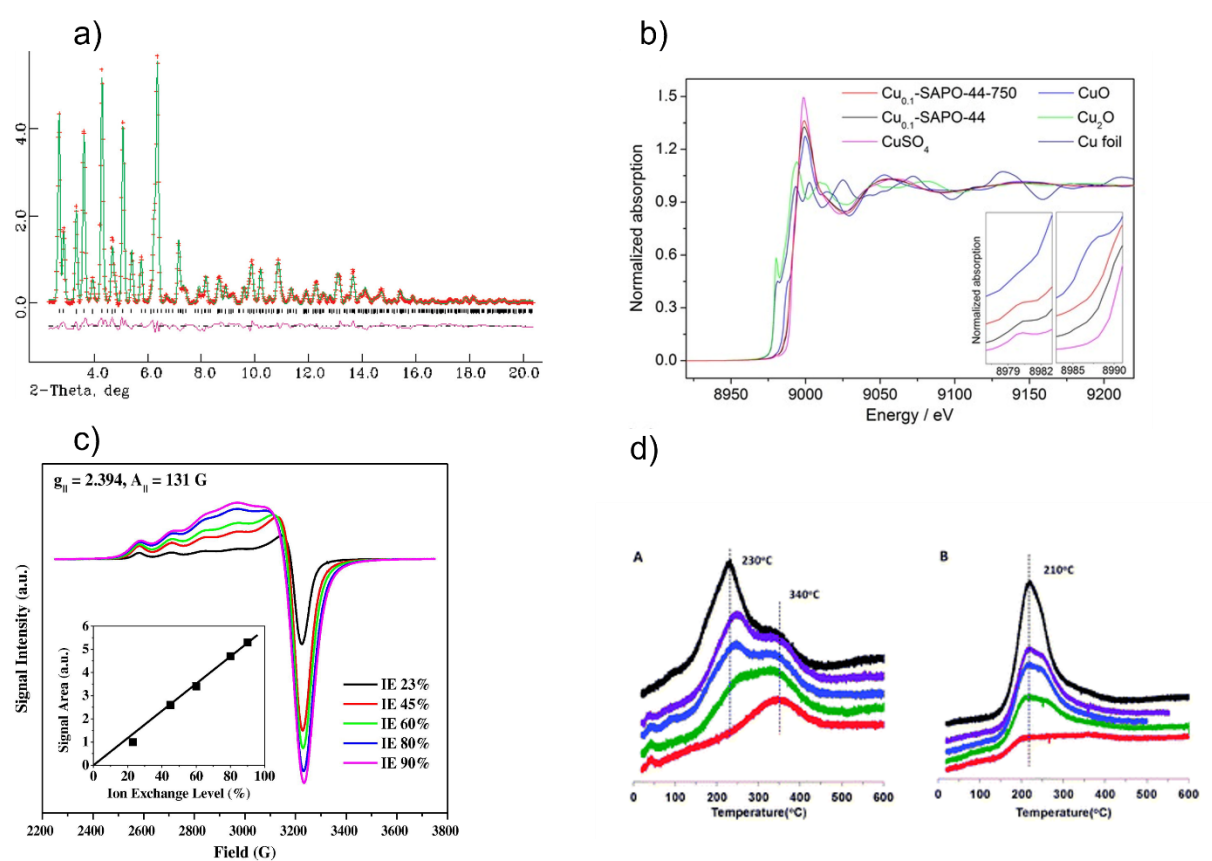


Figure 1.4. Characterization techniques for the isolated Cu²⁺ active sites (a) XRD patterns with observed (crosses) and calculated (line) with the relative difference curve (bottom line) of the refinements of Cu-SSZ-13 patterns,⁸³ (b) Normalized Cu K-edge XANES spectra for Cu-SAPO-44 catalysts and the reference samples,¹⁰² (c) EPR spectra of hydrated Cu-SSZ-13 samples measured at 155 K,¹⁰³ (d) H₂ consumption profiles during H₂-TPR on Cu-SSZ-13. Cu ion exchange level: 20 % (red), 40 % (green), 60 % (blue), 80 % (purple), and 100 % (black)-bottom to top ⁹⁰.

1.3.4 TMI Location: Perspective

The NH₃-assisted SCR chemistry is not straightforward due to the formation of several known and unknown species. Hence, the detailed reaction mechanism for binding and transformation at the active site is still under discussion. Smeets *et al.*¹⁰⁴ and Vanelderen *et al.*¹⁰⁵ have studied the coordination chemistry of TMI (Cu, Fe, Co) in zeolites and demonstrated their ability to activate O₂ and oxo-complexes, in particular, to explore the coordination chemistry of the activated species. It is also evident from the literature that the generation and existence of such species in zeolites have a connection with the topology and framework of the zeolite, and, therefore, the key to controlling the catalytic chemistry of zeolites is to understand the intimate

structural relationship of zeolite framework to TMI, which, however, could open a new door to designing novel materials.

1.4 NH₃-SCR of NOx on TMI-Zeolites

In the 1980s, Cu-exchanged zeolites appeared as an emerging contender in terms of high activity and stability for the SCR of NOx discovered by Iwamoto *et al.* ¹⁰⁶. Since then, zeolites have been very widely studied for this key catalytic reaction. The term de-NOx is often used for the remediation of both NO and NOx, present in exhaust gases. Considering the availability and activity, a small number of TMIs (Cu, Fe, Cr, and Ag) have been established as viable contenders for NH₃-SCR unlike other TMIs (Mn, Co, Zn, Ni, La) ¹⁰⁷⁻¹¹⁵. As noted, the effective performance of zeolites in SCR of NOx is mostly reported with Cu-based zeolites. However, zeolites e.g. ERI, AEI, CHA, and AFX have also been explored with the Fe ions as an active site ¹¹⁶. Some comparison regarding reaction kinetics for both Fe and Cu was also made by Gao and co-workers ¹¹⁷. The fresh Fe-zeolites are comparatively less active than Cu-zeolites under wet conditions (Figure 1.5) ¹¹⁸. To compare the fresh and aged versions of both catalysts, the Fe-version retained more activity than the Cu-version after ageing under high temperatures (above 500°C).

In the so-called "standard NH₃-SCR" reaction in which NO is treated in the presence of ammonia and oxygen to generate N_2 (Eqn. 1.1) ¹¹⁹.

$$4NO + 4NH_3 + O_2 \rightarrow 4N_2 + 6H_2O.$$
 (1.1)

The formation of NO_2 species facilitates the oxidation half-cycle and hence leads to establishing a link for a so-called fast SCR reaction (Eqn. 1.2) 120 .

$$NO + 2NH_3 + NO_2 \rightarrow 4N_2 + 3H_2O.$$
 (1.2)

On the other hand, there is the NO-activation pathway (Eqn. 1.3) proposed by Janssens *et al.* ¹²⁰, which can proceed with the same reduction step as the fast-SCR; however, in the "NO-activation" cycle, the rate does not depend on the concentration of NO₂ while it is dependent on the concentration of NO₂ in the fast SCR ¹²⁰.

$$3NO + 2NH_3 + O_2 \rightarrow 2N_2 + 3H_2O + NO_2.$$
 (1.3)

As noted, Cu and Fe are especially effective since both metals have excellent redox capability (Table 1.3). Notably, Cu-zeolites were found to reach the onset of the highest performance at lower temperatures whereas Fe was mainly seen to exhibit the maximum activity at higher temperatures, as has been widely reported in the literature. We note that the performance of Fe-ZSM-5 appears to be highly dependent on the amount of NO₂ present in the gas mixture and is the rate-determining step in NH₃-SCR ¹²¹. In addition, the rate of the fast SCR reaction over Fe-zeolites is slow as compared to the standard SCR reaction ¹²². It is also arguable that Fe-based catalysts are more prone to be affected by the NH₃ inhibition effect ^{123, 124}. Further comparison between Cu and Fe zeolites showed that Cu is less sensitive to NO₂ ^{125, 126} and is, therefore, under standard SCR conditions Cu is expected to exhibit better activity than Fe at a lower temperature. Recently, the investigation of Fe and Cu has been moved one step further combining both metal ions (used monoliths made up) in different sequential compositions ¹²⁷. Commensurate with this study, Kucherov *et al.* modified a series of Fe-Beta with the introduction of various amounts of Cu contents ¹²⁸.

Table 1.3. List of the TMI-Zeolites tested in SCR of NOx with NH₃.

Top.	Material	M	Si/Al	M/Al	NO/NH ₃ (ppm)	T-range 90% NO conv. (°C)	Ref
СНА	SSZ-13	Cu	9.0	0.18	500/500	200–500	129
		Cu	12	0.20	35/350	175–550	130
		Fe	12	0.20	350/350	360-500	131
AEI	SSZ-39	Cu	9.1	0.32	500/530	270–550	132
		Fe	8.0	0.1	50/60	350–550	133
AFX	SSZ-16	Cu	4.5	0.23	500/500	200-500	129
		Fe	5.2	0.1	50/60	350-550	134
DDR	Sigma-1	Cu	16	0.14	500/500	300-350	129
ERI	LEV	Cu	5.2	0.3	500/530	500-550	134

The ammonia-assisted SCR is a particularly effective reaction to convert one of the major harmful gases such as NOx into N₂, thereby mitigating NOx emissions in the exhausts of power plants and diesel engines. For stationary NH₃-SCR, the preferred catalyst is still vanadium oxide. However, mobile applications have highly dynamic reaction conditions, with the gas flow rate of the lean-burned exhaust gases, and varying temperature demands. They, therefore, requires catalysts that will not only be able to show high activity at low temperatures (< 300°C) but also have better hydrothermal stability at elevated temperatures (< 300°C) ^{135, 136}. The unexchanged zeolite is not, therefore, require catalysts that will not only be able to show high activity at low temperatures (< 300°C) but also have better hydrothermal stability at elevated temperatures (< 300°C) ^{135, 136}. The unexchanged zeolite is not active, as it requires the metal which provides redox-active sites within the zeolite for corresponding SCR reactions. Zeolite Y (FAU), mordenite (MOR), ZSM-5 (MFI), and BETA (BEA) have received considerable attention owing to their applications in catalysis and stability under different temperature conditions. Recently, medium-pore size zeolites such as ZSM-5, and mordenite were thought to be more active than larger pore sizes (e.g. BETA, USY, and Y); and, in recent years more focus is on smaller pore size zeolites mainly with the CHA topology ^{137, 138}. Although, many other TMIs as mentioned earlier have also been explored as potential candidates; however, they appear to have a lesser capacity so, to date, Cu and Fe have been the main focus of research.

In contrast, it is argued by Merberger *et al*¹³⁹. that at low temperatures, nitrate participation in NH₃-assisted SCR reaction is unlikely as it appeared only after the reaction, suggesting that they are not involved in the NH₃-SCR reaction. While at high temperatures, the ammoniated-Cu complex decomposes, and the Cu ion loses an NH₃ ligand as well as its mobility. Subsequently, Cu ions become attached to the wall of zeolite and hence lose their ability to form dimers dynamically and activate oxygen. It is, therefore, conceivable that the oxygen-activated NO step described by Janssens *et al*. ¹²⁰ becomes an appropriate step in NH₃-SCR at high temperatures. Still, the remaining gaps in SCR reaction need to be filled and more experiments (especially high temperature-driven reactions) are required to understand the detailed chemistry behind the NH₃-SCR mechanism over Cu-CHA. Further accurate modelling studies are also clearly needed.

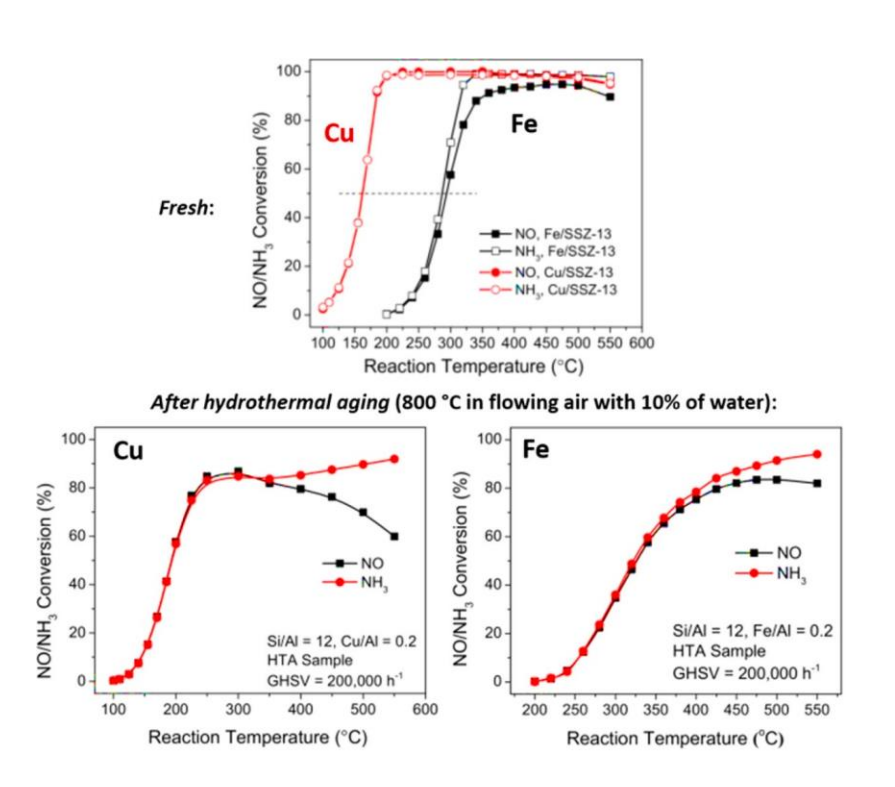


Figure 1.5. Comparing Cu and Fe-SSZ-13 in standard, wet SCR before (fresh) and after hydrothermal ageing. Conditions in the inset. Adapted with permission from ref (¹¹⁸). Copyright 2015 Elsevier. Further work regarding Fe speciation, their transformation, and loading effects is discussed by Peden *et al* ^{140, 141}. In addition, the incorporation of Fe into small pore zeolites was studied by

Martin *et al* ¹³³. They developed a one-pot method to prepare Fe-exchanged zeolites, which they compared with the post-synthetically exchange method. After ageing, the post-synthetically exchanged systems performed less well than the one-pot zeolites, indicating that the latter retain their activity better. The introduction of Fe into zeolite should be carefully undertaken.

Although Fe-exchanged zeolites are not as widely studied as Cu for SCR of NOx decomposition, the Fe in pentasil ring zeolites has attracted considerable attention for its outstanding stability for NOx conversion in the presence of high content of water. Fe-ZSM-5 is also active in the SCR of NOx with olefins ¹⁴² or paraffin (C₃-C₄) ¹⁴³ but in the presence of methane, it is not so efficient ¹²⁷. However, in the presence of NH₃, it is extensively used as a potential contender for SCR of NOx decomposition Although Fe-exchanged zeolites are not as widely studied as Cu for SCR of NOx decomposition, the Fe in pentasil ring zeolites has attracted considerable attention for its outstanding stability for NOx conversion in the presence of a high content of water. Fe is active in the reduction of hydrocarbons, Fe-ZSM-5 is also active in SCR of NOx with olefins ¹⁴² or paraffin (C₃-C₄) ¹⁴³ but in the presence of methane, it is not so efficient ¹²⁷. However, in the presence of NH₃, it is extensively used as a potential contender for SCR of NOx decomposition ¹⁴⁴⁻¹⁴⁷.

Apart from Cu and Fe other TM metals including Mn have also been studied in the NH₃-SCR reactions owing to their various valence states and dynamic redox behaviour ¹⁴⁸⁻¹⁵⁰. Unsupported Mn oxide (MnO) is not an active reagent in the catalytic conversion of NOx however, Mn-exchanged zeolites have displayed excellent activity as explored by Nam *et al.* ^{151, 152}. They developed Mn(20)/ZSM5 and Mn(20)-Fe(10)/ZSM5, and tested them for NH₃-SCR NOx reaction. The injection of 10 wt% of Fe has boosted the catalytic activity

impressively and surpassed the mono counterpart Fe(10)/ZSM5 and Mn(20)-/ZSM5 under low-temperature treatment (below 250°C). Furthermore, it showed 80% conversion of NO into N_2 at 160°C while the Cu/ZSM5 and Cu/zeolites-based commercial catalysts convert only 40% and 30% at 160°C (NO/NH₃ = 500/500 ppm; O_2 = 5 vol%). We note that the role of Fe₂O₃ is to prevent MnO₂ from agglomeration, and as a result, NO can be easily oxidized on highly dispersed MnO₂ catalysts. Although, at high-temperature treatment (above 350°C) the deNOx ability of Mn-exchanged zeolite was comparatively lower than Cu and Co-exchanged zeolite, however, the increased content of Mn enhances the hydrothermal stability ¹⁵³.

1.4.1 Reactivity and Structural Complexity of TMI in Activated Materials

In this section, the role of TMI speciation; in particular, their formation and transformation in the zeolite framework, the activation procedure, and starting chemical composition are highlighted ¹⁵⁴⁻¹⁵⁶. Despite the extensive literature in this field, the complexities associated with TMI speciation in the zeolite framework mean there remain many uncertainties. The early study proposed that Cu-SSZ-13 acts as a single-site catalyst and indicated that the sole position for Cu ion in the dehydrated material is the plane of the 6-MR. However, recent studies suggested that CHA possesses several active sites for both Cu(I) and Cu(II) ions ^{119, 154, 155, 157}. The existence of these multiple sites of Cu may arise from the location of Cu-species being strongly dependent on the physio-chemical environment, the composition of the sample, and the Si/Al or Cu/Al ratio in the framework. In the next section, we discuss the metal speciation to understand the detailed chemistry of the TMI in zeolite under SCR conditions.

TMI-speciation and Activation

The activation of zeolites is a key step for both sorption and catalysis because it is necessary to evacuate water and other molecules to make active sites accessible for reactant species. In contrast, the residual H₂O or hydrocarbons (due to incomplete activation) may block the active sites or modify their activity ¹⁵⁸. It is generally considered that in ion-exchanged zeolites under aqueous conditions, the nature of copper is a hydrated Cu(II) species state. However, upon dehydration, hydrated Cu(II) species undergo progressive reduction to Cu(I) species under an inert atmosphere and elevated temperature ¹⁵⁶. Although several other reduction processes have been proposed, this type of reduction is specially described as "auto-reduction" or "self-reduction"; however, the lack of direct evidence of TMI-species formation and a clear picture of the whole redox reaction is still under investigation.

The presence of divalent [Cu(II)(H₂O)n]²⁺ complexes and their stabilization is favoured in where two framework Al ions are in close proximity. In this case, the dehydration may dissociate water molecules into [Cu(II)(H₂O)n]⁺ and H⁺ (Eqn. 1.4) and the two adjacent frameworks of Al atoms are balanced by these two cationic species, as has been confirmed from the DFT-supported x-ray emission spectroscopy (XES) and x-ray absorption spectroscopy (XAS) studied performed by Borfecchia *et al.*¹⁵⁹. They showed that [Cu(II)(H₂O)n]²⁺ species can be stabilized for higher temperatures (Figure 1.6) in an oxidative environment; otherwise, as a consequence of extra ligand loss they undergo "self-reduction". Alternatively, bare Cu(II) cations can be generated due to the dehydration of [Cu(II)(H₂On)]²⁺ complex (Eqn. 1.5). However, in those sites where there is only one Al in the proximity (1Al Z sites), the aqueous ion exchange leads to the formation of monovalent [Cu(II)(H₂O)n(OH)]⁺ complexes which do not require any water dissociation upon dehydration (Eqn. 1.6).

$$[Cu(II)(H_2O)n]^{2+} \to [Cu(II)(H_2O)n)^{2+} + (n-1)((H_2O) \uparrow \to [Cu(II)(OH)]^{+} + H^{+} \to Cu(I) + (OH) \uparrow + H^{+}.$$
(1.4)

$$[Cu(II)(H_2O)n]^{2+} \to Cu(II) + n((H_2O) \uparrow.$$
 (1.5)

$$[Cu(II)(H_2O)n(OH)]^+ \to [Cu(II)(OH)]^+ + n(H_2O) \uparrow \to Cu(I) + (OH) \uparrow.$$
 (1.6)

Cu-CHA (SSZ-13 and SAPO-34)

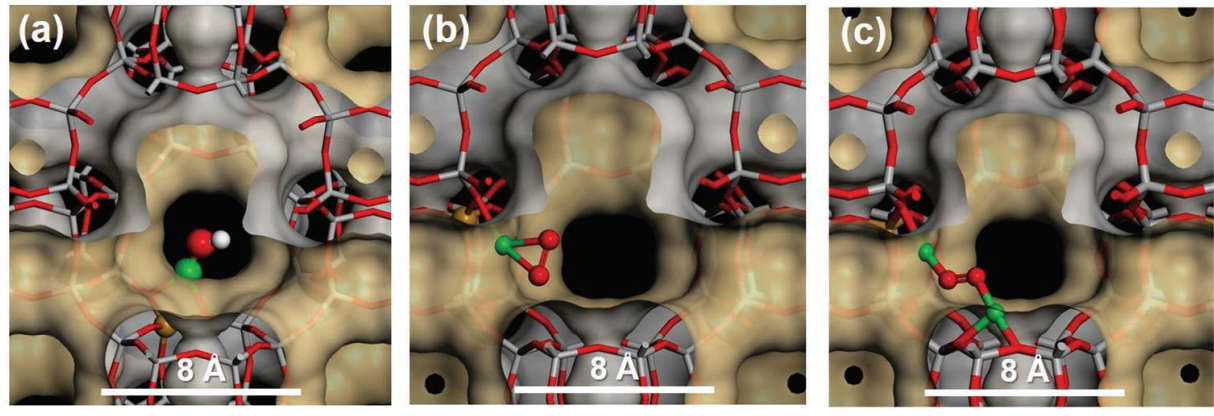


Figure 1.6. Proposed local sites of the copper species in the cage of the CHA at high temperature and under oxygen treatment. a) $[CuOH]^+$ b) $[Cu(II)O_2]^+$ superoxide species c) $[Cu(trans-\mu-1,2-O_2)Cu]^{2+}$. Adapted from ¹⁵⁹.

Paolucci *et al.* ⁷¹ conducted both computational and experimental analyses on coordinated Cu speciation under *operando* SCR, *ex-situ*, and *in-situ* conditions as a function of the catalyst composition. They demonstrated that the number, type, and chemical nature of Cu sites depends on the bulk composition of the zeolites as well as on the environmental conditions. In a notable addition, they demonstrated that the Cu speciation, mobility, and siting are strongly influenced by environmental conditions and are independent of the initial cation sites and framework of zeolites.

As mentioned, the location of Cu in the earlier study was thought to be confined to a single cationic site and located only just outside the 6-MR plane that coordinates to three oxygen atoms. As a consequence, this isolated Cu(II) species was initially proposed as the active site for NH₃-SCR. However, this observation was challenged by the temperature-programmed reduction (TPR) analysis ¹⁶⁰. In particular, in an H₂-TPR experiment, a single H₂ peak for the exchanged zeolite (20%) was evident at 340°C and under 2% H₂/Ar environment; an additional peak appeared at 230°C as the Cu-exchanged level increases. The intensity of the newly developed peak appeared to be proportional to the increase in Cu-loading and achieved a maximum intensity at 100% Cu-exchange. The intensity of the high-temperature peak which appeared at 340°C was observed to be stabilized at 40% exchange and remained unchanged with the increasing Cu-loadings, which is direct proof of the presence of two different Cu(II) sites that have markedly different redox barriers. In addition, the role of H₂O during TPR (2% H₂/Ar + 1% H₂O) was also explored in the same study. Under these reaction conditions, as the Cu-loading increased, two reduction peaks appeared and finally coalesced to a single peak at 210 °C for the 100%-exchange Cu sample.

Together with the evidence from FTIR, these findings were interpreted in terms of two types of Cu ions in Cu-SSZ-13: (i) Cu which is present in the 6- ring (6-MR), proposed to be primarily occupied at the low exchange levels and associated with the high-temperature TPR peak; (ii) Cu in the large cage responsible for the low-temperature H₂ peak and favoured at high exchange levels. The interaction of the H₂O molecules caused Cu ions to move away from the 6MR site towards the large cage of the CHA framework. Gao *et al.* addressed the impact of Si/Al and Cu/Al ratios on the redox behaviour of Cu-SSZ-13 catalysts and for this reason, they collected the H₂ TPR data for a set of samples¹⁶¹ (Figure 1.7). They analyzed the redox mediation of Cu-ions, which can be systematically tuned by changing the composition of the

materials. Both Cu/Al and Si/Al under low values favoured the high-temperature H₂ consumption peak. However, at low temperatures, the peak was also observed for hydrated catalysts. Notably, there was a significant shift of the hydrated sample peak (first reduction) to a lower temperature.

Hoj *et al.* demonstrated that Fe ions are mostly present as monomers inside the zeolite (at ion-exchange positions) at low loading while at higher loadings, they switch to oligomers ¹³. They find a notable relationship between the oxidation state and the catalytic activity indicating that the Fe monomer is the active species for SCR reaction however, although all monomers are not equally active. In addition, their study showed that the formation of the monomer as an active species is the rate-limiting step in the SCR reaction which may be due to the re-oxidation of Fe species leading to subsequent oxidation of NO to NO₂.

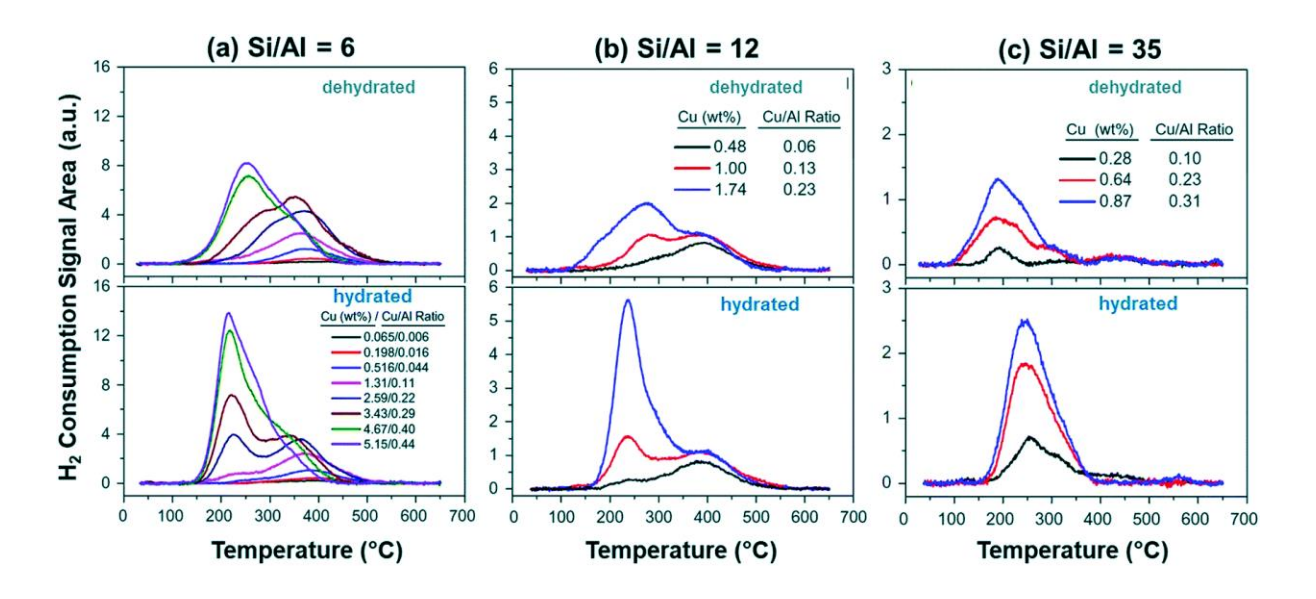


Figure 1.7. Cu-SSZ-13 H₂-TPR results with varying Cu dosage and Si/Al ratio; Top panel represents hydrated samples while the bottom panels report hydrated samples ¹⁶¹.

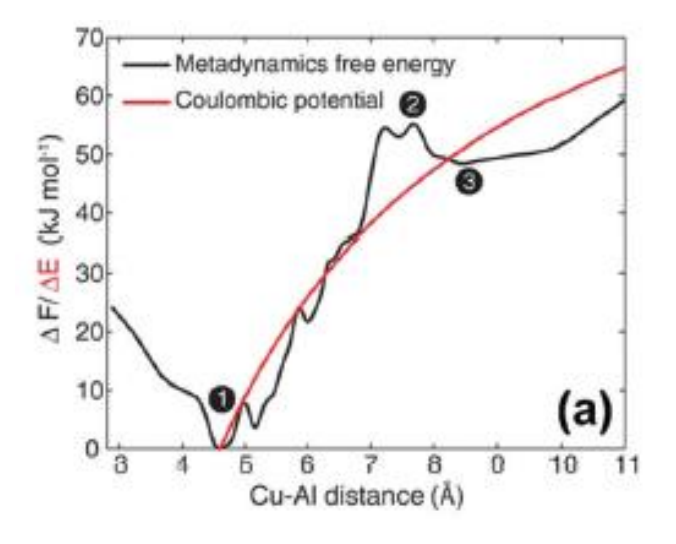
The catalyst composition has a profound effect on the TMI speciation and as such compositiondependent speciation has been reported in several studies, for example, in the case of Cu-zeolite where various species such as isolated, dimeric, and CuO have been reported ^{98, 162}. Some studies reported that Cu species are of two types in CHA zeolites, and the presence of such species within the cage depends on the Cu loading; the Cu²⁺/Cu⁺ dominate mainly at lower loading, whereas CuO occupies the CHA framework at higher loading ⁹¹.

As already discussed (in the "coordination of TMI to the lattice" section) under low loading, the majority of Fe ions are present as a monomer at the ion-exchange positions while at higher loading oligomers of Fe are formed which mainly reside inside the micro-pores of zeolites ¹³. Consequently, at high loading, the lower coordination of TMI to the lattice O may arise from the unavailability of low-energy sites. These sites are difficult to detect as they are masked by other species at high loading. The increased loading of TMI creates more heterogeneous sites which need extra-lattice ligands such as H₂O, and OH. The removal of these ligands under high-temperature pretreatment induces the reduction of TMI and is so-called "auto reduction". These reduced sites have interesting properties and are usually unable to adsorb the lattice oxygen at room temperature. However, the super oxo-complexes have been formed with Cr²⁺ and Cu⁺ in zeolites. At high temperatures, an interesting catalytic core of Cu-ZSM5 has been formed which is analyzed by a unique absorption band around 22700 cm⁻¹. The comprehensive analysis of Co-exchanged zeolites by Bellman et al. declared that not only Co³⁺ but also Co²⁺ were present in the oxide-like cluster and at the exchange position. Co³⁺ species, present in the oxide layer oxidized NO and itself reduced to Co²⁺ which is subsequently reoxidized to Co³⁺ upon exposure to gaseous oxygen, therefore, establishing an active Co³⁺/Co²⁺ pair. In contrast, the Co²⁺ located at the exchange position assists the chemisorption of NO and hence acts as a storage material for NO.

1.4.2 Modelling Mobility and Restructuring of TMI in NH₃-SCR

A key aspect of TMI zeolite catalysts is the location and migration of the TMI. According to *ab initio* molecular dynamics (AIMD) and density functional theory (DFT) studies, the migration of metal ions is limited by the electrostatic tethering of the framework. Furthermore, the presence of the heteroatoms, such as extra-framework cations and the number of coordinated molecules also change the coordination environment of the metal sites which ultimately affects metal migration. As discussed in the previous section, the nature and location of TMI in zeolites provides insight into the type of interactions within the zeolite framework.

Using molecular dynamics, Paolucci *et al.* ¹¹⁹ predicted the mobility of [Cu(NH₃)₂]⁺ inside the CHA framework employing *ab initio* metadynamics. They calculated the free energy (using Cu-Al coordination distance as a collective variable) in a CHA supercell of 72 sites (Figure 1.8a). The free energy minimum is located around at a distance of 4.7 Å which increases with a distance between Cu and Al until 8 Å when Cu ions move through 8-MR between two cages (Figure 1.8b). However, the free energy decreases again as the Cu ion enters the adjacent cage (product state) until the distance rises above 9 Å. Therefore, the maximum diffusion for a distance of 9 Å was predicted for [Cu(NH₃)₂]⁺.



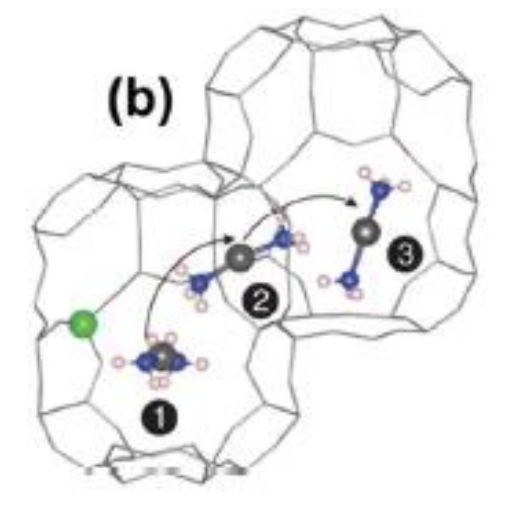


Figure 1.8. a) Free energy profile as a function of the Cu-Al distance; the mobile $[Cu(I)(NH_3)_2]^+$ species and Al atoms of CHA framework for charge balancing; (1) reactant $[Cu(I)(NH_3)_2]^+$ (2) transition state $[Cu(I)(NH_3)_2]^+$ (3) Product state $[Cu(NH_3)_2]^+$. For comparison, the computed point-charge model has also been reported as a red line 9 . b) $[Cu(I)(NH_3)_2]^+$ configuration. Cu; grey, N; blue, Al; green and H; white.

However, the large window of CHA is sufficient for the diffusion of gases which still allows Cu species to interact with the other species within the cage which can lead to cluster or dimer formation 119 . Cu-ZSM-5 has two main Cu sites (i) Cu ions in the close vicinity of one framework Al atom (540 nm emission) and (ii) Cu ions adjacent to two frameworks Al atoms (480 nm emission) with a distinguish IR band of Cu²⁺—NO at 1906 cm⁻¹ assigned to the N-O stretching. Cu²⁺ ESR is an axially symmetrical and split signal with the parameters of the parallel component gn = 2.33 and An =140—160 G $^{103, 163}$.

The restructuring of Cu²⁺ species from square-planar to distorted tetrahedron is a consequence of the Cu-NH₃ interaction. As illustrated previously, the isolated Cu ions are mostly present in the 5-MR while the [Cu-O-Cu]²⁺ is generated as a result of two proximal Cu species ^{164, 165}. This species was thought to be located inside the cage; however, migration of Cu ions can occur which affects the SCR deactivation reaction. In zeolite Y the sites SI, SII, and SIII for Cu²⁺, or Cu⁺ ion are considered to be more predominant locations for the Cu species ^{166, 167}. Site SI is mostly postulated as a dominant site in SSZ-13. However, the limited dimensions of the cavity do not allow the reactant species to pass through. ^{168, 169}. The site although sufficiently active is not accessible for the reactant molecules such as NO and NH₃. Commensurate with the above argument, site SII, located in the 6-MR is considered to be a potentially active site at low temperatures. The Cu ions are highly mobile and can easily migrate to the supercages, changing their coordination by reconstruction with the oxygen atoms within supercages. Similarly, at the SIII site, a dimeric species [Cu-O-Cu] could be formed as a result of interaction with the Cu of the SII site, demonstrating that mobility leads to the generation of multiple species ¹⁷⁰.

However, this phenomenon leads to poor SCR activity; and the migration of Cu ions has a major effect on the SCR deactivation reaction in diesel exhaust streams.

The solvent mobilisation is encompassed at the active sites (Cu ions). This active site has an effectual area of diffusion which significantly restricts its interaction with other active sites within the overlapping area. This dimer can provide the *in situ* multinuclear complexes for activation of O₂ and therefore, can act as an active site. Borfecchia *et al.* investigated the tricoordinated [CuOH]⁺ as a potent for O₂-activation while the bare bi-coordinated Cu⁺ ions were found to be the most dominant species in the 8-MR ¹⁵⁹. The existence of dimeric oxo-Cu species, in this case, appears to be unlikely which shows that monomeric [CuOH]⁺ species are mainly found in the Cu-SSZ-13, a potential contender in the SCR mechanism. Furthermore, the mobility of active sites may be controlled by the composition, structure, and electronic behaviour of the support which solvated these sites. Tuning these parameters may open new horizons in the designing of TMI-exchanged zeolite catalysts for NH₃-SCR reaction.

Yan *et al.* observed the key mechanism for the deactivation of the catalyst is the migration of Cu ions into the Al₂O₃ site, generating CuAl₂O₃ ¹⁷¹. Park *et al.* stated that the Cu which is mainly present either in square-pyramidal or square planner coordination reconstructs into distorted complexes after migration into Al₂O₃ ¹⁷². Recently, Kwark *et al.* compared Cu-SSZ-13, Cu-Beta, and Cu-SSZ-5 and concluded that although very few changes can be observed in the Cu species located in the SSZ-13, and Cu-Beta have CuO or Cu aluminate on the surface. In addition, they observed that even a small degree of Cu ion migration can result in a loss of activity under hydrothermal conditions ¹⁷³. On the other hand, the mobility of TMI ions can act as a sensor for monitoring the NH₃-SCR reaction as revealed by the *in situ* spectroscopic and theoretical studies, this discussion of which is, however, beyond the scope of this study ¹⁷⁴.

Overall, isolated TMI species with little interaction with neighbouring TMI ions could provide stable catalytic systems.

1.4.3 TMI Stability in Zeolites

Recently, it has been widely reported that small-pore zeolites containing metal ions (Fe, Cu, Co, Mn) are hydrothermally more stable than medium or large-pore zeolites ^{175, 176}. In particular, the incorporation of Fe into small pore zeolites leads to a hydrothermally stable NH₃-SCR catalyst ¹⁷⁷. However, conventional iron exchanged methodologies appear to be difficult as the size of the Fe³⁺ aqueous ions (9 Å) is larger than the pore size of the zeolite (3.5 Å) ¹⁷⁸. Martin *et al.* ¹³³. investigated the nature of iron-exchanged zeolite (prepared by one-pot method) using different characterization techniques. They discovered that the material (Fezeolite) synthesized through a one-pot procedure exhibited better NO conversion and hydrothermal stability, which can be attributed to the improved dispersion of iron following a one-pot synthetic protocol as compared to the conventional post-synthetic ion-exchange method. In addition, the same group prepared Fe-Beta zeolites using two different reaction media: i) alkaline conditions and ii) a fluoride media for the synthesis of iron-containing zeolites. A detailed study of the direct preparation of iron-containing was performed to obtain an insight understanding of how the physicochemical conditions of the synthesized catalyst influence the SCR-NOx conversion and the hydrothermal stability under severe conditions ¹⁷⁹.

Ruggeri *et al.* studied the temperature of hydrothermal ageing treatment and its effect on the duration of the Fe-zeolite catalyst ¹⁸⁰. They carefully examined the NH₃ adsorption, oxidation, and its reaction with NOx. The deactivation was very fast and the primary effect of hydrothermal ageing on SCR reaction was the oxidation of NH₃, standard SCR activities, and

the storage ability of NH₃. Additionally, the consequence of hydrothermal ageing on the SCR reaction is predicted by the NH₃ storage capacity. They conducted an experiment on the aged sample (calcined at 650°C) and then fed in ammonia (1000 ppm) at 200°C in the absence of water and oxygen. The adsorption dynamic of the experiment displayed the NH₃ inlet and outlet concentration profile. For the sample aged at 650°C the delay time was shorter and continuously decreased as the ageing temperature (A.T) increased. The change in the dynamic of the NH₃ outlet profile directly corresponds to the NH₃ storage.

The hydrothermal stability of Cu-CHA has been extensively studied recently and is considered the most important criterion for effective NOx-SCR ¹⁸¹⁻¹⁸⁴ catalysts. Despite its promising activity, the switching of Cu from its active to inactive form during NOx-SCR is seriously problematic ¹⁸⁵⁻¹⁸⁷. The hydrothermal stability of Cu-SSZ-13 and Cu_SAPO-34 was investigated by Wang *et al.* ¹⁸⁸. They found that although the latter is robust under high temperatures (850°C), both are active at high ageing temperatures (750°C). Lee *et al.* ¹⁸⁹ comparatively studied NH₃-SCR performance and hydrothermal stability of Cu-SSZ-13, Cu-SSZ-5, CU-BETA, and Cu-UZM-35 after treating at 750°C, and ranked them in the order of Cu-SSZ-13> Cu-UZM-35> Cu-SSZ-5> Cu-BETA. A similar study was also described by Kwak *et al.* ¹⁹⁰ Such materials are simply fabricated by low-cost one-pot synthesis, which can play a vital role in cleaning exhaust gases.

Ryu *et al.* studied the Cu-exchanged LTA zeolite and demonstrated that LTA is a new contender to substitute Cu-SSZ-13 ¹⁹¹. They tested Cu-LTA zeolite after hydrothermal ageing at a high temperature (900°C) under which commercial SSZ-13 deactivates. Also, they found that the local environment of Cu²⁺ in LTA is different from that in SSZ-13. Cu²⁺ is present only at the centre of the 6-MR and not only acts as a catalytically active site but also as a suppressor

of dealumination. Ryu *et al.* studied the effect of Fe on high silica LTA at a hydrothermal ageing temperature of 900°C ¹⁹². They compared the hydrothermal activity and stability of LTA with that of commercial SSZ-13. It is noteworthy, that the hydrothermal stability of both catalysts was found to decrease at 900°C; however, the extent of decrease in the case of Fe-LTA was smaller as compared to Fe-SSZ-13. Furthermore, the activity profile of Fe-LTA was much better than that of Fe-SSZ-13. The active iron species such as Fe³⁺ and FexOy (small oligomeric species) in Fe-LTA are found to be more stable than in Fe-SSZ-13 owing to the difference in the environment of iron sites within the framework. To explore the role of NH₃ in the SCR reaction, Giordanino *et al.* ⁹⁹ investigated three potentially stable adsorption sites for NH₃ molecule *via* NH₃-TPD and IR spectroscopy: the NH₃ coordinated to Cu site and as solvated NH₄⁺ ions are more stable for T< 400 °C, whereas at higher temperatures, the Brønsted acid sites with a bound NH₃ is found to be more stable.

1.4.4 Reaction Mechanism and Kinetics of NH₃-SCR

The main exhaust gases from industrial and diesel engine is NO (>90%) rather NO₂, hence the reaction of NH₃-SCR are mostly known as the "standard SCR", ¹³⁵, while if the reaction proceeds with an equimolar content of both NO and NO₂ it is entitled "fast SCR". Although the key performance and effectual role of TMI have been widely explored, the reaction mechanism is still under debate and its investigation is ongoing ^{103, 193-195}. Generally, the reaction follows the Langmuir-Hinshelwood mechanism, the reactant species (NH₃, NO₂) simultaneously adsorbed on the catalysts and then react to produce N₂ and H₂O.

Yu et al. 196 demonstrated the NH₃-SCR mechanism on Cu-SAPO-34, namely, the NH₃ is adsorbed both on Cu²⁺ and hydroxyls while the NO is oxidized into nitrates or nitrites on Cu²⁺

sites. The generated nitrates and nitrites react with adsorbed NH₃ to produce ammonia nitride and N₂O intermediates respectively. The subsequent decomposition of these intermediates ultimately generates H₂O and N₂. Similarly, Wang *et al.* suggested a reaction pathway of Cu-SAPO-34 in NH₃-SCR employing *in situ* DRIFTS and explored the reaction mechanism on the Lewis acid sites, which involves first the generation of NH₄NO₃ species and then its reaction with NO to generate H₂O and N₂ ⁹³. Notably, the adsorbed NH₃ on Brønsted acid sites migrates to Lewis acid sites, providing more NH₃ for the reaction. Owing to the high reactivity of NH₄NO₃, DRIFTS spectra were unable to detect its presence; however, its involvement in the reaction could not be ruled out. In contrast, Su *et al.* ¹⁹⁷ confirmed the consequent formation and decomposition of NH₄NO₂ species which are generated as a result of the sequential reaction between NH₃ and the generated NO₂.

The whole NH₃-SCR process was well described by Li *et al.* for extraframework Fe and Brønsted acid sites of ZSM-5 zeolite^{37, 198}. They proposed that catalytic decomposition of NO over H-form zeolite (using a cluster model with 5-T sites) either follows direct oxidation of NO to NO₂ and O₂ with the successive formation of N₂O₃ or it is oxidized to N₂O₃ to generate NH₂NO. They explored the oxidation of NO as the rate-limiting step with an activation energy of 15.6 kcal/mol at 373 K. Subsequently, the NH₂NO species decomposes to H₂O and N₂ *via* a hydrogen transfer mechanism. This process can be catalytically driven by the Z⁻[FeO]⁺ species over Fe-exchanged zeolite. Here, NO reacts with NH₃ on the FeO⁺ sites to produce NH₂NO and [FeOH]⁺. The activation barrier is reduced by 3.0 kcal/mol due to the FeO⁺ species.

Bruggemann *et al.* also performed a series of tests to probe the NH₃-SCR mechanism. First, they compared the NO oxidation step and the transformation of N₂O₃ to NH₂NO on Brønsted

acid sites of ZSM-5 ¹⁹⁹. They subsequently calculated the energy barrier for the production of NH₂NO in the gas phase and over the ZSM-5 zeolite. Their results showed that the energy barrier in the case of the zeolite is 20 kcal/mol is more than that in the gas phase (0.16 kcal/mol). They extended the system and investigated the Fe-zeolites using the cluster model approach ^{38,} ²⁰⁰. The catalytical cycle in this case only produces two species: nitramide (NH₂NO₂) and nitrosamine (NH₂NO). They consider Fe as a mononuclear species Z-[FeO]⁺, as mentioned earlier. In addition, several species were found on Fe sites such as FeO₂N, FeONO, and FeO₂NO which are considered the most prominent species in the NO oxidation cycle based on the calculated Gibbs free and activation energies which are calculated by gradient-corrected Density Functional Theory (DFT) implemented in the TURBOMOLE program.

In addition, the decomposition of N₂O over TMI zeolites has been also extensively studied ^{38,} ^{43, 201}. Like NO, N₂O is also an environmentally undesired product in NH₃-SCR, and its decomposition to N₂ is a possible pathway for the generation of N₂. The decomposition of N₂O on a single Fe site and binuclear O bridged Fe site both in the presence and absence of NO and water has been studied by Heyden *et. al* ²⁰². They found that NO-assisted N₂O decomposition more favourably proceeds as the poisoning effect of water on the active sites do not operate for NO. Commensurate with this observation, Bruggemann *et. al* considered it a key part of the SCR pathways in a NO₂-rich environment ³⁸.

Despite the extensive efforts of many academic and industrial groups, a complete picture of all elementary steps during the NH₃-SCR mechanism is still missing. Many mechanisms have been proposed for both high and low temperatures. Recently, J. Rudolph & C.R. Jacob compared the mechanism of the SCR of NOx over Fe and Cu-exchanged zeolites ²⁰³. The pathway starts with the overall neutral models [Z-Fe^{III}(OH)₂] and [Z-Cu^{II}(OH)] and proceeds

via two pathways. In the first NH₃ is adsorbed to generate the [Z-M(OH)₂(NH₃)] intermediate. This step is exothermic and requires a subsequent shifting of the proton from NH₃ to the OH-ligand resulting in the formation of [Z-Fe^{III}(OH)(H₂O)(NH₃)] which can abstract water molecules leading to the [Z-Fe^{III}(OH)(NH₂)] with overall endothermic energy of 82 kJ/mol in the case of Fe while the same steps for Cu need only 56 kJ/mol. In the case of Cu, some previous reports proposed this proton transfer to the zeolite framework rather than to the OH- ligand ¹¹⁹, ²⁰⁴, ²⁰⁵ which requires 114 kJ/mol energy. This intermediate [Z-Fe^{III}(OH)(NH₂)] interacts with NO in two different ways: first, NO coordinates with this intermediate to generate [Z-FeII(OH)(NH₂)(NO)] and reduce the Fe^{III} to Fe^{II} followed by rearrangement that leads to [Z-FeII(OH)(NONH₂)].

Cu speciation in Cu-CHA is dependent on temperature, gas composition, catalyst activation, and composition. Therefore, the structure, coordination, and positions of active Cu sites in SCR catalysts may differ in different catalytic reaction conditions and are likely to change during SCR. In addition, the role of Cu-nitrates gives rise to the question of interest in the NH₃-SCR reaction. As proposed by Janssens *et al.* in the NH₃-SCR over Cu-CHA reaction, the formation of Cu-nitrate species plays an important role (Figure 1.9) ¹²⁰. They observed that it is possible to split the redox cycle and separate the oxidation step from the reduction step by switching between the NH₃ + NO and NO + O₂ atmospheres to study the individual half-cycles. The Cu(II)-nitrate species formed as a result of the NO + O₂ oxidation process is converted to the solvated Cu(I)-NH₃ under NH₃ + NO reductive conditions. Cu(II)-nitrate species are reformed when switching back to NO + O₂ oxidation conditions, closing the catalytic cycle. They proposed this simple mechanism for an NH₃-SCR cycle on isolated Cu-ions, in which the NO reacts with the nitrate intermediate to generate gaseous NO₂ and Cu-nitrate species. This

observation is in agreement with the experimental data as the transient formation of gaseous NO₂ was successfully detected during the SCR reaction.

For lower temperature processes, the most puzzling question is the change in the kinetics from quadratic to linear dependency and the decrease in the apparent reaction order for O₂ (from 0.8 to 0.3) when increasing the Cu density ^{119,206}. Recently, these observations have been examined through steady-state and transient kinetic measurements, first-principles calculations, and XAS. From the findings of Paolluci *et al.*, the NH₃-solvated Cu(1) ions can form transient ion pairs while migrating through zeolite windows and activating oxygen ¹¹⁹. Following this analysis, Chin *et al.* envisaged the role of the Cu-Mn/zeolite as a potential contender for the NH₃-assisted SCR reaction ²⁰⁷. They found that the formation of both NH₃ and NOx on the Cu-zeolite and Cu-Mn/zeolite are similar and suggested that the introduction of Mn only enhanced the concentration of the intermediate. The bidentate nitrate coordinates the metal ion followed by the desorption of water after the adsorption of NO from the catalyst.

Notably, Marberger *et al.* correlated the rate-limiting step to the redox mediation of $[Cu(NH_3)_2]^+$ to $[Cu(NH_3)_2]^{+2}$ using transient and quick-scanning EXAFS methods. This reoxidation process is inhibited by the interaction of NH₃ with Cu(I) complex ¹³⁹. As has been shown previously the SCR kinetics depend on the Cu-density, especially on the Cu/Al ratio; and we note that the analysis of Marberger *et al.* ¹³⁹ mainly depends on data from low Cu-loading samples. Although in these studies, the formation and chemistry of the redox mediation of $[Cu(NH_3)_2]^+$ and $[Cu(NH_3)_2]^{+2}$ complexes are well documented, the nature and role of other reaction intermediates are less clear.

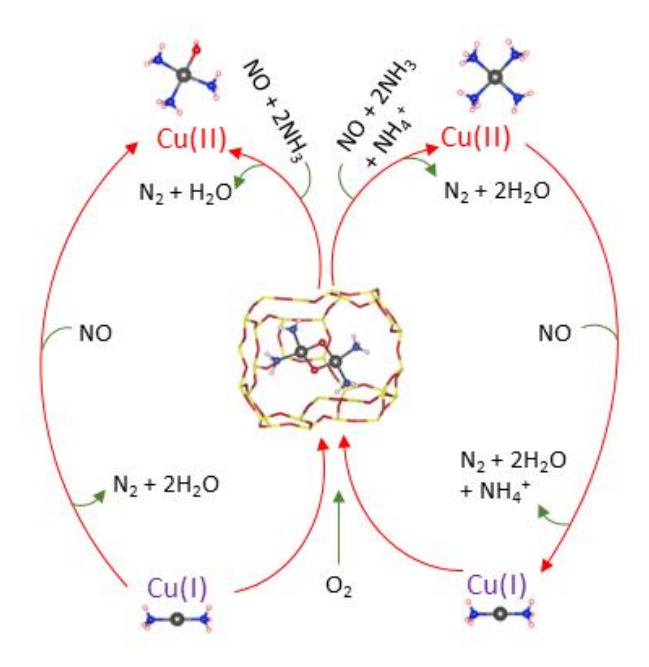


Figure 1.9. The proposed reduction process on isolated Cu (II) ions (residing near one (left) or two (right) framework Al centres). The transportation of Cu(I) ions into the cage and the subsequent oxidation by O₂ (inner step). NH₄⁺ ion is generated in the right-hand cycle to balance the charge and maintain the stoichiometry. Si; yellow, O; red, Cu; grey, N; blue and H; white ¹²⁰.

1.4.5 Industrial Importance of NH₃-SCR Process

The NH₃-SCR process has emerged as a vital technology in the industrial landscape due to its significant role in mitigating harmful emissions from various industrial sources. SCR technology is primarily employed to reduce nitrogen oxide (NOx) emissions, which contribute to air pollution, smog formation, and adverse health effects. NH₃-SCR, in particular, has gained widespread industrial importance due to its efficiency, versatility, and environmental benefits. NOx emissions not only contribute to the formation of smog and acid rain but also serve as precursors for the production of greenhouse gases, such as ozone and nitrous oxide. One of the key reasons for the industrial significance of the NH₃-SCR process is its ability to effectively reduce NOx emissions across a wide range of industrial sectors. Power plants, refineries, chemical manufacturing plants, and other industrial facilities are major sources of NOx emissions. More than 1000 SCR plants have been implemented in the United States alone to mitigate the emissions of NOx from industrial boilers, steel mills, process heaters etc ²⁰⁸. The

domain of mobile sources has witnessed a burgeoning utilization of SCR systems in diesel vehicles, owing to the inherent inadequacy of three-way catalysts (TWC) in tackling the abatement of NOx emissions in lean-burning gasoline and diesel engines ²⁰⁹. By implementing NH₃-SCR technology, these industries can achieve substantial reductions in NOx emissions, thereby complying with stringent environmental regulations and improving air quality.

Furthermore, the NH₃-SCR process offers notable advantages in terms of its efficiency and cost-effectiveness. The technology utilizes a catalytic converter and a reducing agent, typically anhydrous ammonia, to convert NOx into harmless nitrogen and water. The catalytic converter ensures high conversion rates of NOx, even at low temperatures, making it suitable for a wide range of industrial applications. This efficiency translates into cost savings for industries, as it minimizes the consumption of reducing agents and lowers operational costs. Moreover, the environmental benefits associated with the NH₃-SCR process contribute to its industrial importance, since, by significantly reducing NOx emissions, this technology plays a crucial role in combating air pollution and addressing the global challenge of climate change.

The NH₃-SCR process also offers flexibility in terms of its application across different industrial sectors. It can be integrated into existing infrastructure without requiring major modifications, making it an attractive option for industries seeking to retrofit their facilities for emissions reduction. Additionally, the technology can be customized to suit specific industrial needs and accommodate variations in operating conditions, such as temperature and gas composition. This adaptability enables the NH₃-SCR process to be implemented in diverse industries, including power generation, petrochemicals, cement production, and iron and steel manufacturing.

1.5 Objectives

The objective of this thesis is to study the NH₃-SCR process over TMI-doped Zeolite and to provide further information to improve the reaction mechanism. We elucidate how TMIcontaining zeolites can control nitrogen chemistry and investigate the reaction mechanism of NH₃-SCR, which is still not fully explored. A hybrid QM/MM model is employed to study low-temperature NH₃-SCR over Cu-CHA which is based on the suggested multisite reaction proposed by Janssens et al 58. More importantly, the influence of solvent on the reaction energetics of this process is proposed and then thoroughly examined. The study has been extended by an investigation of combined experimental and theoretical approaches, and the influence of solvent on the reaction energetics was the key target to explore as described in our published paper ²¹⁰; the experimental work was performed by Beale and colleagues. Based on the model, the computed values for reaction energies, and the spectroscopic signatures of the complete set of intermediate species are in good agreement with the experimental findings. Furthermore, the role of Fe as a framework cation in BEA zeolite is critically investigated and the result with other similar systems and literature be compared. The work illustrates how experimental and theoretical catalysis can be linked directly. One of the primary objectives of the current effort is to contribute to the advancement of exhaust gas after-treatment systems capable of meeting rigorous emission regulations.

Chapter 2

Computational Methods

"The underlying physical laws necessary for the mathematical theory of a large part of physics and the whole of chemistry are thus completely known, and the difficulty is only that the exact application of these laws leads to equations much too complicated to be soluble. It, therefore, becomes desirable that approximate practical methods of applying quantum mechanics should be developed, which can lead to an explanation of the main features of complex atomic systems without too much computation."

Paul Dirac (1929).

2.1 Introduction

Computational methods are now very widely used to model and predict the behaviour of chemical systems, using methods based on quantum mechanics (QM), molecular mechanics (MM), and hybrid Quantum Mechanics/Molecular Mechanics (QM/MM) methods. QM solves the Schrodinger equation at some level of approximation at the atomic and subatomic levels, while MM use interatomic potentials to describe the interactions between atoms in molecules and materials. ^{211, 212}. Both QM and MM methods can be applied to molecular clusters and periodic systems. In the latter case, periodic boundary conditions (PBCs) represent the system by a repeating unit cell, which is replicated in three dimensions to form an infinite lattice. However, periodic boundary conditions have some limitations, in describing systems with finite sizes and surfaces. Additionally, the use of periodic boundary conditions can lead to an artificial symmetry in the systems, as when defects and sorbed molecules are introduced which can affect the properties of the materials. In contrast, the QM/MM method combines both QM and MM to model localised states and reactions and can be applied to very large systems

including proteins and zeolite ²¹³⁻²¹⁵. The advantages of QM/MM methods also include their ability to accurately describe chemical reactions, as a high level of theory may be employed in the QM region, which may be more difficult with periodic techniques.

In this chapter, we will discuss the computational techniques relevant to the work in this thesis with a strong emphasis on QM/MM techniques along with a discussion of the important considerations that are required when combining two different levels of theory. In addition, we will highlight the detail of all the molecular calculations and benchmarking that are employed in the work reported in the thesis, all of which have been performed using hybrid QM/MM methodology as implemented in Python and Tool Command Language (Tcl) based Chemshell software ^{214, 216, 217}.

2.2 Quantum Mechanics

As noted, QM methods solve the Schrodinger equation at some level of approximation and face the challenge of the many-body problem. Several approximations have been established over the years and Density Functional Theory (DFT) and Hartree-Fock theory (HF) are the two main approaches that are widely used to calculate the electronic structure and energy of the system. The solution of the Schrodinger equation (Eqn 2.1) is the fundamental basis for the electronic structure calculations:

$$\widehat{H}\psi(r,R) = E\psi(r,R) \tag{2.1}$$

For equation 2.1, E is the energy of the system and \widehat{H} is the Hamiltonian operator and is representing the total energy of the system which can be broken down further into kinetic and

potential energy components (Eqn 2.2) while the the symbol " $\psi(r,R)$ " is the wave function, a mathematical function describing the quantum state of the system. It includes information about electron positions "r" and atomic nucleus positions "R." For multi-particle systems, it represents the collective behavior of all particles.

$$\left\{-\frac{\hbar^2}{2m}\nabla^2 + \nu\right\}\psi(r) = E\psi(r) \tag{2.2}$$

h; is the reduced Planck constant, which is given by $h = h / (2\pi)$, a fundamental constant in quantum mechanics and has a value approximately equal to 1.054571×10^{-34} joule-seconds. m; represents the mass of the particle while ∇^2 is the Laplacian operator, also known as the Laplace operator. It is a differential operator that represents the sum of second partial derivatives with respect to each spatial coordinate (x, y, z) in three-dimensional space. For one-electron systems, exact solutions to the Schrodinger equation are accessible however, for the many-electrons system it cannot be solved exactly. So, a series of approximations are needed. The first of these is the Born-Oppenheimer (BO) approximation, which assumes that the motion of nuclei and electrons are separated. This assumption allows us to treat the total energy of the system as a sum of the nuclear and electronic energies, where the nuclear energy is the function of the repulsion between the nuclei while the electron energy is the result of potential energy and kinetic energy owing within the field of the nuclei. The Schrodinger equation remains an N-body problem even though the nuclear motion is excluded, which needs to be simplified before its amplification to a real chemical system.

The Hartree approximation assumes N-body wavefunction as a product of single-electron wavefunction and described each electron in terms of the average potential of the multi-electron

system rather than treating them explicitly. This approximation treats the energy and wave function of the system as a multi-electron system in a stationary state. To construct an accurate potential, an interactive procedure is required where an initial guess provides a good solution that can be used to repeat the calculation and, therefore, improve the effective potential. To this aim, each iteration should improve the result until a self-consistent solution is achieved. The self-consistent approach is widely used as an effective method for electronic structure calculations which allows us to make use of Hartree approximations and Born-Oppenheimer along with other modern developments to achieve better descriptions of the multi-electron system.

2.2.1 Hartree-Fock Theory

The Hartree-Fock approach is built upon Hartree's theory which includes the effect of electron spin. This approach brings more accuracy and allows calculations closely resemble real experimental data. To apply the Hartree-Fock approach to a real system, a finite set of basis functions is introduced to define the spatial component of each particle's coordinates. A collection of K spatial functions generates 2K spin orbitals, half of which are allocated to each of the opposing electron spins, known as α and β . These functions are specified as part of a basis set in a calculation, as detailed in Section 2.3.1. The correlation energy is the energy difference between the HF limit and the optimal solution to the Schrödinger equation that consists of contributions that are ignored due to the mean-field treatment of single-particle wavefunctions. To include the electron correlation effect, significantly more computationally intensive "post-Hartree Fock" approaches must be used, which are not addressed here. Density functional theory provides a simpler, albeit less precise, approach.

2.2.2 Density Functional Theory

The Hartree-Fock method is a wavefunction-based method whose formulation can be obtained directly from the Schrodinger equation. Density Functional Theory (DFT) is an alternative method for calculating electronic structure that is based on the idea that the properties of a system, including its ground-state wavefunction ψ_0 , can be obtained from the ground-state spatially-dependent electron density $\rho(r)$ [Eqn 2.3):

$$\psi_0 = \psi[\rho(r)] \tag{2.3}$$

Quantum mechanics (QM) via DFT calculations in applications to solids commonly employ periodic boundary conditions chosen to approximate a large (infinite) system by using a unit cell. However, when treating localised states in solids the PBC approach can lead to difficulties and applying the hybrid quantum mechanical/molecular mechanical (QM/MM) approach avoids any need for periodic boundary conditions, and only makes use of the finite molecular mechanics (MM) cluster.

2.3 Implementations

When performing QM calculations, the required data to specify atoms (other than their mass, which is usually a fixed value integrated into the software) must be collected inside a set of inputs. The atomic data are frequently in the form of a basis set and is sometimes used in conjunction with an effective core potential. Depending on the study's objectives, basis sets and effective core potentials may be selected to provide fast, qualitative results or high levels of accuracy at a higher computing cost.

2.3.1 Basis Sets

Basis sets are some of the most important input data for QM calculations ²¹⁸. In the context of electronic structure calculations, a basis set is defined as a collection of functions that may be linearly combined to produce molecular orbitals. A basis set can take different forms, however, atom-centred functions are commonly utilized for molecular calculations in vacuum settings in the context of electronic structure calculations. In practice, three types of basis functions are frequently employed: Slater, Gaussian, and plane wave. Gaussian-type orbitals (GTO), or more precisely Gaussian-type functions (GTFs), differ from Slater in the exponent term. GTFs are useful because the product of two GTFs results in a new GTF, which substantially simplifies the computation of integrals. All of the calculations in this thesis are performed employing atom-centred basis sets. A commonly used basis set is the 3-21G (Pople basis set). The "3" in the name refers to the number of GTOs per atom, while the "21G" refers to the number of total primitive Gaussian functions used to construct the GTOs. On the other hand, Karlsruhe's main basis sets are def2-TZVP²¹⁹ (Valence triplet- ζ basis set) and def2-SVP²¹⁹ (Split valence polarisation) include three sets of basis functions: valence, polarization, and diffuse functions. The "def2" in the name refers to the family of basis sets developed by the group of R. Ahlrichs, and the "TZVP" part stands for triple-zeta valence plus polarization. They are widely used because they produce accurate results for all elements up to radon (Z=86). and have the significant advantage of being inexpensive. In this thesis, we used triple basis set def2-TZVP ²¹⁹ for the inner QM1 region while the outer QM2 region (115 atoms), which includes the terminating link H atoms, is treated with a smaller split valence with polarization def2-SVP ²¹⁹ basis set.

2.3.2 Effective Core Potentials

So far, all discussions have assumed that quantum mechanical calculations explicitly account for the action of every electron in the system under study. However, in practice, many of the inner electrons' contributions to the chemical behaviour observed are very little. Given the significant processing resources required for an all-electron model, it is often desirable to combine the inert core electrons with the atomic nucleus to generate an effective core potential (ECP) ²¹⁸. Using an ECP reduces processing expenses significantly without compromising the accuracy of the calculations regarding valence shell properties. The use of an ECP may sometimes improve the accuracy due to the inclusion of relativistic effects within the potential. In an all-electron calculation, relativistic corrections for heavy elements would generally be too expensive to include, but when an ECP is used, the expense associated with these corrections is shifted from the calculation performed by the end user to the one in which the ECP is first fitted.

ECPs are typically constructed by removing the innermost core electrons from the atomic potential and replacing them with a smoother potential that models the effect of these electrons on the valence electrons which is achieved by subtracting the Hartree-Fock potential due to the core electrons from the total Hartree-Fock potential and then adding a smooth potential that models the effect of the core electrons on the valence electrons. The smooth potential used to model the effect of the core electrons is typically chosen to be a sum of terms that are proportional to powers of the distance from the nucleus. The coefficients of these terms, which are called the "fitting parameters" of the ECP, are adjusted to reproduce the properties of interest for the valence electrons.

The fitting parameters for an ECP can be determined by a variety of methods, including empirical fitting to experimental data, fitting to *ab initio* calculations, or using a combination of these methods. In general, the goal is to find the set of fitted parameters that best reproduces the properties of interest for the valence electrons while minimizing the error between the ECP and the actual potential due to the core electrons. Once the fitting parameters have been determined, the resulting ECP can be used in quantum chemical calculations to study the behaviour of molecules containing the atom or group of atoms of interest. ECPs are especially useful for heavy atoms, where a large number of inner core electrons can make quantum chemical calculations computationally prohibitive.

2.4 Molecular Mechanics

Electronic structure calculations discussed above, provide detailed information for chemical systems, but their high computational cost can render them unsuitable for a system with a large number of atoms especially when dynamical behaviour is investigated. Molecular mechanics (MM) is a branch of computational chemistry and chemical engineering that uses classical mechanics to simulate the behaviour of molecules and solids. It is based on the idea that the behaviour of a molecule can be approximated using classical mechanics in conjunction with effective potential functions or forcefields which give the energy of the systems as a function of nuclear coordinates.²²⁰

Different types of force fields are used to simulate different types of chemical systems. For ionic systems, Born model potentials are generally used with the energy given a sum of long-range Coulomb interactions between the ionic charges and sort-range repulsive and dispersive terms. For covalent systems, such as organic and bio-molecules different formulations are used with bond-stretching and bending functions ²²¹. Both ionic and covalent force fields may be

parameterized from experimental data or ab-initio calculations. Examples of such force fields include those developed by Catlow and Lewis²²² for ionic oxides and the Amber²²³ and CHARMM²²⁴ force fields for organic and biomolecules. Zeolites which are semi-ionic/semi-covalent materials can be modelled both by Born model potentials using the parameterisation of Sanders *et al.*²²⁵ or by more covalent-like forcefields using the parameterisation of Hill and Sauer ²²⁶. The latter is used in the MM region in the present work

For reactive systems, force fields specifically designed for chemical reactions, such as ReaxFF or ReaxFF-lg, may be used ²²⁷. These force fields attempt to handle chemical reactions and chemical kinetics. More generally, it is worth noting that the choice of the force field depends on the system and the question. Some force fields are more accurate for specific systems, while others are more generally applicable and computationally efficient. Therefore, it is important to evaluate carefully the capabilities and limitations of different force fields before using them for a particular simulation.

Various MM methods can be used to simulate the behaviour of molecular systems, including static lattice, molecular dynamics, Monte Carlo simulations²²⁸, and normal mode analysis²²⁹. These methods are all powerful tools for simulating and understanding the behaviour of molecular systems, but they also have their own limitations and assumptions. Detailed discussions of these techniques are available in reference ²³⁰. MM simulations have significantly improved system size scalability compared with quantum mechanical simulations. As a result, a calculation involving thousands of atoms is accomplished with ease with MM techniques as compared to *ab initio* simulation. Interatomic potential functions may be parameterised by fitting to empirical data or *ab Initio* energy surfaces. As noted, our QM/MM calculations used the Hill-Sauer force field²²⁶, derived from results of *ab initio* calculations that

is widely used for simulating zeolites. The MM codes used were GULP²³¹ and DL_POLY²³², although when using the latter, dynamical simulations were not performed.

2.5 QM/MM Embedding Techniques

As noted, QM/MM is a computational method that combines QM and MM simulations to study complex chemical systems ²³³; and as discussed above, in QM/MM approaches, the region of the system where the chemical reaction occurs is treated at an appropriate level of QM theory, while the remaining portion of the system is described by a molecular mechanics force field (Figure 2.1). With this method, reactions in large systems like enzymes, and clusters can be studied accurately. This approach is well suited to describing a local active site, as an alternative periodic DFT approach would require a large, supercell calculation to avoid spurious interactions between the periodically repeated reaction sites. It is also more straightforward in a non-periodic model to increase the accuracy of the QM description through the use of hybrid DFT functionals, as in the current study, or post-Hartree-Fock methods as in the study of Piccini and Sauer ²³⁴. The description of the electrostatic environment is more efficiently handled in the QM/MM model through a combination of MM atoms and point charges as detailed below.

Some of the main advantages of the QM/MM methodology include:

- QM/MM simulations may achieve high accuracy, as a high-level QM method may be employed within available computer resources
- QM/MM is particularly effective in modelling large systems with high accuracies, such
 as enzymes and zeolites, which may be difficult to achieve with pure quantum
 mechanical methods.

- QM/MM can be used to study rare events such as conformational changes, chemical reactions, and other processes that occur on long timescales or with low probabilities.
- QM/MM is a flexible method and can be used to simulate a wide range of systems,
 from small molecules to large macromolecules and condensed matter systems.

Although QM/MM is a powerful computational approach used to study complex chemical and biological systems, it is not without its limitations and challenges. Defining the boundary between the QM and MM regions, for instance, is not always straightforward and often requires careful consideration. The introduction of link atoms, used to connect both regions, can inadvertently introduce inaccuracies and perturb the electronic structure, thus potentially affecting the accuracy of the results. To ensure accurate outcomes, selecting an appropriate size for the QM region is crucial. If the QM region is too small, vital electronic and quantum effects may be overlooked, compromising the overall reliability of the simulation. Conversely, if the QM region is too large, the computational cost increases significantly, making the calculations impractical for larger systems. Furthermore, the choice of the QM method and force field can significantly impact the accuracy of the results. Achieving a delicate balance between accuracy and computational cost remains a constant challenge in QM/MM simulations. Additionally, parameterizing and calibrating the simulations for specific systems, particularly for the MM part, can be demanding, especially when dealing with non-standard or novel molecules, thus adding to the complexity of the process. Handling electrostatic interactions across the QM/MM boundary poses another complexity. Methods like the electrostatic embedding scheme, while helpful, can introduce some level of artificial charge transfer between QM and MM regions, potentially influencing the overall accuracy of the simulation. Moreover, QM/MM simulations might encounter issues in accurately representing polarization effects from the QM region within the MM region. Neglecting polarization can lead to inaccuracies in the overall

description of the system, compromising the reliability of the results. Furthermore, the implementation of QM/MM methods is not as widespread as fully quantum or classical simulations. The limited availability of suitable software and user-friendly interfaces may hinder researchers' access to this powerful approach, making it less accessible to some scientists. Nonetheless, despite these challenges, QM/MM remains an invaluable tool for studying chemical reactions, enzyme mechanisms, and other complex processes that demand the simultaneous consideration of quantum and classical effects. Researchers continue to work diligently in improving existing methods and developing new approaches to address these limitations and expand the capabilities of QM/MM simulations.

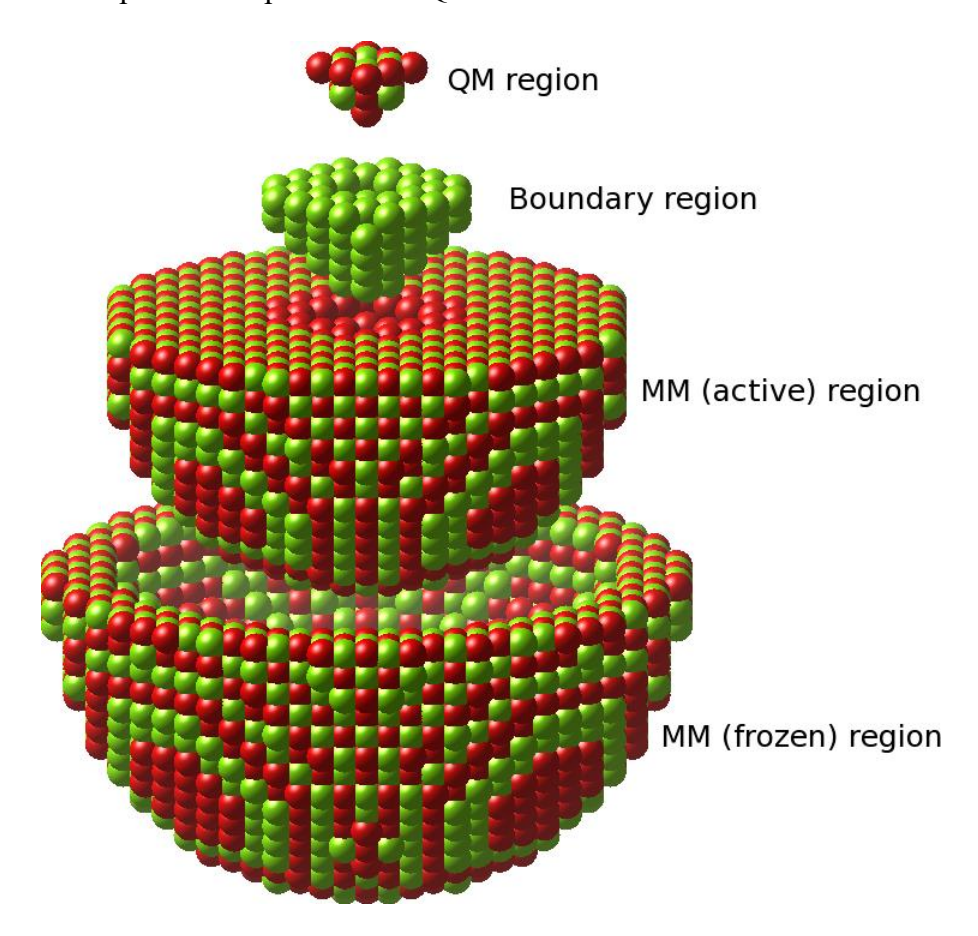


Figure 2.1. QM/MM embedding setup used within both Py and Tcl Chemshell: Progressing from top to bottom; the quantum mechanical region (treated with ab initio calculations), the relaxed MM region (treated with a force field), and the frozen MM ions. The outermost region (not displayed) contains point charges to ensure the Madelung potential in the centre of the cluster is accurately reproduced.

2.5.1 ChemShell QM/MM Coupling

In this thesis, we have employed density functional theory (DFT) using a QM/MM methodology, as implemented in the ChemShell software. ChemShell, a very effective package for QM/MM modelling, was originally developed by Sherwood *et al.* ²³⁵. It can implement various additive and subtractive approaches and has been used in both solid-state and biomolecular modelling. The additive approach (Eqn 2.4) expresses the total energy as a sum of MM, QM, and additional coupling terms:

$$E = E (inner, QM) + E(outer, MM) + E(couple, QM/MM)$$
 (2.4)

where, *E* (couple, QM/MM) describes the interaction between QM and MM regions. To saturate the cluster, link atoms should be employed carefully, to avoid unwanted QM/MM interaction. Link atoms are virtual atoms that are used to connect the QM and MM regions of the system. In the case of the zeolite model (employing the additive approach), the link atoms are only accounted for the intrinsic part of the inner region. But due to the electrostatic coupling (between two regions), they are also accounted for the QM region. Link atoms compensate the charge at terminal positions and act as a bond-dipole correction to ensure an accurate electrostatic potential. Such non-physical double counting should be excluded by omitting the corresponding MM terms in the calculation of the total energy. On the other hand, the alternative subtractive approach (Eqn. 2.5) applies the MM scheme to the whole system and subtracts the MM energy of the inner system to make the correction and thus avoid the double-counting of the inner region and the link atoms.

$$E = E (inner + Link, QM) + E(inner + outer, MM) - E(inner + link MM).$$
 (2.5)

Apart from both additive and subtractive approaches, other intermediate approaches are possible. The subtractive approach can be further exploited to delete the term associated with the link atoms (Eqn. 2.6). In this work, an additive approach has been employed to perform calculations.

$$E = E (inner + Link, QM) + E(inner + outer, MM) - E(couple \frac{QM}{MM} - E(link, MM)). \quad (2.6)$$

2.5.2 QM/MM Implementation

The QM/MM approach avoids any need for periodic boundary conditions, only making use of the finite MM cluster. Atoms at the interface between QM and MM regions are connected by bonds that need careful treatment (charge modifier) with the termination of the QM region by hydrogen atoms, forming O-H groups. A charge modifier is introduced to account for the polarization and electronic effects that arise due to the interactions between the QM and MM regions. These effects can be significant, especially when there are strong electrostatic interactions between the QM and MM regions. In our case, we divided the QM region into two parts and employed a dual basis set strategy: the atoms in the innermost QM1 region (approximately \sim 28 including the intermediates) are treated with the triplet- ζ basis set def2-TZVP²¹⁹ while the outer QM2 region (115 atoms), which includes the terminating link H atoms, are treated with a split valence with polarization def2-SVP 219 basis set. To build the QM/MM model, it is necessary to remove the classical charges from the centres (QM) and make sure that the total charge removed from the system is the same as the total charge of the QM region. The guest species of interest in the zeolite and reactants gaseous species were also treated at the OM level using the higher quality def2-TZVP ²¹⁹ basis set. The coordinates of all atoms (not including the link H atoms) in the QM region and active MM region were fully optimized. Considering that adsorbed molecules can diffuse through the larger channels, all the

adsorbed species including the intermediates were placed within (or near) the 8-membered ring (8-MR) of the CHA/BEA cage. The water (O-end) and ammonia (N-end) molecules were placed at a distance of 2 Å from the Cu/Fe centre with the proton pointing away from the adjacent oxygens and intermediate species to avoid artificial trapping in hydrogen-bonding interactions. We note that hydrogen bonding with framework O can influence chemistry at metal sites by affecting the binding of functionally important Cu–H₂O/NH₃ units.

The boundary atom cutoff radius must be large enough to prevent the "tails" of any diffuse functions present in the QM calculation from being unduly influenced by positive point charges in the MM region. Some crucial factors to take into account when setting up a QM/MM cluster are, first, the MM cutoff radius determines the extent to which the MM calculation will be polarised by changes within the QM region. Secondly, the alignment of the ground-state lattice parameters used in the QM and MM computations must be as near as feasible to prevent artificial strain at the boundary. To reduce the impact of this effect, the interatomic potentials can be adjusted to resemble more closely ab initio results than experimental data.

2.5.3 Choice of Model Clusters

The creation of a QM/MM cluster for use within ChemShell^{214, 216, 217} is a multi-step procedure. For solid-state materials, the first stage is the production of a single unit cell of the target material, relaxed to its equilibrium geometry under periodic boundary conditions using the MM code (GULP)²³¹ to be utilised in the overall QM/MM calculation, which results in a ground-state starting point, which with the assistance of ChemShell software expands to the required size to enable the cutting of a non-periodic cluster. The expanded cluster is again relaxed before use in any production/benchmarking calculations.

To perform the QM/MM calculation, we first created a spherical embedded-cluster model (Figure 2.2) of CHA and BEA zeolites from the unit cell of siliceous CHA and BEA ²³⁶. Both unit cells were initially optimized at the MM level using the GULP package ²³¹ using Hill-Sauer Molecular Mechanical force-field²²⁶. After creating simple CHA-and BEA cluster models, we then constructed active sites. For example, in the case of a Brønsted acid site, we replaced one Si with Al and added a charge-compensating proton on a neighbouring oxygen atom at a site where it is most accessible to facilitate the reaction. The QM region which is contained within the active part of the model includes atoms from the third oxygen shell from the central T-site; and, as noted, we have added the hydrogen (link atoms) to saturate the terminal oxygen atoms. Furthermore, we modified the same cluster by incorporating copper into the cage of the CHA framework, as shown in Figure (2.2).

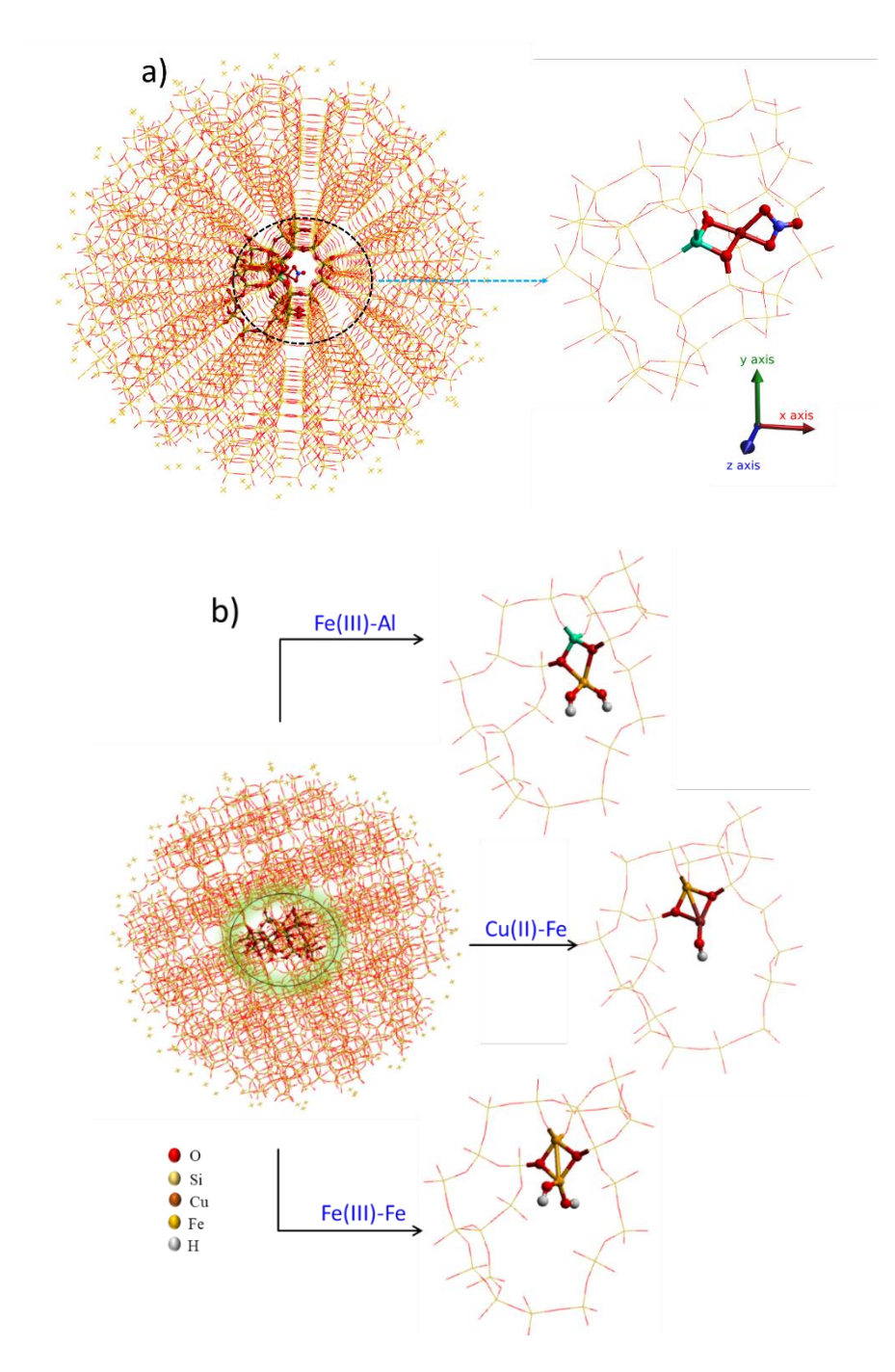


Figure 2.2. The QM/MM embedding setup; a) the CHA cluster (above) and b) the BEA (below) with QM regions for three different active sites; Fe(III)-Fe_F-BEA, Fe-Al_F-BEA, and Cu-Fe_F-BEA. The outermost region contains point charges to ensure the Madelung potential in the centre of the cluster is accurately reproduced. Atom colour codes: Cu (brown), Al (green), Si (yellow), O (red), N (blue), and H (white).

2.6 Geometry Optimisation

The process of finding the lowest energy structure is described by geometry optimisation. For each configuration employed the self-consistent field (SCF) method, also known as the iterative solution of the Kohn-Sham equations which involves an iterative process where the electronic wavefunctions and densities are updated until self-consistency is achieved. We employed the Limited-memory Broyden-Fletcher-Goldfarb-Shanno (LBFGS) minimization method for geometry optimization (implemented in DL-Find code), a type of second-order optimization algorithm that belongs to a class of Quasi-Newton methods. We have geometry optimised all species including gaseous species for the adsorption study and then calculated the adsorption energies using Eqn. 2.7.

$$E_{ads} = E_{ZeOG} - (E_G + E_{ZeOH}).$$
 (2.7)

Here, E_{ads} is the adsorption energy of each gaseous species while E_{ZeOG} is the energy of adsorbate, $E_G + E_{ZeOH}$ are the energies of the appropriate optimised gas-phase molecules and Cu^{2+} -OH-/CHA cluster respectively. Similarly, for the reaction energies, we optimized the relevant intermediates species to obtain the corresponding reaction energies using the following Eqn. 2.8.

$$E_R = E_{SOH + ZeOH} - (E_{SOH} + E_{ZeOH}).$$
 (2.8)

 $E_{SOH+ZeOH}$ is the calculated energy of the resulted intermediate species, generated by the adsorption or desorption of neighbouring gaseous species such as H₂O, N₂, NH₃, NO, and O₂ on the metal active sites, and E_{SOH} and E_{ZeOH} are the energies of the appropriate gas-phase reactant molecules and Cu²⁺-OH⁻/CHA cluster respectively within the QM part of the QM/MM region.

2.7 Lattice Parameter Test

We first optimized the purely siliceous CHA cluster using the ChemShell software and employed the hybrid QM/MM model for zeolites developed by Sherwood ²³⁷. The geometrical parameters obtained for the Si-tetrahedra sites by ChemShell employing two DFT functionals of choice, B97-2²³⁸, and BB1K²³⁹, were found to be in accord with the experimental data (Table 2.1 & 2.2), and hence can be used for further studies including the incorporation of metal ions such as Al and Cu.

Table 2.1. Selected calculated parameters of the optimized silica CHA chabazite, using two different

DFT functional, and their comparison with the experimental data.

Bond	Si-O distance [Å]			Bond	Si-O-Si angle [º]		
Si-O	B97-2	BB1K	Exp. a		B97-2	BB1K	Exp. (Å) a
Si ₁ -O ₁	1.603	1.602	1.609	Si_1 - O_1 - Si_2	127.049	127.230	147.752
Si ₁ -O ₂	1.588	1.588	1.609	Si ₁ -O ₂ -Si ₃	166.093	166.157	150.131
Si ₁ -O ₃	1.595	1.594	1.609	Si ₁ -O ₃ -Si ₄	141.733	141.901	149.304
Si ₁ -O ₄	1.592	1.592	1.610	Si ₁ -O ₄ -Si ₅	163.665	163.774	149.435
Average	1.595	1.594	1.609	Average	149.635	149.765	149.155
					~ 240		

 $[^]a$ Experimental data are taken from ref. 240

In our study of Cu-CHA, we have proposed several catalytic sites for Cu²⁺ locations around Al-tetrahedra (Figure 2.3). To find the most favourable location of Cu²⁺-OH⁻ in Cu-CHA, we performed DFT calculations using a range of exchange-correlation density functionals and selected the B97-2²³⁸ results as providing the most accurate reaction energies and molecular structures. Therefore, the B97-2 data will be used in the thesis. We have found that the extraframework Cu ions are more stable in 8-membered rings (8-MR) than 6-MR, by 0.3 eV (*cf.* a similar finding in reference ⁵⁸), although, the exact position of Cu ions and the active sites in Cu-CHA are still controversial ²⁴¹. It is also reported that in the presence of the adsorbate, the Cu ion relocates its position from 6-MR to 8-MR, as shown by studies of the formation of

Cu²⁺-NO₃ intermediates, where the energy reported in the 8-MR is lower than in 6-MR ^{8b}. The geometric parameters obtained with DFT calculation using ChemShell are in excellent agreement with experiment ²⁴², and therefore, can be used to investigate the NH₃-SCR on Cu-CHA reaction.

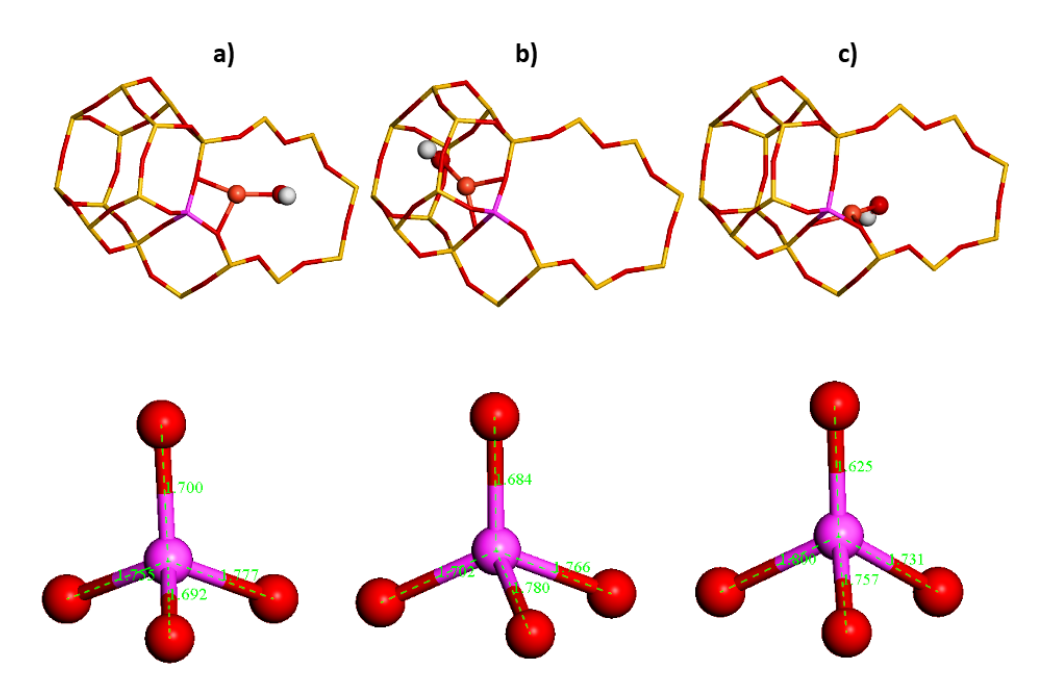


Figure 2.3. The representative Cu²⁺-OH⁻ CHA Al-tetrahedra shows various possible locations of Cu²⁺-OH⁻ within the CHA framework. Color code: Al, purple; Si, yellow; O, red; Cu, gray; N, blue; and H, white;

Table 2.2. The calculated bond lengths of the Al-O (Å) Cu²⁺-OH⁻CHA chabazite for the possible three configurations.

Brønsted acid sites	Cu-a (Å)	Cu-b (Å)	Cu-c (Å)	Exp. (Å) ^a
Al-O1	1.70	1.68	1.62	
Al-O2	1.75	1.78	1.75	
Al-O3	1.77	1.70	1.80	
Al-O4	1.69	1.76	1.73	
Avg.	1.72	1.73	1.72	1.73

 $^a\mathrm{Experimental}$ data are taken from ref. 240

2.8 Energy Barrier and Transition State Search

The rate constant of a reaction (Eqn. 2.9) is given by the Arrhenius equation:

$$k = Ae \frac{-Ea}{k_B T}. (2.9)$$

Here, k is the reaction rate constant at the absolute temperature (T), k_B is the Boltzmann constant, E_a is the activation energy and A is the preexponential factor. The Arrhenius equation and transition state theory (TST) both highlight the idea of activation energy²⁴³ (p. 107-109) To form the product (P) in TST, it is assumed that the reactants (R) must be activated to the transition state $(R^{\#})^{243}$ (p. 108) which is considered to be the highest energy state along the reaction coordinate as shown in Figure 2.4. The energy difference between the $R^{\#}$ and R is called the activation barrier.

We have investigated the minimum energy path between the initial and final states during a transition state search. The transition state, which is also the saddle point of the potential surface. It is important to keep in mind that the saddle point is the local maximum along the reaction direction but the local minimum in all other directions. Numerous techniques have been created to determine the minimum energy path, and the nudged elastic band (NEB) method is one of the most effective techniques in this quest ²⁴⁴. The NEB approach creates several images between the initial point and the final state. The term elastic band is used since spring forces are added along the band between images to ensure the path's continuity. Also, to ensure that each image has a minimum energy, each iteration should estimate the tangent to the path in order to decompose the spring force and true force (that arises from the potential energy landscape of the system). During the minimisation, only the parallel component of the spring force and the perpendicular component of the real force are taken into account.

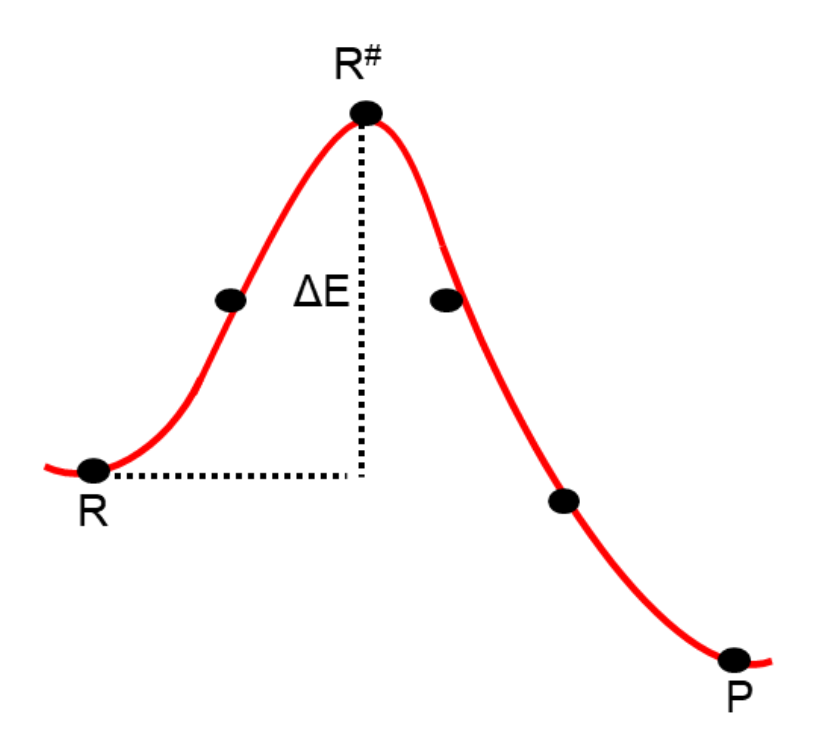


Figure 2.4. Schematic representation of the transition state theory (TST).

2.9 Vibrational Calculations

Vibrational calculations are of great value in many areas of chemical science as they provide the spectroscopic signatures of both short-lived and long-lived species. Based on the analysis of vibrational modes, both structure and composition of molecules can be determined²⁴⁵ (p. 130). In addition, they are needed to calculate the entropy, and zero point energy, and to find the minimum and saddle points on the potential energy surface.

To perform the vibrational study, we have determined the vibrational frequencies by solving the eigenvalue problem as shown in equation (Eqn. 2.10), based on the harmonic approximation of the potential energy surface.

$$DL = \Lambda L. \tag{2.10}$$

where D represents the dynamical matrix containing second-order derivatives of QM/MM energies with respect to nuclear displacements around a configurational equilibrium in mass-weighted Cartesian space. Λ and L are the diagonal matrix of eigenvalues and the eigenvectors-composed matrix, respectively. In the following, the eigenvectors here will be called normal modes, and L is used as the transformation matrix whose columns are exactly the eigenvectors of the dynamical matrix D, transferring nuclear displacements in mass-weighted Cartesian coordinates to normal modes coordinates. Vibrational frequencies of normal modes are taken as the square roots of eigenvalues in the diagonal matrix Λ . The local modes are considered more appropriate for interpreting the experimental data, compared to normal modes, as the latter is delocalised throughout the vibrational system. In the Zeolite QM/MM cluster, a normal mode involves delocalised combinations of vibrational motions from different chemical groups, for example, nitrate and nitrosamine groups, for which only fractions can be resolved in experimental vibrational spectra.

To overcome the delocalisation problem, we analyse the vibrational frequencies along with localised modes by first transforming the normal modes into a set of localised vibrations of individual species ²⁴⁶. Here in the case of the Chabazite structure, a local mode will in general be dominated by vibrations of single species. Of course, localised modes contribute to similar signatures in experimental spectra and they allow us to learn more accurately about the environment of the species, for example, the presence of solvent and ammonia in the silicious environment affects the vibrational properties of active sites. A previous study²⁴⁶ introduced a method that applies unitary transformation repetitively, the so-called Jacobi sweeps procedure, to maximise the atomic contributions in individual modes, by taking fractions of kinetic energies of atomic species in normal modes, or to achieve the largest separations between centres of any repair of individual modes (Eqn. 2.11- 2.13). Since only a pair of modes have

been involved in a unitary rotation during the localisation procedure, the orthogonality has been maintained. In our work, we choose the latter criterion according to a previous report ²⁴⁷ that the localisation is effected using the maximal separations among modes. Once the unitary transformation is no longer able to increase the separations, the local modes are obtained.

$$\tilde{C}_{ip}^{sub} = \sum_{a=x,y,z} \left(\tilde{Q}_{i\alpha,p}^{sub} \right)^2. \tag{2.11}$$

$$R_p^{center} = \sum_{i=1}^n \tilde{C}_{ip}^{sub} R_i.$$
 (2.12)

$$\xi_{dist} \left(\tilde{Q}^{sub} \right) = \sum_{p=1}^{k} (R_p^{center})^2 = \sum_{p=1}^{k} (\sum_{i=1}^{n} \tilde{C}_{ip}^{sub} R_i)^2.$$
 (2.13)

Where \tilde{C}_{ip}^{sub} represents the contribution of nucleus i to the normal mode $\tilde{Q}_{i\alpha,p}^{sub}$. This contribution can be measured by determining the fraction of kinetic energy associated with this specific atom within the normal mode. R_p^{center} refers to the "center" of the mode, which is determined by weighing the atomic coordinates (R_i) with their corresponding contributions to the normal mode.

2.9.1 Validational Scaling Factor

The computed quantum chemical harmonic vibrational frequencies (v) are typically greater than the fundamentals (\tilde{v}) observed experimentally, and, therefore, are often scaled by empirical factors, to bring them closer to the "true" fundamental frequency. However, it is also known that it is impossible to describe well all bands of a complex diverse system using just one scaling factor, which can be related to the different behaviour of different chemical bonds (*cf.* single bonds vs double bonds vs triple bonds). The reliability of our scaled vibrational frequencies is demonstrated by comparing them with the experimentally measured Diffuse Reflectance Fourier Transform Spectroscopy (DRIFTS) vibrational spectra, where all major

bands are in very good agreement. In particular, we have used different scaling factors obtained from the comparison of the corresponding gas phase experimental and calculated values, for which we carefully chose reference molecules that are very close in structure and bonding to the corresponding intermediate species. For example, in the case of bidentate nitrate species with a double N-O_{str} bond, we calculated the scaling factor value based on the theoretical and experimental values for HNO₃ as a reference molecule, whereas for a resonance N-O_{str} bond (single to double) in nitrosamine species, we chose an average of NO fractions from similarly bonded NO₂ and N₂O molecules – see figure below (2.5).

$$R^{1} \stackrel{\bigcirc}{\longrightarrow} R^{2}$$
1a
$$R^{1} \stackrel{\bigcirc}{\longrightarrow} R^{2}$$
1b

Figure 2.5. Resonating structure of nitrosamine species

To this end, we first obtained the scaling factor of all species for which harmonic vibrational calculations are performed. For example, in the case of nitrate species, we choose HNO₃ as a reference molecule (Table 2.3). The estimated scaling factor (0.943) is determined by comparing the theoretical (1814 cm⁻¹) and experimental (1710 cm⁻¹).

Table 2.3. Calculated scaling factor value based on the theoretical and experimental values for N-O_{str} of HNO₃ as a reference molecule.

Theoretical	3775	1814	1389	1342	936	809	677	603	492
Experimental	3550	1710	1331	1325	879	647	579	762	456
Scaling factor		0.943							

Similarly, for nitrosamine species, we calculated the scale factor for N-O stretching based on the theoretical and experimental values and chose an average of NO fractions from similarly bonded NO₂ and N₂O molecules (Table 2.4-2.7) as reference molecules.

Table 2.4. Calculated scaling factor value based on the theoretical and experimental values for N-O_{str} of NO₂ as reference molecules.

Theoretical	1769	1432	781
Experimental	1618	1318	750
Scaling factor	0.915	0.92	

Table 2.5. Calculated scaling factor value based on the theoretical and experimental values for N-O_{str} of N₂O as reference molecules.

Theoretical	2401	1372	637
Experimental	2230	1250	600
Scaling factor		0.91	

Average = 0.915 + 0.92 + 0.91/3 = 0.915 (average of NO fractions from NO₂ and N₂O molecules)

Table 2.6. Calculated scaling factor value based on the theoretical and experimental values for N-N_{str} of N₂O as reference molecules.

Theoretical	2401	1372	637
Experimental	2230	1250	600
Scaling factor	0.929		

Table 2.7. Calculated scaling factor value based on the theoretical and experimental values for $N-N_{str}$ of N_2H_2 as reference molecules.

Theoretical	3283	3252	1696	1686	1363	1360
Experimental	3128	3120	1583	1529	1286	1350
Scaling factor				0.907		

Average = 0.907+0.929/2 = 0.918 (average of N-N fractions from N_2H_2 and N_2O molecules

2.10 Resources

We have employed two QM codes, GAMESS-UK²⁴⁸ (General Atomic and Molecular Electronic Structure System) ²⁴⁸ and NWChem²¹⁶ to perform the electronic structure and vibrational calculations within the ChemShell^{214, 216, 217} environments. MM codes such as GULP (General Utility Lattice Program)²³¹ and DL-POLY²³² packages were used for all interatomic potential-based calculations presented within this thesis. UK National computing facilities, especially ARCHER and ARCHER2¹ were used to perform the major calculations. Other HPC resources are also used including THOMAS, YOUNG², and KATHLEEN³ clusters owned by UCL, as well as computing resources provided by STFC Scientific Computing Department's SCARF cluster⁴.

2.10.1 Justification of the Choice of Software

The work was performed primarily with the ChemShell^{214, 216, 217} packages integrating with the NWChem and GAMESS-UK²⁴⁸ as the QM drivers and DL-POLY²³² as the MM driver. Further porting of the zeolite model in Py-ChemShell then allows a shift to GULP²³¹ as the MM driver, especially for vibrational calculations. The QM calculations are benchmarked and tested against jobs run using Gamess-UK. ChemShell implements the embedded cluster hybrid QM/MM methodology – the method of choice in our studies – on massively parallel platforms and does not have viable alternatives.

2.11 Benchmarking

¹ https://www.archer2.ac.uk/

² https://www.rc.ucl.ac.uk/docs/Clusters/Young/

³ https://www.rc.ucl.ac.uk/docs/Clusters/Kathleen/

⁴ https://www.scarf.rl.ac.uk/

We performed some test studies to benchmark our calculation using Chemshell^{214,216,217} software on the UK's new National computing machine ARCHER2 as shown in Figure 2.6. The purpose of this study is to examine the usage of feasible nodes for the particular study and to avoid unnecessary computational costs.

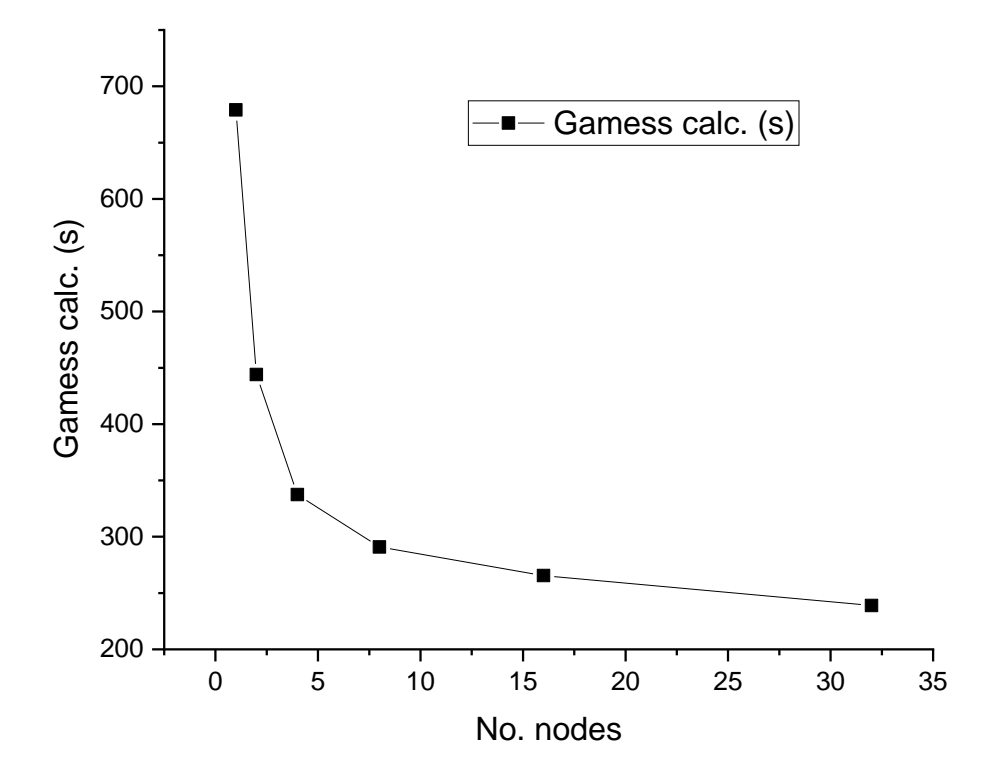


Figure 2.6. Benchmarking of Gamess-UK calculations by varying nodes on Archer2 machine.

Chapter 3

Reactivity of Cu-CHA in NH₃-SCR

3.1 Introduction

As discussed in Chapter 1, small pore zeolites containing copper such as Cu-SSZ-13 possessing the chabazite (CHA) topology, have shown outstanding performance in the NH₃-SCR reaction ^{84, 87, 249}. It has been reported that Cu-CHA not only possesses several active sites, including Cu⁺ and Cu²⁺ ions in NH₃-SCR but also species beyond single ions and with higher Cu ion nuclearity ^{119, 139}. For low-temperature SCR (Temp; < 200-250 °C), it has been proposed that Cu ions of higher nuclearity are active, which is, however, not the case for the high-temperature SCR where ions of low nuclearity have been proposed ²⁵⁰. Following the NH₃-SCR cycle, the reaction proceeds either through a standard-SCR (Eqn. 3.1) or NO-activation pathway (Eqn. 3.2), which can proceed with the same reduction step as the fast-SCR (Eqn. 3.3); however, in the "NO-activation" cycle, the rate does not depend on the concentration of NO₂ while it is dependent on the concentration of NO₂ in the fast SCR ¹²⁰.

$$4NO + 4NH_3 + O_2 \rightarrow 4N_2 + 6H_2O.$$
 (3.1)

$$3NO + 2NH_3 + O_2 \rightarrow 2N_2 + 3H_2O + NO_2.$$
 (3.2)

$$NO + 2NH_3 + NO_2 \rightarrow 4N_2 + 3H_2O.$$
 (3.3)

To understand how Cu cations can control nitrogen chemistry in CHA zeolite, the reaction mechanisms have been investigated with both modelling and experimental techniques (Figure 3.1). For this purpose, we have employed density functional theory (DFT) using a quantum

mechanical/molecular mechanical (QM/MM) methodology (as implemented in the ChemShell software), and Diffuse Reflectance Fourier Transform Spectroscopy (DRIFTS) experiments (undertaken by Andrew Beale and colleagues) which allow us to observe the formation and consumption of short-lived intermediates in the catalytic reaction. We elucidate the reactivity of Cu-CHA sites in the NH₃-SCR reaction where we report a comprehensive study in which the computational analysis provides a clear assignment of all main spectroscopic features of the NH₃-SCR catalytic cycle, that are in good agreement with DRIFTS experiment.

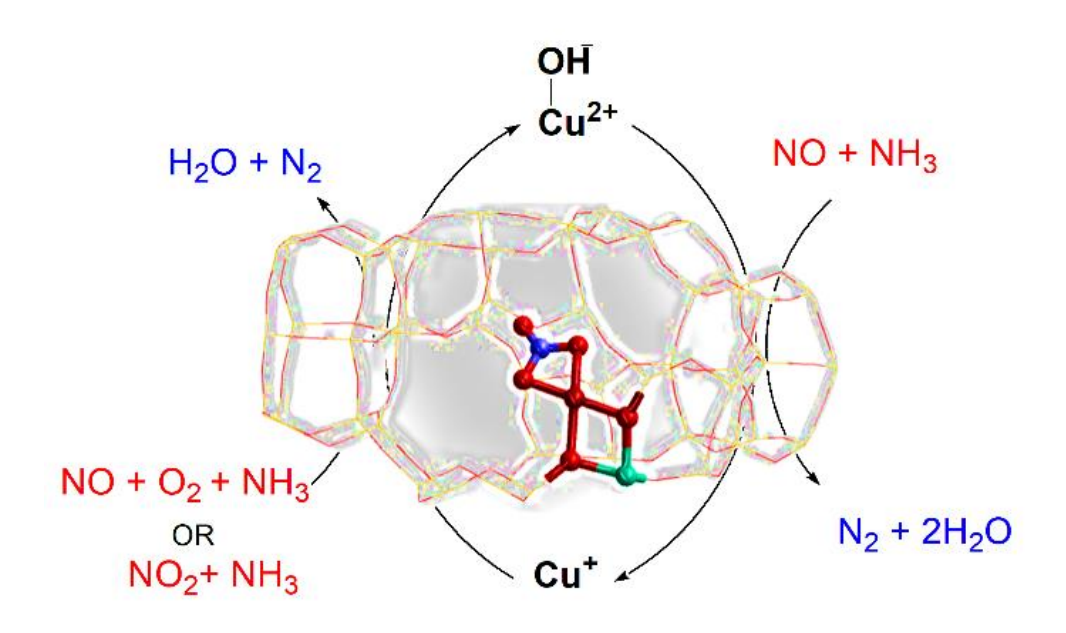


Figure 3.1. Schematic representation of NH₃-SCR of NO_x catalytic cycle.

3.2 Computational and Experimental Methodologies

3.2.1 QM/MM Methodologies

A hybrid QM/MM model^{251, 252} using the ChemShell software^{214, 216, 217}, discussed in Chapter 2 was employed to study the NH₃-SCR process over Cu-CHA. We set an active region, where all constituent atoms are allowed to relax freely, extending to a radius of 15 Å (~28.3 Bohr)

from the chosen centre containing Al site. A central core of the active region is modelled as a relatively small QM cluster embedded in a much larger MM cluster (Figure 2). The active region is in turn surrounded by a frozen spherical layer with a thickness of *ca.* 15 Å. The total number of atoms in our CHA-cluster model is 6007, of which 700 are active atoms, with ~143 QM atoms, not including hydrogen link atoms. A judicious choice of the basis set discussed further below, allows us to employ moderate basis sets in the QM region; thus, in the nitrate case, there are 2983 and 2797 Cartesian and harmonic basis functions, respectively, for the largest systems of interest (containing intermediate reacting species). The calculations for the QM clusters were performed using the GAMESS-UK package²⁴⁸, while for the MM part, the DL_POLY package²³² was employed, with the Hill-Sauer Molecular Mechanical force-field²²⁶, which assumes that the atoms bind to each other by polar covalent bonds. The outer shell of point charges whose values have been fitted to reproduce accurately the electrostatic field in the active region of the infinite CHA-zeolite framework.

3.2.2 Choice of Model Cluster

To perform the QM/MM calculation, we first created a spherical embedded-cluster model (Figure 3.2) of CHA from the unit cell of siliceous CHA ²³⁶ optimized at the MM level using the GULP package ²³¹. After creating a simple CHA-cluster model, we construct active sites. For example, in the case of a Brønsted acid site, we replaced one Si with Al and added a charge-compensating proton on a neighbouring oxygen atom at a site where it is most accessible to facilitate the reaction. The QM region which is contained within the active part of the model includes atoms from the third oxygen shell from the central T-site; and, as noted, we have added the hydrogen (link atoms) to saturate the terminal oxygen atoms. Link atoms compensate the charge at terminal positions and act as a bond-dipole correction to ensure an accurate

electrostatic potential. Furthermore, we modified the same cluster by incorporating copper into the cage of the CHA framework.

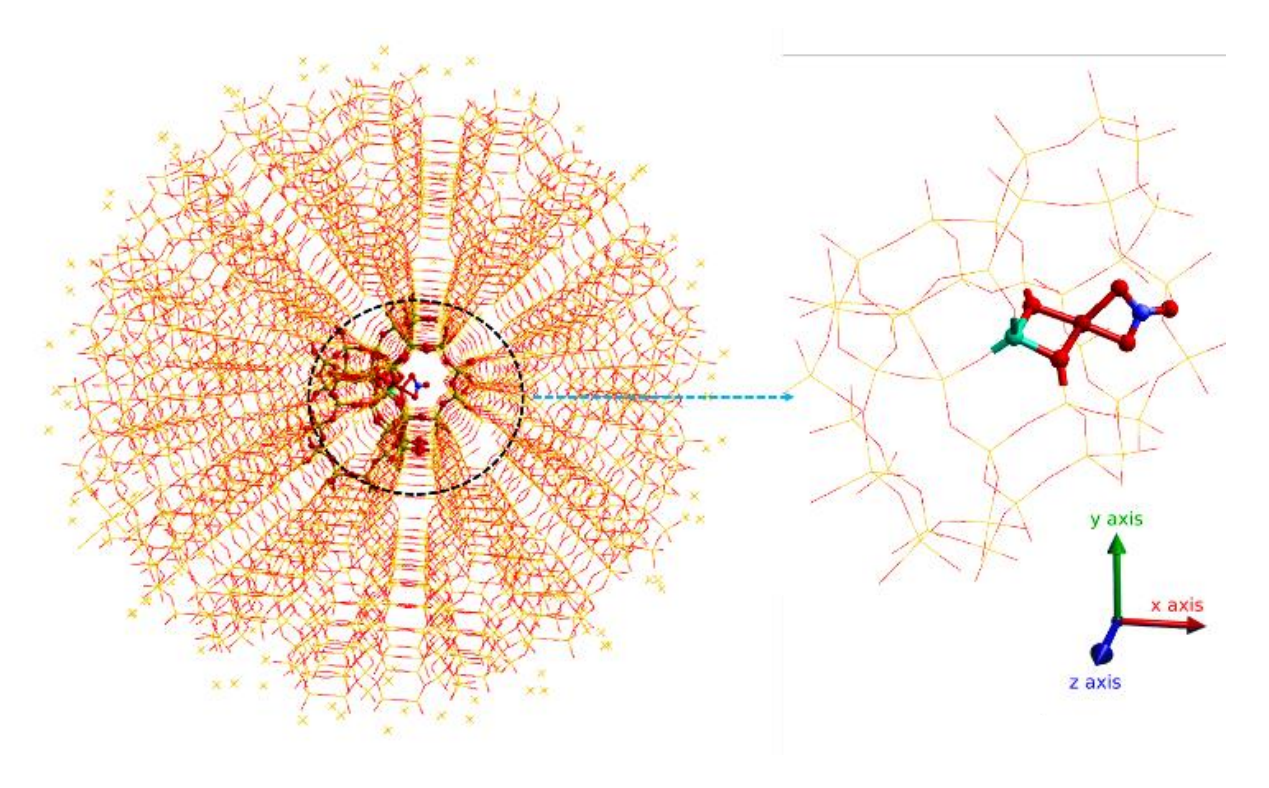


Figure 3.2. The QMMM embedding setup; the CHA cluster (left) with a quantum mechanical region containing nitrate species (right). The outermost region contains point charges to ensure the Madelung potential in the centre of the cluster is accurately reproduced. Atom colour codes: Cu (brown), Al (green), Si (yellow), O (red), N (blue), and H (white).

3.2.3 Vibrational Calculations

For vibrational frequencies at a local active site modelled by the hybrid QM/MM approach, only nuclear displacements of the active sites are included, i.e., a frozen phonon approximation from the expanded environment accounting for electrostatic interactions is applied throughout the vibrational calculations. We chose an active region that contains atoms around the Al centre within 3 coordination spheres (5T-site) including the atoms of the intermediate species and calculated normal and localised modes. Full details of the approach used for vibrational frequency calculations are given in Chapter 2.

3.3 Result and Discussions

In this chapter, we studied the NH₃-SCR reaction mechanism which has been proposed by Janssens *et al.* ⁵⁸, who reported both standard and fast NH₃-SCR of NOx in a complete cycle (Figure 3.3) that can produce the correct stoichiometry for the reaction. However, in our study, additional insight into the reaction mechanism from the insight of hybrid-QM/MM calculations and concentration modulation ME DRIFTS experiment is included. The computational mechanistic study focuses on these results which complement and give insight into the experimental findings. We also report a comprehensive study in which the computational analysis provides a clear assignment of all main spectroscopic features of the NH₃-SCR catalytic cycle, that are in good agreement with the experiment.

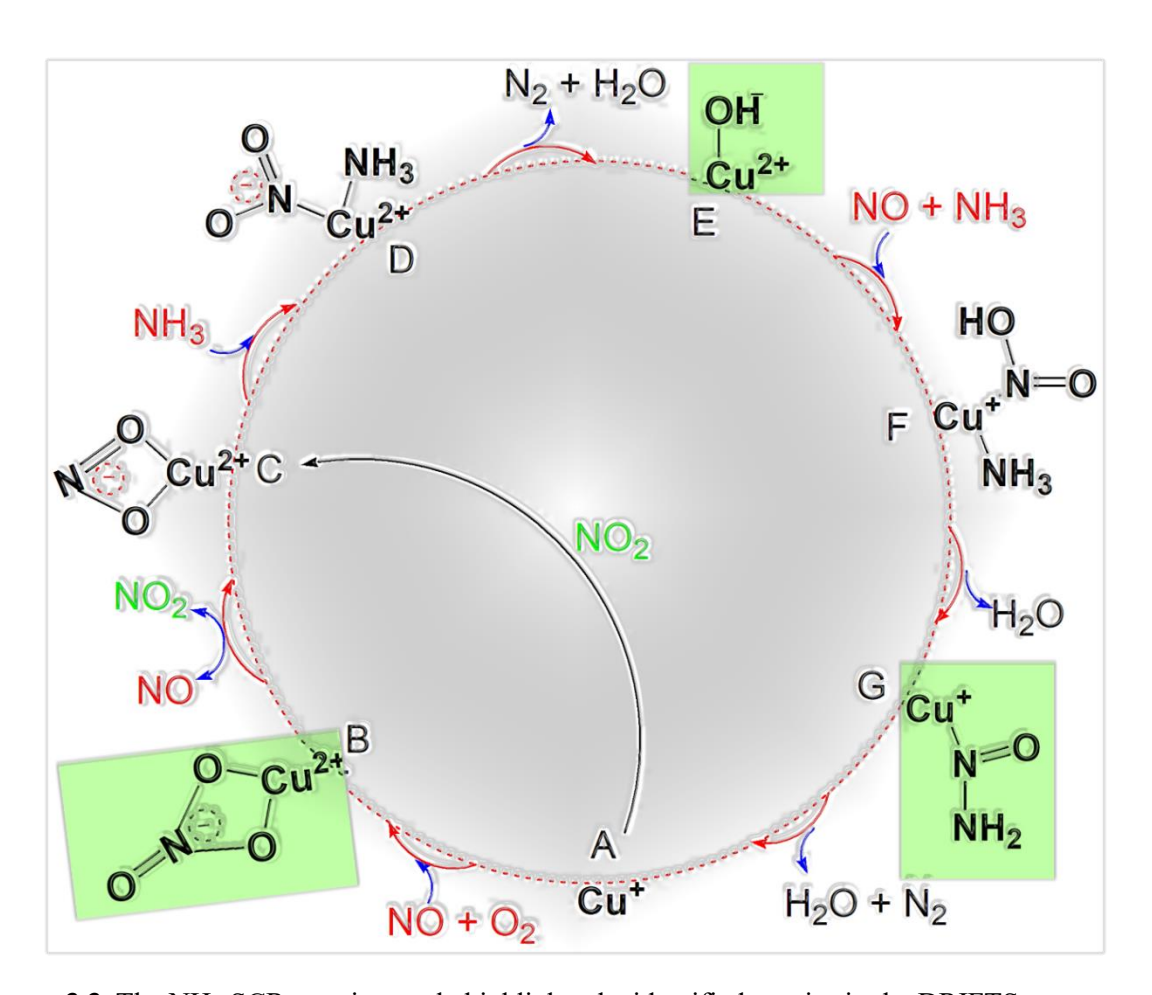


Figure 3.3. The NH₃-SCR reaction cycle highlights the identified species in the DRIFTS spectra.

3.3.1 Vibrational Study

First, Beale and co-workers performed DRIFTS experiments exploiting (concentration) modulation excitation spectroscopy (MES), and phase-sensitive detection (PSD), to determine the evolution of species in response to a stimulus; in this case, the NO flow during a constant stream of 500 ppm NH₃, 10000 ppm O₂ produce N₂ akin to the standard NH₃-SCR reaction at 250 °C. They used facilities in the Catalysis Hub Centre on the Harwell Science and innovation Campus. DRIFTS spectra were recorded on a Bruker Vertex 70 spectrometer equipped with a liquid-N₂ cooled HgCdTe detector and a Praying Mantis mirror unit (Harrick)- details are in the appendices A.2. This approach allows us to observe the formation and consumption of short-lived intermediates in the catalytic reaction, crucially, the detection of species, which had not been previously observed experimentally. The data are shown in Figure 3.4. Notable observations included the initial consumption of [Cu²⁺(OH)]⁻ to form an important intermediate, which has been identified as copper nitrosamine (Cu-N(=O)-NH₂) based on the observation of evolving bands in the IR spectrum at 1436 cm⁻¹ (N=O_{str}), 1330 cm⁻¹ (N=O_{str}), and 1258 cm⁻¹ (N-H_{bend}). Below 1200 cm⁻¹, we are unable to collect reliable spectroscopic data due to the overlapping of zeolite framework vibrations with other bands. The next species detected in the cycle was a bidentate nitrate (N=O_{str} at 1606 cm⁻¹). Note that all bands appear with a different 'phase', or time during the experiment indicating that the corresponding species are not typically present at the same time.

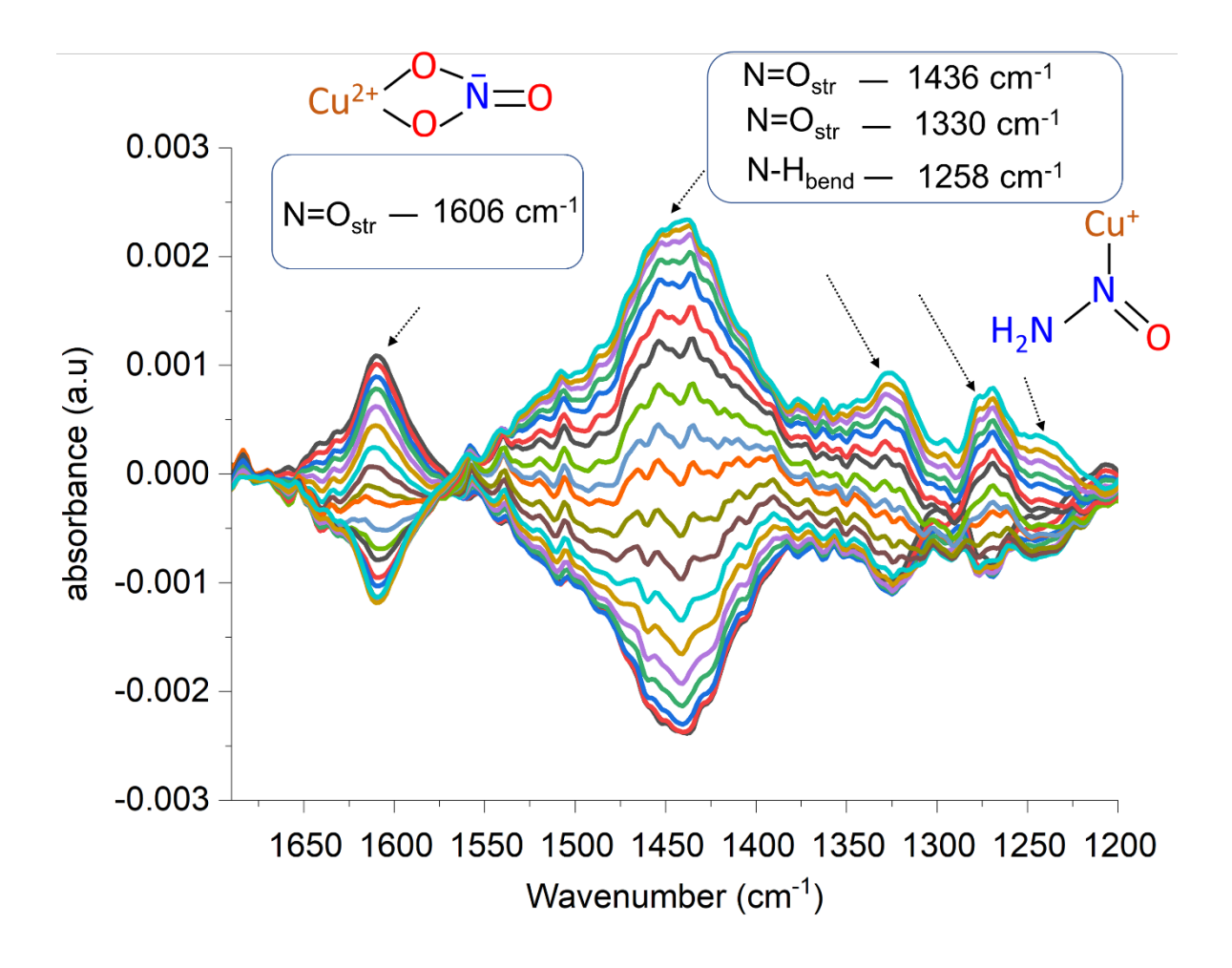


Figure 3.4. Spectroscopic Signatures; (a) Concentration modulation ME DRIFTS experiment with corresponding phase-resolved spectra for bidentate Cu nitrate (Cu–NO₃) and Cu-nitrosamine (Cu–N(=O)–NH₂) species.

Secondly, we calculated the harmonic vibrational spectra of selected intermediates. The harmonic values obtained were scaled using vibrational scaling factors (see methodology section), which were determined by comparing experimental and computational harmonic values using a representative set of gas phase molecules. We focused on bands of nitrosamine (N-O_{str}, and N-N_{str}) and nitrate (N-O_{str}); the yielded scaling factor to calculate the vibrational frequency of N-O_{str} of nitrosamine is 0.915 while for the N-N_{str} is 0.918. Similarly, the corresponding scaling factor we applied for the N-O_{str} of nitrate is 0.943.

As shown in Figure 3.5, for the bare Cu-nitrosamine (Cu-N(=O)-NH₂) species, we found a vibrational stretching band around 1478 cm⁻¹ compared to our experimental value of 1436 cm⁻¹ ¹, tentatively ascribed to the N=O_{str} mode (Table 3.1). Haszeldine and Jander reported the N=O_{str} band at 1488 cm⁻¹ which is close to our calculated frequency ²⁵³. Also, bands in the region 1408—1486 cm⁻¹ have been reported by Piskorz and Urbanski²⁵⁴ and Tarte²⁵⁵ and assigned to the N=O_{str} frequency of nonassociated dialkylnitrosamine (in nonpolar solvent: CCl₄). They also reported peaks for N=O_{str} between 1346–1265 cm⁻¹ and 1321–1292 cm⁻¹, which can be broad and strong, or of medium strength. Importantly, this can be also seen in our measured DRIFTS spectra [(N=O_{str}), 1330 cm⁻¹]. Further, Kedrova et al. have observed the vibrational frequencies of associated nitrosamine and identified both N=O_{str} (1470 cm⁻¹-1495 cm⁻¹) and N-N_{str} (1055 cm⁻¹-1060 cm⁻¹) bands ²⁵⁶. The lower frequency spectral features found in our QM/MM calculations are in particular due to N-N stretching vibrations of Cunitrosamine (Cu-N(=O)-NH₂) species. For the bare site, the N-N stretching frequency is calculated as 1124 cm⁻¹ as compared to the reported experimental values in the Nitrosodimethylamine (1052 cm⁻¹) and Di-N-nitroso-pentamethylenetetramine (1106 cm⁻¹) ²⁵⁴. In addition to the N=O_{str} and N-N_{str} bands for nitrosamine species, we also examined the N-H bend, which is likely to appear in this region; the computed value for the bare site is at 1225 cm⁻¹.

 $N-O_{str}$ — 1478 cm⁻¹ $N-N_{str}$ — 1124 cm⁻¹

 $N-H_{bend}$ — 1225 cm⁻¹

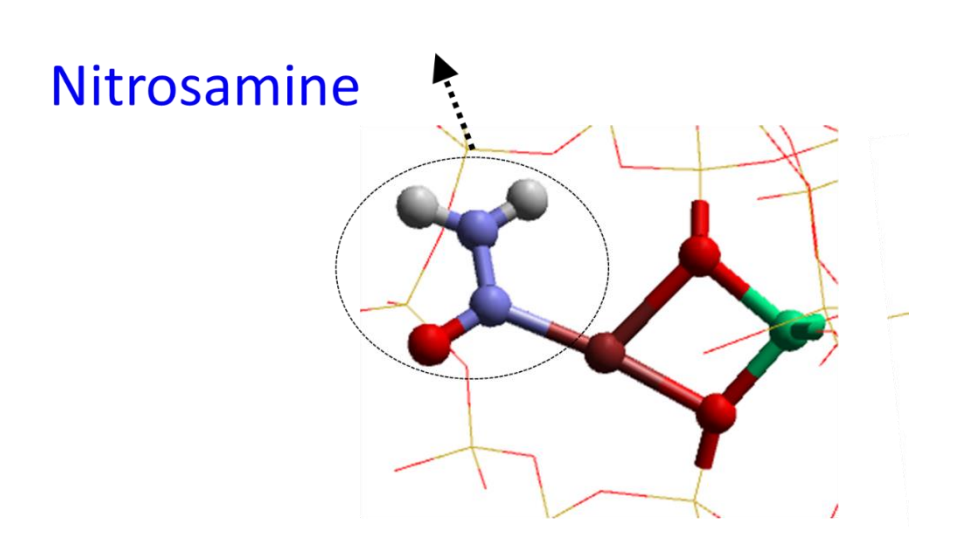


Figure 3.5. Spectroscopic Signatures; data yielded from QM/MM calculations for Cu-nitrosamine (Cu-N(=O)-NH₂) species. **Atom color codes**: Cu (brown), Al (green), O (red), N (blue), and H (white). The framework SiO₂ is shown using a wire framework motif.

Table 3.1. Scaled vibrational frequencies for the nitrosamine species.

Assignments	Frequencies	Scale factor	Freq. after scaling
N-O stretch	1615	0.915	1478
N-N stretch	1225	0.918	1124

Next, we investigated a bidentate nitrate species (Figure 3.6, Table 3.2) with a focus on the $N=O_{str}$ stretching mode. Generally, nitrate species have four notable modes $^{257, 258}$. Our calculations show that the bare bidentate Cu–NO₃ structure possesses the main $N=O_{str}$ stretching frequency of 1620 cm^{-1} which is quite close to our experimental DRIFTS value of 1606 cm^{-1} . In addition, small broad bands that appeared in our experimental findings in the region of 1225 cm^{-1} to 1250 cm^{-1} could be assigned to the antisymmetric stretch (v_3 (E')) of the

N-O band, as reported by Zapata and García-Ruiz 257 . However, our QM/MM calculation shows this band at relatively lower frequencies (1172 cm $^{-1}$) for this mode. Finally, two bands that originated due to out-of-plane and in-plane deformation modes for nitrate species are displayed. The out-of-plane deformation band (v_2 (A"₂)) is normally located within the range of 800 - 900 cm $^{-1}$ while the in-plane band (v_4 (E')) ranges from 700-780 cm $^{-1}$ in nitrate salts 257,258 . Our calculated out-of-plane deformation occurs at a somewhat higher frequency as seen in Figure 3.6, however, the in-plane deformation has appeared almost in the same region as previously reported 257 .

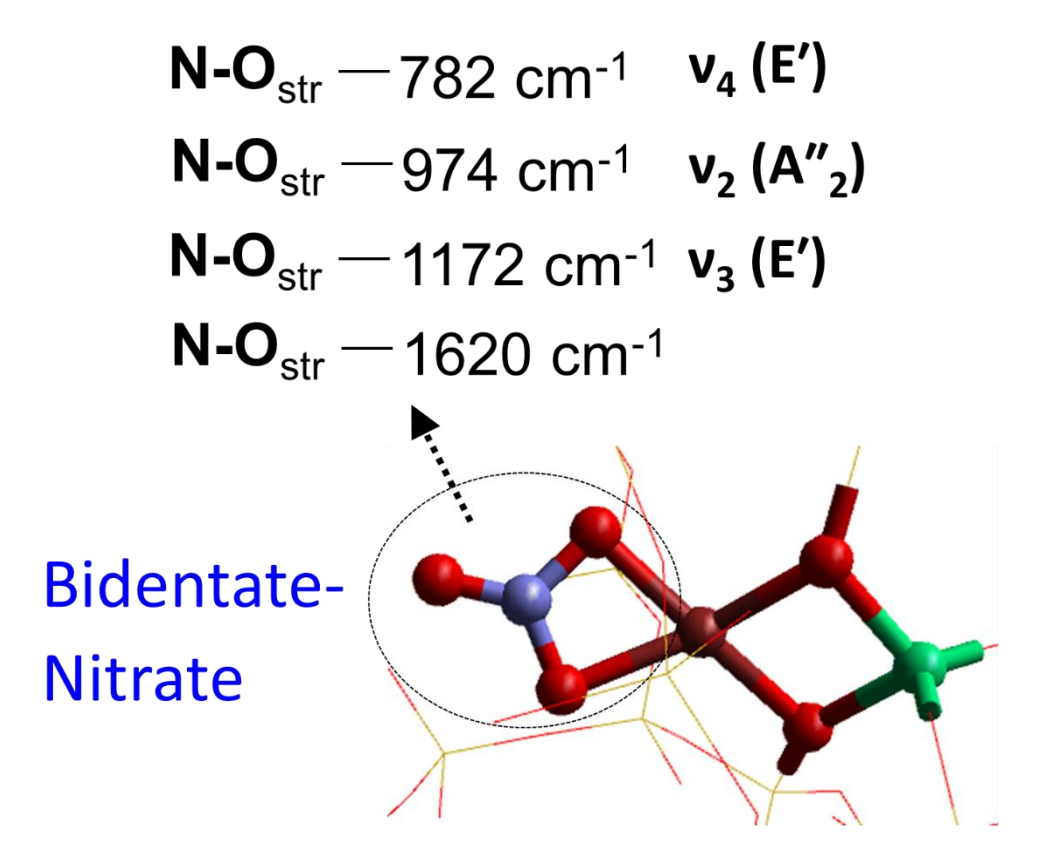


Figure 3.6. Spectroscopic Signatures; (a) Concentration modulation ME DRIFTS experiment with corresponding phase-resolved spectra, and (b) data yielded from QM/MM calculations for bidentate Cu nitrate (Cu–NO₃) and Cu-nitrosamine (Cu–N(=O)–NH₂) species. **Atom colour codes**: Cu (brown), Al (green), O (red), N (blue), and H (white). The framework SiO₂ is shown using a wire framework motif.

Table 3.2. Scaled vibrational frequencies for the bare nitrate species.

Assignments	Frequencies	Scale factor	Freq. after scaling
1 st N-O stretch	1718	0.943	1620
2 nd N-O stretch	1243	0.943	1172
3 rd N-O stretch	1033	0.943	973
4th N-O stretch	830	0.943	782

Based on the above analysis, we propose the following scaled assignment (Table 3.3) of the DRIFTS spectra as shown in Figure 3.4.

Table 3.3. Features observed in a concentration ME DRIFTS experiment's time-resolved spectrum under SCR conditions (NO gas switch pulse sequence). Assignment is based on an analysis of literature and calculated vibrational spectra of reactant intermediates shown in Figure 3b.

DRIFTS	Vibrational mode	Strength	Width	Calculated IR modes	Ref.
(cm ⁻¹)					
1606	N=O stretch (nitrate)	medium	Sharp	1620 (B), 1609 (H), 1600 (N)	259, 260
1436	N=O stretch	strong	Sharp	1478 (B), 1467 (H), 1462 (N)	253-256
	(nitrosamine)				
1330	N=O stretch	small	Medium		255
	(nitrosamine)				
1258	N-H bend (nitrosamine)	small	Sharp	1225 (B), 1224 (H), 1210 (N)	-
1230-1250	N-O anti-symm. stretch	small	Broad	1172 (B), 1192 (H), 1202 (N)	257, 258
	(nitrate)				
1210	N-N stretch	small	Medium	1124 (B), 1123 (H), 1111 (N)	254, 256

[B] bare [H] physisorbed-H₂O [N] physisorbed-NH₃

Moreover, we also did a separate vibrational analysis on $Cu-(N(=O)-OH)-NH_3$, a postulated species which further decomposes to the $(Cu-N(=O)-NH_2)$ species. The N-O_{str} appeared for this intermediate at 1585 cm⁻¹(Figure 3.7).

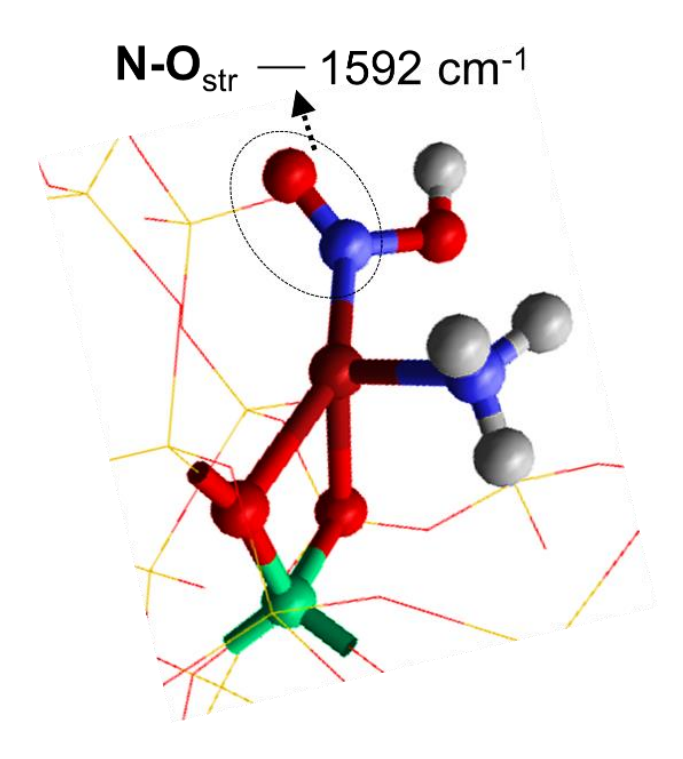


Figure 3.7. Vibrational spectroscopic analysis of the Cu-(N(=O)-OH)-NH₃ species.

Further, we examine the N=O_{str} vibrational mode of bidentate-nitrite (Cu–NO₂) (Figure 3.8) to determine whether the 1606 cm⁻¹ band in the DRIFTS spectrum originates from the nitrate or nitrite. The computed N=O_{str} band of this particular species is, however, found significantly lower than the N=O_{str} band of the bidentate-nitrate species at 1273 cm⁻¹. The calculated bands are comparable with the experimental values of *ca.* 1229 cm⁻¹ for the isostructural linear nitrite species reported in references ^{261, 262}.

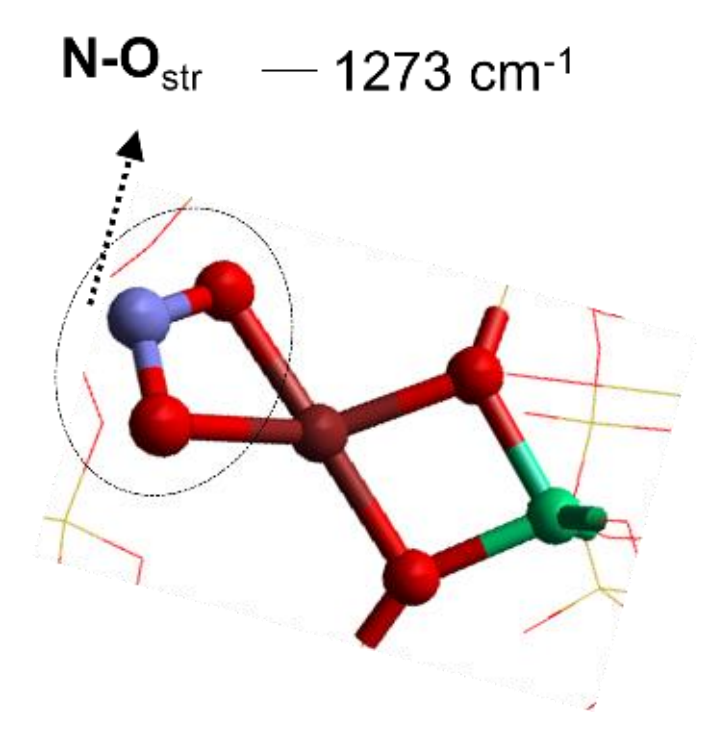


Figure 3.8. Vibrational spectroscopic analysis of the N=O_{str} vibrational mode of bidentate-nitrite (Cu–NO₂) species for all three sites.

We have performed a similar calculation on (Cu–(NO₂)–NH₃) (Figure 3.9); however, again we found that the NO band for this species is lower than the 1606 cm⁻¹ band in the DRIFTS spectrum assigned to N=O_{str} vibration. Based on the calculated vibrational modes, we infer that the spectroscopic signatures that appear in the DRIFTS spectrum can be tentatively assigned to the nitrate and nitrosamine species. Furthermore, we do not detect the N-O signatures in the DRIFTS spectrum for the nitrite (species C) and the species D and F in the cycle (see Figure 3.3), and even the first Cu-NO(OH) interactions on NO adsorption, indicating that these species are too short-lived to be observed in the experiment.

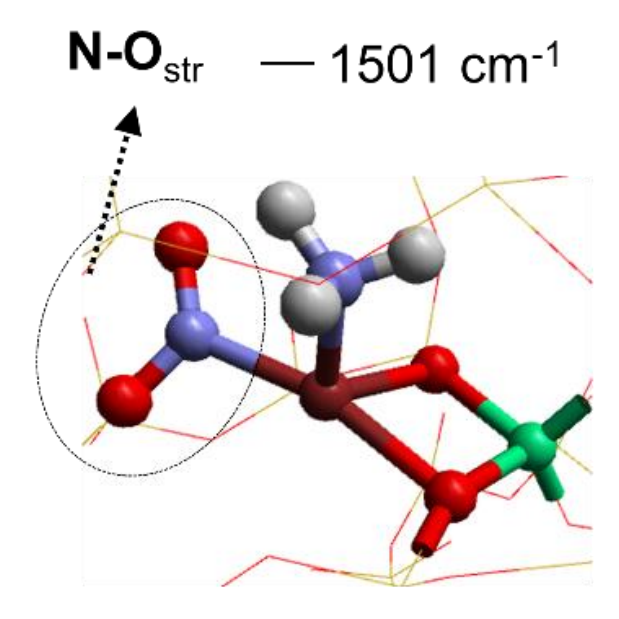


Figure 3.9. Vibrational spectroscopic analysis of the N=O_{str} vibrational mode of bidentate-nitrite (Cu–(NO₂)–NH₃) species for all three sites.

Our computational analysis provides a clear assignment (Table 3.4) of all main spectroscopic features of the species presented in the catalytic cycle Figure 3.3.

Table 3.4. Calculated vibrational bands of key intermediate species presented in the NH₃-SCR catalytic cycle – see Figure 3.3.

Species	Wavelength (cm ⁻¹)	Description of IR active mode
Cu-NO ₃ (species B)	1600	N=O stretch
Cu-NO ₂ (species C)	1273	N=O stretch
(Cu-(NO ₂)-NH ₃) (species D)	1501	N=O stretch
	3445	N-H stretch
Cu-(N(=O)-OH)-NH ₃ (species F)	1585	N=O stretch
	3313	N-H stretch
	3197	O-H stretch
(Cu-N(=O)-NH ₂) (species G)	1478	N=O stretch
	3482	N-H stretch
[Cu ²⁺ (OH)] ⁺ adsorbed NH ₃	3336	N-H stretch
	3668	O-H stretch
	1620	N-H bend
Brønsted acid site adsorbed NH ₃	3279	N-H stretch
	1455	N-H bend

Furthermore, Figure 3.10 shows the 2400 DRIFTS spectrum collected throughout the course of the modulation experiment in which NO is turned "on/ off" repeatedly between 0 and 500 ppm while the concentration of other reactive components, NH₃ and O₂, remains constant. Note that no discernible changes can be detected since the continuous presence of NH₃, as well as products of the reaction (H₂O), dominate the spectrum, particularly in the region between 2500 - 3500 cm⁻¹. We examine the O-H and N-H_{str} vibrational features for the competing [Cu²⁺(OH)]⁺ and Brønsted acid sites under an NH₃-SCR environment. In the DRIFTS spectrum (Figure S5) there are multiple vibrational bands in the region between 2500 – 3500 cm⁻¹ as the spectrum is mostly dominated by NH₃ and H₂O. The most notable feature in the phase-resolved spectrum is, however, that at 3655 cm⁻¹, which is indicative of [Cu²⁺(OH)]⁺ species that exhibit a greater fluctuation than those related to silanol groups or bridging hydroxyls, which is also reported by the Giordanino et al. 99. Our calculated value (3668 cm⁻¹) is in good accord with the DRIFTS experimental value and with the reported data²⁵⁹. The experimental attribution of this band to a [Cu²⁺(OH)]⁺ species was based on its response to changes in gas composition, indicating that this species actively participates in the catalytic mechanism²⁶³. The vibrational signatures of the likely NH₃ adsorption on the Cu²⁺ active sites are also confirmed by theory and experiment. In the corresponding DRIFTS spectrum, the N-H band which appears at 3332 cm⁻¹ is in good accord with the computed value of 3336 cm⁻¹. Moreover, we detect the N-H bending features at 1620 cm⁻¹ in the DRIFTS spectrum which is reproduced in our calculations with an accuracy better than 1 cm⁻¹ and agrees well with previous work ²⁶⁴. To study the competitive reactive pathway between NH₃ adsorbed on Cu sites and Brønsted sites, we analyzed the vibrational signatures of the NH3 adsorption on the Brønsted acid site, the interaction which may lead to the evolution of NH₄⁺ ions owing to the NH₃ protonation over these acid sites. The band intensity grows from ca. 1454 cm⁻¹ in the DRIFTS spectrum indicating the consumption of the v(O-H) band associated with the Brønsted acid sites. The

position of this band is confirmed by our computed value of 1455 cm⁻¹ and previous work⁹⁹ for the NH₄⁺ ions. The N-H stretching band of NH₄⁺ ions appears at 3272 cm⁻¹ in the DRIFTS spectrum which also agrees with the calculated vibrational value at 3278 cm⁻¹.

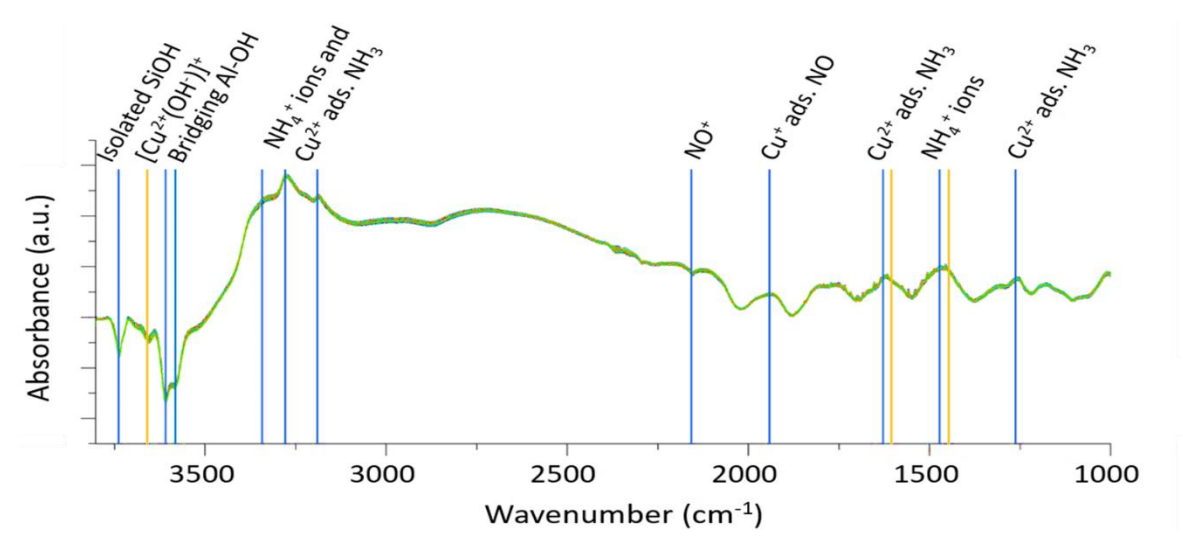


Figure 3.10. DRIFTS spectra showing various species that are collected during the NO concentration modulation experiment. The experiment is conducted by Andrew Beale's group.

3.3.2 Adsorption Properties of the Cu-CHA

We examined first the binding energies of the gaseous reactant molecules both on the Cu(I)-CHA and Cu(II)-CHA sites. From the results reported in Figure 3.11 considering the behaviour on the Cu(I) site, we note that the adsorption of NO, NH₃, and H₂O on the Cu⁺-/CHA site are, as expected, exothermic. The binding energy for NH₃, yielding NH₃-Cu⁺, is calculated as -0.84 eV (-81 kJ/mol) ^{58, 265} where the reported average experimental heat of adsorption for ammonia on Cu-Beta²⁶⁶ and Cu-CHA²⁶⁷ is nearly -100 kJ/mol. The experimental values, however, should be treated with caution as Cu-exchanged zeolites would still have a significant fraction of strongly adsorbing acid sites.^{268, 269} We have also examined the interaction of ammonia with the Brønsted acid site and found a binding energy of -1.1 eV (-106 kJ/mol), which is appreciably higher than that of the Cu Lewis site and is close to the experimental report. The heat of NH₃ adsorption over non-exchanged zeolites H-CHA has been reported to be as high

as -145 kJ/mol (obtained using microcalorimetry techniques)²⁷⁰, which is still appreciably stronger and could be related to the Brønsted acid complexes, which warrants a separate investigation.

Furthermore, these studies also suggest that the heat of adsorption decreases with increased ammonia coverage²⁶⁷. It is reported that the binding of NH₃ on Cu⁺ deeply influences the interaction of Cu with the framework of CHA; however, depending on the number of NH₃ molecules bound and temperature, cation mobility can become possible ²⁷¹. In this context, we observed that a single physisorbed NH₃ molecule detaches Cu⁺ from one of the framework O atoms making a new coordination adduct, H₃N-Cu-O with a distance between Al and Cu of 2.645 Å. H₂O also exothermically binds to the Cu(I)-CHA sites with a binding energy of -0.62 eV (-59 kJ/mol), but the monovalent Cu remains attached to the two framework O atoms. Furthermore, Lercher and co-workers employed a periodic PBE+D3 approach and obtained an adsorption energy of -77 kJ/mol for water on the Brønsted acid site of H-MFI ²⁷², whereas a value of -78 kJ/mol is obtained for the H-CHA by a hybrid MP2:PBE calculation²⁷³. We also observed that NO weakly adsorbs on bare Cu(I)-/CHA, through the N atom, (with a binding energy of only -0.08 eV), however, it is more favourable on solvated ammonia Cu(I) (-1.25 eV) and water Cu(I)(-0.58 eV) sites; where the corresponding experimental heat of adsorption is -65 kJ/mol (-0.70 eV) on Cu-Beta²⁶⁶.

Turning now to the Cu(II) sites, NH₃ and NO interact favourably with divalent Cu (II)-OH sites. NO binds through the O atom (-OH) (-1.01 eV) suggesting that it preferentially binds to the OH- site of Cu(II)-OH generating a HONO species. The formation of the HONO species has been described earlier ^{261, 274}. In the case of NH₃, strong bonding to the Cu(II) site is calculated, with a binding energy of -0.97 eV (-93 kJ/mol) and as seen in Figure 3.11, the

attachment of Cu(II) with the framework O is intact. We also calculate that water can interact strongly with the divalent Cu-site (with a binding energy of -0.91 eV), suggesting that water can affect the reactivity of active sites.

Based on the interaction of molecules with the active sites, we conclude that the adsorption of NO species with the O-end down is uncompetitive (positive) on both Cu⁺(0.11 eV) and Cu²⁺(0.12 eV) sites, suggesting that N-end down is the only feasible attachment to Cu-CHA sites. We found that O₂ preferably binds to Cu(I) sites with a binding energy of -0.18 eV (-17 kJ/mol) as reported before while on the Cu²⁺-OH⁻/CHA site, the adsorption energy is calculated to be positive (0.01 eV) ²⁷¹, which rules out the possibility of O₂ binding to the Cu²⁺-OH⁻/CHA, hence, signifying that O₂ plays a key role in the reoxidation of the Cu⁺-site.

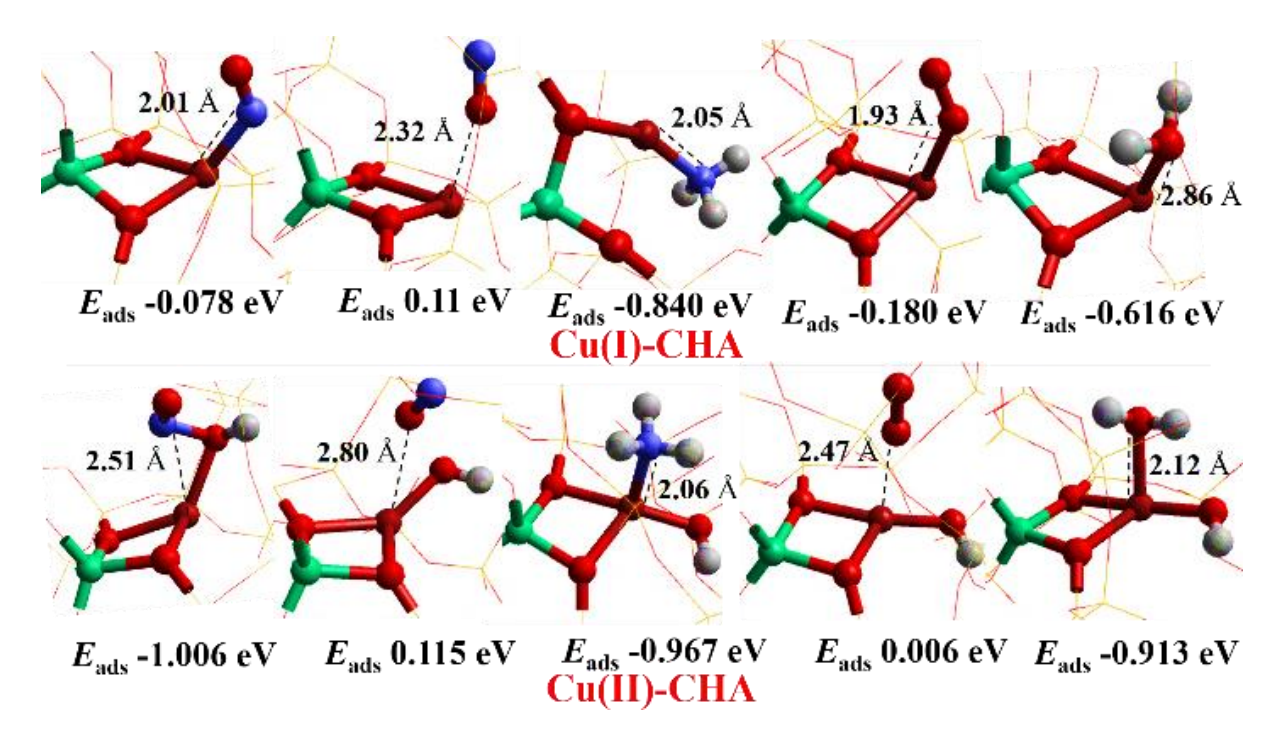


Figure 3.11. The reaction adsorption energies of NH₃, NO (with both O and N end-down), H₂O, and O₂ on Cu(I)-CHA and Cu(II)-OH/CHA sites. The model used is shown as an extra framework. **Color codes:** Cu (brown), Al (green), O (red), N (blue), and H (white). The framework SiO₂ is shown using a wire framework motif.

3.3.3 Comparison of Reaction Energetics with Experiment

To assess our procedure, we compared the simulated data with experimental measurements and analyze the results obtained for several case studies. To examine more thoroughly, we have tested different theories [CCSD(T), CR-CCSD(T)] and DFT functionals such as B97-2²³⁸, B97-3²⁷⁵, and BB1K²³⁹ on various Def2 basis sets²⁷⁶ e.g. Def2-SVP, Def2-TZVP, Def2-QZVP, Def2-TZVPD, Def2-QZVPD.

First, we calculated the reaction energy for Eqn. 3.2; a NO-activation pathway. The overall experimental $\Delta_f H^\circ_0$ value is -9.007 eV (-869.02 kJ/mol) which is calculated based on the enthalpy of formation of the gaseous species involved in this reaction. The calculated theoretical value is -8.37 eV which is similar to the previous calculations⁵⁸. Both the calculated and experimental values, although close (within 0.11 eV/molecule of each other) still did not fully agree. We then made some corrections and additions to achieve better agreement and improve the model. We have improved the value to some extent while employing higher def2 basis sets²⁷⁶ such as def2-QZVP (-8.421 eV) and def2-QZVPD (-8.460 eV). But the effect of the higher basis sets was not significant, as shown in below Table 3.5.

Table 3.5. The calculated reaction energies (eV) for NO-activation reaction (Eqn 3.2); both theoretical and experimental values. All theoretical calculations are performed using def2 basis sets ²⁷⁶.

DFT	Def2-svp	Def2-tzvp	Def2-qzvp	Def2-tzvpd	Def2-qzvpd
B97-2	-7.817	-8.366	-8.421	-8.406	-8.458
B97-3	-7.865	-8.352	-8.455	-8.399	-8.481
Bb1k	-7.816	-8.309	-8.385	-8.350	-8.410
Exp	-9.007				
Post-HF	Def2-svp	Def2-tzvp	Def2-qzvp	Def2-tzvpd	Def2-qzvpd
CCSD(T)	-9.567	-9.925	-9.435	-9.124	-9.475
CR-CCSD(T)	-9.534	-9.0232	-9.370	-9.329	-9.849

Experimental $\Delta_f H^{\circ}_0 = -9.007 \text{ eV } (-869.02 \text{ kJ/mol})$

Theoretical = -8.366 eV

The experimental data such as standard enthalpy of formation for all gaseous species in a tubulated form is given in Table 3.6 along with an additional table (Table 3.7) that shows how we calculated the reaction energies based on these values for Eqn. 2.11 in Chapter 2.

Table 3.6. The standard enthalpy of formation values of the species at temperatures 298°C and 0°C.

Species	Δ _f H° (298.15 K)/kJ.mol ⁻¹	H° (298.15 K) - H° (0)/kJ.mol ⁻¹	H° (0)
NO	91.3	8.675	99.975
NH_3	-45.94	10.043	-35.897
NO_2	33.2	13.015	46.215
H_2O	-241.826	9.905	-231.921
N_2	0	8.67	8.67
\mathbf{O}_2	0	8.68	8.68

Standard enthalpy of formation $\Delta_h H^\circ$ at 298.15 K, the quantity H° (298.15 K) - H° (0). Note that the value of 0 in the $\Delta_h H^\circ$ column for an element indicates the reference state for that element.

Table 3.7. The calculated reaction energies for reaction (Eqn 3.2) are based on the standard enthalpy of formation of the species involved.

Temperature (°C)	Reactants (kJ/mol)	Products (kJ/mol)	$\Delta_f H^{\circ}$ (kJ/mol)	$\Delta_f H^{\circ} \text{ (eV)}$
298	182.02	-692.278	-874.298	-9.06
0	236.811	-632.208	-869.019	-9.01

Secondly, we compared the N_2 association energy of simulated data with experimental measurement. However, the obtained theoretical value of 9.88 eV is only 0.08 eV greater than the experimental value for the standard enthalpy of formation of 9.80 eV (Table 3.8).

Table 3.8. The calculated N_2 association energies (eV); both theoretical and experimental values. All theoretical calculations are performed using def2 basis sets 276 .

DFT	Def2-svp	Def2-tzvp	Def2-qzvp	Def2-tzvpd	Def2-qzvpd
B97-2	9.839	9.885	9.890	9.896	9.905
B97-3	9.854	9.917	9.926	9.925	9.936
Bb1k	9.344	9.404	9.412	9.413	9.423
Exp	9.80				

Experimental $\Delta_0 H^{\circ}_0 = 9.80 \text{ eV } (945.556 \text{ kJ/mol})$

Theoretical = 9.88 eV

3.3.4 Catalytic Cycle

It is possible to split the NH₃-SCR redox cycle and separate the oxidation from the reduction step (Figure 3.3), which is achieved experimentally by switching between the NH₃ + NO and NO + O_2^{277} atmospheres to study the individual half-cycles ¹²⁰. The Cu(II)-nitrate species formed as a result of the NO + O_2 oxidation process, can be converted back to the Cu(I)-state under NH₃ + NO reductive conditions. Furthermore, NO can react with the nitrate intermediate to generate gaseous NO₂ and Cu-nitrite species. Such NO activation, which has been reported for both single Cu-sites and Cu(II)-pair mediated systems, accounts for Cu(II) reduction and is often considered necessary for the NH₃-SCR reaction ^{107, 278}. The formation of NO₂ species facilitates the oxidation half-cycle and hence leads to establishing a link to the so-called fast SCR reaction ²⁷⁹.

During the NH₃-SCR cycle, molecules including NO, NH₃, O₂, N₂, and H₂O are either adsorbed or desorbed from the Cu-CHA site, and the intermediate species are generated at each step. The adsorption of NO and O₂ on Cu⁺-/CHA generates nitrate and nitrite species which undergo

decomposition to N₂ and H₂O; this half cycle of the NH₃-SCR is, as noted, known as the oxidation part, which is followed by the reduction of Cu²⁺ where Cu²⁺-OH⁻/CHA reacts with both NO and NH₃, with Cu²⁺ reduced to Cu⁺ while generating N₂ and H₂O as a product, as is evident from both experimental and theoretical studies ²⁷¹. The calculated adsorption energies of the corresponding gaseous species allow us to obtain the reaction energies.

Considering the NH₃-SCR of the NOx cycle: the corresponding reaction energy landscape is shown in Figure 3.12. The optimized reaction step for this cycle is shown in Figure 3.13. The starting point for the reaction is an isolated Cu(I) site that activates the O₂ molecule (Step I). The energy diagram demonstrates that O₂ adsorption is exothermic (-0.18 eV) over the Cu(I)-CHA site which is followed by NO adsorption that generates Cu⁺-NO⁻₃ species with a formation energy of -1.34 eV while simultaneously oxidizing Cu(I) to Cu(II) (Step II).

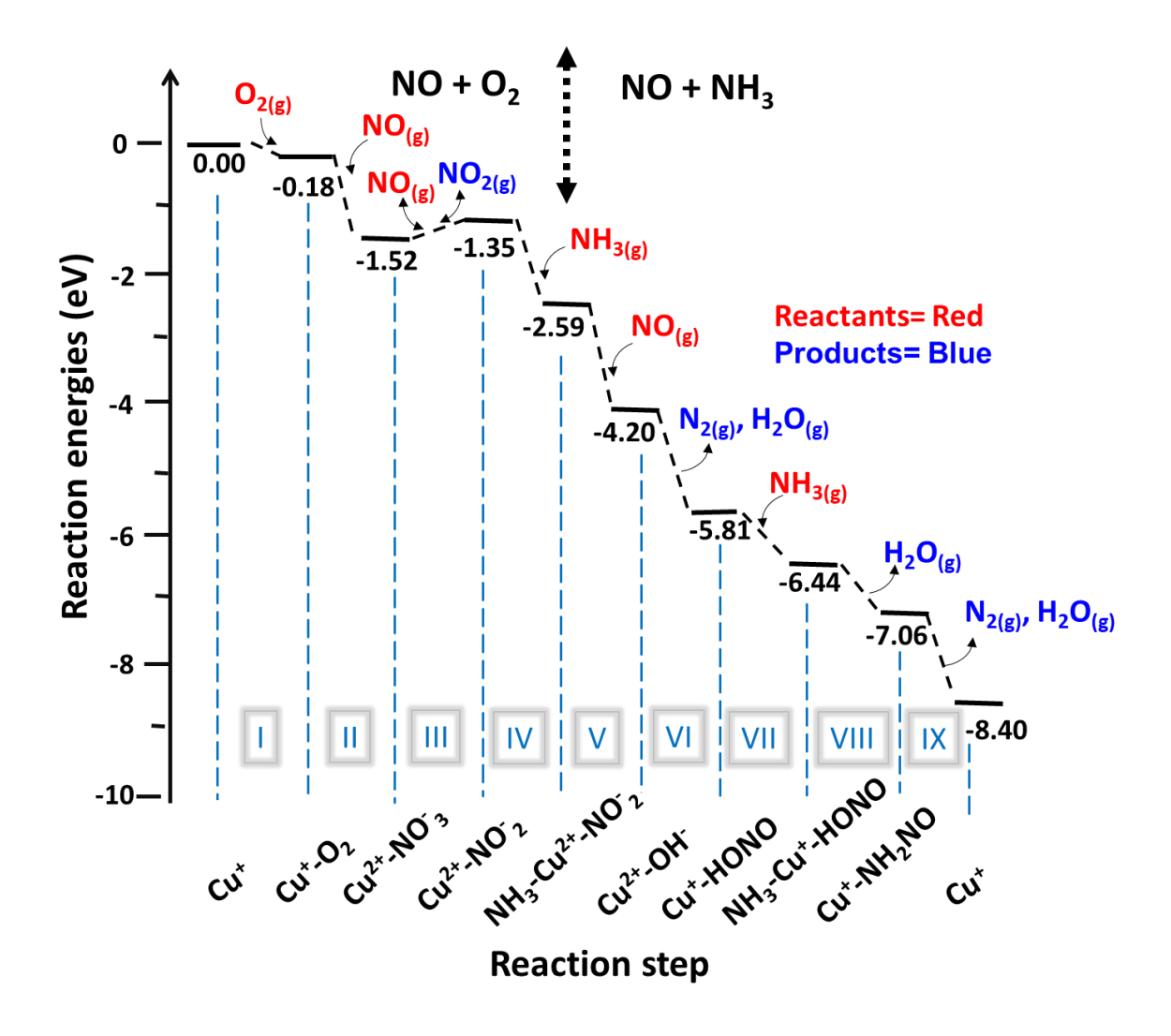


Figure 3.12. The relative potential energy landscape of NO-activated NH₃-SCR of NOx catalytic cycle on bare Cu-CHA site.

It is evident from previous reports that gaseous NO₂ can react with the Cu⁺-site yielding bidentate Cu nitrite Cu-NO₃ species (Step III) that are often considered a Fast-SCR ²⁸⁰; meanwhile, nitrate species have been detected during *in situ* experiments ^{263, 279}. The reaction of gaseous NO with nitrate ²⁸¹ is reported to be a two-step process where first NO coordinates with the nitrate species and then decomposes to nitrite with the release of gaseous NO₂. To this end, we found a total energy change of 0.17 eV from the nitrate to nitrite step. In the case of the NH₃ reaction with nitrite species, an intermediate (Step IV) is formed with a formation energy of -1.24 eV. Furthermore, we found that NH₃ can also react with the Cu-HONO site

that generates NH₃-Cu-HONO intermediate (step VII) with an H₃N-Cu bond length of 2.160 Å and formation energy of -0.63 eV. Subsequently, it decompose and leads to the generation of an important intermediate the Cu-nitrosamine (Cu-N(=O)-NH₂) (step VIII) which is considered to play a key role in the NH₃-SCR reaction. The QM/MM results are augmented with our concentration modulation excitation DRIFTS data.

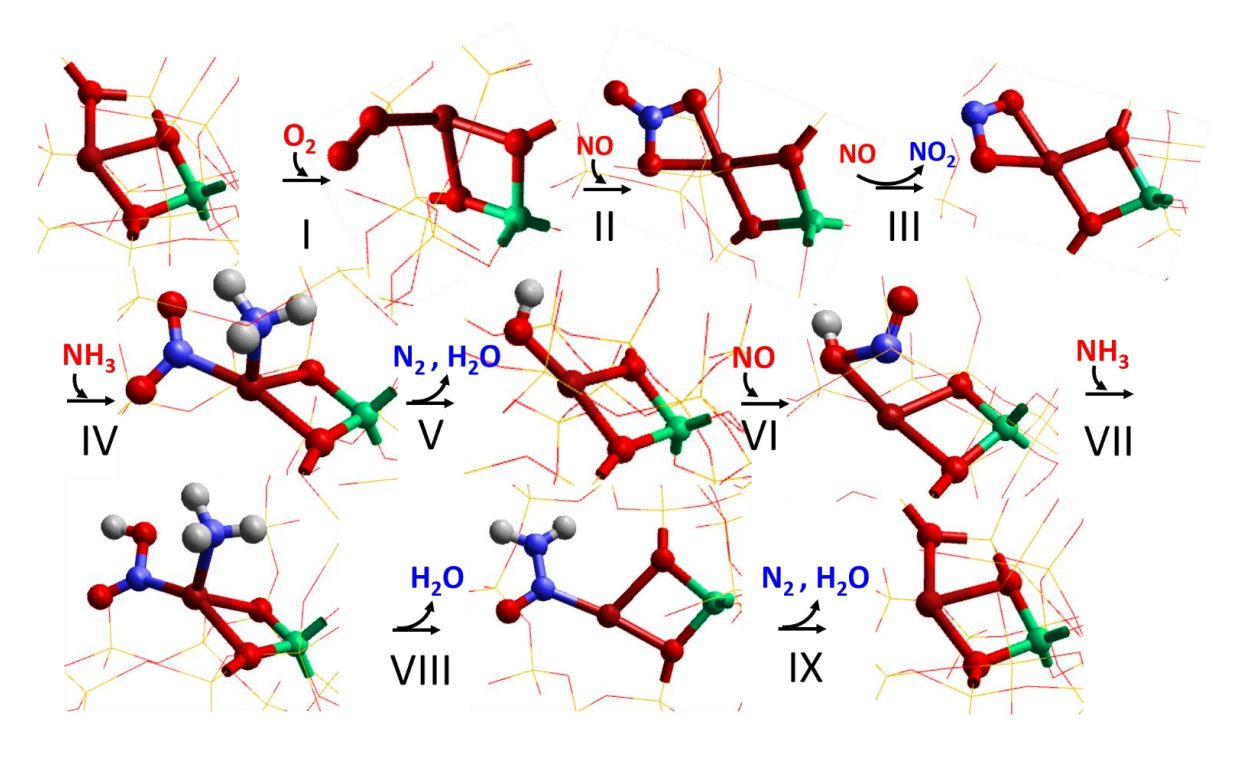


Figure 3.13. The structures of each corresponding intermediate species reside on bare Cu-CHA. The model used is shown as an extra framework. **Atom color codes**: Cu (brown), Al (green), O (red), N (blue), and H (white). The framework SiO₂ is shown using a wire framework motif.

The proposed SCR reaction is found to be exothermic, similarly, all the steps in the reduction part [Cu(II) to Cu(I)] of the cycle, including the reaction of NO and NH₃ with the Cu²⁺-OH to reduce Cu²⁺ to Cu⁺, are exothermic reactions. Notably, the subsequent oxidation of Cu⁺ by NO and O₂ back to Cu²⁺ ions and the generation of nitrate species (species E) is exothermic; however, the formation of nitrite species (species F) is endothermic (see Figure 3.3). This is probably the NO-activation step and the endothermic observation in this regard indicates the equilibrium reaction, given that this step of the cycle can proceed in both directions ^{120, 282}.

In the standard SCR reaction, the rate-limiting step is either the oxidation of NO to nitrate (step II) or the activation of NO to nitrite (releasing of NO₂ species) (step III) ⁵⁸. We have, therefore, especially focused on the calculation of transition state energy for these two steps. In our initial approximation, the calculated energy for nitrite, however, indicates that the oxidation of NO to nitrate is the rate-determining step. The estimated activation energy in excess of 3 eV we calculated is much higher than the experimental value of 69 kJ/mol (0.72 eV) ¹²⁰, which is due to the fact that in an experiment, other factors such as the effect of coordination to solvent and possible water ligands which are not included herein.

The O_2 molecule on adsorption starts bending towards the NO molecule, then binds to it which finally leads to the formation of nitrate species (Figure 3.14). This observation is confirmed by the NEB calculation that shows the sequential incorporation of O atoms from the adsorbed O_2 molecules through an 'end-on' configuration that eventually leads to the formation of the nitrate. We are refining this calculation to obtain accurate transition state energies.

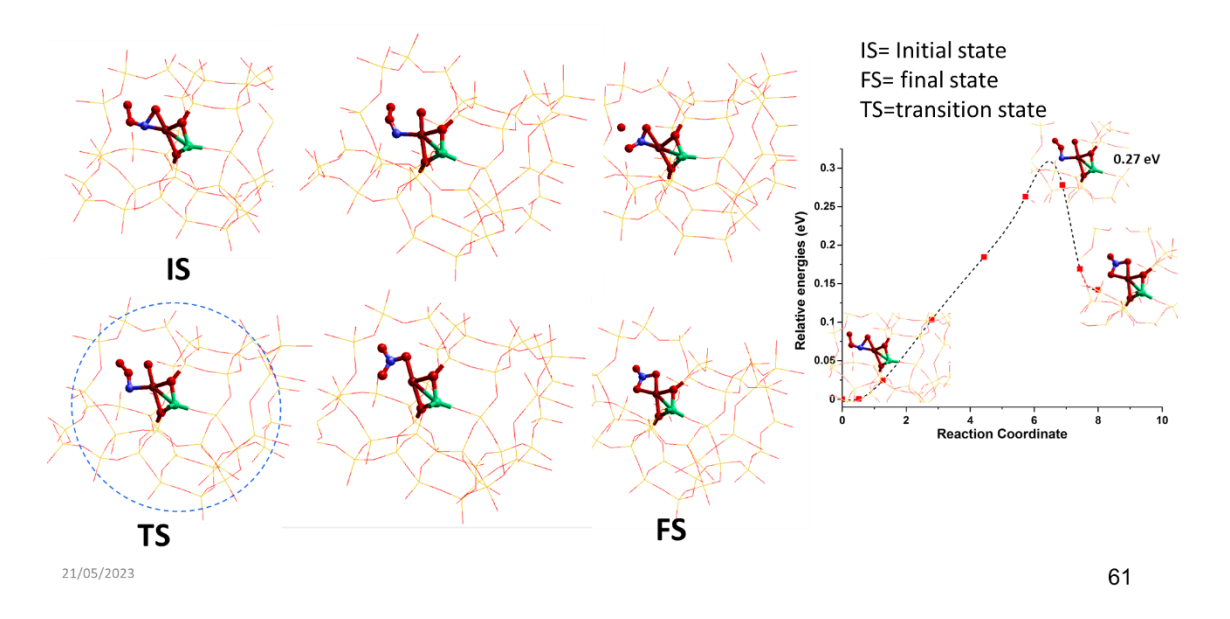


Figure 3.14. NEB calculations; the NEB images showing the formation pathway of nitrate species, and their relative energies landscape.

3.3.5 H₂NNO Decomposition

An important step in the NH₃-SCR mechanism is the reaction of NH₃ with HONO that generates the NH₃-Cu-HONO intermediate which eventually leads to the formation of the key intermediate Cu-nitrosamine (Cu-N(=O)-NH₂) as shown in Figure 3.15.

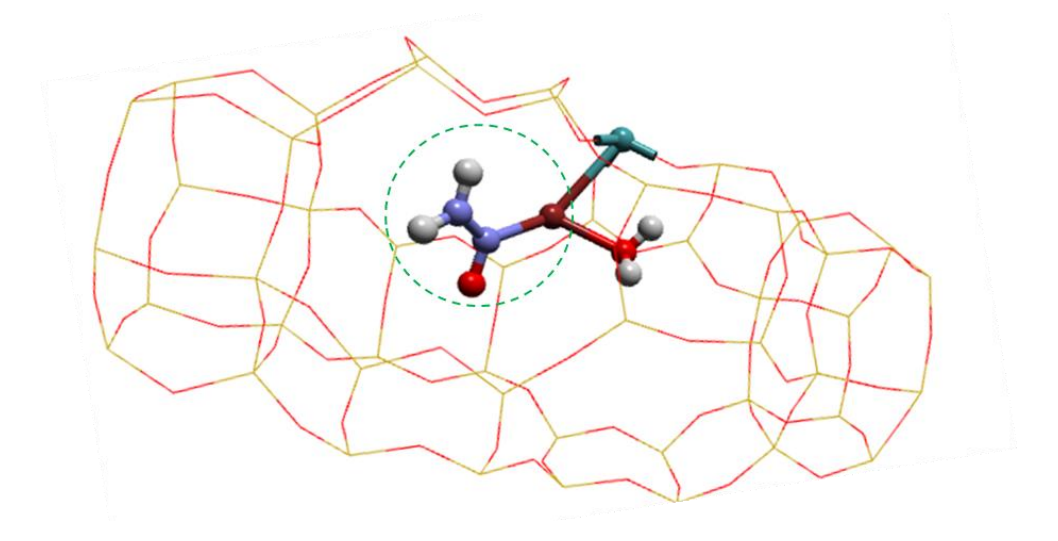


Figure 3.15. The optimized structure of Cu-nitrosamine (Cu-N(=O)-NH₂).

The decomposition of H₂NNO has been extensively investigated and proceeds through the transformation of several important isomers with high activation barriers ²⁸³⁻²⁸⁵. DFT calculations showed that the energy barrier for the H₂NNO decomposition is considerably reduced *via* proton exchange between H₂NNO and a Brønsted acid site over V₂O₅ ²⁸⁶, the mechanism of which is similar to dehydrogenation of propane over vanadia ²⁸⁷. A similar study has been conducted over Cu-CHA where the decomposition of H₂NNO and HONO is investigated on Brønsted acid sites ²⁸⁸. Such a study has also been reported over Cu-SAPO-34 ²⁸⁹ and ZSM-5 ^{290, 291} using a cluster-based computational approach. As it is found that solvent can coordinate to the Cu-site, we, therefore, investigated the decomposition pathway of H₂NNO on isolated Cu-CHA active sites. The schematic illustrations of isomeric decompositions of H₂NNO intermediates and the corresponding potential energy surfaces are shown in Figure 3.16. The adduct rearrangement process of H₂NNO species starts with 1,3 H-

transfer, breaking one N-H bond with the transfer of an H to an adjacent O atom which leads to the formation of an O-H bond. The total energy change from structure (I) to (II) and (III) are calculated as 0.04 eV and 0.06 eV on the bare site; while with ligated water, it is -0.33 eV and -0.46 eV, respectively; suggesting some positive impact of solvated sites on the energetics of this step. From H₂NNO to HNNOH, the H-transfer is accompanied by a shortening of the N-N bond (from 1.35 Å to 1.299 Å) while lengthening of the N-O bond (from 1.208 Å to 1.306 Å) that eventually ends with the termination of respective bonds and generation of H₂O and N₂ as products.

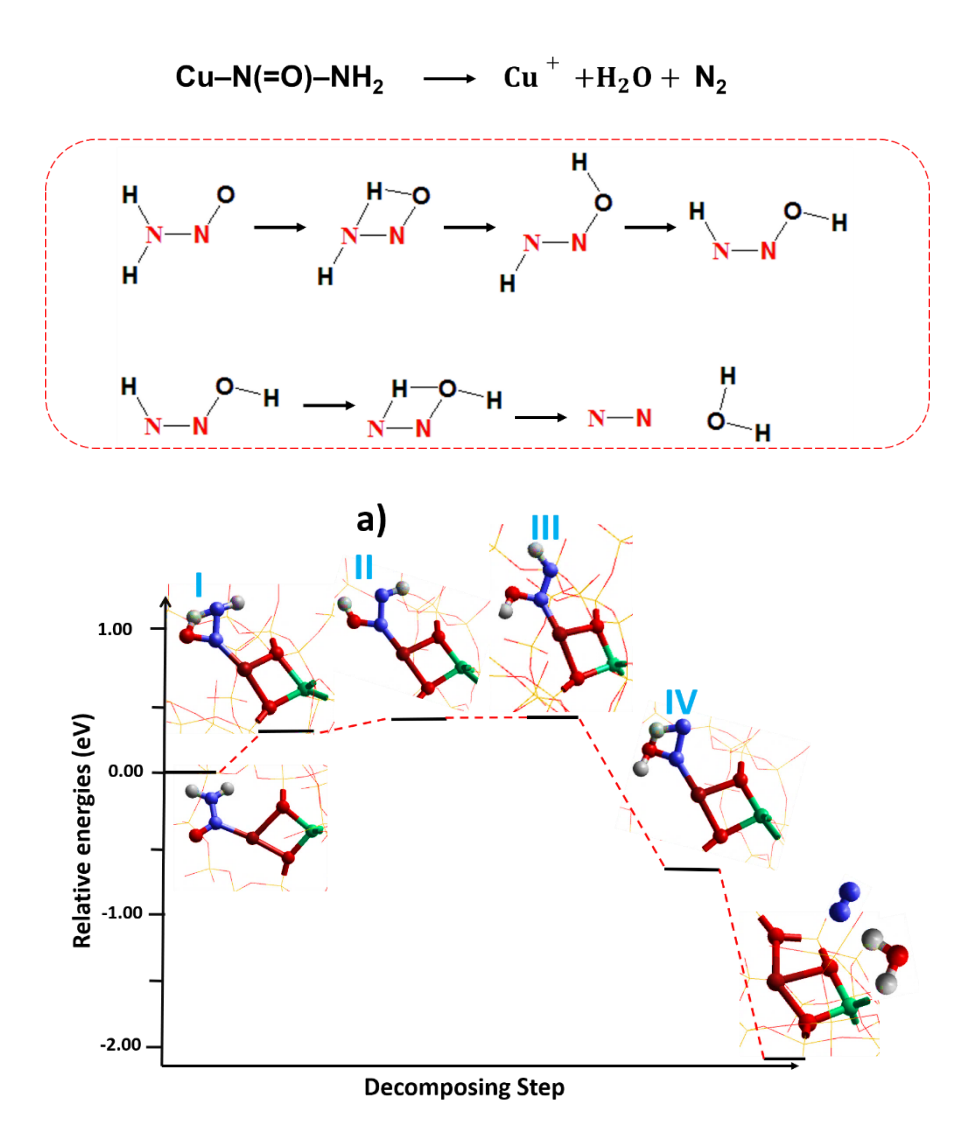


Figure 3.16. Calculated potential energy surfaces for H₂NNO isomerization The model used is shown as an extra framework. **Atom color codes**: Cu (brown), Al (green), O (red), N (blue), and H (white). The framework SiO₂ is shown using a wire framework motif.

3.3.6 Reactivity of HONO

We also examined the reactivity of HONO species toward NH₃, H₂O, O₂, and NO, which are the main reactants and products in the NH₃-SCR reaction. We have noted that NO can bind with the Cu(II)-(OH) site forming the Cu-HONO species ^{278, 292, 293} that can react with NH₃ to yield NH₄NO₂, an unstable species which can decompose to N₂ and H₂O. The subsequent desorption of HONO is endothermic (with an energy of 0.145 eV)²⁹² as previously reported; we, therefore, conducted a series of calculations to study the interaction of other species with the Cu-HONO site as displayed in Figure 3.17. Considering the approach of solvent molecules, we found that the interaction of both NH₃ and H₂O with HONO is endothermic. The binding energy of H₂O is calculated to be 1.53 eV with a bond distance between O to Cu of 2.155 Å. In the case of NH₃, the binding energy is found to be 0.99 eV with a bond distance between N and Cu of 2.160 Å. The interaction of dioxygen with the Cu-HONO site is in superoxo (O²⁻) mode with an average bond distance of 2.127 Å between O and Cu. We also note the interaction of NO with Cu-HONO, forming a NO-Cu-HONO adduct.

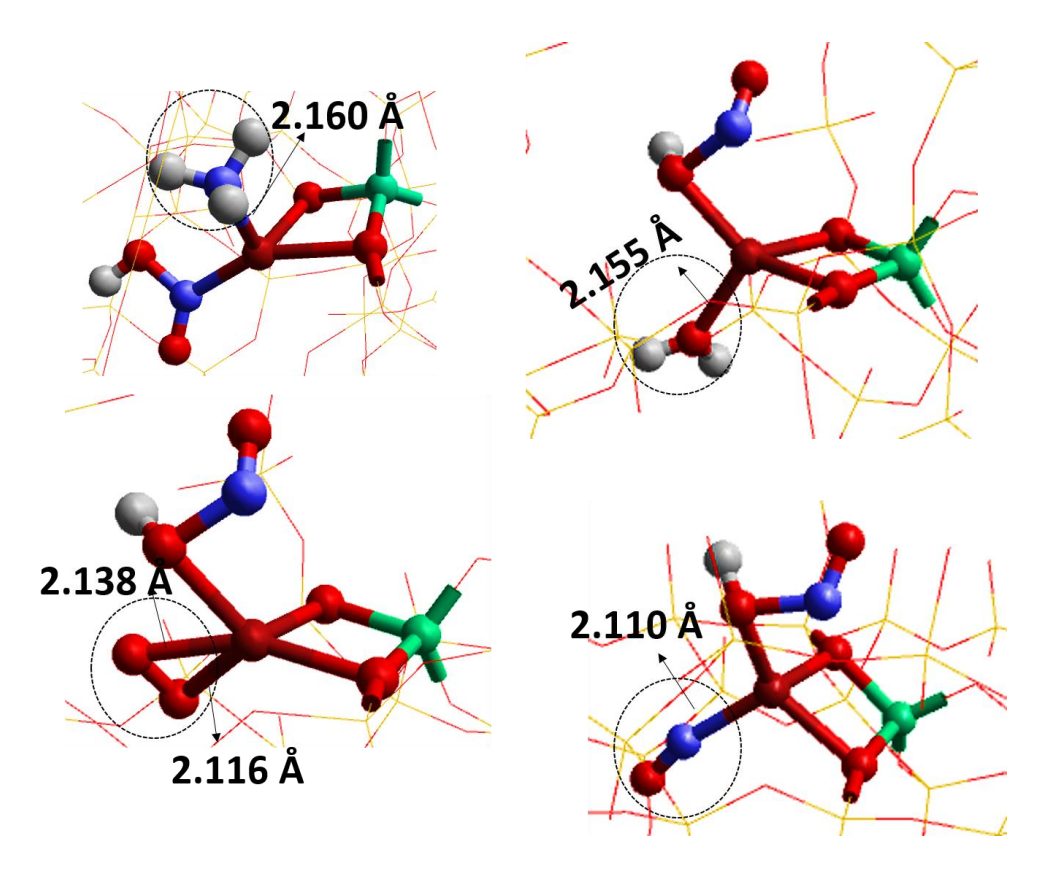


Figure 3.17. The binding of HONO species with NH₃, H₂O, O₂, and NO. **Color code:** Al, green; Si, yellow; O, red; Cu, brown; N, blue; and H, white;

3.4 Summary and Conclusion

We investigated the NH₃-SCR of NOx reaction employing hybrid QM/MM embedded technique over Cu-CHA catalyst. The study examined the reactivity of Cu-CHA site towards the adsorption of reactant species and the formation of key intermediates. The main catalytically active sites that facilitate the adsorption of species are both monovalent- and divalent-copper sites that can drive the NH₃-SCR to generate important intermediate species such as nitrates and nitrites. DRIFTS data showed the formation and consumption of short-lived intermediates in the catalytic reaction, crucially, the detection of important bands for both nitrosamine and bidentate nitrate species, which is in accord with the calculated frequencies by QM/MM calculation giving further credence to the cyclical nature of the proposed mechanism.

Our computational analysis provides a clear assignment of all main spectroscopic features of the NH₃-SCR catalytic cycle, that are in good agreement with the experiment. In addition, we studied the decomposition of nitrosamine species, and the process is found to be exothermic. We also examined the reactivity of HONO species toward NH₃, H₂O, O₂, and NO, which are the main reactants and products in the NH₃-SCR reaction. The results reported in this chapter have been published²¹⁰. The following chapter will explore how the mechanisms are influenced by the presence of solvent molecules.

Chapter 4

Reactivity of Solvated Cu-CHA in NH₃-SCR

4.1 Introduction

Solvent molecules such as ammonia and water are the key components of the NOx-containing exhaust gases, and their inevitable presence could lead to adsorption on the transition metal sites, affecting the energetics of the intermediate species ²⁹⁴. Liu *et al.*²⁹⁵ investigated the effect of water on NH₃-SCR activity over Cu-LTA and found a promoting effect of water on Low-temperature SCR activity with a plausible solvated [H₂O-Cu-NH₃]⁺ species. Similarly, the experimental study by Yu *et al.*²⁹⁶ over Cu-SAPO-34 catalyst showed the promoting effect of water and reported that in the presence of water, the reducibility of Cu²⁺ species at high temperature is improved while the NH₃ oxidation is inhibited. It is also found that ammonia does not block the formation of nitrates when water is present in the feed as reported by Lee *et al.* ²⁹⁷. In addition, some studies show that enhanced Cu-ion mobility is caused by ligated water molecules, leading to better NH₃-SCR activity ^{295, 298}.

To optimize the catalytic process, not only the chemistry of active sites and the intrinsic NH₃–NO reaction kinetics need careful attention, but also the diffusion of the counter ion must be understood which is strongly affected by the ligation of solvent molecules such as H₂O and NH₃. Generally, Al sites are responsible for restricting the mobility of counterions, due to electrostatic attraction to the framework. [Cu(NH₃)₂]⁺ mobility inside the CHA framework at the sub-second time scale is predicted by Paolucci *et al.* ¹¹⁹ who found displacement by 9Å for [Cu(NH₃)₂]⁺ by *ab initio* metadynamics. Furthermore, employing molecular dynamics (MD)

simulation O'Malley *et al.* found that the strong coordination of NH₃ with Cu²⁺ in the centre of the chabazite cage hinders the interaction of other molecules with the Cu-sites ²⁷⁷.

To understand how solvated Cu-cations can control nitrogen chemistry in CHA, we investigate reaction mechanisms employing modelling techniques that can explore reaction mechanisms at the active site (Figure 4.1). To this end we have employed the QM/MM techniques used in the previous chapter 3 and discussed in Chapter 2. We elucidate the influence of physisorbed solvents on the reactivity of Cu-CHA sites and their effect on the energetics of intermediates. In particular, our investigation provides new insight into the NH₃-SCR reaction by understanding the chemistry of the solvated-Cu-CHA sites and their impact on the key steps in the reaction.

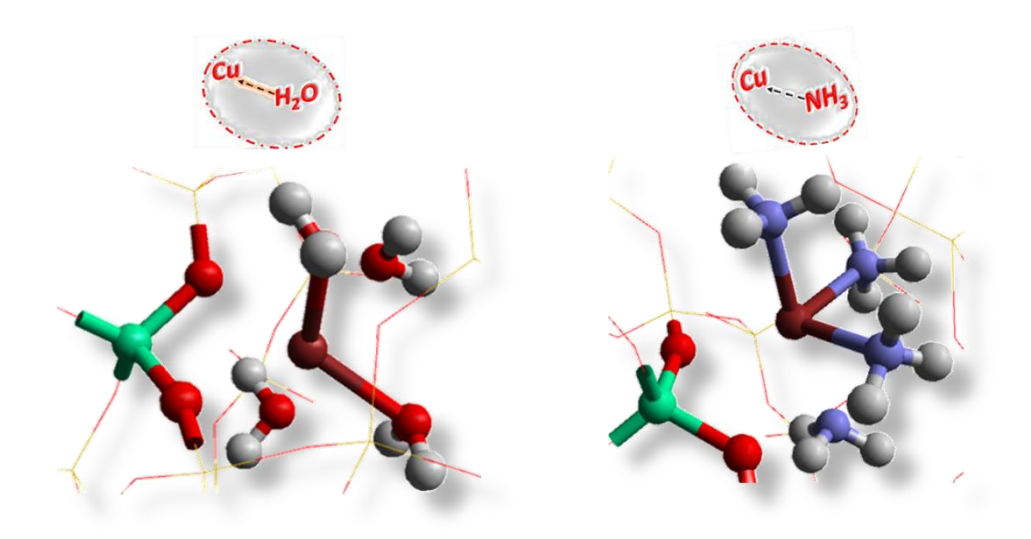


Figure 4.1. Solvated active sites i) H₂O coordinated Cu-CHA, and ii) NH₃ coordinated Cu-CHA.

4.2 Computational Approach

4.2.1 QM/MM Methodologies

We used the same CHA cluster as described in the previous chapter; however, we added physisorbed solvent molecules such as NH₃ and H₂O onto the Cu-CHA active sites. The guest

species of interest in the zeolite and reactants gaseous species were treated at the QM level using the higher quality def2-TZVP basis set. The coordinates of all atoms (not including the link H atoms) in the QM region and active MM region were fully optimized. Considering that adsorbed molecules can diffuse through the larger channels, all the adsorbed species including the intermediates were placed within (or near) the 8-MR of the CHA cage. The water (O-end) and ammonia (N-end) molecules were placed at a distance of 2 Å from the Cu centre with the proton pointing away from the adjacent oxygens and intermediate species to avoid artificial trapping in hydrogen-bonding interactions. We note that hydrogen bonding with framework O can influence chemistry at metal sites by affecting the binding of functionally important Cu–H₂O/NH₃ units.

To perform the QM/MM calculation, we first created a spherical embedded-cluster model (Figure 4.2) of CHA from the unit cell of siliceous CHA ²³⁶ optimized at the MM level using the GULP package ²³¹. After creating a simple CHA-cluster model, we construct active sites. For example, In the case of a Brønsted acid site, as discussed in the previous chapter, we replaced one Si with Al and added a charge-compensating proton on a neighbouring oxygen atom at a site where it is most accessible to facilitate the reaction. The QM region which is contained within the active part of the model includes atoms from the third oxygen shell from the central T-site; and, as noted, we have added the hydrogen (link atoms) to saturate the terminal oxygen atoms

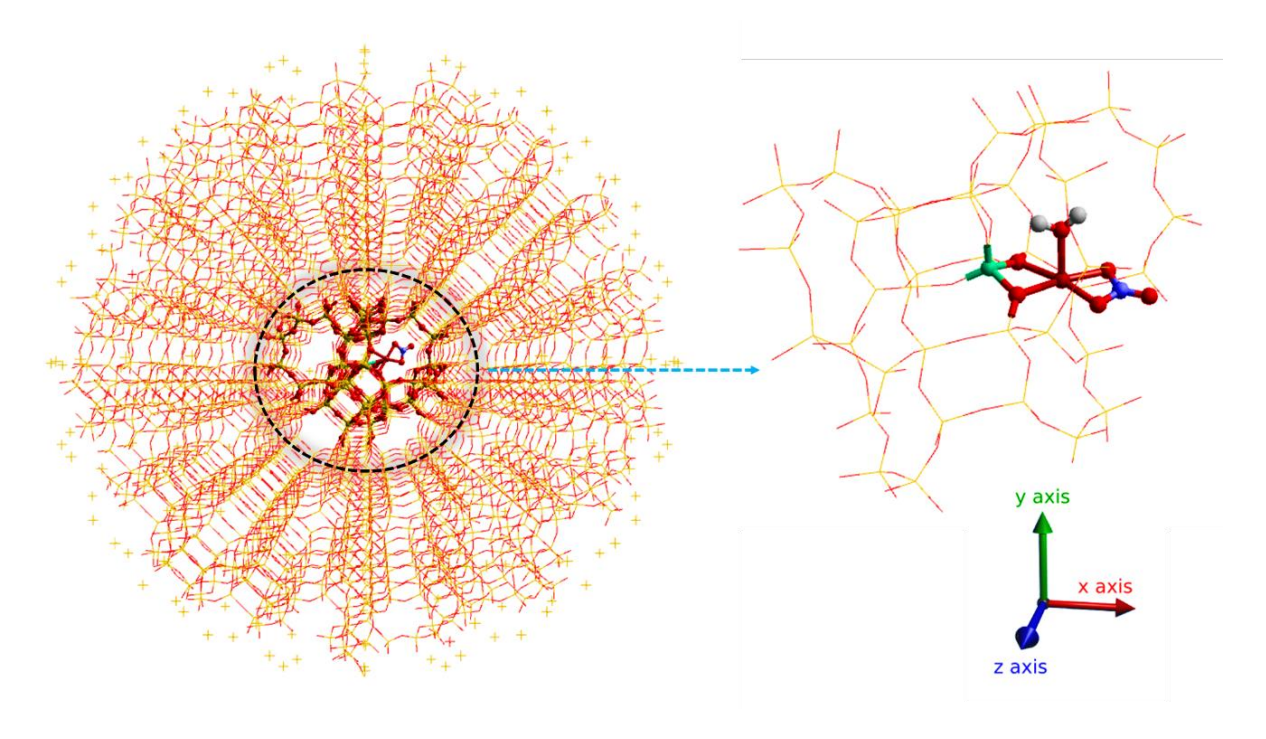


Figure 4.2. The QMMM embedding setup; the CHA cluster (left) with a quantum mechanical region containing solvated-nitrate species (right). The outermost region contains point charges to ensure the Madelung potential in the centre of the cluster is accurately reproduced. Atom colour codes: Cu (brown), Al (green), Si (yellow), O (red), N (blue), and H (white).

4.3 Result and Discussion

In this chapter, our study focuses on the solvent effects on the reactivity of the Cu-CHA and, as argued, it provides key insight into the reaction mechanism from accurate hybrid-QM/MM calculations. Hybrid-QM/MM investigations, DRIFTS experiment, and in-depth scrutiny of solvent effects allowed us to explore the intermediate-solvent interactions and identify the important species participating in the NH₃-SCR event on the solvated sites. The results of the computational mechanistic study complement and give insight into the experimental findings.

4.3.1 Vibrational Study on Solvated Sites

We calculated the harmonic vibrational spectra of selected intermediates such as nitrosamine and bidentate nitrate on solvated Cu-CHA sites. The harmonic values obtained were scaled using vibrational scaling factors, which were determined by comparing experimental and computational harmonic values using a representative set of gas phase molecules. We focused on bands of nitrosamine (N-O_{str}, and N-N_{str}) and nitrate (N-O_{str}); the scaling factor to calculate the vibrational frequency of N-O_{str} of nitrosamine is 0.915 while for the N-N_{str} is 0.918. Similarly, the corresponding scaling factor we applied for the N-O_{str} of nitrate is 0.943.

As shown in Figure 3.6 (Chapter 3), for the bare Cu-nitrosamine (Cu–N(=O)–NH₂) species, we found a vibrational stretching band around 1478 cm⁻¹ compared to our experimental value of 1436 cm⁻¹, tentatively ascribed to the N=O_{str} mode. However, on the physisorption of water (Figure 4.3a) (Table 4.1) and ammonia (Figure 4.3b)(Table 4.2) at Cu sites, we observed the N-O_{str} band shift down to 1467 cm⁻¹ and 1462 cm⁻¹, respectively. The lower frequency spectral features found in our QM/MM calculations are in particular due to N-N stretching vibrations of Cu-nitrosamine (Cu–N(=O)–NH₂) species. For the bare site, the N-N stretching frequency is calculated as 1124 cm⁻¹ as compared to the reported experimental values in the Nitrosodimethylamine (1052 cm⁻¹) and Di-N-nitroso-pentamethylenetetramine (1106 cm⁻¹) ²⁵⁴. While for the water and ammonia-solvated sites, the N-N_{str} is found at 1123 cm⁻¹ and 1111 cm⁻¹, respectively.

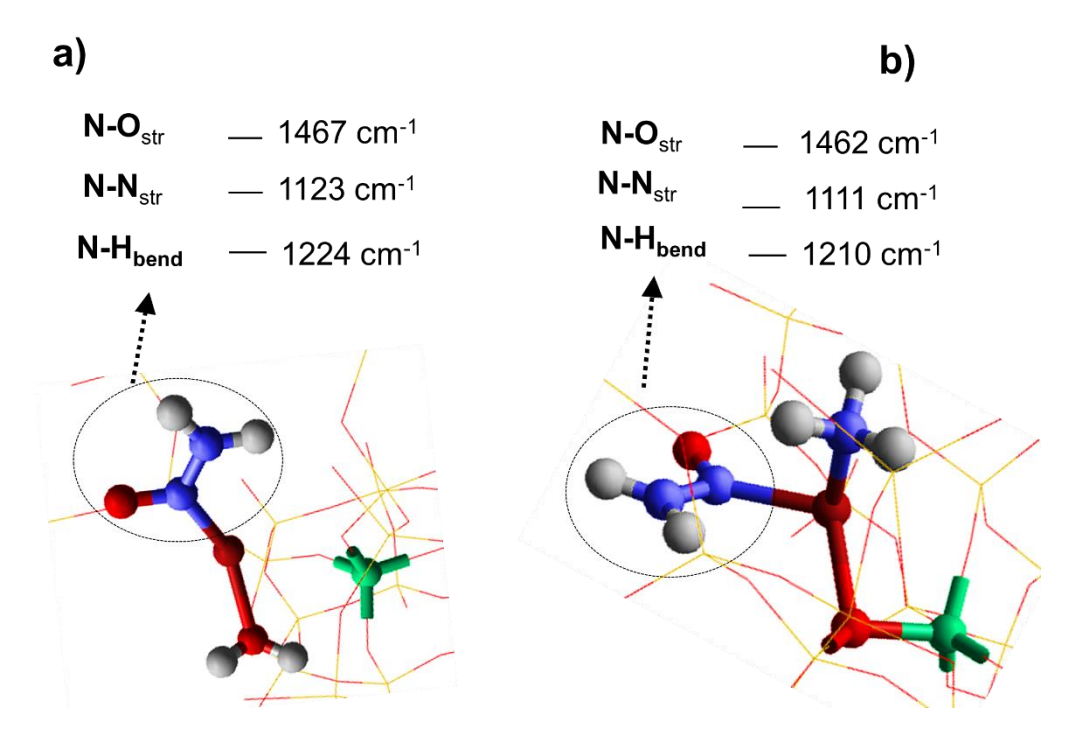


Figure 4.3. Spectroscopic Signatures of solvated nitrosamine; a) physisorbed water and b) physisorbed ammonia Cu-nitrosamine (Cu–N(=O)–NH₂) species. **Atom colour codes**: Cu (brown), Al (green), O (red), N (blue), and H (white). The framework SiO₂ is shown using a wire framework motif.

Table 4.1. Scaled vibrational frequencies for the physisorbed water nitrosamine species.

Assignments	Frequencies (cm ⁻¹)	Scale factor	Freq. after scaling(cm ⁻¹)
N-O stretch	1603	0.915	1467
N-N stretch	1224	0.918	1123

Table 4.2. Scaled vibrational frequencies for the physisorbed ammonia nitrosamine species.

Assignments	Frequencies (cm ⁻¹)	Scale factor	Freq. after scaling (cm ⁻¹)
N-O stretch	1597	0.915	1462
N-N stretch	1210	0.918	1111

Next, we investigated a bidentate nitrate species (Figure 4.4) with a focus on the N=O_{str} stretching mode. Generally, nitrate species have four notable modes ^{257, 258}. Our calculations show that the bare bidentate Cu–NO₃ structure possesses the main N=O_{str} stretching frequency of 1620 cm⁻¹ while for the physisorbed water and ammonia it is found at 1609 cm⁻¹ and 1600

cm⁻¹, respectively (Figure 4.4a & 4.4b) (Table 4.3 & 4.4). All these three bands are quite close to our experimental DRIFTS value of 1606 cm⁻¹ (see Figure 3.4 in Chapter 3) In addition, small broad bands that appeared in our experimental findings in the region of 1225 cm⁻¹ to 1250 cm⁻¹ could be assigned to the antisymmetric stretch (v₃ (E')) of the N-O band, as reported by Zapata and García-Ruiz ²⁵⁷. However, our QM/MM calculation shows this band at relatively lower frequencies for this mode; for instance, it is seen at 1172 for the bare site while for physisorbed water and ammonia sites, it appears at 1192 cm⁻¹ and 1202 cm⁻¹, respectively. Finally, two bands that originated due to out-of-plane and in-plane deformation modes for nitrate species are displayed. The out-of-plane deformation band (v₂ (A"₂)) is normally located within the range of 800 – 900 cm⁻¹ while the in-plane band (v₄ (E')) ranges from 700-780 cm⁻¹ in nitrate salts ^{257, 258}. Our calculated out-of-plane deformation (997 cm⁻¹ for physisorbed water and 996 cm⁻¹ for ammonia) occurs at a somewhat higher frequency, however, the in-plane deformation has appeared almost in the same region as previously reported ²⁵⁷. For instance, the calculated value appears at 786 cm⁻¹ in the case of physisorbed water while for ammonia it is at 790 cm⁻¹.

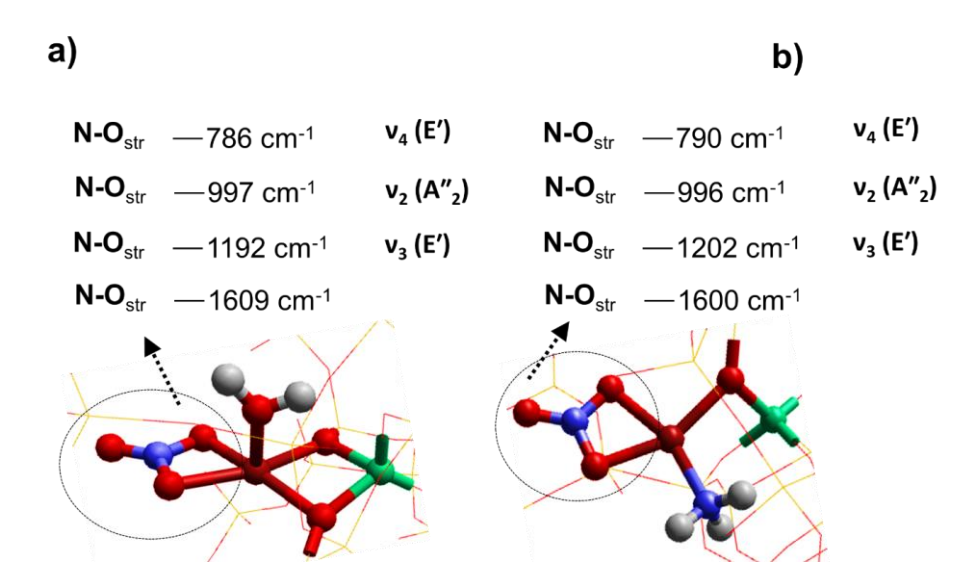


Figure 4.4. Spectroscopic signatures of solvated nitrate; a) physisorbed water and b) physisorbed ammonia Cu-nitrate (Cu–NO₃) species. **Atom colour codes**: Cu (brown), Al (green), O (red), N (blue), and H (white). The framework SiO₂ is shown using a wire framework motif.

Table 4.3. Scaled vibrational frequencies for the physisorbed water nitrate.

Assignments	Frequencies (cm ⁻¹)	Scale factor	Freq. after scaling (cm ⁻¹)
1st N-O stretch	1707	0.943	1609
2 nd N-O stretch	1265	0.943	1192
3rd N-O stretch	1058	0.943	997
4th N-O stretch	834	0.943	786

Table 4.4. Scaled vibrational frequencies for the physisorbed ammonia nitrate.

Assignments	Frequencies (cm ⁻¹)	Scale factor	Freq. after scaling (cm ⁻¹)
1st N-O stretch	1697	0.943	1600
2 nd N-O stretch	1275	0.943	1202
3 rd N-O stretch	1057	0.943	996
4th N-O stretch	838	0.943	790

One of the significant effects of solvation is the possibility of site deprotonation due to a proton transfer to solvent even if only as a transient species. Therefore, we completed this analysis by studying vibrations of a negatively charged intermediate species that would result from such deprotonation by possibly abstracting the proton from the -NH₂ group of nitrosamine to form NH₄⁺ ions (see Figure 4.5). The calculated N-O_{str} (1416 cm⁻¹) band is found at somewhat lower frequencies for the deprotonated nitrosamine NH₄⁺(Cu–N(=O)–NH) species compared to the neutral system (1478 cm⁻¹). While the N-N_{str} stretching bands for this species appear at a relatively higher frequency of 1308 cm⁻¹ than the neutral system (1124 cm⁻¹). There is a mixed asymmetric stretch mode of the NH₄⁺ group combined with N-N_{str}, which may be the reason that N-N_{str} appears at a higher frequency than expected.

Conversely to the deprotonation of nitrosamine species, we also examined the likely protonation of Cu-nitrosamine (Cu-N(=O)-NH₂) that generates an -OH site, i.e., (Cu-N(=OH)-NH₂). The calculated N-O_{str} band (1592 cm⁻¹) in this case was found at significantly higher frequencies compared to both deprotonated nitrosamine (1416 cm⁻¹) and neutral system

(1478 cm⁻¹). Based on the obtained result, we infer that the experimental DRIFTS data show either neutral or deprotonated nitrosamine rather than protonated species.

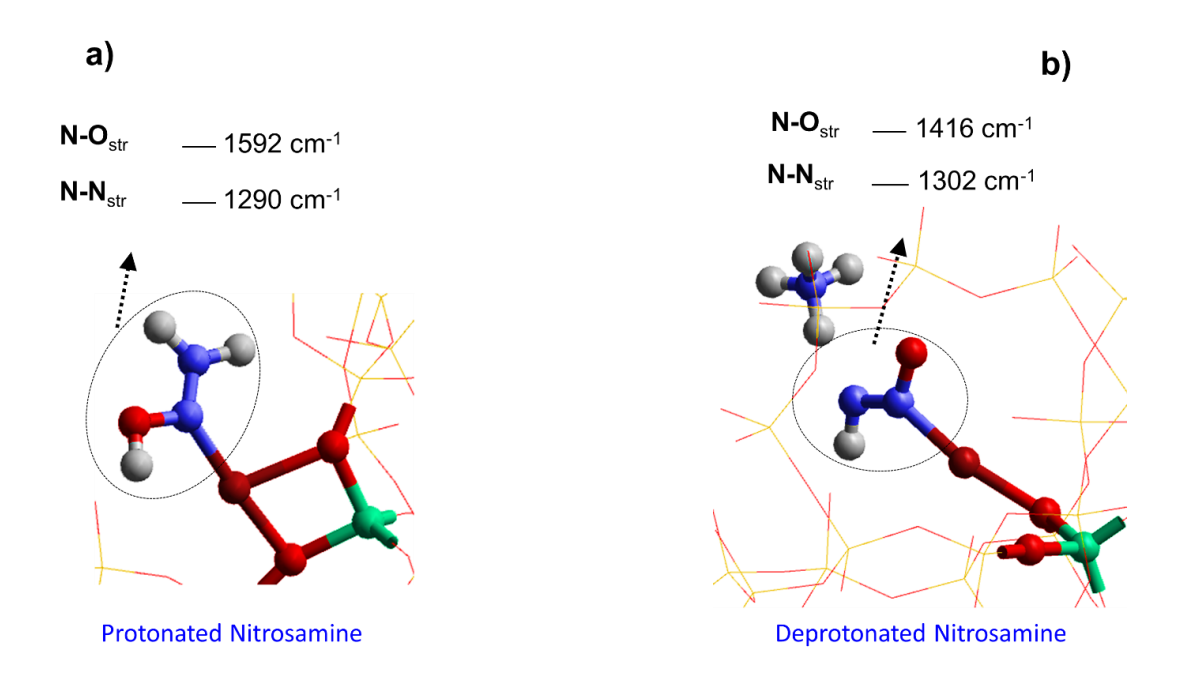


Figure 4.5. Spectroscopic Signatures of nitrosamine; a) protonated and b) deprotonated Cunitrosamine (Cu–N(=O)–NH₂) species. **Atom colour codes**: Cu (brown), Al (green), O (red), N (blue), and H (white). The framework SiO₂ is shown using a wire framework motif.

Since we have already discussed the N=O_{str} vibrational mode of bidentate-nitrite (Cu–NO₂) (in chapter 3, Figure 3.9) to determine whether the 1606 cm⁻¹ band in the DRIFTS spectrum originates from the nitrate or nitrite. The computed N=O_{str} band of this particular species is, however, found significantly lower than the N=O_{str} band of the bidentate-nitrate species which appeared at 1273 cm⁻¹ for the bare nitrite while for the solvated H₂O and NH₃ active sites it is observed at 1263 cm⁻¹ and 1260 cm⁻¹, respectively (Figure 4.6). Notably, the calculated bands are comparable with the experimental values of *ca.* 1229 cm⁻¹ for the isostructural linear nitrite species reported in references ^{261, 262}.

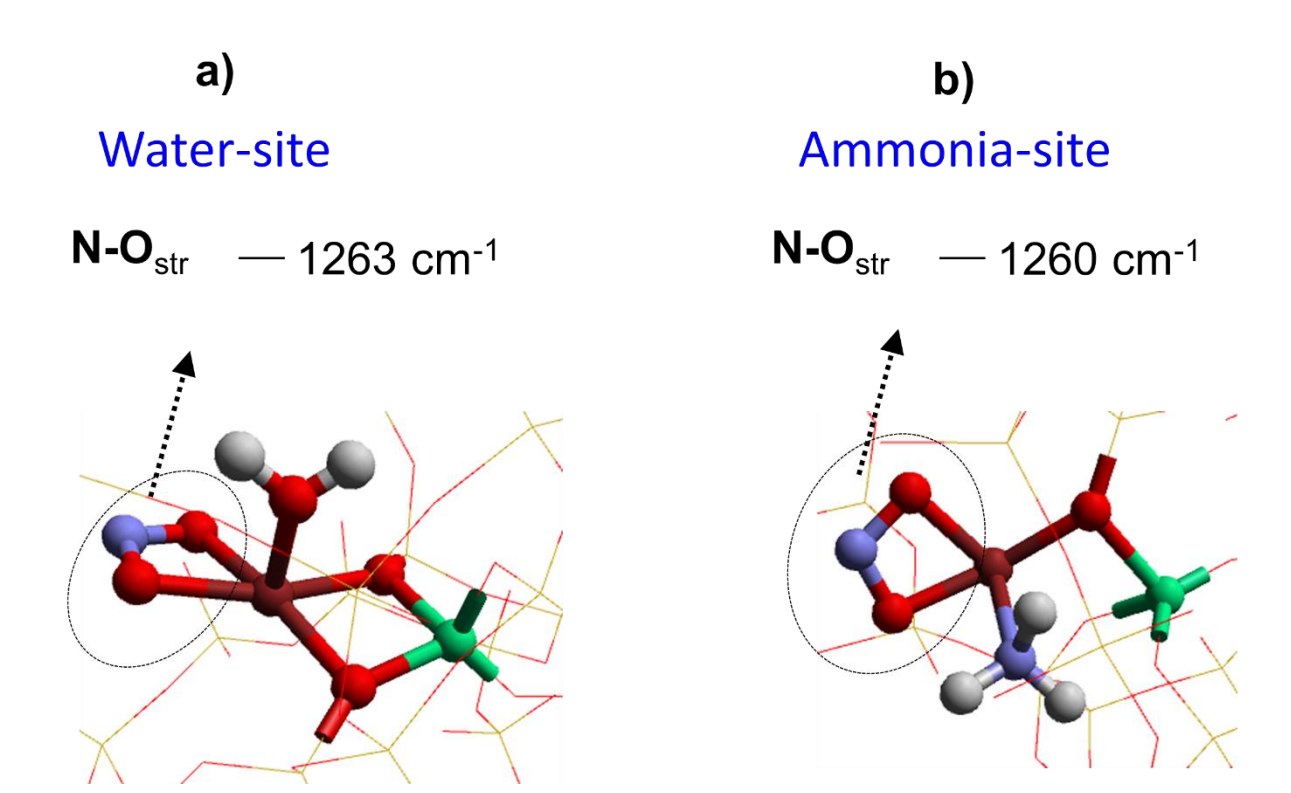


Figure 4.6. Spectroscopic signatures of solvated nitrite; a) physisorbed water and b) physisorbed ammonia Cu-nitrite (Cu-NO₂) species. **Atom colour codes**: Cu (brown), Al (green), O (red), N (blue), and H (white). The framework SiO₂ is shown using a wire framework motif.

We have already discussed the vibrational features of (Cu–(NO₂)–NH₃) (Figure 3.9, chapter 3). Here, we focused on the influence of solvent on the vibrational signature, especially on the N=O_{str} of (Cu–(NO₂)–NH₃) (Figure 4.7). These calculations aim to compare the N=O_{str} signatures with the DRIFTS data where the assigned band 1606 cm⁻¹ is attributed to the nitrate species. We found that the NO band for this species is lower than the 1606 cm⁻¹ band in the DRIFTS spectrum assigned to N=O_{str} vibration for all three sites. Based on the calculated vibrational modes, we infer that the spectroscopic signatures that appear in the DRIFTS spectrum can be tentatively assigned to the nitrate and nitrosamine species. Hence, we propose the following complete assignment of the calculated vibrational modes of all species in Figure 3.3 (Table 4.5).

Table 4.5. Calculated vibrational bands of key intermediate species presented in the NH₃-SCR catalytic cycle – see Figure 3.4, chapter 3.

Species	Wavelength (cm ⁻¹)	Description of IR active mode
Cu-NO ₃ (species B)	1620 (B), 1609 (H), 1600 (N)	N=O stretch
Cu-NO ₂ (species C)	1273 (B), 1263 (H), 1260 (N)	N=O stretch
(Cu-(NO ₂)-NH ₃) (species D)	1501 (B), 1481 (H), 1464 (N)	N=O stretch
	3445 (B), 3450 (H), 3447 (N)	N-H stretch
Cu-(N(=O)-OH)-NH ₃ (species F)	1585 (B), 1579 (H), 1575 (N)	N=O stretch
	3313 (B), 3471 (H), 3485 (N)	N-H stretch
	3197 (B), 3216 (H), 3226 (N)	O-H stretch
(Cu-N(=O)-NH ₂) (species G)	1478 (B), 1467 (H), 1462 (N)	N=O stretch
	3482 (B), 3493 (H), 3517 (N)	N-H stretch
[Cu ²⁺ (OH)] ⁺ adsorbed NH ₃	3336	N-H stretch
	3668	O-H stretch
	1620	N-H bend
Brønsted acid site adsorbed NH ₃	3279	N-H stretch
	1455	N-H bend

[B] bare [H] physisorbed-H₂O [N] physisorbed-NH₃

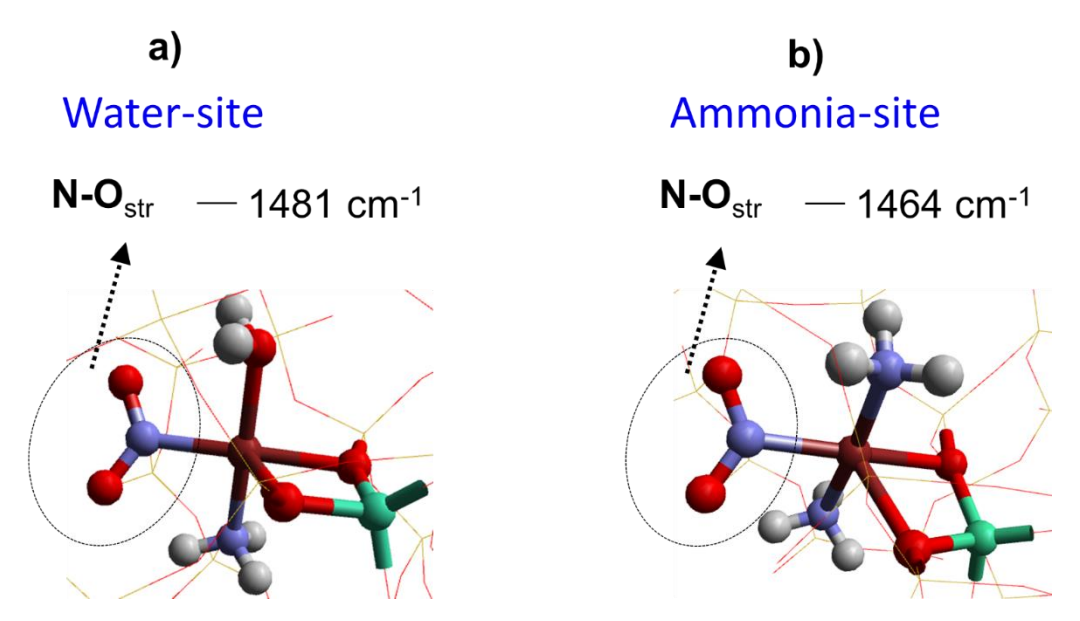


Figure 4.7. Spectroscopic Signatures; data yielded from QM/MM calculations for protonated and deprotonated Cu-nitrosamine (Cu-N(=O)-NH₂) species. **Atom colour codes**: Cu (brown), Al (green), O (red), N (blue), and H (white). The framework SiO₂ is shown using a wire framework motif.

4.3.2 Cu Displacement on Solvation

The promoting effect of the water on the migration of Cu species suggested that unanchored Cu ions migrate to defect sites to form active sites which can promote the SCR reaction ²⁹⁸. In our calculations summarized in Figure 4a, we observe that an increase in water and NH₃ coordination to the Cu- active sites displaces the Cu species away from the CHA framework. As the number of H₂O molecules around the Cu(I)-CHA increases, the interaction between the framework and Cu species becomes weaker. In the case of four H₂O molecules, the distance between Al and Cu is calculated to be 8.07 Å, suggesting that water molecules can promote the mobility of Cu-ions species (Figure 4.8). Similarly, the effect of NH₃ solvation during the oxidation part of the SCR reaction is crucial. Some previous reports suggest that the NH₃-solvated Cu(I) sites interact weakly with the zeolite framework, and move away as a mobile species to react with the O₂ and yield an O-bridged Cu(II) dimer ¹¹⁹; and we find an increase in bond length between Al and Cu as the number of NH₃ molecules increases, suggesting that an enhanced number of NH₃ molecules can detach Cu species from the framework.

Ab initio molecular dynamics (AIMD) simulations have shown that after the adsorption of one NH₃ molecule in Cu-SAPO-34²⁷¹ at 298 K, the Cu⁺ cation is somewhat displaced but yet remains coordinated with one of the framework oxygens to form the H₃N-Cu-O bond, which is also evident from the experiment on Cu-SSZ-13⁹⁹. These studies demonstrated that the Cu-O bond in the Cu⁺-NH₃ system is broken by the adsorption of a second NH₃ molecule, resulting in the formation of a linear Cu⁺(NH₃)₂ complex that can move readily inside the pore. Our QM/MM simulations agree with these findings, as can be observed in Figure 4.8. Furthermore, Paolucci *et al.* ²⁹⁹ used *ab initio* metadynamics and a supercell with a minimum image distance in excess of 10 Å to evaluate the mobility of Cu^I(NH₃)₂ complexes over time scales, which are inaccessible to conventional AIMD. Their results are supported by experimental observations

showing a ~9 Å diffusion length for a Cu ion that penetrates an 8-MR window separating two adjacent CHA cages. In our study, we employed a more realistic model of the solvent behaviour in the Cu-SSZ-13 system. Similar to the above study, we start our analysis with a single solvent adsorbate molecule simulating both water and ammonia. Next, we introduced stepwise a series of solvent molecules bringing the solvent content to four molecules per cage. Upon adsorption, we observed a pronounced displacement of the Cu ion away from the framework Al site. In the case of water, the calculated distance between Al and Cu is 8.07 Å, while for the solvated Cu-NH₃ case, it is 6.16 Å, consistent with the understanding that solvent molecules promote the mobility of Cu ions. In contrast to the report by Paolucci *et al.* ²⁹⁹ we do not observe the penetration through the 8-MR window, which could be attributed to the more realistic boundary conditions in our simulations. Notably, the Cu ions in our study are not forced to move away from the Al site but displace spontaneously as a result of geometry optimization from their initial position close to the Al site in response to the strong interaction of the polar solvent with both framework and extraframework metal cations.

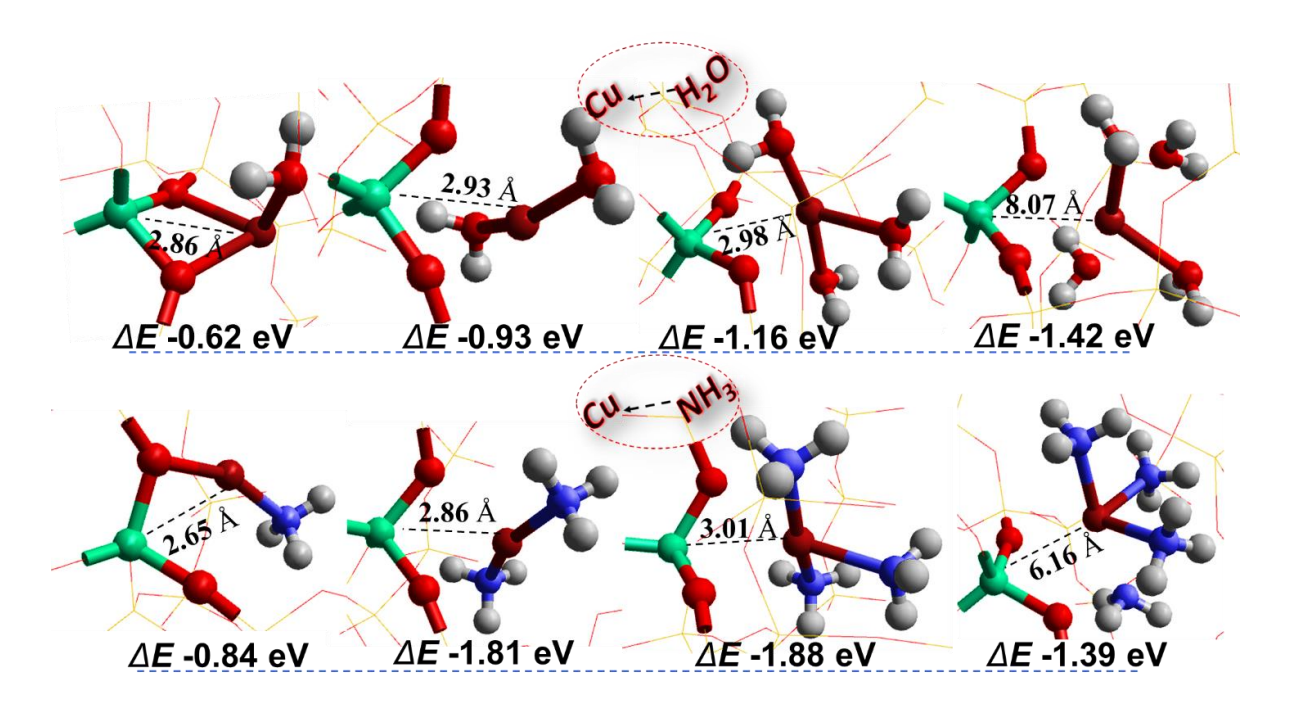


Figure 4.8. The interaction of physisorbed a) water and ammonia, and b) the behaviour of NO on solvated Cu(I)-CHA site. The model used is shown as an extra framework. **Atom colour codes**: Cu (brown), Al (green), O (red), N (blue), and H (white).

We also examined the approach of NO towards the solvated Cu(I)-CHA and infer that in the presence of water, the effect of NO is vital, as it restricts to some extent the displacement of the Cu-ions species from the framework (Figure 4.9), which is apparent from the corresponding bond distances (2.96 Å) between the Cu and Al when compared with those when NO is not present; which can prevent Cu(II) dimer formation and promotes the formation of nitrate species^{281, 293}. In addition, it also suggests that the presence of NO might prevent the mobility of Cu-ions in the presence of water. We, however, observed a complete detachment of Cu-ions from the framework when NO interacts with three-NH₃ coordinated sites with a bond distance of 3.071 Å between Cu and Al. The experimental findings by Andrew Beale's observed the formation of nitrosamines and nitrate the structure of which was proposed by computational modelling and the suggested Cu species appear to be in close proximity to the zeolite framework.

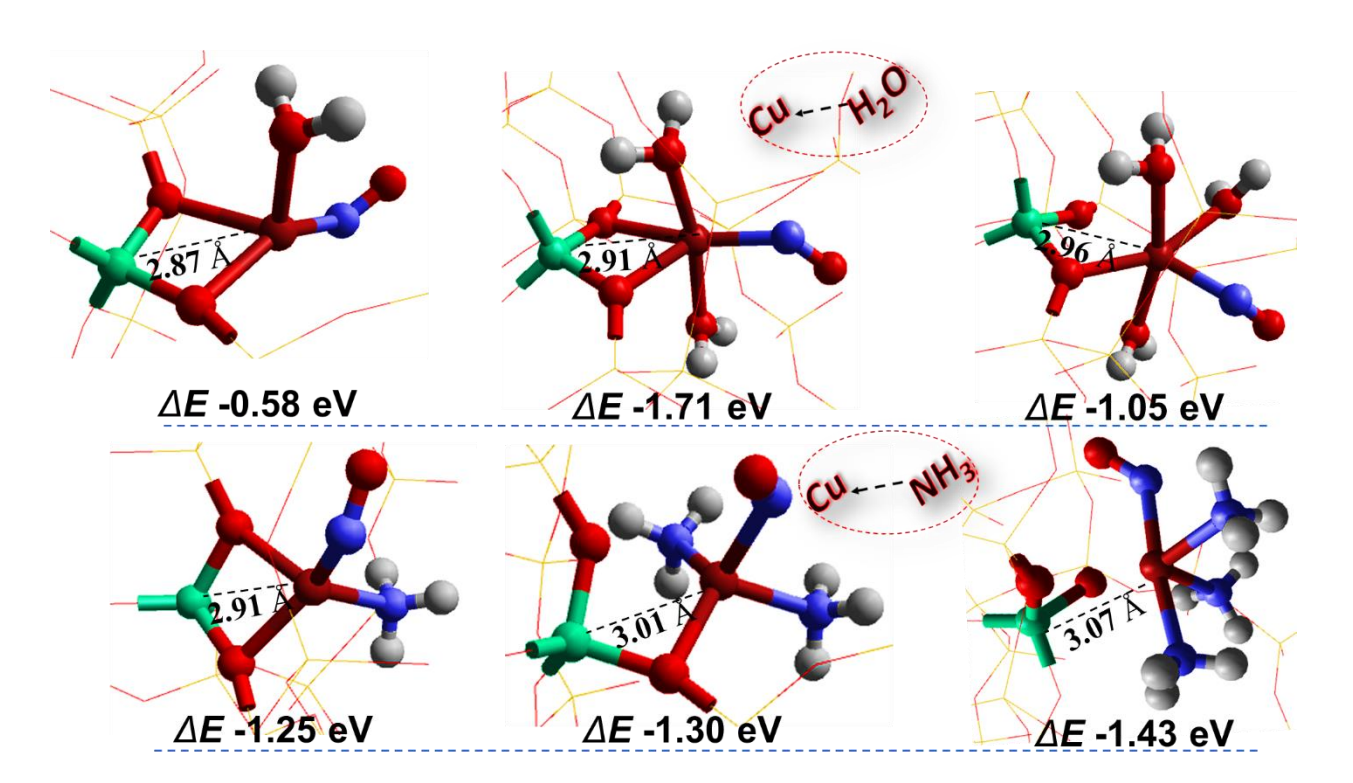


Figure 4.9. The behaviour of NO on solvated Cu(I)-CHA site. The model used is shown as an extra framework. **Atom colour codes**: Cu (brown), Al (green), O (red), N (blue), and H (white). The framework SiO_2 is shown using a wire framework motif.

4.3.3 Catalytic Cycle

We have studied the reaction energetics on both water and ammonia-solvated Cu-CHA sites and made their comparison with each other and with the bare sites. To perform this study we used the same computational parameters in each case.

Effect of Water Solvation

Water is also one of the main products of the NH₃-SCR reaction, and, therefore, the hydrated state of the active sites cannot be ignored ¹⁵⁹. Taking into account the calculated adsorption energies of H₂O on Cu(I)-CHA (-0.616 eV) and Cu(II)-CHA (-0.913 eV) sites, we suggest that the NH₃-SCR reaction proceeds differently on solvated Cu-CHA sites. Using the same computational approach, we have studied the influence of water on the formation of the intermediate species; single water molecules are physisorbed on the isolated Cu(I)/ Cu(II) active sites to which intermediate species are bound. The starting point for the reaction is the adsorption of O₂ on the solvated Cu(I) site followed by NO which leads to the generation of important solvated nitrate species. This step is considered crucial for the NH₃-SCR cycle since it determined the oxidation part of the cycle. We found that the formation of nitrate in the presence of water-solvated Cu-CHA sites is relatively more feasible as compared to bare sites. Conversely, we found that the reduction part of the cycle is not favourable when reducing Cu(II) to Cu(I). This step mainly proceeds when both NO and NH₃ interact with the Cu(II) site leading to nitrosamine species. The structures of each corresponding intermediate species residing on solvated (H₂O) Cu-CHA are shown in the following Figure 4.10.

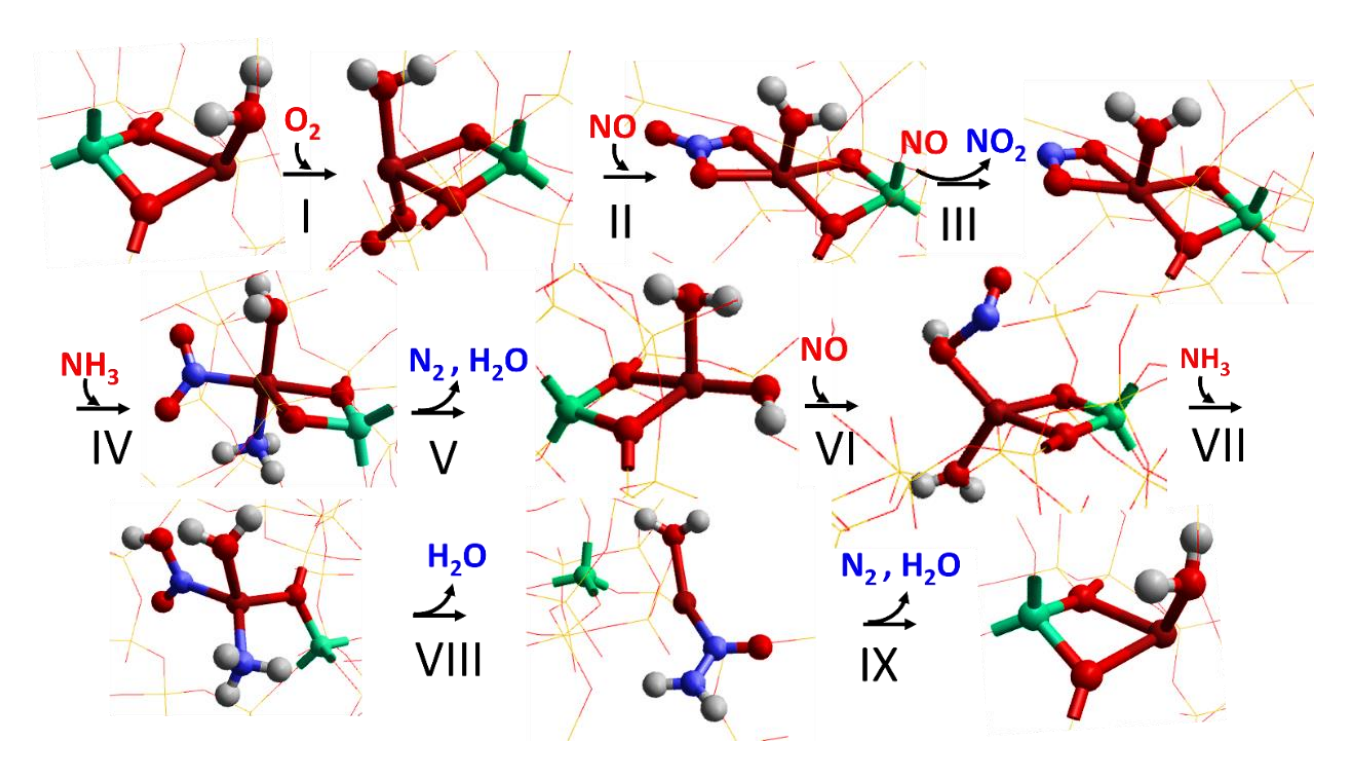


Figure 4.10. The structures of each corresponding intermediate species residing on solvated (H_2O) Cu-CHA. **Atom colour codes**: Cu (brown), Al (green), O (red), N (blue), and H (white). The framework SiO_2 is shown using a wire framework motif.

The corresponding reaction energy landscape is shown in Figure 4.11 as red lines. The starting point for the reaction is the interaction of the O₂ molecule with the physisorbed water Cu(I) site forming H₂O-Cu-O₂ species with a total energy change of -0.08 eV. We observe notable differences in the formation energies of some important steps as compared to the bare site. For example, our results show that without physisorbed water, the formation of nitrate species is less favourable (-1.34 eV) than in the presence of water (-1.69 eV) (Figure 4.11) suggesting that water can promote the re-oxidation half-cycle, which is also supported by experimental findings as reported by Wan *et al.*²⁹⁸, showing that water could markedly enhance NO reduction. In contrast, we found that on the water occupied -Cu-CHA site, the formation of Cu-nitrosamine (Cu-N(=O)-NH₂) is less favourable (-0.11 eV) than in the absence of water (-0.66 eV), suggesting that water can slow down the formation of this species, which can ultimately affect the reduction part of the NH₃-SCR cycle. Commensurate with this, it has also been reported previously that residual H₂O or hydrocarbons can block the active sites or alter their

activity ¹⁵⁸. In addition, we observed that the formation of nitrite species is endothermic (0.18 eV) on the physisorbed water Cu(II). The formation of (Cu–(NO₂)–NH₃) is found to be exothermic with a formation energy of -1.34 eV as compared to the bare site of -1.24 eV.

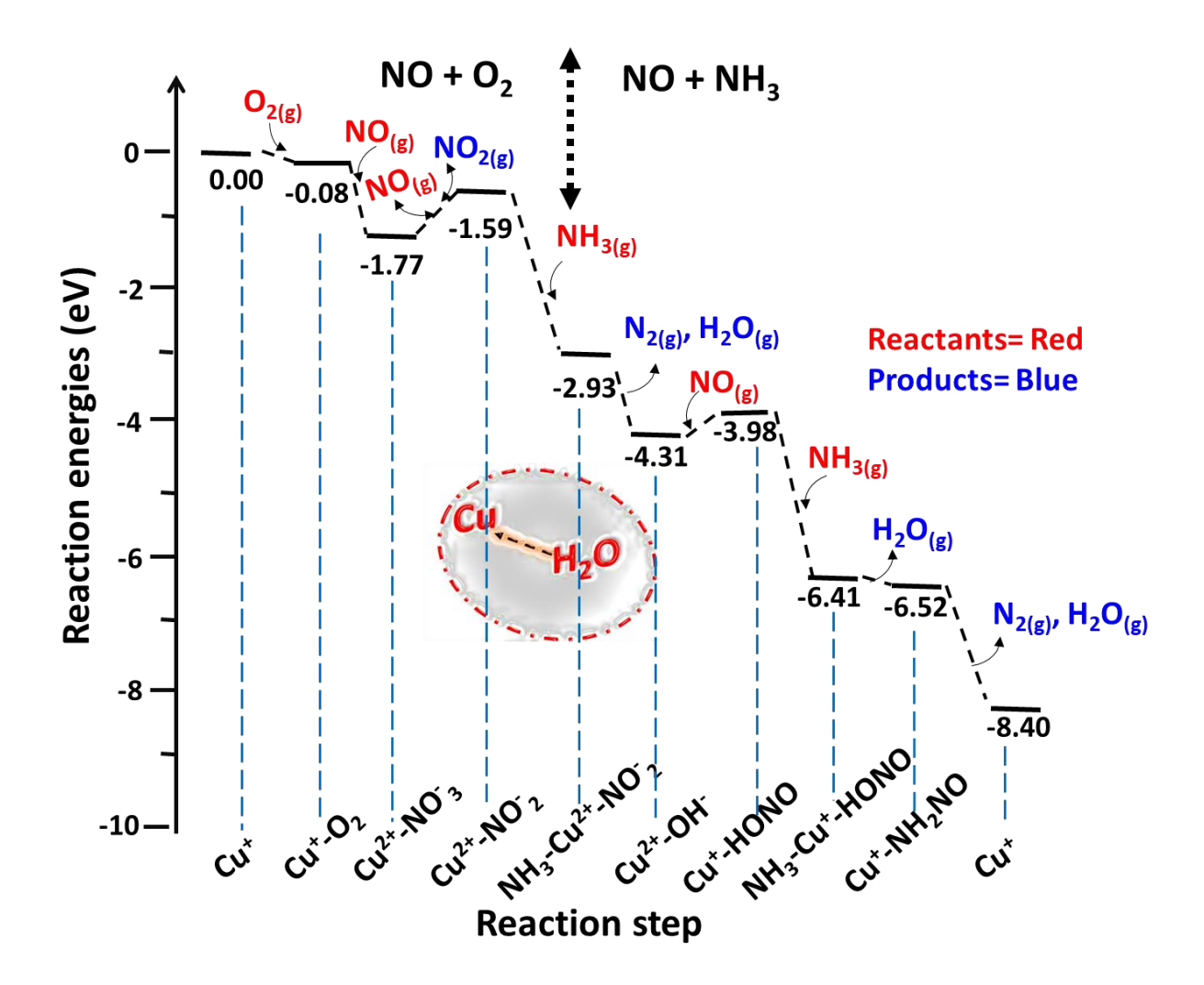


Figure 4.11. The relative potential energy landscape of the NO-activated NH₃-SCR of NOx catalytic cycle on the physisorbed water Cu-CHA site is presented in the lower panel. The model used is shown as an extra framework.

Effect of Ammonia Solvation

Previous experimental evidence showed that preadsorbed NH₃ at 300 °C or 250 °C can enhance NOx reduction; however, low activity of NO reduction was observed below 150°C ³⁰⁰. From the calculated binding energies of NH₃ for both Cu(I)-CHA (-0.616 eV) and Cu(II)-CHA (-0.913 eV) sites, we can infer that the reactive sites occupied by NH₃ molecules can

influence the mechanism. The structures of each corresponding intermediate species residing on solvated (NH₃) Cu-CHA are shown in the following Figure 4.12.

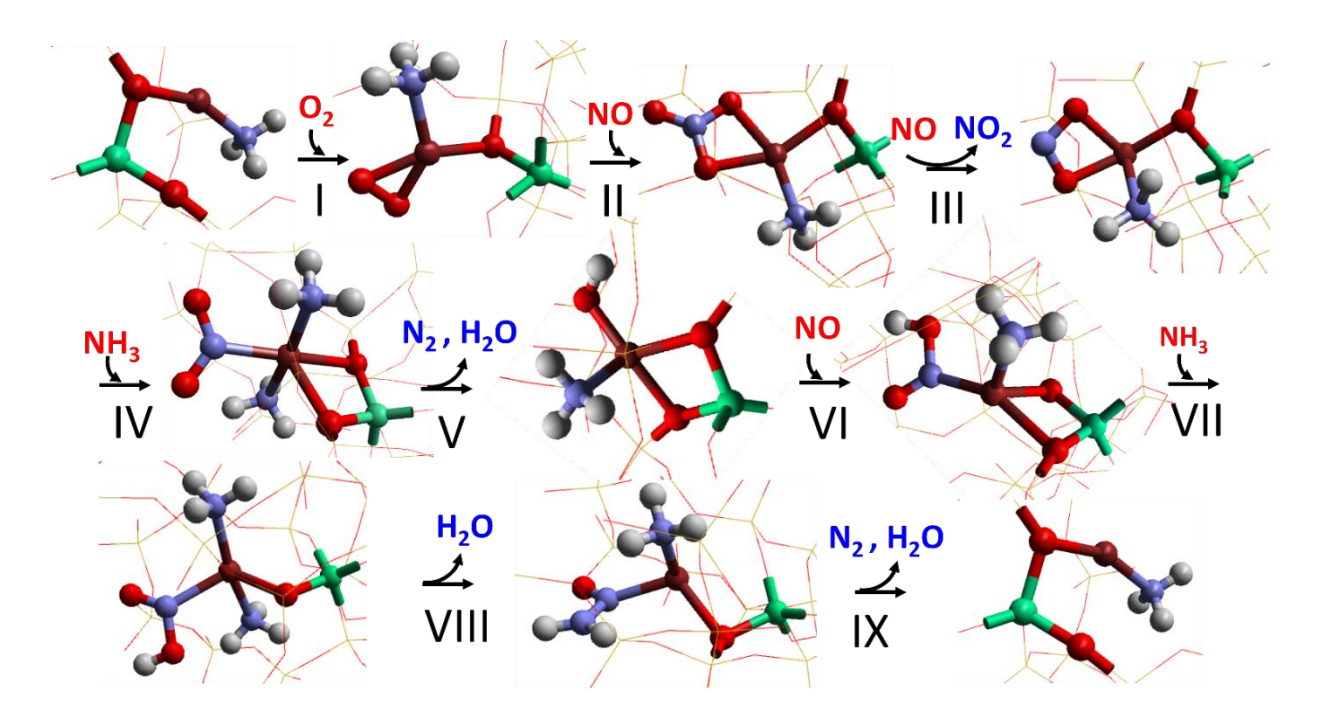


Figure 4.12. The structures of each corresponding intermediate species residing on solvated (H₂O) Cu-CHA. **Atom colour codes**: Cu (brown), Al (green), O (red), N (blue), and H (white). The framework SiO₂ is shown using a wire framework motif.

We have investigated the effect of ammonia on the formation of the intermediate species as shown in the energy profile (Figure 4.13). Notably, the formation of Cu bidentate nitrate species (Cu-NO₃) on the physisorbed NH₃ site is found to be more favourable (-1.59 eV) than in the presence of bare (-1.34 eV). In the case of physisorbed water and the bare site, the formation of nitrite under the release of NO_2 is endothermic but for physisorbed ammonia, it is exothermic. In addition, the formation of the important intermediate, Cu-nitrosamine (Cu-N(=O)-NH₂) is less favourable on the physisorbed ammonia active sites (-0.31 eV), when compared to the bare (-0.66 eV), indicating that ammonia may block the active sites for the NH₃ + NO activation half cycle. In particular, we calculated that the formation of nitrite species is exothermic (-0.12 eV) on the physisorbed ammonia Cu(II) in contrast to the physisorbed

water and bare site. We also found the formation of (Cu–(NO₂)–NH₃) an exothermic step with a formation energy of -0.6 eV as compared to the physisorbed water of -1.34 eV and bare site of -1.24 eV.

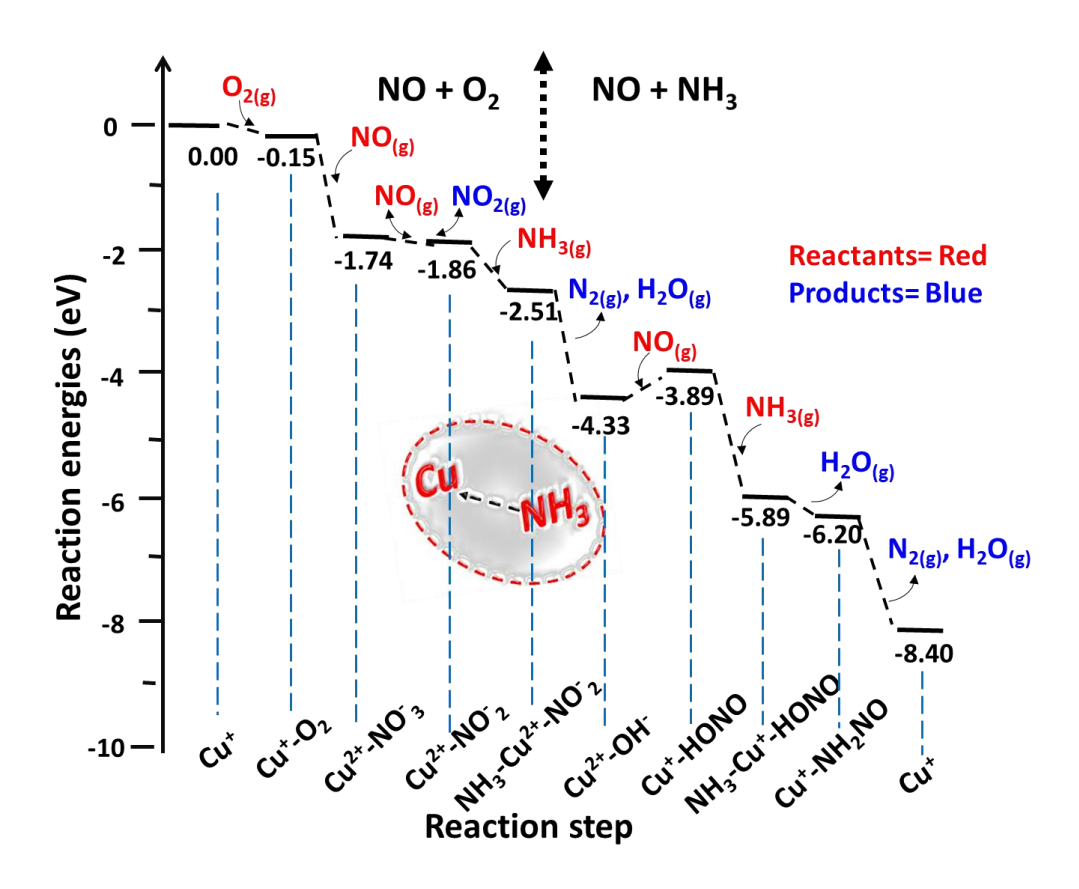


Figure 4.13. The relative potential energy landscape of NO-activated NH₃-SCR of NOx catalytic cycle on the physisorbed water Cu-CHA site is presented in the lower panel. The model used is shown as an extra framework.

Comparative Study

Overall, when comparing the accumulative effect on the reactivity (Figure 4.14), we observe that the effect of water on nitrosamine is more significant (+0.55 eV) than on the nitrate (-0.35 eV) which infers that the impact of water could be a (slight) net negative influence on activity. Similarly, regarding the accumulative effect of ammonia on the reactivity, the effect of ammonia on nitrosamine is found to be more significant (+0.35 eV) than on the nitrate (-0.25

eV) suggesting an impact of ammonia could be a net negative influence on activity. It is possible to split the NH₃-SCR redox cycle and separate the oxidation from the reduction step, which is achieved experimentally by switching between the NH₃ + NO and NO + O₂ ²⁷⁷ atmospheres to study the individual half-cycles ¹²⁰. For this purpose, we can easily control the reaction step and, therefore, take advantage of the solvent in the oxidation part of the cycle. In the case of, Cu(II)-nitrate species formation which formed as a result of the NO + O₂ oxidation process, can be accelerated in the presence of a solvated atmosphere. In contrast, the conversion of Cu(II) to Cu(I)-state under NH₃ + NO reductive conditions, we can design reactor to remove solvent content during reduction half cycle. This finding explains why there is some debate concerning the effect of water and ammonia on the reaction since it seems to affect some parts of the cycle positively and others negatively.

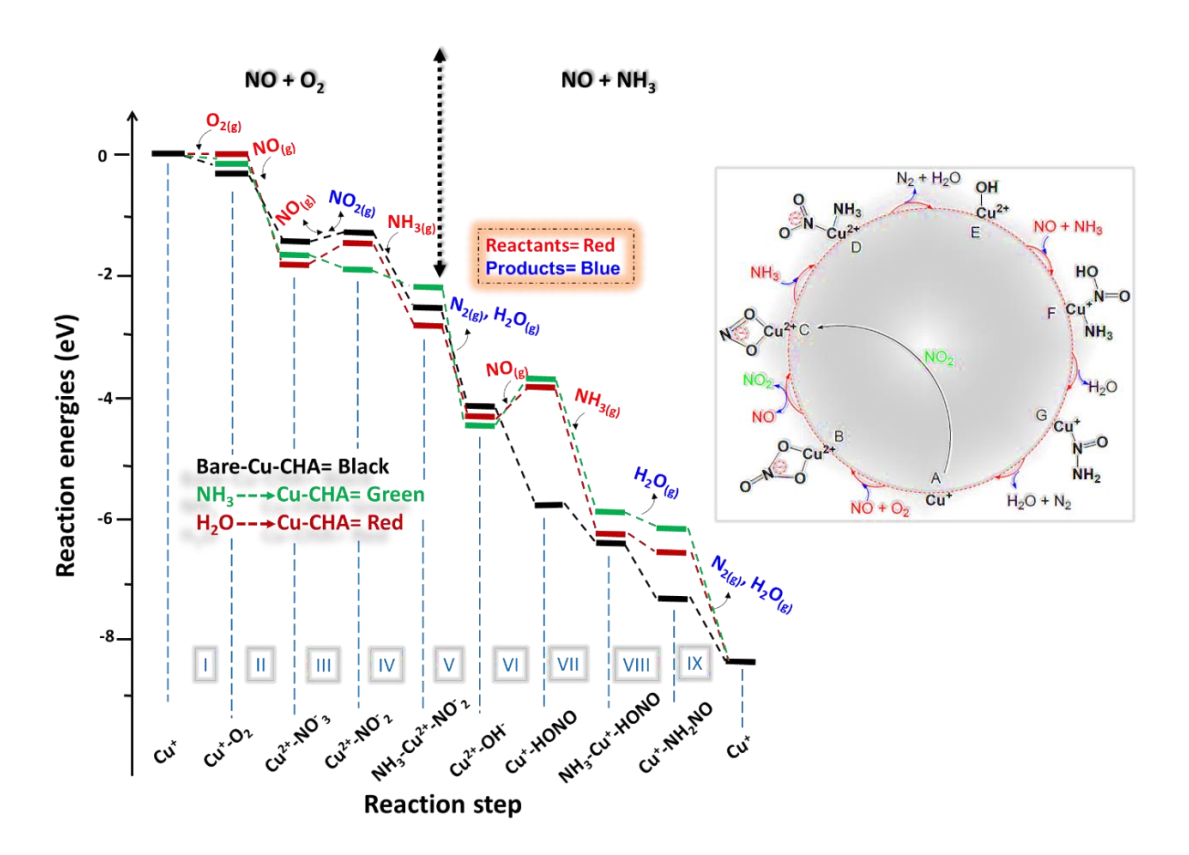


Figure 4.14. The relative potential reaction-energy landscape at room temperature for NH_3 -SCR on activated Cu-CHA site; (black) on bare-site, (green) with physisorbed ammonia, and (red) with physisorbed water. Inset right: No-activated NH_3 -SCR of NOx catalytic cycle.

4.3.4 Solvent Effect on H₂NNO Decomposition

It is reported that solvent can coordinate to the Cu-site, we, therefore, investigated the decomposition pathway of H₂NNO on isolated Cu-CHA active sites both in the absence and presence of physisorbed water. The schematic illustrations of isomeric decompositions of H₂NNO intermediates are shown in Figure 4.15.

$$Cu-N(=O)-NH_2 \longrightarrow Cu^+ + H_2O + N_2$$

$$H \longrightarrow N-N \longrightarrow H \longrightarrow N-N \longrightarrow H$$

$$H \longrightarrow N-N \longrightarrow N-N \longrightarrow H$$

$$H \longrightarrow N-N \longrightarrow N-N \longrightarrow H$$

Figure 4.15. The schematic illustrations of isomeric decompositions of H₂NNO intermediates.

The adduct rearrangement process of H₂NNO species starts with 1,3 H-transfer, breaking one N-H bond with the transfer of an H to an adjacent O atom which leads to the formation of an O-H bond. Without physisorbed water, the H-transfer leads to two isomers - *cis-trans* (II) and *trans-cis* (III) through the four-membered ring(I). The total energy change from structure (I) to (II) and (III) are calculated as 0.04 eV and 0.06 eV on the bare site; while with ligated water, it is -0.33 eV and -0.46 eV, respectively; suggesting some positive impact of solvated sites on the energetics of this step (Figure 4.16). From H₂NNO to HNNOH, the H-transfer is accompanied by a shortening of the N-N bond (from 1.35 Å to 1.299 Å) while lengthening of the N-O bond (from 1.208 Å to 1.306 Å) that eventually ends with the termination of respective bonds and generation of H₂O and N₂ as products.

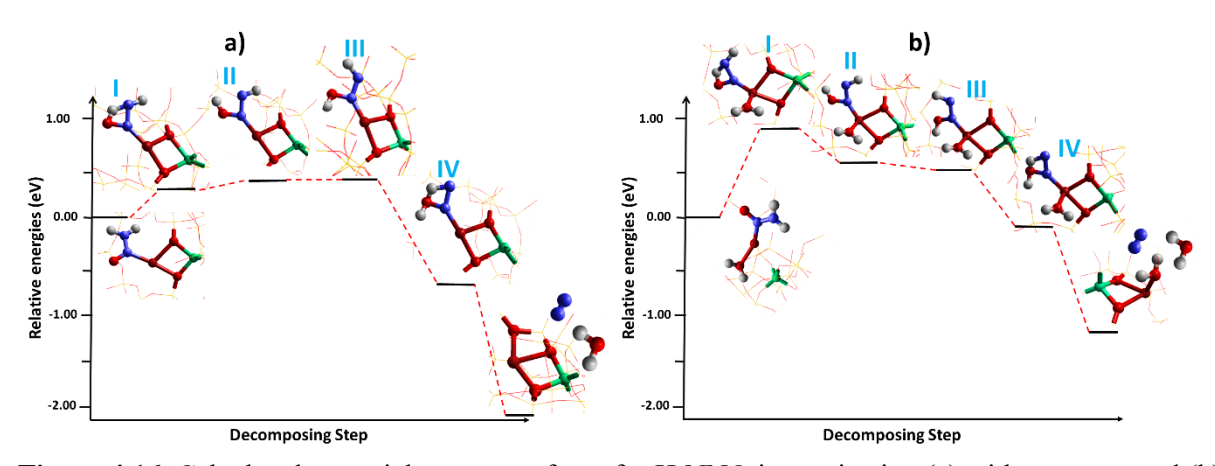


Figure 4.16. Calculated potential energy surfaces for H₂NNO isomerization (a) without water and (b) in the presence of physisorbed water on the Cu-CHA sites. The model used is shown as an extra framework. **Colour codes**: Cu (brown), Al (green), O (red), N (blue), and H (white).

We have found that the increased coordination of H₂O molecules, detached Cu-H₂NNO from the framework (Figure 4.17), showing that the solvent can affect the binding of Cu-H₂NNO species to the framework. We observed an increase in water coordination (from one to two water molecules) to the Cu-active sites containing the nitrosamine species liberating the whole intermediate species away from the CHA framework. The interaction between the framework and Cu species becomes weaker in the presence of increased water molecules. In the case of two H₂O molecules, the distance between Al and Cu is calculated to be 3.07 Å, consistent with the understanding that solvent molecules cause the mobility of intermediate species inside the CHA cage.

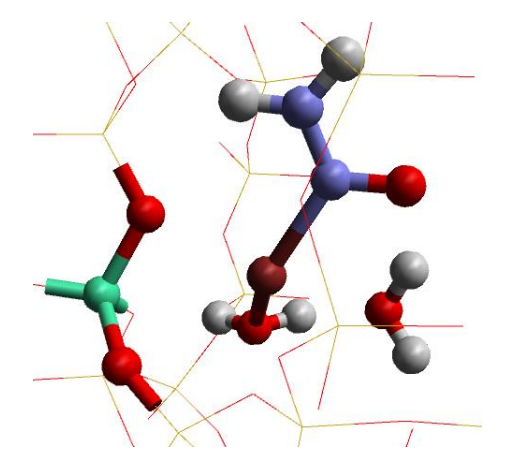


Figure 4.17. Solvent-occupied (water) active sites H₂NNO (nitrosamine) intermediates.

4.4 Summary and Conclusion

The present study has studied the influence of solvent on the NH₃-SCR reaction. By understanding the parallels between the water and ammonia interactions with active sites, we find that an increase in solvent coordination to the Cu- active sites displaces the Cu species away from the CHA framework. To understand the role of solvents on the kinetics of the NH₃-SCR cycle, the adsorption of gaseous species and the formation of intermediates and their spectroscopic signatures on the solvated active sites have been investigated which can help tune the rational design of important reaction steps. From the potential energy landscapes, we observed that the formation of nitrate species is energetically more favourable on solvated active sites than on the bare site, suggesting that solvents can promote the re-oxidation part of the NH₃-SCR cycle. This effect is more significant in the case of water than ammonia. In contrast to the potential benefits seen on the oxidative part, both water and ammonia are found to inhibit the reduction part of SCR since the formation of important intermediates such as Cunitrosamine is relatively less favourable on solvated active sites than on the bare sites, suggesting that solvent can slow down the reduction part of the NH₃-SCR cycle. This finding explains why there is some debate concerning the effect of water and ammonia on the reaction since it seems to affect some parts of the cycle positively and others negatively. In addition, solvating ammonia species were also found to accelerate the oxidation part of the cycle, which is also apparently evident from experimental data showing that preadsorbed NH₃ at 300 °C to 250 °C can enhance the NOx reduction. Our study provides additional understanding, helping to unravel the influence of solvent on the energetics of the active sites and provides guidance into a future pathway for optimizing the NH₃-SCR process. The work presented in this chapter has been published ²¹⁰.

Chapter 5

Fe-Beta Zeolite in NH₃-SCR

5.1 Introduction

As discussed in chapter 1, Fe-zeolites have a wide range of applications in the petrochemical, environmental protection, fine chemical, and other catalysis-based industries including ammonia-assisted SCR of NOx due to their zeolitic properties and the redox chemistry conferred by the addition of Fe species. The nature of the incorporated Fe is critical for the catalytic properties. Both the introduction procedures/conditions and the zeolite's inherent characteristics—such as porosity and acidity—determined the state of the Fe species in zeolite, which has a substantial influence on the material's properties (redox properties, acidity, stability) of Fe-zeolite. It is, therefore, crucial to have a thorough understanding of the structure-activity connection of Fe zeolites.

It is evident from the experimental findings³⁵ that the NH₃-SCR reaction occurs on several Fesites with distinct energetics, hence leading to different turnover frequencies. Under low loading, the majority of Fe ions are present as a monomer at the ion-exchange positions while at higher loading the oligomers of Fe are formed which mostly reside inside the micro-pores of zeolites ¹³. Liu *et al.* reviewed different active sites of Fe such as monomeric, dimeric, and oligomeric type species ³⁶. They investigated Fe complexes in ZSM-5 and concluded that the distribution of mononuclear sites of Fe species (FeO)⁺ is not sensitive to the local environment while binuclear sites preferentially reside in the 8-MR.

Taking monomeric species (FeO)⁺ as an active site, a series of reaction pathways were explored using the B3LYP hybrid DFT method the energies for various species were stated by Li *et al.*37 and Bruggeman *et al.*38 relating to the N₂O decomposition in the NH₃-SCR process. We would expect that when two exchange Fe species are in close proximity, the dimer of Fe species is readily generated which is evident from the previous reports ³⁹⁻⁴⁵. Brandenberger *et al.* performed a Poisson distribution, a method used for the prediction of rare but possible events in a fixed interval to estimate the fraction of content of Fe species in zeolites ⁴⁶. The results obtained through this method have a satisfactory accuracy which shows the correlation of the degree of Fe exchange species with active sites. Commensurate with this observation, there is a consensus that more than one site can be present in the zeolite, and the monomeric Fe ions in this regard are a more likely generated species under low exchange degree ⁴⁶.

Another assumption regarding Fe exchange zeolites is that bare Fe³⁺ is only coordinated to oxygen and is unstable in high silica zeolites due to the lack of negative charge within the zeolite lattice to counterbalance the trivalent ions ⁷⁶. There is also experimental evidence that trivalent ions can be present in the framework owing to their similar chemical state as Al ⁷⁹. Thus, Fe ions (Fe³⁺ ions) can be incorporated into high silica zeolites as a framework cation; however, the steaming of ferrisilicates induced the removal of Fe from the framework and introduced it into the extra-framework sites. The auto-reduction of Fe³⁺ to Fe²⁺ under He treatment is characterized by X-ray absorption spectroscopy ^{73, 74}. The switching behaviour of Fe³⁺ to Fe²⁺ is attributed to the desorption and dehydration of Fe³⁺(OH)₂ to liberate O₂ and form two Fe²⁺(OH) species ⁷⁵. The characterization of such trivalent ions especially Fe³⁺ is challenging. The identification and the chemistry of the Fe ions in aqueous solution are well defined from the existence of various mono-, di, and poly-complexes bearing different species

such as oxygen, water molecule, and OH groups (depending on the reaction media e.g. pH) 77 , 78 . Fe³⁺ exists only in the acidic solution (pH < 3), where proton exchange can easily occur.

A recent report ³⁰¹ shows Cu -Fe combination (FeCu-SSZ-13) which is prepared through a one-pot synthesis method, using high temperature (600°C) and long time (4 h), and activated diatomite as a silicon and iron source while copper-amine complex as a structure-directing agent as well as a copper source. The Fe-Cu-SSZ-13 catalyst obtained showed excellent activity in NH₃-SCR with a wide reaction temperature window (200°C - 500°C) and good stability. The contribution of isolated Cu²⁺ and framework Fe³⁺ ions to the improved performance of FeCu-SSZ-13 is suggested. However, high copper loading may lead to the formation of CuOx and deactivate the catalyst. The role of framework-Fe³⁺ or extra-framework-Fe³⁺ in the improvement is still unclear, as some studies suggest that the Fe³⁺ in the framework may not contribute to the SCR reaction and its removal from the framework under high-temperature hydrothermal ageing could lead to framework collapse ³⁰².

In this chapter, we have investigated the NH₃-SCR reaction at several active sites of the Fe-BEA system with Fe species as both framework and extraframework cations (Figure 5.1). Density functional theory (DFT) using the quantum mechanical/molecular mechanical QM/MM methodology has been employed, discussed in Chapter (2) and elucidated the reactivity of Fe-BEA on the energetics of intermediates. Our study provides insight into the NH₃-SCR reaction by understanding the chemistry of the Fe-BEA, especially the role of Fe species in the key steps of the reaction.

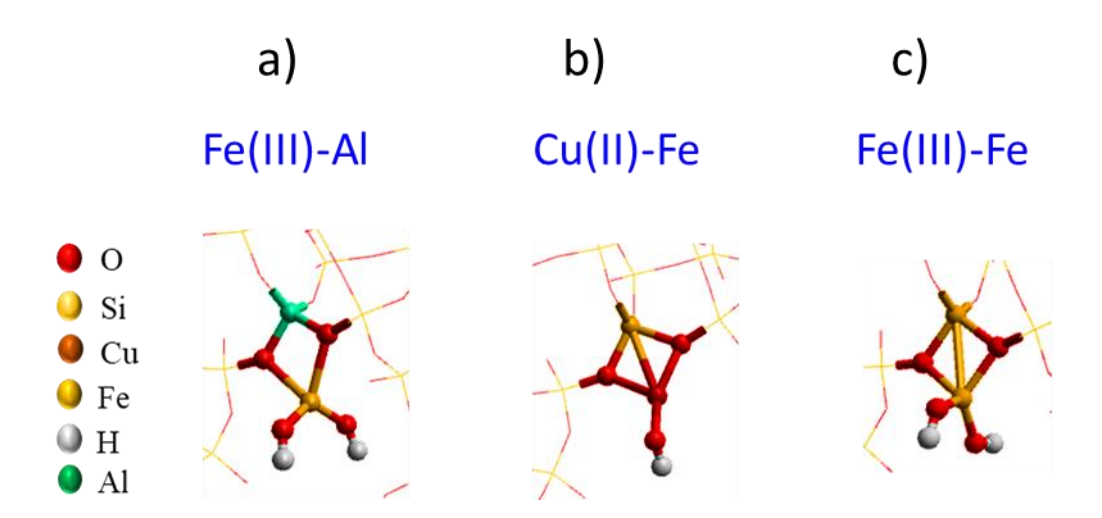


Figure 5.1. Fe-BEA: framework and extra framework cations in BEA zeolite a) Fe(III)-Al, b) Cu(II)-Fe, c) Fe(III)-Fe.

5.2 Computational Approach

5.2.1 QM/MM Methodologies

We again used the QM/MM techniques available in the Chemshell code as discussed in Chapter (2). We divided the QM region into two parts and employed a dual basis set strategy; ~22 atoms are in the innermost QM1 region, including the intermediates which are treated with the triplet-ζ basis set Def2-TZVP ²¹⁹ while the outer QM2 region (64 atoms), which includes the terminating link H atoms, is treated with a split valence with polarization Def2-SVP ²¹⁹ basis set. To build the QM/MM model, it is necessary to remove the classical charges from the centres (QM) and make sure that the total charge removed from the system is the same as the total charge of the QM region. The guest species of interest in the zeolite and reactants gaseous species were also treated at the QM level using the higher quality Def2-TZVP basis set. The coordinates of all atoms (not including the link H atoms) in the QM region and active MM region were fully optimized. Considering that adsorbed molecules can diffuse through the larger channels, all the adsorbed species including the intermediates were placed within (or near) the 12-membered ring (12-MR) of the BEA cage. Water (O-end) and ammonia (N-end)

molecules were placed at a distance of 2 Å from the Fe centre with the proton pointing away from the adjacent oxygens and intermediate species to avoid any trapping in hydrogen-bonding interactions. We note that hydrogen bonding with framework O can influence chemistry at metal sites by affecting the binding of functionally important Fe–H₂O/NH₃ units.

5.2.2 Choice of Model Cluster

To perform the QM/MM calculation, we first created a spherical embedded-cluster model (Figure 5.2) of BEA from the unit cell of siliceous BEA ²³⁶ optimized at the MM level using the GULP package ²³¹. After creating a simple BEA-cluster model, we construct active sites. For example, in the case of a Brønsted acid site, we replaced one Si with Al/Fe and added a charge-compensating proton on a neighbouring oxygen atom at a site where it is most accessible to facilitate the reaction. The QM region which is contained within the active part of the model includes atoms from the third oxygen shell from the central T-site; and, as noted, we have added the hydrogen (link atoms) to saturate the terminal oxygen atoms. Furthermore, we modified the same cluster by incorporating Fe, and Cu into the cage of the BEA framework. We constructed three QM clusters based on the Fe position where Fe_F represents the Fe framework cation: for Cu-Fe_F/BEA, Cu is metal is placed as an extra framework cation while Fe is a framework ion; while for the Fe-Fe_F/BEA, one Fe is an extra framework and the other one is a framework ion. Similarly, in the case of Fe-Al/BEA, Al is placed as a framework and Fe as an extra framework cation, as shown in Figure 5.2.

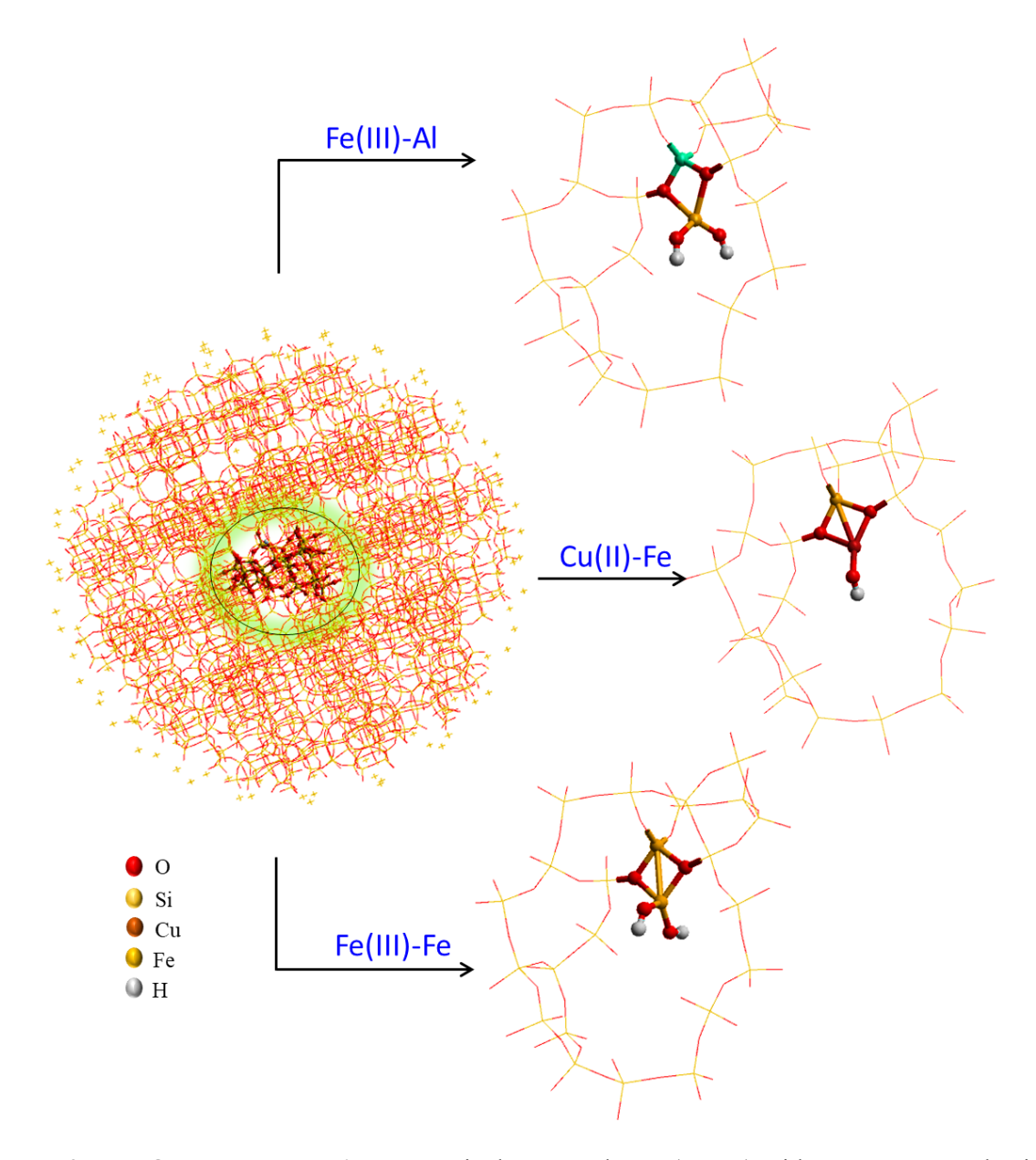


Figure 5.2. The QMMM embedding setup; is the BEA cluster (centre) with a quantum mechanical region of Fe(III)-Fe_F-BEA, Fe-Al-BEA, and Cu-Fe_F-BEA. The outermost region contains point charges to ensure the Madelung potential in the centre of the cluster is accurately reproduced. Atom colour codes: Fe (yellow), Cu (brown), Al (green), Si (yellow), O (red), and H (white).

5.3 Result and Discussions

We have proposed several catalytic sites for Fe species both as a framework and an extra framework. First, we explore the most favourable location of Fe in BEA zeolite and found that 12-MR is the most stable site. Next, we conducted systematic QM/MM simulations to study the NH₃-SCR reaction on various Fe-based BEA zeolite systems: Fe-Fe_F-BEA, Fe-Al-BEA,

and Cu-Fe_F-BEA. First, we study the reduction of intra-framework Fe(III) to Fe(II). Secondly, we investigate the behaviour of reactant and product species on the active sites. To this aim, first, the Fe-Al-BEA system is studied where Al acts as a framework cation and Fe as an extra framework. Then we replace Al with Fe (bound by four framework oxygens) and start adding an extra framework cation either Fe or Cu cations (Figure 5.2) to study the adsorption of reactant and product species, and formation of important intermediates, including nitrate and nitrosamine.

5.3.1 Reduction of Intra-framework Fe-BEA

Here, we computed the reduction potential for intraframework Fe^{3+} sites in the BEA zeolite using hybrid functionals (B97-2 238) and def2-TZVP 219 basis sets.

From the undoped parent BEA framework, we create distinct embedding clusters, each of which is centred on a tetrahedral Si atom (T-site) with a unique structural makeup within a framework active site at a channel intersection of the 12-T site. All other active site members, any additional Si atoms that are first neighbours to the active site, and all related linking oxygen atoms are included in the QM zone that surrounds this centre atom (see Figure 5.3). Even though larger clusters are only required for larger molecules interacting with the whole channel, and may not be required for such straightforward chemisorption processes, nevertheless, we still maintain a relatively large QM region (containing 86 atoms) for this study as discussed in the QM/MM methodology section. To describe the reduced Fe²⁺ state, we introduced an extra H atom coordinated with an O atom that is next to the core Fe species (Figure 5.3). The reduction potential is then defined as shown in Eqn (5.1).

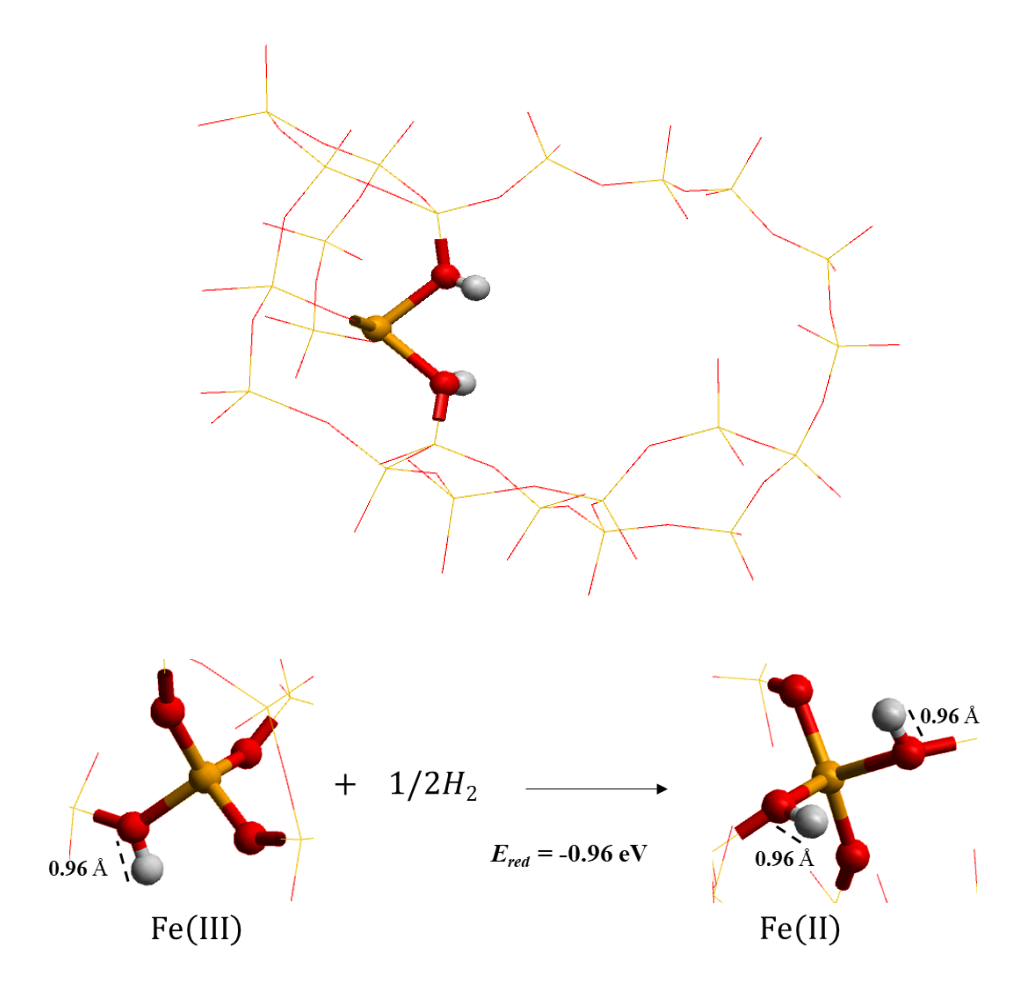


Figure 5.3. Illustrate the Fe(II) species surrounded by the QM atoms, and the reduction of Fe(III) to Fe(II).

$$E^{Red}(Fe^{3+/2+}) = E^{tot}(Fe^{2+} - BEA) - [E^{tot}(Fe^{3+} - BEA) + 1/2E^{tot}(H_2)].$$
 (5.1)

Where $E^{tot}(H_2)$ is the energy of the gas-phase hydrogen dimer. Experimental voltammetry performed by Pérez-Ramrez *et al.* ³⁰³, produced extremely low reduction energies for intraframework Fe³⁺ V_{Red} (Fe³⁺/2+_{red}) 0.15 eV. There is, therefore, a significant effect brought by the siliceous framework³⁰⁴, as compared to the corresponding reduction potential of Fe³⁺ in a hexagonally coordinated [Fe(H₂O)₆]³⁺ complex which, for example, estimated as 1.07 eV at PBE level. The result obtained for the framework Fe³⁺/2+_{red} in ZSM-5 by Berger *et al.* ³⁰⁵ using the hybrid QM/MM technique shows a negative value up to a maximum of -0.4 eV. We used however, the more detailed boundary conditions and a larger QM cluster using the B97-2²³⁸

functional and triple- ζ basis set def2-TZVP²⁷⁶ to study the framework Fe^{3+/2+}_{red} reduction potential of BEA zeolite system. Our result, however, shows a reduction potential of -0.9 eV which is in excess of half eV as compared to the computed value by Berger *et al.* ³⁰⁵. In addition, we did a similar study with CHA zeolite using the same parameters and found a reduction potential value of -0.7 eV. Further, we performed additional calculation using PBE functional and triple- ζ basis set def2-TZVP²⁷⁶ and computed a value of -0.5 eV for the framework Fe^{3+/2+}_{red} reduction potential in BEA zeolite which is quite close to the result obtained by Berger *et al.* ³⁰⁵ using ZSM-5.

5.3.2 Adsorption Properties of the Fe-BEA

In this section, we, examine the binding energies of the gaseous reactants and product molecules on various Fe-based active sites such as Fe-Fe_F-BEA, Fe-Al_F-BEA, and Cu-Fe_F-BEA.

Fe-Al-BEA

First, we consider the adsorption properties of the Fe-Al_F-BEA site, where Al is in the framework and Fe is an extra framework, and observe the behaviour of species on both Fe(II) and Fe(III) sites in the aluminosilicate BEA system (Figure 5.4). We note from the results in (Table 5.1) that the binding of O_2 , NH_3 , and H_2O with the Fe⁺²-/BEA site is, as expected, exothermic.

Table 5.1. Fe-Al_F-BEA system; the reaction adsorption energies (eV) of NH₃, NO (with both the O-and N-end down), H₂O, N₂ and O₂ on Fe(II)-(OH)-BEA and Fe(III)-(OH)₂-BEA sites.

	Fe-H ₂ O	Fe-NH ₃	Fe-O ₂	Fe-NO	Fe-ON	Fe-N ₂
Fe(II)-Al	-0.68	-1.06	-1.26	0.22	0.11	-0.04
Fe(III)-Al	-0.60	-0.85	-0.73	0.01	0.15	0.25

The binding energy for NH₃ to NH₃-Fe⁺² is calculated as -1.06 eV (-102 kJ/mol) where the reported average heat of adsorption for ammonia on Cu-Beta²⁶⁶ is nearly -100 kJ/mol. Both NH₃ and NO interact favourably with trivalent Fe(III) sites. For NH₃ on the Fe³⁺-BEA site, the binding energy is -0.85 eV (-82 kJ/mol) with a bond distance between (N)-NH₃ and Fe are 2.121 Å, suggesting that ammonia can easily bind to Fe³⁺-BEA. Furthermore, we noted that NO binding with Fe³⁺-BEA through both the N end down and O end down is endothermic with a binding energy of 0.01 eV and 0.15 eV respectively. In addition, we find that H₂O exothermically binds to both Fe²⁺-BEA and Fe³⁺-BEA sites with a binding energy of -0.68 eV (-66.2 kJ/mol) and -0.60 eV (-58.3 kJ/mol). The bond distances between [Fe(II) and (O)-H₂O] are 2.149 Å while in the case of [Fe(III) and (O)-H₂O], it is 2.07 Å. On Fe²⁺-BEA (Fe(II)-Al/BEA), NO weakly adsorbs through both the N atom and O atoms, with a binding energy of 0.22 eV and 0.11 eV, respectively. The adsorption of O₂ to both Fe(II) (-1.26 eV) sites and Fe(III) (-0.73 eV) is exothermic; however, it is more likely to interact strongly with the Fe(II) site suggesting that O₂ plays a key role in the reoxidation of the Fe²⁺ site.

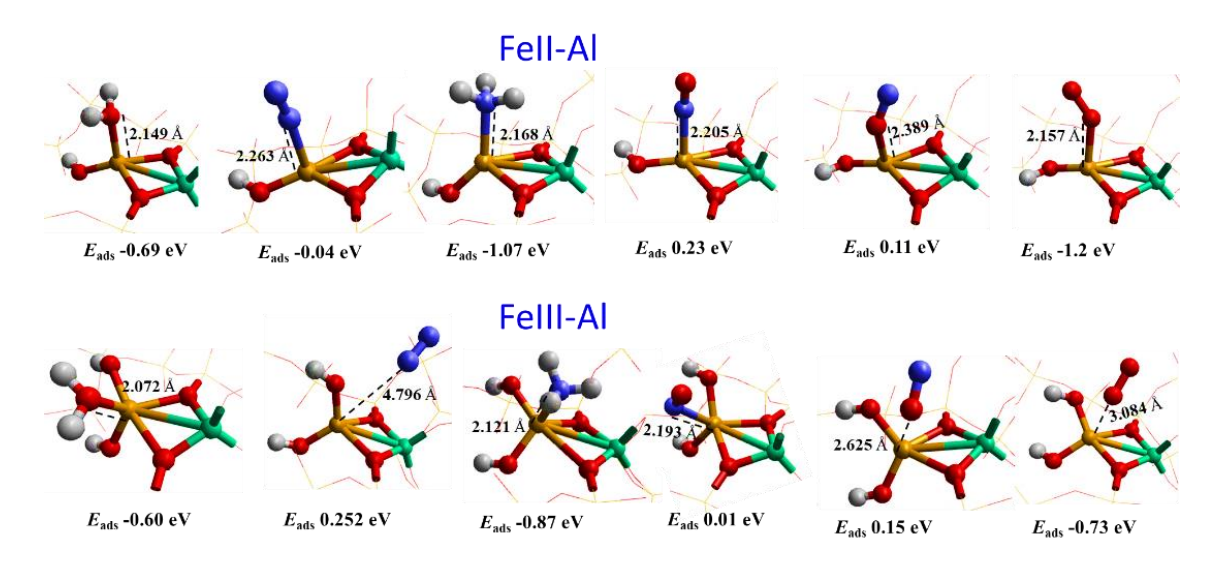


Figure 5.4. The adsorption energies of NH₃, NO, and H₂O on Fe(II)-Al/BEA and Fe(IIII)-Al/BEA sites. The model used is shown as an extra framework. **Atom colour codes:** Cu (brown), Al (green), O (red), N (blue), and H (white). The framework SiO₂ is shown using a wire framework motif.

Cu-FeF/BEA

Turning now to the adsorption properties of the Cu-Fe_F/BEA site; we envisage the binding behaviour of gaseous species on extraframework Cu(I) and Cu(II) sites (Figure 5.5) (Table 5.2). To this end, first, we have studied the behaviour of Cu(I)-Fe/BEA and the approach of NO, NH₃, and H₂O with the active sites. Note, that Fe acts as a framework cation while Cu is an extraframework in this system.

Table 5.2. Cu-Fe_F-BEA system; the reaction adsorption energies of NH₃, NO (with both the O- and N-end down), H₂O, and O₂ on Cu(I)-BEA and Cu(II)-(OH)-BEA sites.

	Cu-H ₂ O	Cu-NH ₃	Cu-O ₂	Cu-NO	Cu-ON	Cu-N ₂
Cu(I)-Fe	-0.22	-5.32	-2.29	-4.09	-3.63	0.07
Cu(II)-Fe	-0.43	-1.32	0.26	0.07	0.07	-0.05

As expected, the binding of NH₃ to Cu⁺¹-Fe/BEA, yielding NH₃-Cu⁺¹, is found to be highly exothermic with a binding energy of -5.32 eV (-513 kJ/mol), which is similar to the system when Al is present in the framework. Furthermore, the binding of NH₃ to the Cu²⁺ site yielding NH₃-Cu⁺²-Fe/BEA is also found feasible with a binding energy of -1.32 eV (-127 kJ/mol) suggesting that NH₃ can bind to both Cu(I) and Cu(II) site. In addition, we noticed that H₂O can interact with both Cu⁺-Fe/BEA and Cu²⁺-Fe/BEA sites with a binding energy of -0.22 eV (-21.2 kJ/mol) and -0.432 eV (-41.6 kJ/mol) respectively. The bond distances in both cases are 2.187 Å between Cu(I) and (O)-H₂O and 2.008 Å between Cu(II) and (O)-H₂O. NO is noted to be strongly adsorbed on Cu¹⁺-Fe/BEA through both the N atom and O atoms, with a binding energy of -4.1 eV (-395.6 kJ/mol) and -3.63 eV (-350.2 kJ/mol) respectively. However, no interaction of NO with Cu²⁺-Fe/BEA is noted, suggesting that NO can only bind with Cu⁺-Fe/BEA sie. As expected, the binding of O₂ to the Cu(I) sites is feasible with a negative energy

(-3.917 eV) while it is unfavourable at Cu(II) sites (0.21 eV) as displayed in Figure 5.5, suggesting that O₂ plays a key role in the reoxidation of the Cu²⁺-Fe/BEA site.

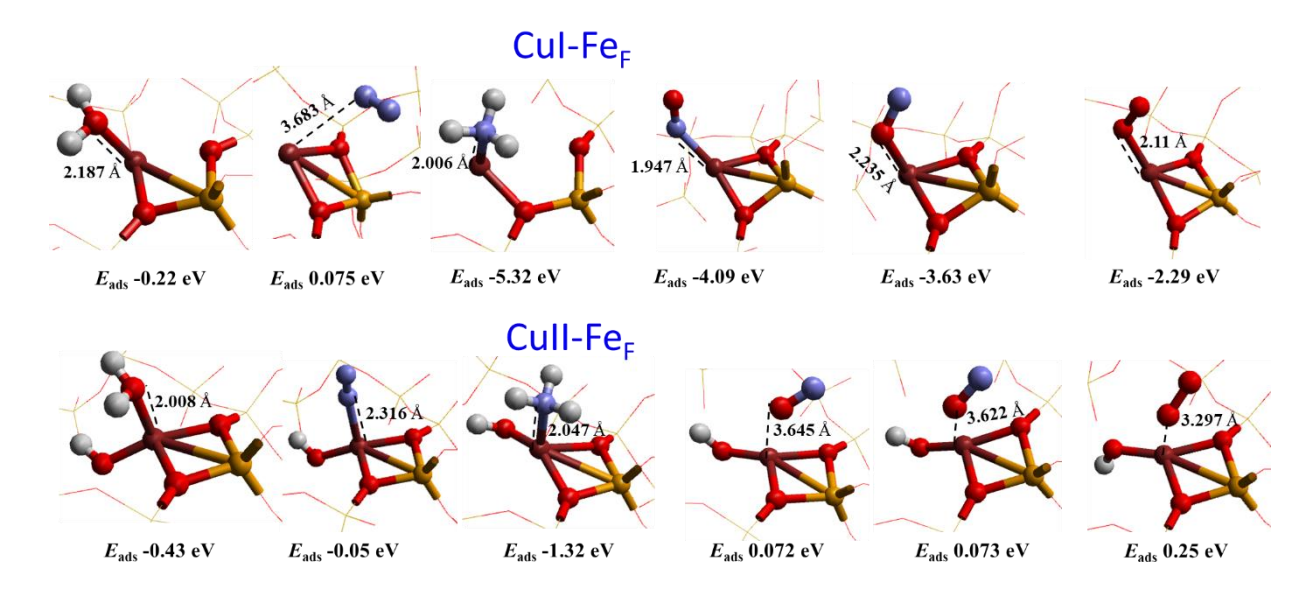


Figure 5.5. The adsorption energies of NH₃, NO, and H₂O on Cu(I)-Fe_F/BEA and Cu(II)-Fe_F/BEA sites. The model used is shown as an extra framework. **Atom colour codes:** Cu (brown), Al (green), O (red), N (blue), and H (white). The framework SiO₂ is shown using a wire framework motif.

Fe-Fe-BEA

After examining the properties of the Fe-Al-BEA and Cu-Fe_F/BEA site; we then studied the most important Fe-Fe_F-BEA system where one Fe atom acts as an extra-framework and another Fe_F as a framework cation (Figure 5.6). The system is of particular interest since there are reports that Fe ions can be present as framework species in the zeolite. We, therefore, explored the binding and transformation of these important active sites (both on Fe(II)-Fe_F-BEA and Fe (III)-Fe_F-BEA). First, we study the behaviour of Fe(II)-Fe/BEA and examine the approach of reactants and product species towards the active sites (Table 5.3).

Table 5.3. Fe-Fe_F-BEA system; the reaction adsorption energies of NH₃, NO (with both the O- and N- end down), H₂O, and O₂ on Fe(II)-(OH)-BEA and Fe(III)-(OH)₂-BEA sites.

	Fe-H ₂ O	Fe-NH ₃	Fe-O ₂	Fe-NO	Fe-ON	Fe-N ₂
Fe(II)-Fe	-0.49	-5.60	-3.27	-4.28	-4.13	0.065
Fe(III)-Fe	-0.70	-0.94	-0.86	0.14	0.14	-0.22

The adsorption of NH₃ on Fe⁺²-Fe/BEA, yielding NH₃-Fe⁺², is noted to be very favourable (exothermic) with a binding energy of -5.60 eV, suggesting that NH₃ adsorption on Fe⁺²-Fe_F/BEA site is comparable to the NH₃ binding to the Cu⁺¹-Fe_F/BEA system. Similarly, the binding of NH₃ to the Fe³⁺ site yielding NH₃-Fe⁺³-Fe_F/BEA is also exothermic with a binding energy of -0.94 eV suggesting that NH₃ can bind to both Fe⁺²-Fe_F/BEA and Fe⁺³-Fe_F/BEA sites. The bond distance between (N) of NH₃ and Fe⁺²-Fe_F/BEA is 2.157 Å and with the Fe⁺³-Fe_F/BEA, 2.120 Å. Similarly, we note that H₂O can interact with both Fe⁺²-Fe_F/BEA and Fe⁺³-Fe_F/BEA sites with a binding energy of -0.49 eV (-47.2 kJ/mol) and -0.70 eV (-67.5 kJ/mol) respectively. NO is calculated to be strongly adsorbed on Fe²⁺-Fe_F/BEA through both N atom and O atoms, with a binding energy of -4.28 eV and -4.13 eV respectively. While on Fe³⁺-Fe_F/BEA, NO does not interact with either mode. Importantly, we found that O₂ strongly binds to the Fe²⁺-Fe_F/BEA sites (-3.2 eV) while with Fe³⁺-Fe_F/BEA is weak (-0.87 eV), suggesting that O₂ plays a key role in the reoxidation of the Fe²⁺-Fe_F/BEA site.

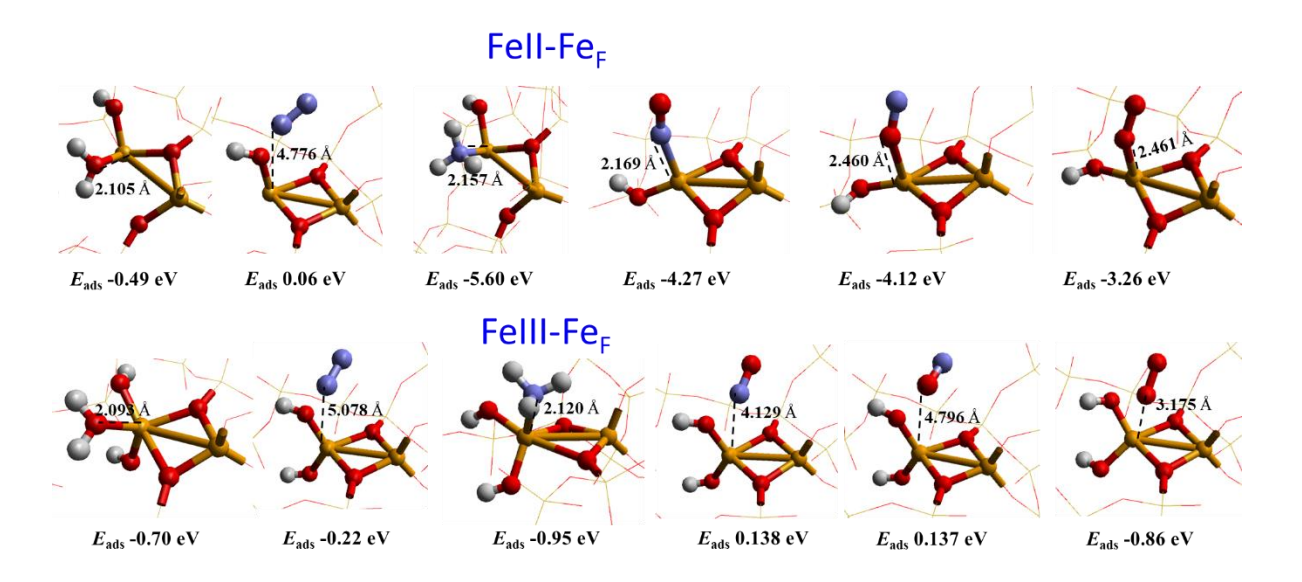


Figure 5.6. The adsorption energies of NH₃, NO, and H₂O on Fe(II)-Fe_F/BEA and Fe(III)-Fe_F/BEA sites. The model used is shown as an extra framework. Note, Fe_F act as a framework cation and Fe as an extra framework. **Atom colour codes:** Cu (brown), Al (green), O (red), N (blue), and H (white). The framework SiO₂ is shown using a wire framework motif.

5.3.3 NH₃ Binding Study

The starting point for the NH₃-SCR reaction is almost certainly, the adsorption of NH₃ on the active sites of the catalyst as shown in Figure 5.7. To understand the binding nature of NH₃, we performed hybrid QM/MM DFT calculations and studied the interaction of NH₃ on different active sites including the Brønsted acid in BEA zeolite. The study was first performed on the extra framework active sites such as Cu(II)-Fe_F/BEA, Fe(III)-Al_F/BEA and Fe(III)-Fe_F/BEA as reported above. Although the interaction of NH₃ with all these sites is favourable, it is much stronger with framework Fe sites. Based on the calculated adsorption energies (Eqn 5.2), we found that the binding of NH₃ with the Cu(II)-Fe_F/BEA sites (-1.33 eV) is stronger than with the Fe(III)-Al_F/BEA (-0.86 eV) and Fe(III)-Fe_F/BEA (-0.95 eV) active sites.

We further study the binding of NH₃ with the Brønsted acid site in the presence of Fe as a framework cation that generates NH₄⁺ ions (Figure 5.7). Using Eqn 5.3, the formation energy of NH₄⁺ ions is computed ³⁰⁶⁻³⁰⁸. The computed binding energy of -1.76 eV (-170 kJ/mol) for NH₃ over the framework Fe-Bronsted acid site is notably lower than the binding energy of NH₃ on the above-mentioned three Lewis acid sites, and it has been reported that the experimental heat of adsorption for NH₃ on BEA zeolite in the presence of framework Al (at 373 K) are -128 kJ/mol for Brønsted acid sites and -160 kJ/mol for Lewis acid sites ³⁰⁹ which is also smaller than the framework Fe-Bronsted acid site (-170 kJ/mol).

$$S + NH_3(g) \rightarrow NH_3 - S. \tag{5.2}$$

$$Z - OH + NH_3(g) \rightarrow Z - O^- + NH_4^+$$
. (5.3)

where Z-OH denotes the Brønsted acid, and S the Lewis acid sites.

Considering the relatively larger computed value for the Fe BEA Brønsted acid site -1.76 eV (-170 kJ/mol) as compared to the experimental Al Brønsted acid site (-128 kJ/mol)³⁰⁹ suggesting the acidic strength of Fe Brønsted acid site which can be attributed to the highly acidic nature of Fe as compared to Al. Furthermore, we also compare the formation energies of NH₄⁺ ions over the framework Fe-BEA with the aluminosilicate CHA (Al-CHA) system. The computed formation energy of -1.1 eV (-106 kJ/mol) for NH₄⁺ ions over Al-CHA is smaller than that for the framework Fe-Bronsted acid site. In another study, the heat of adsorption for NH₃ over non-exchanged zeolites H-CHA has been reported to be as high as -1.5 eV (145 kJ/mol), obtained using microcalorimetry techniques ²⁷⁰.

Moreover, the interaction of NH₃ with the Lewis site of Fe-BEA and Cu-CHA has similar binding energies; we found the binding energy of NH₃ on the Lewis site of Cu(II)-CHA is -0.967 eV while on Cu(I) is -0.840 eV. For Fe-BEA, the binding of NH₃ with the Cu(II)-Fe_F/BEA (-1.33 eV), Fe(III)-Al_F/BEA (-0.86 eV) and Fe(III)-Fe_F/BEA (-0.95 eV) are almost of the same as with the Lewis site of Cu-CHA.

For an MFI zeolite, earlier density functional theory calculations estimated an NH₃ adsorption enthalpy of -112 kJ/mol ³¹⁰. The relatively higher computed value for the NH₃ interaction with framework Fe BEA Brønsted acid site (-170 kJ/mol) as compared to the experimental framework Al Brønsted acid site (-128 kJ/mol) ³⁰⁹ suggests that the strength of Fe Brønsted acid site can be attributed to the highly acidic nature of Fe as compare to the Al.

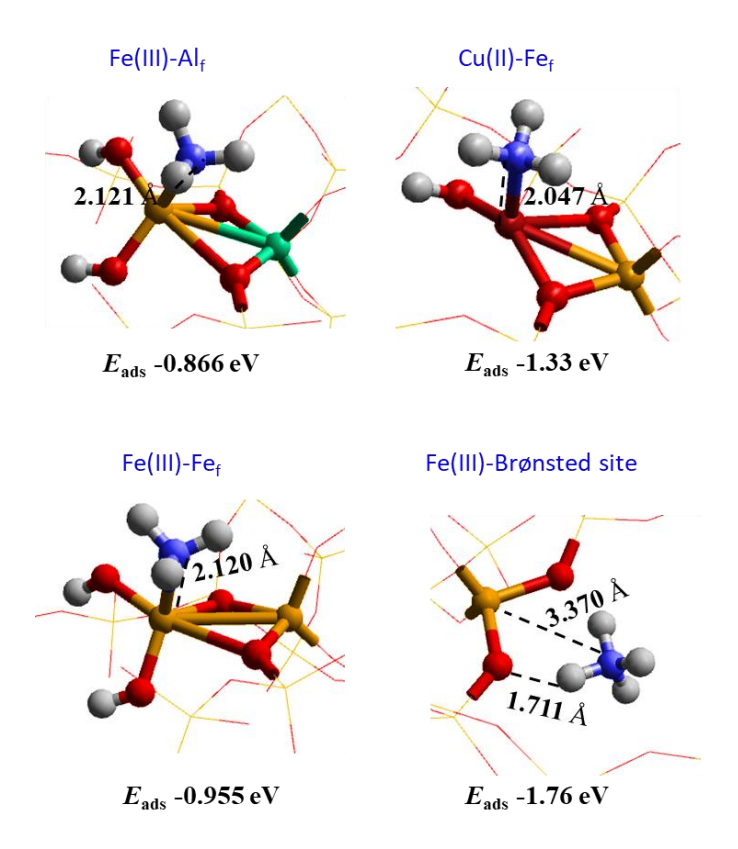


Figure 5.7. The reaction adsorption energies of NH₃ on different active sites in BEA zeolite including the Brønsted acid site.

5.3.4 Catalytic Cycle

Even though Fe sites in NH₃-SCR on Fe-based zeolites have been extensively studied, there is still some debate regarding the reaction pathway. At low temperatures, the NH₃-SCR reaction typically follows the Langmuir-Hinshelwood mechanism, in which NH₃ and NO randomly bind to the active site and produce significant intermediate species that subsequently break down to produce H₂O and N₂. Here, we studied the energetics of various Fe-based active sites including Fe-Fe_F-BEA, Fe-Al_F-BEA, and Cu-Fe_F-BEA. By switching between the NH₃ + NO and NO + O₂ atmospheres to analyse the different half-cycles, we can split the NH₃-SCR redox cycle and isolate the oxidation from the reduction step (Figure 5.8) ¹²⁰. Under NH₃ + NO reductive conditions, the Fe(III)-BEA can be reduced to Fe(II)-BEA. The Fe(II)-BEA can then be re-oxidised as a result of the NO + O₂ oxidation process. To this aim, we have investigated each half of the catalytic cycle on the three active sites of BEA zeolite.

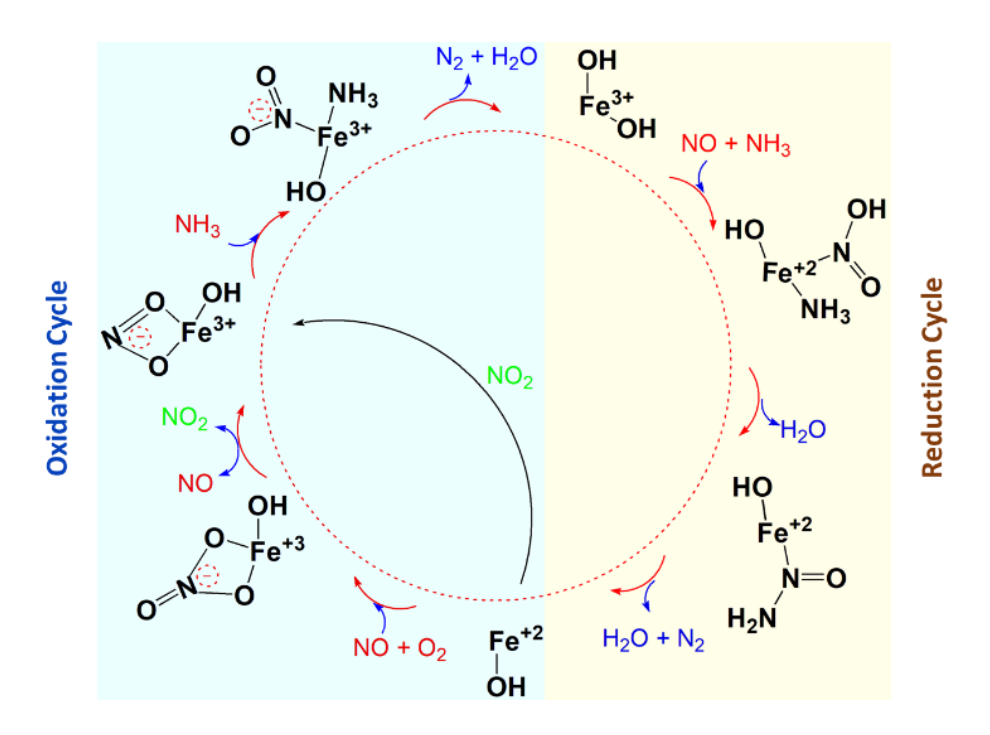


Figure 5.8. The mechanistic representation of NH₃-SCR cycle on Fe-BEA catalyst; yellow represents the reduction cycle and blue - the oxidation cycle.

*Reduction of Fe(III) by NO and NH*₃

We employ hybrid QM/MM calculations as described in section 5.2 to explore the reduction of the extraframework cationic species [Fe(III) and Cu(II)] in the BEA zeolite. First, we study the reduction of Fe(III) in the Fe-Al_F-BEA system. We started from the [Fe³⁺⁽OH)₂]⁺ species which is proposed to be the most stable species below 600 °C, according to calculations made by the Schneider group of the phase diagram of mononuclear Fe species at isolated Al in CHA zeolites ³¹¹. As a result, the [Fe³⁺⁽OH)₂]⁺ species was considered as the starting structure of the active Fe species for the Fe-Al_F-BEA system. Three spin multiplicities for Fe (III) (singlet, triplet, and quintet) were initially investigated to identify the system's most favoured spin state, with the quintet showing the lowest energy among them. Figure 5.9 displays the reaction coordinates as well as the energy profile of the quintet state. To generate HONO species over Fe-Al_F-BEA, NO molecules were adsorbed on [Fe³⁺⁽OH)₂]⁺ species attached to its OH group with a formation energy of 0.013 eV (1.25 kJ/mol), and in the case of the Cu-Fe_F-BEA system,

with a formation energy of 0.07 eV (6.7 kJ/mol) for the HONO species; while for the Fe-Fe_F-BEA system, it is 0.14 eV (13.4 kJ/mol).

Following equation (5.4), we investigate the formation of the nitrosamine (NH₂NO) intermediate which represents the reduction part of the cycle, and therefore, its formation and dissociation can indicate the reactivity of the active sites in this half part of the cycle. The introduction of NO in the presence of NH₃ under SCR reaction conditions results in the reduction of metal sites as evident from experiment ³¹². To this end, we computed the formation energy of the nitrosamine intermediate which is the most likely outcome of this reduction process. Fe³⁺-OH/BEA reacts with both NO and NH₃ and reduces Fe³⁺ to Fe²⁺ while generating N₂ and H₂O as a product leading to the formation of nitrosamine species which is evident from both experimental and theoretical studies ²⁷¹. We, therefore, studied this process on three separate active sites as reported above (Figure 5.9). As shown in the energy landscape the formation energy of nitrosamine species on Cu(II)-Fe_F/BEA (-1.94 eV) sites is more negative than the Fe-Al_F-BEA (-1.15 eV) and Fe-Fe_F-BEA (-1.58 eV). Taking into consideration the formation of nitrosamine species, we infer that the effect of framework Fe sites (Cu(II)-Fe_F/BEA, Fe-Fe_F-BEA) has had an overall more positive impact than the framework Al site (Fe-Al_F-BEA).

$$M + NO + NH_3 \rightarrow M - NH_2NO + H_2O.$$
 (5.4)

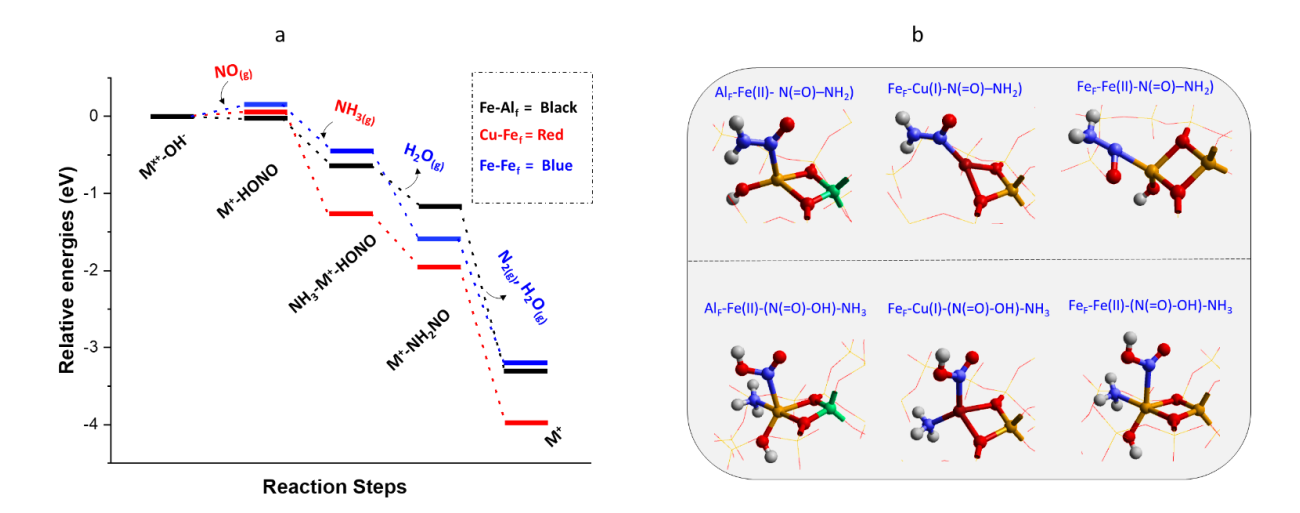


Figure 5.9. (a) The reduction half cycle of the NH₃-SCR cycle and its corresponding landscape energy representation on three active sites - [Fe(III)-Al_F-BEA, Cu(II)-Fe_F-BEA, and Fe(III)-Fe_F-BEA]. Where M in the above diagram represents the metal site. **Atom colour codes:** Fe (yellow), Cu (brown), Al (green), O (red), N (blue), and H (white). The framework SiO₂ is shown using a wire framework motif.

Oxidation of Fe(II) by O_2 and NO

The adsorption of NO and O₂ on Fe⁺²-/BEA can generate nitrate and nitrite species which undergo decomposition to N₂ and H₂O; this half cycle of the NH₃-SCR is, as noted, is known as the oxidation part. According to reports, the reoxidation rate at low temperatures limits standard SCR rates ^{293, 299}. Therefore, it is essential to model this reoxidation phase to understand standard SCR at low temperatures. To understand this whole process, first, we study the activation of O₂ over Fe(II)-Al_F-BEA to generate O₂-Fe(II)-Al_F-BEA species. O₂ molecules tend to bind to Fe(II)-Al_F-BEA species through the Fe(II) site owing to the electrostatic interaction with a binding energy of -1.26 eV (-121.6 kJ/mol). While on the Fe-Fe_F-BEA system, we found the binding energy of O₂ with the Fe(II) is -1.04 eV (-100.3 kJ/mol). We also studied the Cu-Fe_F-BEA system and compared it with the Fe(II) site. On the Cu-Fe_F-BEA site, we computed a binding energy of -0.43 eV (-41.5 kJ/mol) for O₂ with the Cu(I) site. On all three sites, the process of O₂ binding is exothermic with the most favourable sites being those with the extraframework Fe site (Fe(II)-Fe_F/BEA, Fe-Al_F-BEA).

Next, we modelled the formation of the nitrate species which is formed by the interaction of NO with the activated O₂-Fe(II)-Al_F-BEA species. We, therefore, computed the formation energy of nitrate (M-NO₃) intermediate which is considered to be the important intermediate of the re-oxidation phase of the SCR reaction. The process is investigated on the three separate active sites (Figure 5.10). As demonstrated in the energy landscape, the formation energy of nitrate species on Cu(II)-Fe_F/BEA (-1.94 eV) sites is more negative than the Fe-Al_F-BEA (-1.15 eV) and Fe-Fe_F-BEA (-1.58 eV). Taking into consideration the formation of nitrate species, we deduce that the effect of the framework Fe-Fe_F system (Fe-Fe_F-BEA) has had an overall more positive impact than the framework Fe-Al_F-BEA and Cu(II)-Fe_F/BEA. The mechanisms and rates associated with the reoxidation of metal sites [e.g. Fe(II) and Cu(I) are still under investigation. In addition, it is unclear how Brønsted acid sites and H₂O affect the re-oxidation half cycle of the NH₃-SCR. In chapter 4, we have reported ²¹⁰ that the formation of nitrate species is energetically more favourable on the solvated (NH₃, H₂O) Cu sites than in the absence of solvent molecules, demonstrating the positive influence of solvent on the oxidation component of the NH₃-SCR cycle. On the other hand, we found that both solvent molecules (ammonia and water) inhibit the reduction phase of the NH3-SCR cycle. Furthermore, there is a report that demonstrates the O₂ activation over Cu(I)-CHA sites and the formation of the ZCu(I)O2 complex as a result of ZCu(I) exposure to O2 at low temperatures which is in accord with the experimental reports ²⁹⁹. Electron paramagnetic resonance (EPR) and in situ FTIR spectroscopy analyses313,314 show that the reoxidation of Cu(I) sites in the presence of NO and O2 under dry conditions results in the formation of Cu-nitrate species $(ZCuNO_3)$.

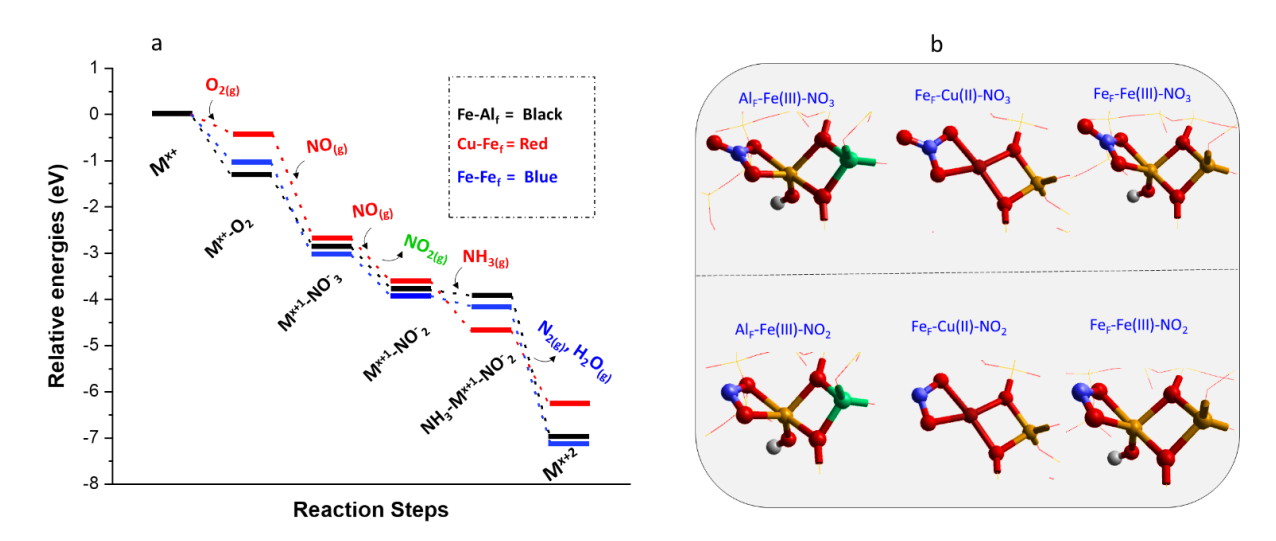


Figure 5.10. Formation of nitrate; (a) the corresponding landscape energy description and (b) the schematic representation of nitrate species formation on three active sites [Fe(III)-Al_F-BEA, Cu(II)-Fe_F-BEA, and Fe(III)-Fe_F-BEA]. **Atom colour codes**: Cu (brown), Al (green), O (red), N (blue), and H (white). The framework SiO₂ is shown using a wire framework motif.

5.3.5 Reaction Pathway

To study the whole reaction pathway, we performed hybrid QM/MM calculations on all possible intermediate species. Taking into consideration the nature of active sites, the starting point of the reaction scheme is considered to be either Fe(II) or Cu(I) sites that activate the O₂ molecule and serve as the initial step for the reaction.

Fe-Al-BEA

First, we examined the reaction pathway over the Fe-Al_F-BEA system (Figure 5.11). The calculated O₂ adsorption energies over the Fe(II)-BEA site is exothermic (-1.26 eV), which can be enough to oxidize Fe(II) to Fe(III), which is followed by NO adsorption, produces Fe(III)-NO₃- species with a formation energy of -1.28 eV (Step II). The reaction of gaseous NO with nitrate ²⁸¹ is reported to be a two-step process where first NO coordinates with the nitrate species and then decomposes to nitrite with the release of gaseous NO₂. We, therefore, found a total energy change of 0.08 eV from the nitrate to nitrite step. Next, we considered the reaction

of NH₃ with nitrite species that form an intermediate (Step IV) with a formation energy of -0.15 eV. We also found that NH₃ can also react with the Fe-(HO)₂NO site that generates NH₃-Fe-(HO)₂NO intermediate (step VII) with an H₃N-Fe bond length of 2.160 Å and formation energy of -0.42 eV. Subsequently, it decomposes and leads to the generation of an important intermediate the Fe-nitrosamine (Fe-(HO)-N(=O)-NH₂) (step VIII) with a formation energy of -0.74 eV which is considered to play a key role in the NH₃-SCR reaction

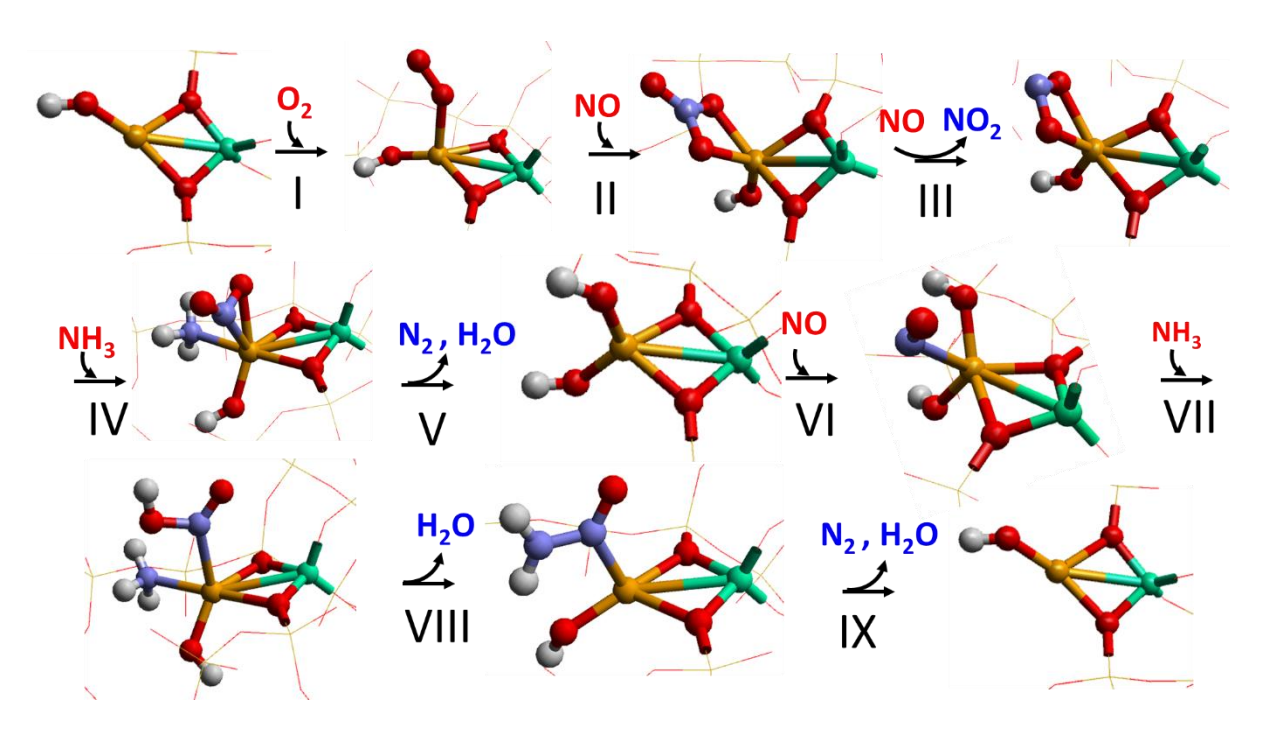


Figure 5.11. The structures of each corresponding intermediate species reside on bare Cu-CHA. The model used is shown as an extra framework. **Atom colour codes**: Cu (brown), Al (green), O (red), N (blue), and H (white). The framework SiO₂ is shown using a wire framework motif.

Cu-Fe-BEA

Next, we assessed the reaction pathway over the Cu-Fe_F-BEA system (Figure 5.12). The calculated O₂ adsorption energies for the Cu(I)-BEA site is highly exothermic (-2.2 eV), which potentially oxidized Cu(I) to Cu(II). Also, an energy of -0.25 eV for the Cu(II)-NO₃- species is computed (Step II). We calculated a total energy change of 0.04 eV from the nitrate to nitrite step. In the case of the NH₃ reaction with nitrite species, an intermediate (Step IV) is formed

with a formation energy of -1.06 eV. Furthermore, we found that NH₃ can also react with the Cu-(HO)NO site that generates NH₃-Cu-(HO)NO intermediate (step VII) with an H₃N-Cu bond length of 2.160 Å and formation energy of -2.3 eV. Subsequently, it decomposes and leads to the generation of an important intermediate the Fe-nitrosamine (Cu-N(=O)-NH₂) (step VIII) which is considered to play a key part in the NH₃-SCR reaction.

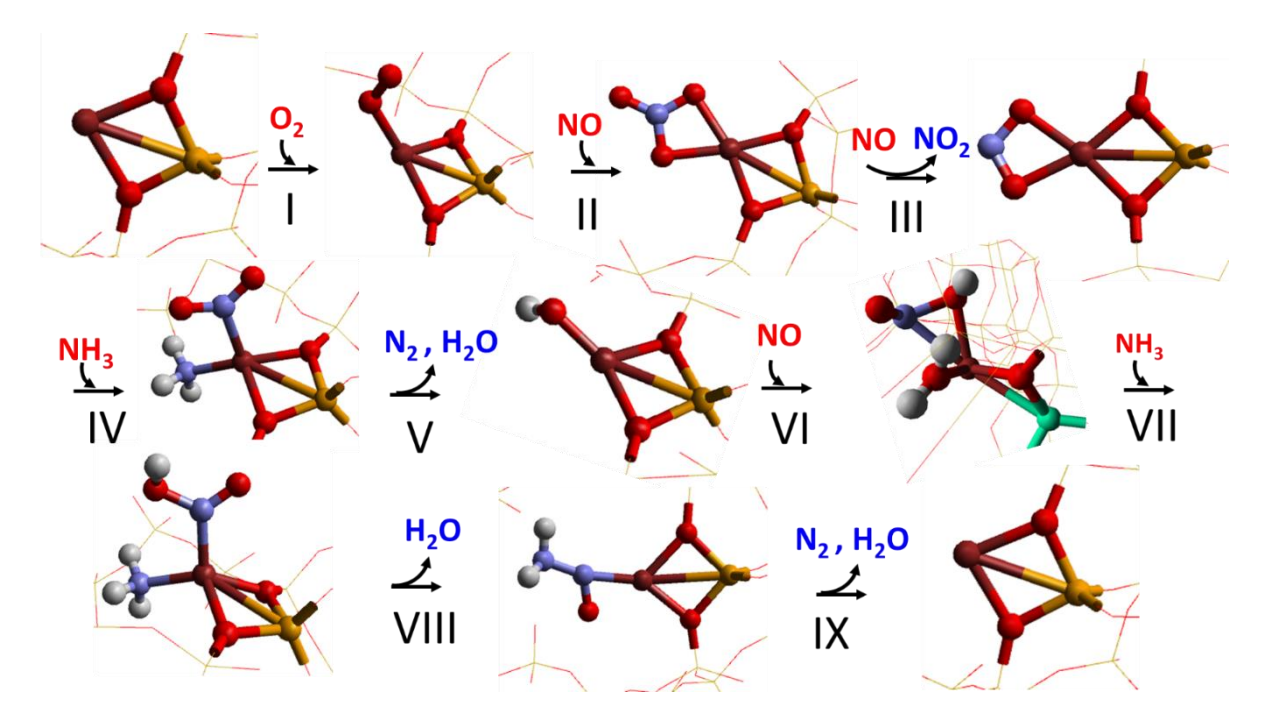


Figure 5.12. The structures of each corresponding intermediate species reside on bare Cu-CHA. The model used is shown as an extra framework. **Atom colour codes**: Cu (brown), Al (green), O (red), N (blue), and H (white). The framework SiO₂ is shown using a wire framework motif.

Fe-Fe-BEA

Finally, we investigated the formation and consumption of the reaction intermediates over the Fe-Fe_F-BEA system (Figure 5.13). Starting from the O₂ binding; the process is found to be highly exothermic (-3.26 eV) that oxidized Fe(II) to Fe(III). Next, NO interacts with O₂-Fe(II)-BEA species that generates important nitrate species Fe(III)-NO₃ (formation energy of -1.23 eV) (Step II), which is followed by the reaction of NO with the nitrate species that decompose it to nitrite with the release of gaseous NO₂. The total energy change from the nitrate to nitrite step is 0.083 eV. In the case of the NH₃ reaction with nitrite species, an intermediate (Step IV)

is formed with a formation energy of -0.28 eV. Furthermore, we found that NH₃ can also react with the Fe-(HO)₂NO site that generates an NH₃-Fe-(HO)₂NO intermediate (step VII) with an H₃N-Fe bond length of 2.160 Å and formation energy of -0.57 eV. Afterwards, it decomposes and leads to the formation of an important intermediate: the Fe-nitrosamine (Fe-(HO)-N(=O)-NH₂) (step VIII) with a formation energy of -1.15 eV.

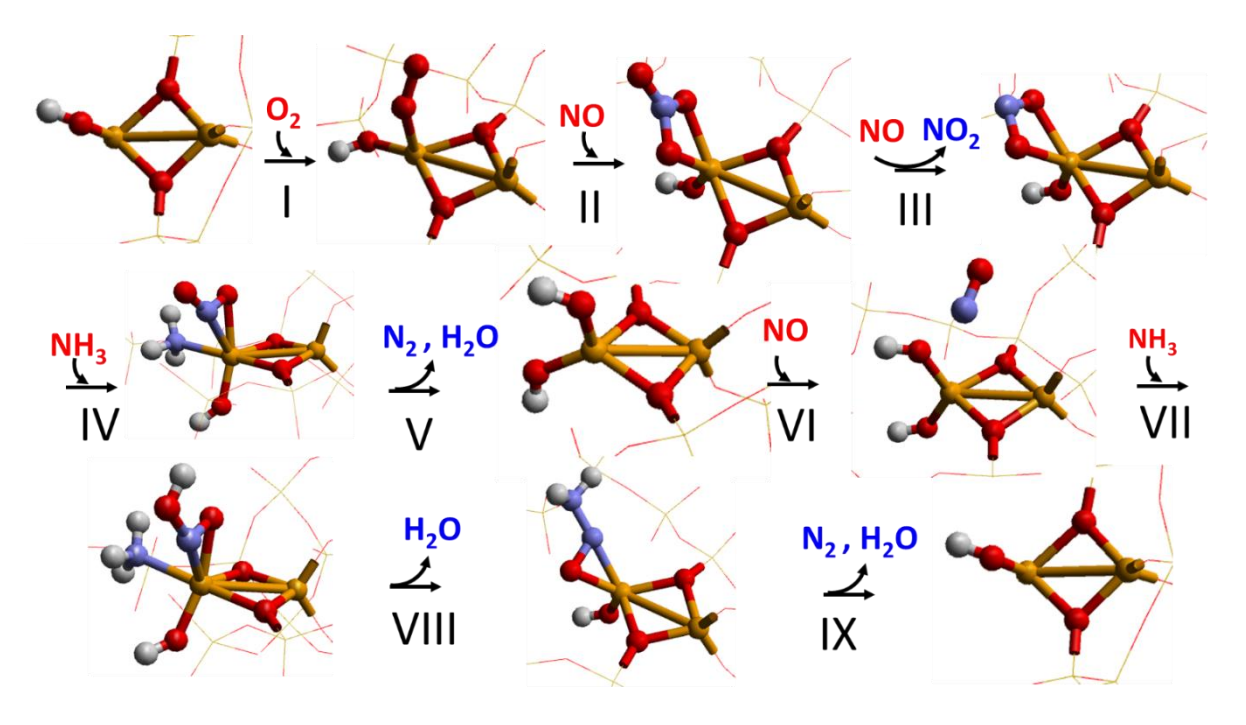


Figure 5.13. The structures of each corresponding intermediate species reside on bare Cu-CHA. The model used is shown as an extra framework. **Atom colour codes**: Cu (brown), Al (green), O (red), N (blue), and H (white). The framework SiO₂ is shown using a wire framework motif.

5.4 Summary and Conclusion

We have investigated the NH₃-SCR of NOx reaction employing a hybrid QM/MM embedded technique over Fe-BEA catalyst. The study examined the reactivity of various Fe-based BEA active sites including the framework Fe cation and investigated the adsorption of reactant species and the formation of key intermediates. The main catalytically active sites include Fe-Fe_F-BEA, Fe-Al-BEA, and Cu-Fe_F-BEA on which we study the formation and consumption of key intermediates including nitrosamine and nitrate species. First, we have studied the

reduction potential for intraframework Fe³⁺/Fe²⁺ in the BEA zeolite and found that the process is feasible in the presence of a Brønsted acid site. In addition, the interaction of NH₃ with different active sites including the Brønsted acid of BEA zeolite was investigated. The relatively large computed value for the NH₃ interaction with framework Fe BEA Brønsted acid site (-170 kJ/mol) as compared to the experimental framework Al Brønsted acid site (-128 kJ/mol) ³⁰⁹ suggests that the strength of Fe Brønsted acid site can be attributed to the highly acidic nature of Fe as compare to the Al. Next, the interaction of reactants and product molecules with all active sites was carefully examined. Our results suggested the formation of nitrosamine and nitrate species. For the formation of nitrosamine, we found that the effect of framework Fe sites (Cu(II)-Fe_F/BEA, Fe-Fe_F-BEA) has an overall more positive impact than the framework Al site (Fe-Al_F-BEA); while in the case of nitrate, we deduce that the effect of the Fe-Fe_F system (Fe-Fe_F-BEA) on the formation of nitrate has an overall positive influence than the Fe-Al_F-BEA and Cu(II)-Fe_F/BEA. Overall our study on Fe-BEA zeolite contributes to the comprehension of the impact of framework Fe cation in the BEA zeolite and offers insights for improving the efficiency of the existing Fe-based zeolitic system in the NH₃-SCR reaction.

Chapter 6

Binuclear-Cu(II) Dimer Species in NH₃-SCR

6.1 Introduction

As is clear from the earlier chapters in this thesis, the identification of TMI speciation such as monomer, dimer, and oligomers and their redox mediation behaviour is necessary to understand de-NOx catalysis A particularly interesting case was the discovery of two distinct reactive species of Cu core mono(μ-oxo)-dicopper in ZSM-5, which has been used as a de-NOx catalyst. One of the reasons for the formation of dimer species is the solvent mobilization which surrounds the active sites (Cu ions). The dimer can form *in situ* the multinuclear complexes for activation of O₂ and therefore, can act as an active site. Thus, Borfecchia *et al.* investigated the tri-coordinated [CuOH]⁺ as a site for O₂-activation while the bare bicoordinated Cu⁺ ions were found to be the dominant species in the 8-MR of Cu-SSZ-13 ¹⁵⁹. Furthermore, the mobility of active sites may be regulated by the composition, structure, and electronic behaviour of the support which solvated these particular sites. Tuning these parameters may open new horizons in the designing of TMI-exchanged zeolite catalysts for NH₃-SCR reaction.

Cu-zeolite chemistry is well-known for its oxygen-bridged Cu dimers chemistry ^{315, 316}, which operates under low temperatures ^{317, 318}. The dimers can use different oxygen-bridging arrangements ³¹⁹. It is necessary to revise the previous mechanisms (see Chapter 3, Figure 3.4) to include the dynamic coupling of isolated Cu species in the presence of O₂ molecules, as shown in the illustration (Figure 6.1). Some studies suggest that at high temperatures, the Cu-solvated complex decomposes, and the Cu ion loses an NH₃ ligand as well as its mobility.

Subsequently, Cu ions become attached to the wall of zeolite and hence lose their ability to form dimers dynamically and activate oxygen ¹³⁹. The Cu²⁺ ions in SSZ-13 are mainly located in the 6-MR but the Cu-Cu interaction is not observed over the structure at all which otherwise could open a window for the generation of Cu cluster or dimer formation ³²⁰⁻³²². However, the large window of CHA is sufficient for the diffusion of gases and still allows Cu species to interact with the other species within cage ¹¹⁹. Some studies reported that Cu species are of two types in CHA zeolites, and the existence of such species within the cage depends on the Cu loading; the Cu²⁺/Cu⁺ are dominant at lower loading whereas CuO occupies the CHA framework at higher loading ⁹¹. Apart from Cu binuclear dimer species, the NH₃-SCR reaction can also occur on dimeric Fe with different energetics and hence leading to different turnover frequencies as shown from experiment ³⁵. Liu *et al.* reviewed different active sites of Fe including monomeric, dimeric, and oligomeric species ³⁶. They investigated Fe complexes in ZSM-5 and concluded that the distribution of mononuclear sites of Fe species (FeO)⁺ can occur in several local environments while binuclear sites preferentially reside in the 8-MR.

To understand the Cu dimer species formation in CHA zeolite, we have investigated the oxidation half cycle (left) of the NH₃-SCR reaction. For this purpose, density functional theory (DFT) using a quantum mechanical/molecular mechanical (QM/MM) methodology is again employed.

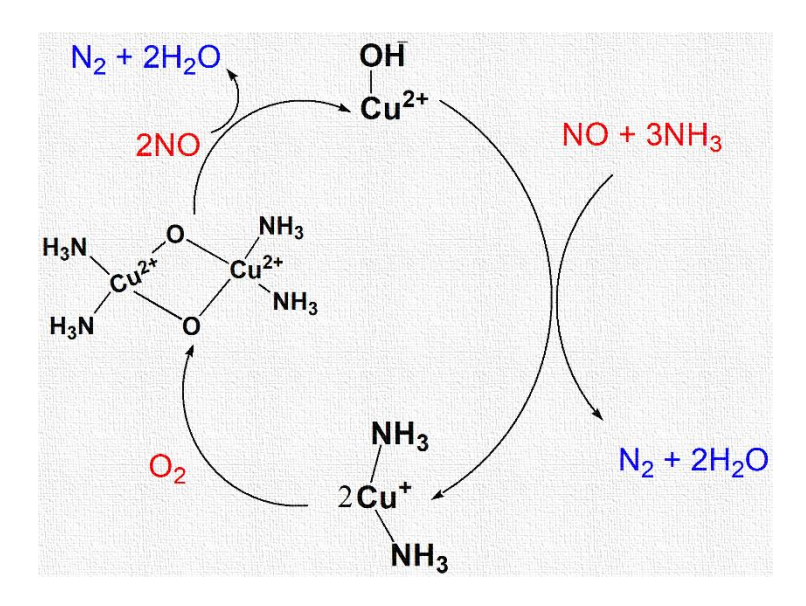


Figure 6.1. Schematic representation of low-temperature NH₃-SCR of NO_x over binuclear Cu(II) sites.

6.2 Computational Approach

6.2.1 QM/MM Methodologies

A hybrid QM/MM model^{251, 252} using the ChemShell software^{214, 216, 217} discussed in Chapter 2, was employed to study the formation of Cu dimer species in Cu-CHA. We set an active region, where all constituent atoms are allowed to relax freely, extending to a radius of 15 Å (~28.3 Bohr) from the chosen centre containing the Al site as described in detail in Chapter 2. For this study, the QM cluster is created to have a complete CHA cage that can accommodate big molecules such as Cu(II) dimer species. Unlike our previous methodology that used ~150 QM atoms (see chapters 3 and 4), here we construct a bigger QM region (~ 250 atoms, not including the link atoms). To perform the QM/MM calculation, we first created a spherical embedded-cluster model of CHA from the unit cell of siliceous CHA ²³⁶ optimized at the MM level using the GULP package ²³¹. After creating a CHA-cluster model, we constructed active sites and incorporated two Al into the cage avoiding any Al-Al first-nearest neighbours (in accordance with Loewenstein's rule)³²³. In order to create the structures shown in Figure 6.2, a cluster with 50 T-sites was utilized, which included two Al atoms such that each Cu ion could

compensate for one Al atom. To investigate systematically, first, a single aluminum atom (Al1) was randomly substituted into a T-site of the cage. All was then kept in place while a second aluminum atom (Al2) was successively introduced into the cage almost on the opposite side to ensured all investigated structures lie exactly at the centre of the cage as illustrated below (Figure 6.2).

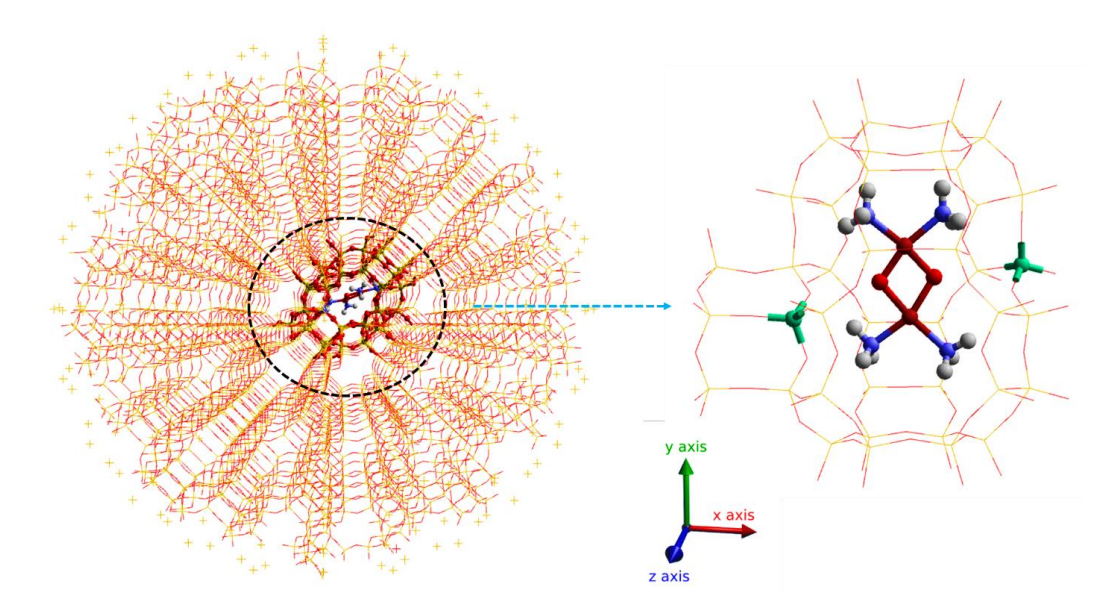


Figure 6.2. The QM/MM embedding setup; is the CHA cluster with a quantum mechanical region containing Cu-dimer species. The outermost region contains point charges to ensure the Madelung potential in the Centre of the cluster is accurately reproduced. Atom colour codes: Fe (yellow), Cu (brown), Al (green), Si (yellow), O (red), N (blue), and H (white).

6.3 Results and Discussions

Cu-CHA is widely recognized as the best catalyst for SCR of NOx in SCR reactions. However, the exact role of Z2Cu²⁺ (containing two Al atoms to compensate Cu²⁺) as an active site for SCR, in low-temperature reactions is still a topic of discussion. In addition, there is considerable debate, focusing on the location and the nature of cations as active sites in the zeolite. Izquierdo *et al.* ⁵² and Morpurgo *et al.* ⁵³ employed DFT-ONIOM and Cluster methods to investigate the isolated as well as the dimer species of Cu in Cu-ZSM-5 as case examples. These studies revealed that both species can catalyze NO decomposition but the process needs additional energy to overcome the energy barrier in the case of dimeric Cu^{+ 54}. To this aim, we

study the formation of binuclear Cu speciation in CHA cage for NH₃-SCR reaction at low temperatures.

6.3.1 Mobility and Restructuring of Cu-species

We first examined the mobility of Cu-bound framework species as it is reported that increased solvent coordination can detach Cu species. The isolated Cu species can form dimer species as is evident from many reports ^{250, 324}. As discussed in Chapter 4 (section 4.3.2.)⁵, using molecular dynamics, Paolucci *et al.*¹¹⁹ predicted the [Cu(NH₃)₂]⁺ mobility inside the CHA framework on the time scale (employing *ab initio* metadynamics) which is almost inaccessible by standard ab initio molecular dynamics. In line with their observation, we employed hybrid QM/MM simulation and found Cu mobility both in the presence of water and ammonia up to 8 Å and 6 Å, respectively (Figure 6.3) which is described in detail in the previous Chapter 4. Some previous reports suggest that the NH₃-solvated Cu(I) sites interact weakly with the zeolite framework, and move away as a mobile species to react with the O₂ and yield an O-bridged Cu(II) dimer ¹¹⁹. In addition, some reports suggested that Cu²⁺ ions in SSZ-13 are mainly located in the 6-MR; therefore, the Cu-Cu interaction does not occur ³²⁰⁻³²². However, the large window of CHA is sufficient for the diffusion of gases which can allow Cu species to interact with the other species within the cage which can lead to cluster or dimer formation ¹¹⁹.

⁵ 4.3.2. Cu displacement on solvation

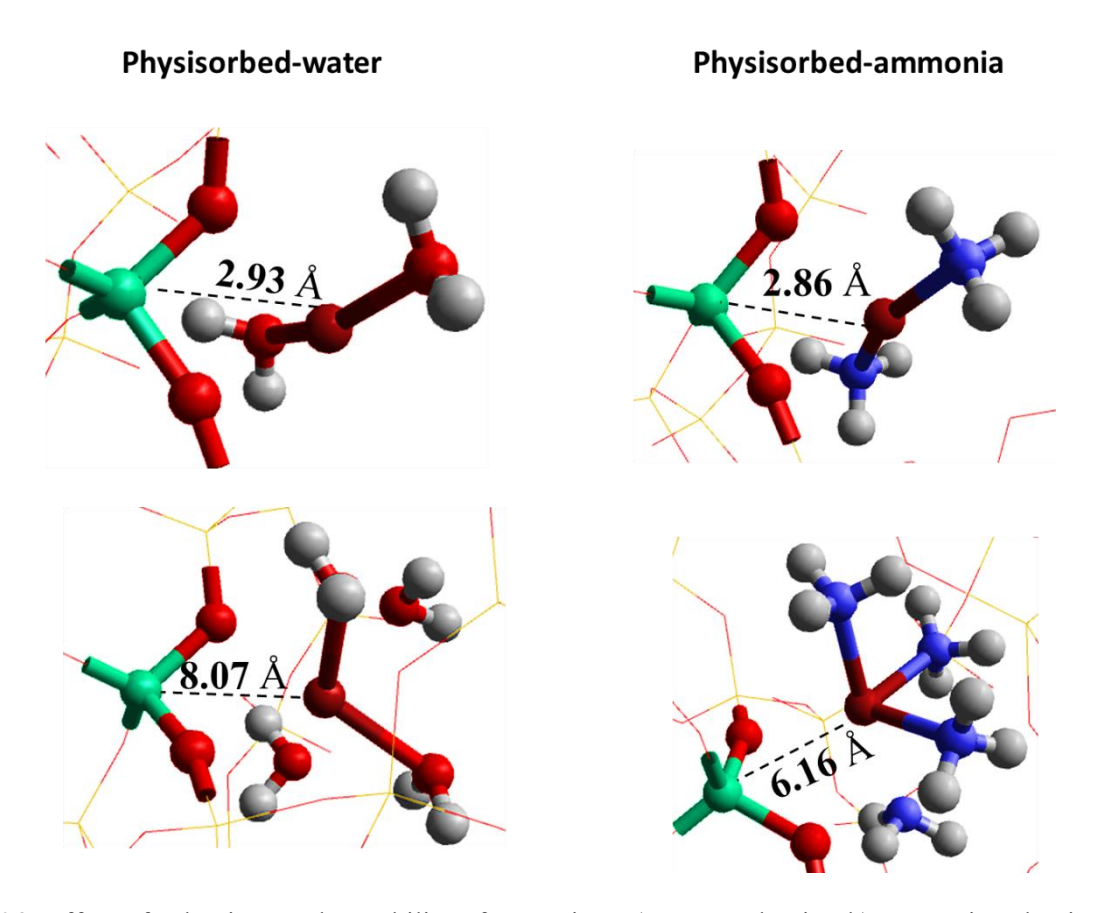


Figure 6.3. Effect of solvation on the mobility of Cu cations a) water solvation b) ammonia solvation as shown in chapter 4.6

6.3.2 Oxidation Half-cycle

Various reaction schemes show the formation of binuclear Cu(II)-dimer species from the reaction of O₂ with the Cu(I) site ^{12,325}, which is normally followed by NO to give nitrite species that further decompose into N₂ and H₂O. In this study, we have modelled a similar reaction that elucidates the reaction of NO with the dynamic binuclear Cu(II) species (Figure 6.4). The main focus is to understand the formation of binuclear Cu(II) species and the energetics of the oxidation-half cycle.

⁶ 4.3.2. Cu displacement on solvation

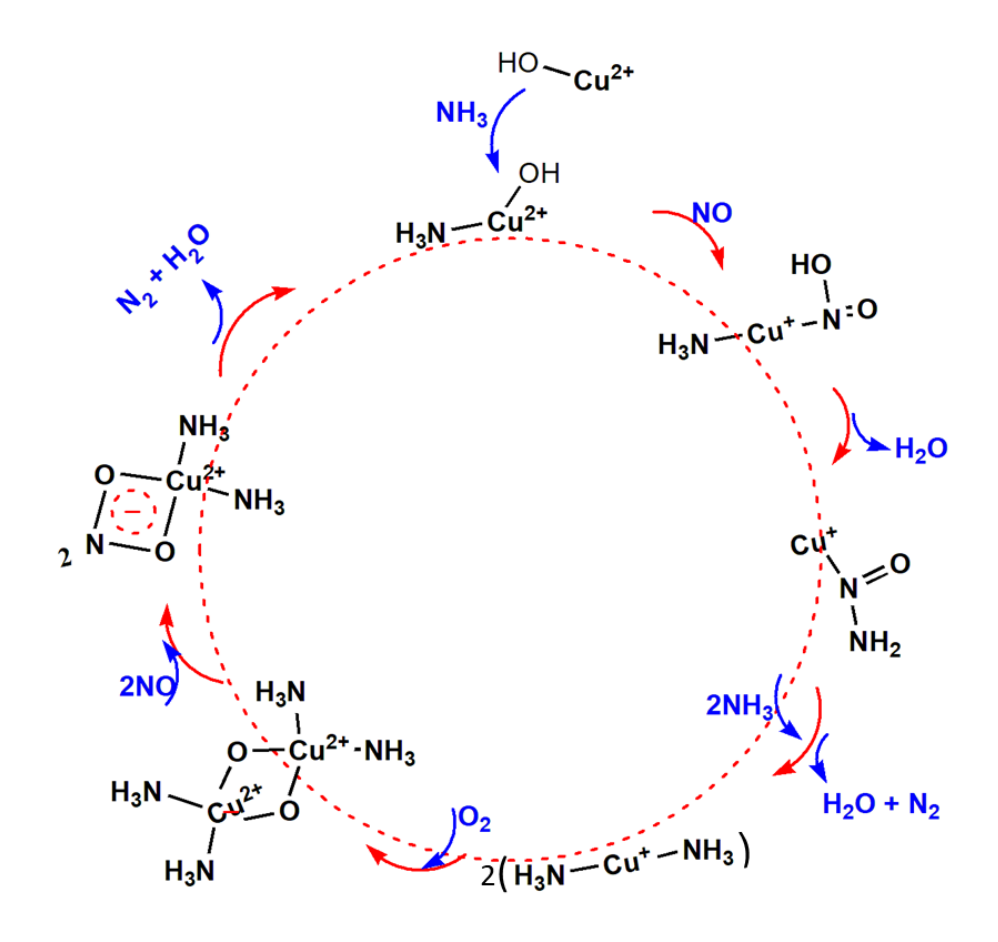


Figure 6.4. The proposed catalytic NH₃-SCR cycle contains dimeric Cu-species.

We employed our hybrid QM/MM technique to examine first, the viability of the interaction between two caged Cu(I)(NH₃)₂ centres (Figure 6.5). To this aim, two Cu(I)(NH₃)₂ ions sharing a CHA cage were initially taken into account to observe any possible interaction between them. As calculated by Paolucci *et al.*,²⁹⁹ the transition state energy for one Cu^I(NH₃)₂ to diffuse into the adjacent (that shares an Al T-site vertex Figure 6.5,) Cu^I(NH₃)₂-containing cage through an 8-MR window is 35 kJ mol⁻¹, which is an agreement with prior estimates of Cu(I)(NH₃)₂ diffusion barriers into an empty cage^{326, 327}. Contrary to their report, we did not see any pairing phenomenon between two isolated Cu(I)(NH₃)₂ ions. The isolated Cu(I)(NH₃)₂ ions in our study are not forced to move away from the Al site but displace spontaneously as a result of geometry optimization from their initial position close to the Al sites in response to the strong interaction of the polar solvent with both framework and extraframework metal cations.

According to Hu *et al.*, ³²⁸, the inter-cage transportation medium is made up of CuII(OH)(NH₃), which is structurally related to CuI(NH₃)₂⁺ and contains one charge and two ligands. It is anticipated that transport across adjacent Al-sharing cages will be simple at catalytically relevant temperatures.

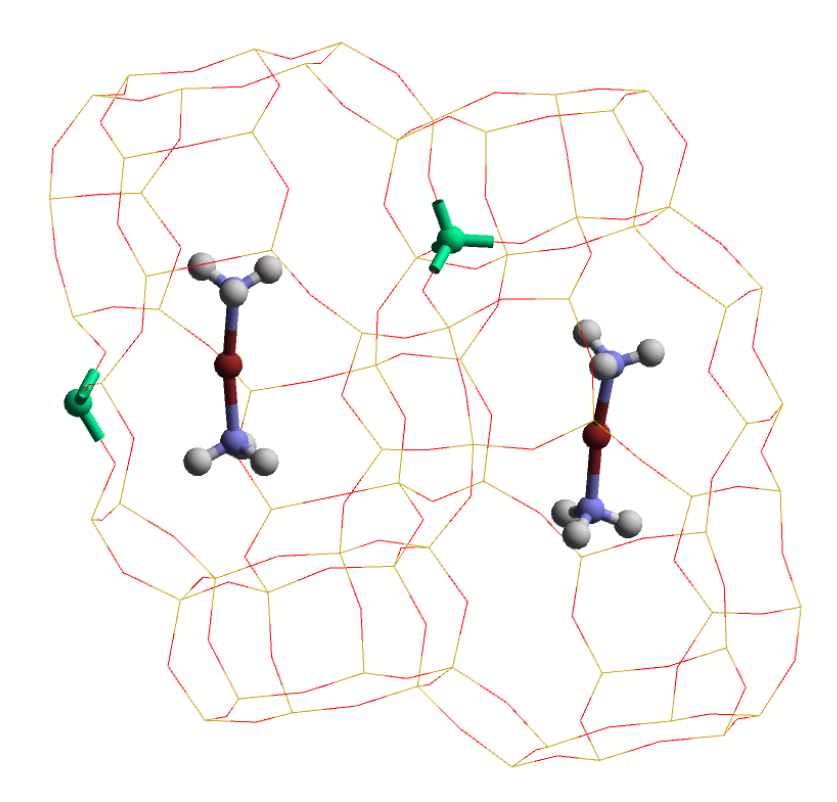


Figure 6.5. CHA cluster of QM region showing two Al compensating two CuI(NH₃)₂ species.

In the NH₃-SCR of NOx to N₂, the activation of O₂ is the key step for Cu-exchanged zeolites. Some previous studies suggested that O atoms of NO or N₂O presumably adsorb on the Cu sites and release N₂ while the activated O atoms desorb in the form of molecular oxygen ³²², ^{329, 330}. In contrast, there is a report²⁹⁹ that shows the molecular oxygen binds the pair of Cu^I(NH₃)₂ that help in the re-oxidation of Cu(I) to Cu(II) through a formation of Cu(II) dimer species as shown in the following Eqn. 6.1.

$$2[Cu^{I}(NH_{3})_{2}] + O_{2} \rightarrow [(NH_{3})_{2}Cu^{II} - O_{2} - Cu^{II}(NH_{3})_{2}]$$
(6.1)

Taking into consideration the formation of dimer species and investigating the reoxidation of Cu(I) to Cu(II) by O₂ as a sole oxidant and without NO assistance, we studied the above reaction (Eqn 6.1).

The dimers can use different oxygen-bridging arrangements ³¹⁹. The pseudo-bimolecular interaction involving two Cu(I)(NH₃)₂ ions with an interaction of O₂ during the transient experiment is suggested by the second-order Cu dependency (Figure 6.6) ²⁹⁹. We, therefore, first investigated the O₂ activation on a pair of [Cu(NH₃)₂]⁺ (structure I) as reported earlier for a similar system ²⁹⁹. Paolucci et al.,²⁹⁹ also reported that the pairing of two Cu(I)(NH₃)₂ ions through bridging O₂ is more effective compared to isolated Cu¹(NH₃)₂. The activation of O₂ and the corresponding dissociation proceeds via two sequential elementary steps. The dissociation of O_2 leads to dimeric $[Cu_2(NH_3)_4(O_2)]^{+2}$ species where each μ -O site binds to two Cu centres (Structure II). This dimer motif can form the *in situ* multinuclear complexes for activation of O2 and therefore, can be an active site. Borfecchia et al. investigated the tricoordinated [CuOH]⁺ as a site for O₂ activation while the bare bi-coordinated Cu⁺ ions were found to be the dominant species in the 8-MR ¹⁵⁹. The end-on spin-triplet species is probably produced by the initial reaction, whereas structure IV (di-oxo), is finally produced by further rearrangement and O2 dissociation across two Cu(I) centres. Structure III is afterwards converted into Structure IV with a low barrier. Some work suggests that the relocation of Cu(I) via the 8-MR is the rate-limiting mechanism for the whole cascade (I to IV). Subsequently, the reaction energies are calculated to be independent of the zeolite cage ²⁹⁹. Therefore, regulating Cu(I) mobility is the zeolite support's main function in this oxidation process.

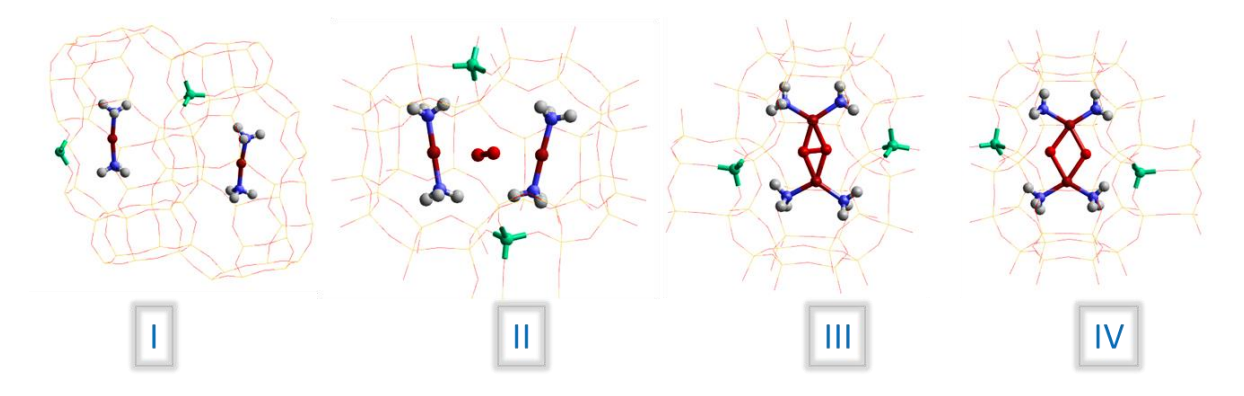


Figure 6.6. O₂ activation on pair of $[Cu(NH_3)_2]^+$ and the corresponding optimized structures.

The initial reaction results in the formation of the end-on spin-triplet species displayed in Figure 6.7 (structure II). Subsequent chemical changes and the separation of O₂ across two Cu(I) centres lead to the generation of structure IV, which consists of two copper centres with four-fold coordination. The conversion of structure II to structure III is not possible due to spin restrictions, with an estimated barrier of 20 kJ/mol for similar ligand environments ³¹⁷. Structure IV is coherent with the observed Cu(II) oxidation state in XANES and the extracted features from EXAFS, as described in the referenced literature ¹¹⁹. In the experimental findings, another distinct Cu(II) state of the catalyst is reported, separate from the Cu(II) bound to the framework observed after oxidative treatments, as well as the NH₃-solvated Cu(II) detected during low-temperature ^{195, 326}. When exposed the samples to NO and NH₃ at 473 K, following the transient O₂ oxidation experiments, reduces all sites back to the mononuclear Cu(I) state. This demonstrates that through sequential stoichiometric reactions, the SCR redox cycle can be closed. The presence of a small amount of dimeric Cu species at low Cu densities explains the change in the standard SCR turnover rate, transitioning from a quadratic dependence to a linear dependence on Cu ion density as Cu density increases. Both transient and, steady-state experiments along with DFT models, provide support for a Cu(I)→Cu(II) half-cycle that involves two CuI(NH₃)₂ complexes and one O₂ molecule, resulting in the formation of a previously unobserved binuclear CuII intermediate.

However, the probability that O₂ activation occurs on a constant small fraction of Cu ion pairs is ruled out by the referenced literature ³³¹. It is noted that the fraction of isolated Cu(I)(NH₃)₂ complexes that can be oxidized with O₂ is ten times greater than the fraction of Cu pairs within a single cage if Cu were randomly distributed on the zeolite support. Also, the steady-state and transient rates of Cu(I) oxidation with O₂ would demonstrate a first-order dependence on Cu density, as observed with NO₂ as the oxidant. Instead, these results suggest a pseudo-homogeneous reaction between equivalent isolated Cu(I) ions that have mobilities that are restricted in a way that limits the total fraction of sites that react with O₂.

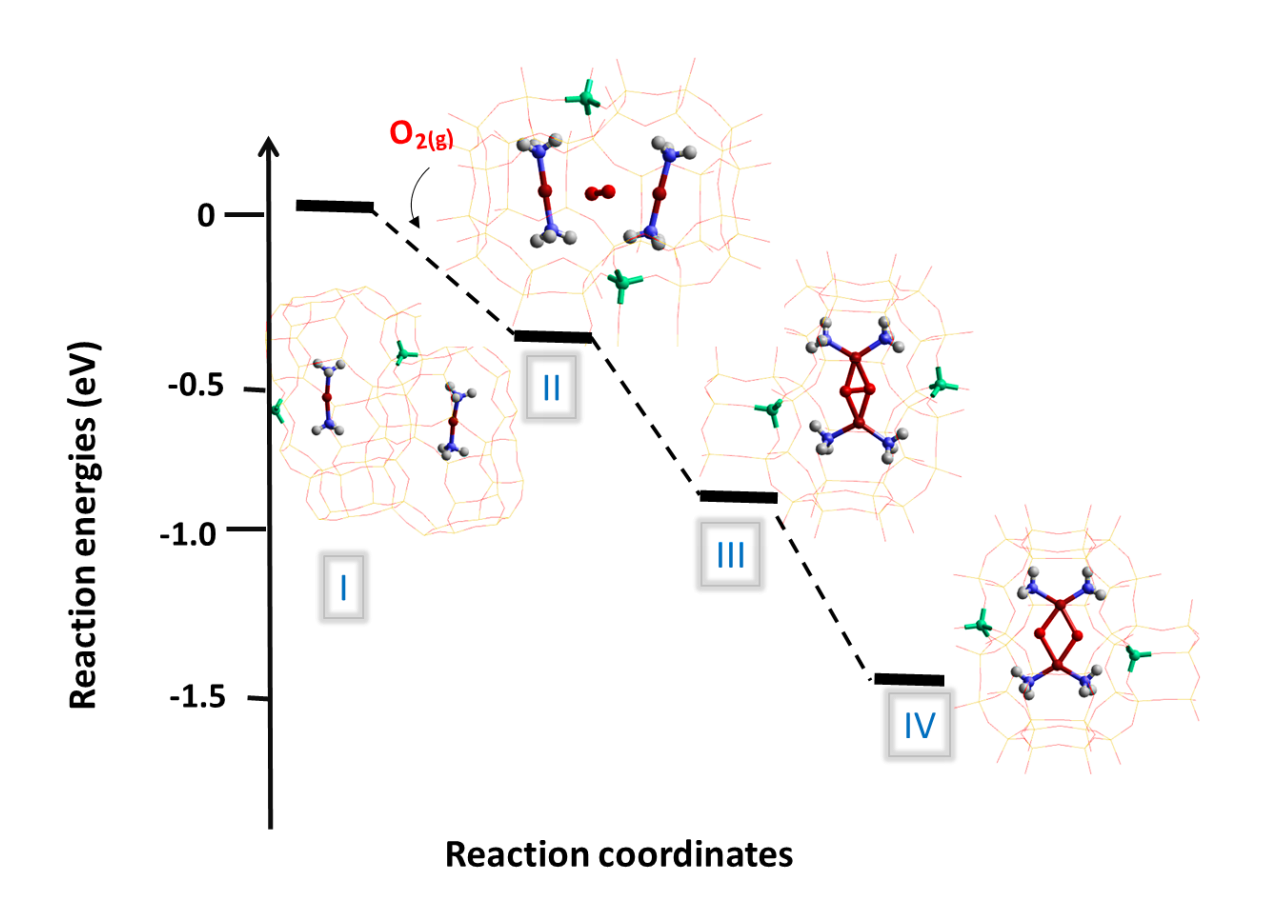


Figure 6.7. Energy landscape of O₂ adsorption and oxidation of two Cu(I)(NH₃)₂ equivalents. The different elements are represented by distinct colours: green for Al, grey for Cu, red for O, blue for N, and white for H.

6.4 Summary

In this chapter, we studied the formation of Cu-dimers which are considered one of the possible species in the NH₃-SCR of the NOx reaction. We investigated the reactivity of isolated Cu(I)(NH₃)₂ species, their mobility, and the formation of [(NH₃)₂Cu^{II}-O₂-Cu^{II}(NH₃)₂] in the CHA zeolite. The mobility and restructuring of Cu-species were analyzed using QM/MM simulations. We found that the isolated Cu species can form dimer species in the presence of a solvent. Solvent molecules coordinated to framework-bound Cu species help to isolate it from the framework of zeolite. The Cu ions in our study are not forced to move away from the Al site but displace spontaneously as a result of geometry optimization from their initial position close to the Al site in response to the strong interaction of the polar solvent with both framework and extraframework metal cations. We then modelled the oxidation half-cycle of the NH₃-SCR reaction and found that the formation of binuclear Cu(II)-dimer species from the reaction of O₂ with the Cu(I) site is viable. Our study contributes to the understanding of the formation of binuclear Cu(II) species and the energetics of the oxidation-half cycle in the NH₃-SCR reaction.

Chapter 7

7.1 Summary, Conclusions and Future Perspective

In this thesis, we have brought mechanistic insight into NH₃-SCR of NOx reaction over transition metal exchanged zeolites. Two different transition metals i.e. Cu and Fe have been studied in two different zeolites (CHA and BEA). The first focus was on investigating the coordination and location of these metal ions in different member rings of the zeolite cage. The hybrid QM/MM technique was employed to investigate the structural-activity correlation, and where possible, experimental comparisons have been made to support the simulated data. In this final chapter, we offer an overview of the work covered in Chapters 3, 4, 5, and 6 as well as some thoughts on potential future developments in the field.

First, we performed a theoretical investigation of the NH₃-SCR of NOx reaction on the bare site of the Cu-CHA and developed a detailed model of the NH₃-SCR reaction of NOx on the bare site of the Cu-CHA catalyst. As many have suggested, the role of Cu redox chemistry is important in driving the full catalytic cycle. However, in our study, additional insight into the reaction mechanism from the hybrid-QM/MM calculations and the modulation excitation (ME) DRIFTS experimental data, was obtained by Beale and coworkers. Our study employed a combination of harmonic vibrational analysis, DRIFTS experiments, and DFT calculations to gain insight into the reaction mechanism of NH₃-SCR reaction over Cu-CHA zeolite. Based on the calculated vibrational modes, we concluded that the spectroscopic signatures that appear in the DRIFTS spectrum can be tentatively assigned to the nitrate and nitrosamine species since we did not detect the N-O signatures in the DRIFTS spectrum for other species including nitrite, and the first Cu-NO(OH) interactions on NO adsorption, indicating that these species are too short-lived to be observed in the experimental study. Based on the interaction of

molecules with the active sites, we conclude that the adsorption of NO species with the O-end down is uncompetitive (endothermic) on both Cu⁺ and Cu²⁺ sites, suggesting that N-end down is the only feasible binding mode to Cu-CHA sites. The binding of NH₃ on Cu⁺ strongly influences the interaction of Cu with the CHA framework; however, depending on the number of NH₃ molecules bound and temperature, cation mobility can become possible ²⁷¹.

Next, we elucidated the role of physisorbed solvents on the Cu-CHA active sites, which we proposed will be affected by solvent molecules. To understand the role of solvents on the kinetics of the NH₃-SCR cycle, the adsorption of gaseous species and the formation of intermediates and their spectroscopic signatures on the solvated active sites were investigated which can help tune the rational design of important reaction steps. By understanding the parallels between the water and ammonia interactions with active sites, we deduce that an increase in solvent coordination to the Cu- active sites liberates the Cu species away from the CHA framework. From the potential energy landscapes, we observed that the formation of nitrate species is energetically more favourable on solvated active sites than on the bare site, suggesting that solvents can promote the re-oxidation part of the NH₃-SCR cycle. This effect is found to be more significant in the case of water than ammonia. In contrast to the oxidative part, both water and ammonia are found to inhibit the reduction part of SCR since the formation of important intermediates such as Cu-nitrosamine is relatively less favourable on solvated active sites than on the bare sites, suggesting that solvent can slow down the reduction part of the NH₃-SCR cycle. These findings explain why there is some debate concerning the effect of water and ammonia on the reaction since it seems to affect some parts of the cycle positively and others negatively. Therefore, our study provides additional understanding, helping to unravel the influence of solvent on the energetics of the active sites and provides guidance into a future pathway for optimising the NH₃-SCR process.

We also studied the various active sites of the Fe-BEA system, to investigate the reactivity of different Fe-based BEA active sites, such as the framework Fe cation, and explore the adsorption of reactants and the formation of key intermediates. The main catalytically active sites include Fe-Fe_F-BEA, Fe-Al-BEA, and Cu-Fe_F-BEA on which we study the formation and consumption of important intermediates including nitrosamine and nitrate species. First, we studied the reduction potential for intraframework Fe³⁺/ Fe²⁺ in BEA zeolite and found that the process is highly feasible in the presence of a proton. In addition, we investigated the interaction of NH₃ on different active sites including the Brønsted acid of BEA zeolite. The study of the NH₃-SCR reaction shows that NH₃ interacts strongly with framework Fe sites over other active sites in BEA zeolite such as Cu(II)-FeF/BEA, Fe(III)-AlF/BEA and Fe(III)-FeF/BEA. The computed binding energy of NH₃ on the framework Fe-Bronsted acid site is -1.76 eV (-170 kJ/mol), which is greater than observed experimentally at the Al Brønsted acid site (-128 kJ/mol). This difference can be attributed to the higher acidic nature of Fe compared to Al. The investigation of the formation of nitrosamine and nitrate species yielded interesting results. For the formation of nitrosamine, we found that the effect of framework Fe sites (Cu(II)-Fe_F/BEA, Fe-Fe_F-BEA) has had an overall more positive impact than the framework Al site (Fe-Al_F-BEA). While in the case of nitrate, we noted that the effect of the Fe-Fe_F system (Fe-Fe_F-BEA) on the formation of nitrate has an overall positive influence compared to the Fe-Alf-BEA and Cu(II)-Fef/BEA. Overall, our study on Fe- BEA zeolite helps our understanding of the role of the framework Fe cation in the BEA zeolite and offers insights for improving the efficiency of the existing Fe-based zeolitic system in the NH₃-SCR reaction.

We also studied the formation of Cu-dimer species which are considered as contributing to the NH₃-SCR of the NOx reaction. The study investigated the reactivity of isolated Cu(I)(NH₃)₂

species, their mobility, and the formation of [(NH₃)₂CuII-O₂-CuII(NH₃)₂] in CHA zeolite. The mobility and restructuring of Cu-species were analyzed using QM/MM simulations. We found that the isolated Cu species can form dimer species in the presence of a solvent which initially helps to isolate Cu from the framework of zeolite. The study also modelled the oxidation half-cycle of the NH₃-SCR reaction and found that the binuclear Cu(II)-dimer species form from the reaction of O₂ with the Cu(I) site is viable. The study helps our understanding of the formation of binuclear Cu(II) species and the energetics of the oxidation-half cycle in the NH₃-SCR reaction.

7.1.1 Future Perspective

The use of transition metal-ions-based (TMI) zeolites is expanding rapidly in the field of NH₃-assisted SCR of NOx reactions. The coordination and location of these metal ions in zeolites are of key importance. For example, Cu^{2+} is preferentially coordinated in 6-MR and distorts the rings to make 4-fold coordination while Co^{2+} is preferably coordinated in 3 or 5-fold coordination. In the case of Fe and Mn and other metals, the location and structure of the site depend on the Al content. Developing a comprehensive picture of the structure and mechanism in TMI exchanged zeolites is an essential step in understanding the NH₃-SCR of NOx reactions, and the identification of TMI speciations such as monomer, dimer, and oligomers and their redox mediation behaviour is needed. An important case was the discovery of two distinct reactive species of Cu core mono(μ -oxo)-dicopper in ZSM-5. This dimer [Cu-O-Cu]²⁺ is generated after Cu is preferentially coordinated with O_2 and N_2O species.

Theoretical simulations by *Ab Inition* Molecular Dynamics (AIMD) reveal the dynamic nature of metal-ions active species at the molecular level. The diffusion of the Cu ions is generally

determined by the electrostatic tethering of the zeolite framework revealed by simulation., which shows how the zeolite framework influences the movement of metal ions species. Conventional spectroscopic techniques such as *in situ operando* DRIFTS, XANES, EPR, and DRUVS, can provide indirect evidence regarding the NH₃ solvation on isolated metal sites by detecting the change in the metal coordination environment. Some techniques such as impedance-based *in situ* modulation spectroscopy can directly track the relaxation of the metal site under operating reaction conditions. All are more powerful when combined with modelling studies of the type reported here.

The main obstacle for zeolite-based SCR reactions is their durability under hydrothermal conditions. Recently, it has been reported that small-pore zeolites containing metal ions (Fe, Cu, Co, Mn) are hydrothermally more stable than medium or large-pore zeolites. In particular, the incorporation of Fe into small pore zeolites results in a hydrothermally stable NH₃-SCR catalyst. However, there is no assurance that zeolite-based catalysts will fulfil all the diverse requirements and a key target is the combination of high activity at low temperatures with stability at high temperatures. Due to the complex dynamic nature, the metal-ions as isolated sites are neither treated as a fixed site nor as unbound free sites; therefore, more appropriate models that mimic the real reaction system need to be investigated. Through a more accurate computational model, the effect of ion mobility on spectroscopic data can be determined so as to improve the resolution of spectroscopic signatures. A detailed understanding of the dynamics of species through the combination of experimental and computational modelling will help establish reliable methodologies for the development of novel concepts employed in low-NH₃-SCR catalysts. Understanding TMI as a catalytic site in zeolites will be essential in gaining mechanistic insight into the NH₃-SCR reaction. To this aim, QM/MM techniques will allow

for more accurate simulations of catalytic reactions enabling researchers to study complex systems such as zeolites for the NH_3 -SCR and other key reactions.

References

- 1. Y. Li and J. Yu, *Nature Reviews Materials*, 2021, **6**, 1156-1174.
- 2. A. Nicula, D. Stamires and J. Turkevich, *J. Chem. Phys.*, 1965, **42**, 3684-3692.
- 3. J. Turkevich, Y. Ono and J. Soria, *J. Catal.*, 1972, **25**, 44-54.
- 4. M. H. Groothaert, J. A. van Bokhoven, A. A. Battiston, B. M. Weckhuysen and R. A. Schoonheydt, *J. Am . Chem. Soc.*, 2003, **125**, 7629-7640.
- 5. R. Hamada, Y. Shibata, S. Nishiyama and S. Tsuruya, *Phys. Chem. Chem. Phys.*, 2003, **5**, 956-965.
- 6. M. H. Groothaert, P. J. Smeets, B. F. Sels, P. A. Jacobs and R. A. Schoonheydt, *J. Am. Chem. Soc.*, 2005, **127**, 1394-1395.
- 7. S. K. Hoekman and C. Robbins, Fuel Processing Technology, 2012, **96**, 237-249.
- 8. P. Granger and V. I. Parvulescu, *Chem. Rev.*, 2011, **111**, 3155-3207.
- 9. E. Borfecchia, P. Beato, S. Svelle, U. Olsbye, C. Lamberti and S. Bordiga, *Chem. Soc. Rev.*, 2018, **47**, 8097-8133.
- 10. A. Westermann, B. Azambre, M. Bacariza, I. Graça, M. Ribeiro, J. Lopes and C. Henriques, *Applied Catalysis B: Environmental*, 2015, **174**, 120-125.
- 11. O. B. Ayodele, *Journal of CO2 Utilization*, 2017, **20**, 368-377.
- 12. W. Hu, F. Gramigni, N. D. Nasello, N. Usberti, U. Iacobone, S. Liu, I. Nova, X. Gao and E. Tronconi, *ACS Catalysis*, 2022, **12**, 5263-5274.
- 13. M. Høj, M. J. Beier, J.-D. Grunwaldt and S. Dahl, *Applied Catalysis B: Environmental*, 2009, **93**, 166-176.
- 14. M.-Y. Choo, L. E. Oi, T. C. Ling, E.-P. Ng, Y.-C. Lin, G. Centi and J. C. Juan, *Journal of Analytical and Applied Pyrolysis*, 2020, **147**, 104797.
- 15. T. X. H. Le, M. Drobek, M. Bechelany, J. Motuzas, A. Julbe and M. Cretin, *Microporous and Mesoporous Materials*, 2019, **278**, 64-69.
- 16. S.-U. Lee, T.-W. Kim, K.-E. Jeong, S. Lee, M. C. Shin and C.-U. Kim, *RSC Advances*, 2023, **13**, 2168-2180.
- 17. V. Van Speybroeck, K. Hemelsoet, L. Joos, M. Waroquier, R. G. Bell and C. R. A. Catlow, *Chemical Society Reviews*, 2015, **44**, 7044-7111.
- 18. Q. Sun, N. Wang and J. Yu, *Advanced Materials*, 2021, **33**, 2104442.
- 19. J. Li, A. Corma and J. Yu, *Chemical Society Reviews*, 2015, **44**, 7112-7127.
- 20. Q. Wang and D. Astruc, *Chemical reviews*, 2019, **120**, 1438-1511.
- 21. P. J. Smeets, J. S. Woertink, B. F. Sels, E. I. Solomon and R. A. Schoonheydt, *Ilnorg. Chem.*, 2010, **49**, 3573-3583.
- 22. C. Catlow, A. George and C. Freeman, *Chemical Communications*, 1996, 1311-1312.
- 23. C.-S. Yang, J. M. Mora-Fonz and C. R. A. Catlow, *The Journal of Physical Chemistry C*, 2011, **115**, 24102-24114.
- 24. T. Takaishi, M. Kato and K. Itabashi, *Zeolites*, 1995, **15**, 21-32.
- 25. T. Takaishi, M. Kato and K. Itabashi, *The Journal of Physical Chemistry*, 1994, **98**, 5742-5743.
- 26. M. Sato, K. Maeda and K. Hirasawa, in *Studies in Surface Science and Catalysis*, Elsevier, 1994, vol. 84, pp. 589-596.
- 27. J. Dědeček, Z. Sobalík and B. Wichterlová, Catal. Rev., 2012, **54**, 135-223.
- 28. B. E. Snyder, M. L. Bols, R. A. Schoonheydt, B. F. Sels and E. I. Solomon, *Chemical reviews*, 2017, **118**, 2718-2768.
- 29. O. H. Han, C. S. Kim and S. B. Hong, *Angew. Chem. Int. Ed.*, 2002, **41**, 469-472.
- 30. V. Gábová, J. Dědeček and J. Čejka, *Chem. comm.*, 2003, 1196-1197.
- 31. D. E. Perea, I. Arslan, J. Liu, Z. Ristanović, L. Kovarik, B. W. Arey, J. A. Lercher, S. R. Bare and B. M. Weckhuysen, *Nat. Commun.*, 2015, **6**, 7589.

- 32. B. E. Snyder, M. L. Bols, R. A. Schoonheydt, B. F. Sels and E. I. Solomon, *Chem. Rev.*, 2017, **118**, 2718-2768.
- 33. J. Armor, *Microporous and mesoporous materials*, 1998, **22**, 451-456.
- 34. Y. Chai, W. Dai, G. Wu, N. Guan and L. Li, *Accounts of Chemical Research*, 2021, **54**, 2894-2904.
- 35. S. Brandenberger, O. Kröcher, A. Tissler and R. Althoff, *Appl. Catal.*, *B.*, 2010, **95**, 348-357.
- 36. F. Liu, Y. Yu and H. He, *Chem. Commun.*, 2014, **50**, 8445-8463.
- 37. J. Li and S. Li, J. Phys. Chem. C, 2008, **112**, 16938-16944.
- 38. T. Bruggemann and F. Keil, *J. Phys. Chem. C*, 2011, **115**, 23854-23870.
- 39. S. Shwan, J. Jansson, L. Olsson and M. Skoglundh, *Applied Catalysis B: Environmental*, 2014, **147**, 111-123.
- 40. J. Kim, A. Jentys, S. M. Maier and J. A. Lercher, *The Journal of Physical Chemistry C*, 2013, **117**, 986-993.
- 41. S. Shwan, J. Jansson, J. Korsgren, L. Olsson and M. Skoglundh, *Catalysis today*, 2012, **197**, 24-37.
- 42. N. Hansen, A. Heyden, A. T. Bell and F. J. Keil, *J. Phys. Chem. C*, 2007, **111**, 2092-2101.
- 43. H. Guesmi, D. Berthomieu, B. Bromley, B. Coq and L. Kiwi-Minsker, *Phys. Chem. Chem. Phys.*, 2010, **12**, 2873-2878.
- 44. H. Guesmi, D. Berthomieu and L. Kiwi-Minsker, *J. Phys. Chem. C*, 2008, **112**, 20319-20328.
- 45. F. Gao, Y. Zheng, R. K. Kukkadapu, Y. Wang, E. D. Walter, B. Schwenzer, J. n. Szanyi and C. H. Peden, *ACS Catal.*, 2016, **6**, 2939-2954.
- 46. S. Brandenberger, O. Kröcher, A. Tissler and R. Althoff, *Appl. Catal.*, A., 2010, **373**, 168-175.
- 47. J. Dědeček and B. Wichterlová, J. Phys. Chem. B, 1999, **103**, 1462-1476.
- 48. J. Dědeček, D. Kaucký and B. Wichterlová, *Micropor. Mesopor. Mat.*, 2000, **35**, 483-494.
- 49. J. Dědeček, L. Čapek, D. Kaucký, Z. Sobalık and B. Wichterlova, *J. Catal.*, 2002, **211**, 198-207.
- 50. M. P. Attfield, S. J. Weigel and A. K. Cheetham, *J. Catal.*, 1997, **170**, 227-235.
- 51. M. C. Dalconi, G. Cruciani, A. Alberti, P. Ciambelli and M. Rapacciuolo, *Micropor. Mesopor. Mat.*, 2000, **39**, 423-430.
- 52. R. Izquierdo, L. J. Rodríguez, R. Añez and A. Sierraalta, *J. Molec. Catal. A: Chem.*, 2011, **348**, 55-62.
- 53. S. Morpurgo, G. Moretti and M. Bossa, *J. Molec. Catal. A: Chem.*, 2012, **358**, 134-144.
- 54. Y. Mao, H. F. Wang and P. Hu, *Int. J. Quantum Chem.*, 2015, **115**, 618-630.
- 55. J. Dědeček, D. Kaucký and B. Wichterlová, *Microporous and Mesoporous Materials*, 2000, **35**, 483-494.
- 56. M. Lee, S. Hong, D. Kim, E. Kim, K. Lim, J. C. Jung, H. Richter, J.-H. Moon, N. Choi and J. Nam, *ACS applied materials & interfaces*, 2019, **11**, 3946-3960.
- 57. J.-S. McEwen, T. Anggara, W. Schneider, V. Kispersky, J. Miller, W. Delgass and F. Ribeiro, *Catal. Today*, 2012, **184**, 129-144.
- 58. T. V. Janssens, H. Falsig, L. F. Lundegaard, P. N. Vennestrøm, S. B. Rasmussen, P. G. Moses, F. Giordanino, E. Borfecchia, K. A. Lomachenko and C. Lamberti, *ACS catalysis*, 2015, **5**, 2832-2845.
- 59. F. Göltl, R. E. Bulo, J. r. Hafner and P. Sautet, *J. Phys. Chem. Lett.*, 2013, **4**, 2244-2249.

- 60. S. T. Korhonen, D. W. Fickel, R. F. Lobo, B. M. Weckhuysen and A. M. Beale, *Chemical Communications*, 2011, **47**, 800-802.
- 61. M. J. Rice, A. K. Chakraborty and A. T. Bell, *J. Phys. Chem. B*, 2000, **104**, 9987-9992.
- 62. M. J. Rice, A. K. Chakraborty and A. T. Bell, *J. Catal.*, 2000, **194**, 278-285.
- 63. J. H. Kwak, D. Tran, J. Szanyi, C. H. Peden and J. H. Lee, *Catalysis letters*, 2012, **142**, 295-301.
- 64. S. Sklenak, P. C. Andrikopoulos, S. R. Whittleton, H. Jirglova, P. Sazama, L. Benco, T. Bucko, J. Hafner and Z. Sobalik, *J. Phys. Chem. C*, 2013, **117**, 3958-3968.
- 65. E. L. Uzunova, F. Göltl, G. Kresse and J. r. Hafner, *J. Phys. Chem. C*, 2009, **113**, 5274-5291.
- 66. E. L. Uzunova, H. Mikosch and J. Hafner, *J. Phys. Chem. C*, 2008, **112**, 2632-2639.
- 67. M. H. Groothaert, K. Pierloot, A. Delabie and R. A. Schoonheydt, *Phys. Chem. Chem. Phys.*, 2003, **5**, 2135-2144.
- 68. A. Delabie, K. Pierloot, M. H. Groothaert, R. A. Schoonheydt and L. G. Vanquickenborne, *Eur. J. Inorg. Chem*, 2002, **2002**, 515-530.
- 69. K. Pierloot, A. Delabie, A. Verberckmoes and R. Schoonheydt, 1999.
- 70. E. Dooryhee, C. Catlow, J. Couves, P. Maddox, J. Thomas, G. Greaves, A. Steel and R. Townsend, *The Journal of Physical Chemistry*, 1991, **95**, 4514-4521.
- 71. F. Gao, Y. Zheng, R. K. Kukkadapu, Y. Wang, E. D. Walter, B. Schwenzer, J. Szanyi and C. H. Peden, *ACS Catalysis*, 2016, **6**, 2939-2954.
- 72. Z. Sobalík, J. Dědeček, I. Ikonnikov and B. Wichterlová, *Micropor. Mesopor. Mat.*, 1998, **21**, 525-532.
- 73. A. Zecchina, M. Rivallan, G. Berlier, C. Lamberti and G. Ricchiardi, *Phys. Chem. Chem. Phys.*, 2007, **9**, 3483-3499.
- 74. S. Lai, Y. She, W. Zhan, Y. Guo, Y. Guo, L. Wang and G. Lu, *J. Mol. Catal. A-Chem.*, 2016, **424**, 232-240.
- 75. L. J. Lobree, I.-C. Hwang, J. A. Reimer and A. T. Bell, *J. Catal.*, 1999, **186**, 242-253.
- 76. B. Wichterlová, *Top. Catal.*, 2004, **28**, 131-140.
- 77. C. Baes and R. Mesmer, *Malabar*, *Fla.: RE Krieger*.
- 78. P. Ratnasamy and R. Kumar, *Catalysis Today*, 1991, **9**, 329-416.
- 79. B. Wichterlová, *Topics in catalysis*, 2004, **28**, 131-140.
- 80. K. Pierloot, A. Delabie, M. H. Groothaert and R. A. Schoonheydt, *Physical Chemistry Chemical Physics*, 2001, **3**, 2174-2183.
- 81. S. M. Seo, W. T. Lim and K. Seff, *The Journal of Physical Chemistry C*, 2012, **116**, 963-974.
- 82. W. J. Mortier, *Compilation of extra framework sites in zeolites*, Butterworth Scientific Limited on behalf of the Structure Commission of the ..., 1982.
- 83. D. W. Fickel and R. F. Lobo, *The Journal of Physical Chemistry C*, 2010, **114**, 1633-1640.
- 84. U. Deka, A. Juhin, E. A. Eilertsen, H. Emerich, M. A. Green, S. T. Korhonen, B. M. Weckhuysen and A. M. Beale, *The Journal of Physical Chemistry C*, 2012, **116**, 4809-4818.
- 85. V. F. Kispersky, A. J. Kropf, F. H. Ribeiro and J. T. Miller, *Physical Chemistry Chemical Physics*, 2012, **14**, 2229-2238.
- 86. U. Deka, I. Lezcano-Gonzalez, S. J. Warrender, A. L. Picone, P. A. Wright, B. M. Weckhuysen and A. M. Beale, *Microporous and Mesoporous Materials*, 2013, **166**, 144-152.
- 87. A. M. Beale, F. Gao, I. Lezcano-Gonzalez, C. H. Peden and J. Szanyi, *Chemical Society Reviews*, 2015, **44**, 7371-7405.

- 88. R. Martínez-Franco, M. Moliner, P. Concepcion, J. R. Thogersen and A. Corma, *Journal of catalysis*, 2014, **314**, 73-82.
- 89. Z. Nour, H. Petitjean and D. Berthomieu, *The Journal of Physical Chemistry C*, 2010, **114**, 17802-17811.
- 90. J. H. Kwak, H. Zhu, J. H. Lee, C. H. Peden and J. Szanyi, *Chemical Communications*, 2012, **48**, 4758-4760.
- 91. D. Wang, L. Zhang, J. Li, K. Kamasamudram and W. S. Epling, *Catalysis Today*, 2014, **231**, 64-74.
- 92. D. Wang, Y. Jangjou, Y. Liu, M. K. Sharma, J. Luo, J. Li, K. Kamasamudram and W. S. Epling, *Applied Catalysis B: Environmental*, 2015, **165**, 438-445.
- 93. D. Wang, L. Zhang, K. Kamasamudram and W. S. Epling, *Acs Catalysis*, 2013, **3**, 871-881.
- 94. F. Gao, E. D. Walter, N. M. Washton, J. Szanyi and C. H. Peden, *Applied Catalysis B: Environmental*, 2015, **162**, 501-514.
- 95. A. Godiksen, F. N. Stappen, P. N. Vennestrøm, F. Giordanino, S. B. Rasmussen, L. F. Lundegaard and S. Mossin, *The Journal of Physical Chemistry C*, 2014, **118**, 23126-23138.
- 96. F. Gao, E. D. Walter, N. M. Washton, J. Szanyi and C. H. Peden, *Acs Catalysis*, 2013, **3**, 2083-2093.
- 97. T. Yu, J. Wang, Y. Huang, M. Shen, W. Li and J. Wang, *ChemCatChem*, 2014, **6**, 2074-2083.
- 98. W. Su, Z. Li, Y. Peng and J. Li, *Physical Chemistry Chemical Physics*, 2015, **17**, 29142-29149.
- 99. F. Giordanino, E. Borfecchia, K. A. Lomachenko, A. Lazzarini, G. Agostini, E. Gallo, A. V. Soldatov, P. Beato, S. Bordiga and C. Lamberti, *The journal of physical chemistry letters*, 2014, **5**, 1552-1559.
- 100. I. Lezcano-Gonzalez, U. Deka, H. Van Der Bij, P. Paalanen, B. Arstad, B. Weckhuysen and A. Beale, *Applied Catalysis B: Environmental*, 2014, **154**, 339-349.
- 101. J. Xue, X. Wang, G. Qi, J. Wang, M. Shen and W. Li, *Journal of Catalysis*, 2013, **297**, 56-64.
- 102. Y. Xin, X. Wang, Q. Li, X. Ma, Y. Qi, L. Zheng, J. A. Anderson and Z. Zhang, *ChemCatChem*, 2016, **8**, 3740-3745.
- 103. F. Gao, E. D. Walter, E. M. Karp, J. Luo, R. G. Tonkyn, J. H. Kwak, J. Szanyi and C. H. Peden, *Journal of catalysis*, 2013, **300**, 20-29.
- 104. P. J. Smeets, J. S. Woertink, B. F. Sels, E. I. Solomon and R. A. Schoonheydt, *Inorg. chem.*, 2010, **49**, 3573-3583.
- 105. P. Vanelderen, J. Vancauwenbergh, B. F. Sels and R. A. Schoonheydt, *Coord. Chem. Rev.*, 2013, **257**, 483-494.
- 106. M. Iwamoto, H. Furukawa, Y. Mine, F. Uemura, S.-i. Mikuriya and S. Kagawa, *J. Chem. Soc. Chem. Commun.*, 1986, 1272-1273.
- 107. S. Brandenberger, O. Kröcher, A. Tissler and R. Althoff, *Catalysis Reviews*, 2008, **50**, 492-531.
- 108. K. Rahkamaa-Tolonen, T. Maunula, M. Lomma, M. Huuhtanen and R. L. Keiski, *Catalysis Today*, 2005, **100**, 217-222.
- 109. R. Long, R. Yang and K. Zammit, *Journal of the Air & Waste Management Association*, 2000, **50**, 436-442.
- 110. G. Ramis, L. Yi, G. Busca, M. Turco, E. Kotur and R. J. Willey, *Journal of catalysis*, 1995, **157**, 523-535.
- 111. A. Salker and W. Weisweiler, 2004.

- 112. A. Salker and W. Weisweiler, *Applied Catalysis A: General*, 2000, **203**, 221-229.
- 113. A. Salker, B. Maurer and W. Weisweiler, *Chemie Ingenieur Technik*, 1998, **70**, 566-570.
- 114. A. Garrido Pedrosa, M. Souza, A. Silva, D. Melo and A. Araujo, *Journal of thermal analysis and calorimetry*, 2006, **84**, 503-509.
- 115. W. Van Kooten, J. Kaptein, C. Van den Bleek and H. Calis, *Catalysis letters*, 1999, **63**, 227-231.
- 116. F. Gao, M. Kollár, R. K. Kukkadapu, N. M. Washton, Y. Wang, J. Szanyi and C. H. Peden, *Appl. Catal.*, *B.*, 2015, **164**, 407-419.
- 117. F. Gao, Y. Wang, M. Kollár, N. M. Washton, J. Szanyi and C. H. Peden, *Catal. Today*, 2015, **258**, 347-358.
- 118. M. Dusselier and M. E. Davis, *Chemical reviews*, 2018, **118**, 5265-5329.
- 119. C. Paolucci, I. Khurana, A. A. Parekh, S. Li, A. J. Shih, H. Li, J. R. Di Iorio, J. D. Albarracin-Caballero, A. Yezerets and J. T. Miller, *Science*, 2017, **357**, 898-903.
- T. V. Janssens, H. Falsig, L. F. Lundegaard, P. N. Vennestrøm, S. B. Rasmussen, P. G. Moses, F. Giordanino, E. Borfecchia, K. A. Lomachenko and C. Lamberti, *ACS Catal.*, 2015, 5, 2832-2845.
- 121. M. Devadas, O. Kröcher, M. Elsener, A. Wokaun, N. Söger, M. Pfeifer, Y. Demel and L. Mussmann, *Applied Catalysis B: Environmental*, 2006, **67**, 187-196.
- 122. M. Schwidder, S. Heikens, A. De Toni, S. Geisler, M. Berndt, A. Brückner and W. Grünert, *Journal of Catalysis*, 2008, **259**, 96-103.
- 123. J.-Y. Luo, X. Hou, P. Wijayakoon, S. J. Schmieg, W. Li and W. S. Epling, *Applied Catalysis B: Environmental*, 2011, **102**, 110-119.
- 124. M. Devadas, O. Kröcher, M. Elsener, A. Wokaun, G. Mitrikas, N. Söger, M. Pfeifer, Y. Demel and L. Mussmann, *Catalysis Today*, 2007, **119**, 137-144.
- 125. A. Grossale, I. Nova, E. Tronconi, D. Chatterjee and M. Weibel, *Topics in Catalysis*, 2009, **52**, 1837.
- 126. M. Colombo, I. Nova and E. Tronconi, *Catalysis Today*, 2010, **151**, 223-230.
- 127. H.-Y. Chen, X. Wang and W. M. Sachtler, *Applied Catalysis A: General*, 2000, **194**, 159-168.
- 128. A. V. Kucherov, D. E. Doronkin, A. Y. Stakheev, A. L. Kustov and M. Grill, *Journal of Molecular Catalysis A: Chemical*, 2010, **325**, 73-78.
- 129. D. W. Fickel, E. D'Addio, J. A. Lauterbach and R. F. Lobo, *Applied Catalysis B: Environmental*, 2011, **102**, 441-448.
- 130. F. Gao, Y. Wang, M. Kollár, N. M. Washton, J. Szanyi and C. H. Peden, *Catalysis Today*, 2015, **258**, 347-358.
- 131. F. Gao, M. Kollár, R. K. Kukkadapu, N. M. Washton, Y. Wang, J. Szanyi and C. H. Peden, *Applied Catalysis B: Environmental*, 2015, **164**, 407-419.
- 132. M. Moliner, C. Franch, E. Palomares, M. Grill and A. Corma, *Chemical Communications*, 2012, **48**, 8264-8266.
- 133. N. Martín, P. N. Vennestrøm, J. R. Thøgersen, M. Moliner and A. Corma, *ChemCatChem*, 2017, **9**, 1754-1757.
- 134. N. Martín, C. Paris, P. N. Vennestrøm, J. R. Thøgersen, M. Moliner and A. Corma, *Applied Catalysis B: Environmental*, 2017, **217**, 125-136.
- 135. M. Koebel, M. Elsener and M. Kleemann, *Catal. Today*, 2000, **59**, 335-345.
- 136. P. L. Gabrielsson, *Top. Catal.*, 2004, **28**, 177-184.
- 137. U. Deka, I. Lezcano-Gonzalez, B. M. Weckhuysen and A. M. Beale, *ACS catalysis*, 2013, **3**, 413-427.

- 138. J. H. Kwak, R. G. Tonkyn, D. H. Kim, J. Szanyi and C. H. Peden, *Journal of Catalysis*, 2010, **275**, 187-190.
- 139. A. Marberger, A. W. Petrov, P. Steiger, M. Elsener, O. Kröcher, M. Nachtegaal and D. Ferri, *Nat. Catal.*, 2018, **1**, 221.
- 140. L. Kovarik, N. M. Washton, R. Kukkadapu, A. Devaraj, A. Wang, Y. Wang, J. Szanyi, C. H. Peden and F. Gao, *ACS Catal.*, 2017, **7**, 2458-2470.
- 141. F. Gao, Y. Zheng, R. K. Kukkadapu, Y. Wang, E. D. Walter, B. Schwenzer, J. n. Szanyi and C. H. Peden, *ACS Cataly.*, 2016, **6**, 2939-2954.
- 142. H.-Y. Chen and W. M. Sachtler, *Catalysis Today*, 1998, **42**, 73-83.
- 143. T. V. Voskoboinikov, H.-Y. Chen and W. M. Sachtler, *Applied Catalysis B: Environmental*, 1998, **19**, 279-287.
- 144. T. Günter, M. Casapu, D. Doronkin, S. Mangold, V. Trouillet, T. Augenstein and J. D. Grunwaldt, *Chemie Ingenieur Technik*, 2013, **85**, 632-641.
- 145. P. S. Metkar, M. P. Harold and V. Balakotaiah, *Chemical engineering science*, 2013, **87**, 51-66.
- 146. T. Selleri, F. Gramigni, I. Nova and E. Tronconi, *Applied Catalysis B: Environmental*, 2018, **225**, 324-331.
- 147. N. Martín-García, P. N. Ravnborg, J. R. Thogersen, M. Moliner Marin and A. Corma Canós, *Chemistry-A European Journal*, 2017, **23**, 13404-13414.
- 148. X. Lu, Y. Zheng, Y. Zhang, H. Qiu and H. Zou, *Micro Nano Lett.*, 2015, **10**, 666-669.
- 149. F. Gao, X. Tang, H. Yi, S. Zhao, C. Li, J. Li, Y. Shi and X. Meng, *Catalysts*, 2017, **7**, 199.
- 150. J. Chen, Y. Zheng, W. Cai, H. Zou, W. Zheng, Y. Zhang, X. Chen and B. Fu, *Micro Nano Lett.*, 2017, **12**, 6-10.
- 151. Y. J. Kim, H. J. Kwon, I. Heo, I.-S. Nam, B. K. Cho, J. W. Choung, M.-S. Cha and G. K. Yeo, *Appl. Catal.*, *B-Environ.*, 2012, **126**, 9-21.
- 152. J. W. Choung, I.-S. Nam, H. J. Kwon, Y.-J. Kim, D.-H. Kang and M.-S. Cha, *Journal*, 2011.
- 153. E.-Y. Choi, I.-S. Nam and Y. G. Kim, *J. Catal.*, 1996, **161**, 597-604.
- 154. C. W. Andersen, E. Borfecchia, M. Bremholm, M. R. V. Jørgensen, P. N. R. Vennestrøm, C. Lamberti, L. F. Lundegaard and B. B. Iversen, *Angew. Chem., Int. Ed.*, 2017, **56**, 10367-10372.
- 155. C. Paolucci, A. A. Parekh, I. Khurana, J. R. Di Iorio, H. Li, J. D. Albarracin Caballero, A. J. Shih, T. Anggara, W. N. Delgass and J. T. Miller, *J Am Chem Soc.*, 2016, **138**, 6028-6048.
- 156. F. Llabrés i Xamena, P. Fisicaro, G. Berlier, A. Zecchina, G. T. Palomino, C. Prestipino, S. Bordiga, E. Giamello and C. Lamberti, *J. Phys. Chem. B*, 2003, **107**, 7036-7044.
- 157. J. M. Fedeyko, B. Chen and H.-Y. Chen, *Catal. Today*, 2010, **151**, 231-236.
- 158. S. Bordiga, C. Lamberti, F. Bonino, A. Travert and F. Thibault-Starzyk, *Chem. Soc. Rev.*, 2015, **44**, 7262-7341.
- 159. E. Borfecchia, K. Lomachenko, F. Giordanino, H. Falsig, P. Beato, A. Soldatov, S. Bordiga and C. Lamberti, *Chem. Sci.*, 2015, **6**, 548-563.
- 160. J. H. Kwak, H. Zhu, J. H. Lee, C. H. Peden and J. Szanyi, *Chem. comm.*, 2012, **48**, 4758-4760.
- 161. F. Gao, N. M. Washton, Y. Wang, M. Kollár, J. Szanyi and C. H. Peden, *J. Catal.*, 2015, **331**, 25-38.
- 162. J. H. Kwak, D. Tran, S. D. Burton, J. Szanyi, J. H. Lee and C. H. Peden, *Journal of Catalysis*, 2012, **287**, 203-209.

- 163. W. Gruenert, N. W. Hayes, R. W. Joyner, E. S. Shpiro, M. R. H. Siddiqui and G. N. Baeva, *J. Phys. Chem.*, 1994, **98**, 10832-10846.
- 164. M. K. Neylon, C. L. Marshall and A. J. Kropf, *J. Am. Chem. Soc.*, 2002, **124**, 5457-5465.
- 165. S. C. Larsen, A. Aylor, A. T. Bell and J. A. Reimer, *J. Phys. Chem.*, 1994, **98**, 11533-11540.
- 166. K. Pierloot, A. Delabie, M. H. Groothaert and R. A. Schoonheydt, *Phys. Chem. Chem. Phys.*, 2001, **3**, 2174-2183.
- 167. S. M. Seo, W. T. Lim and K. Seff, J. Phys. Chem. C, 2011, 116, 963-974.
- 168. S. Bordiga, D. Scarano, G. Spoto, A. Zecchina, C. Lamberti and C. O. Areán, *Vib. Spectrosc.*, 1993, 5, 69-74.
- 169. S. Bordiga, E. Garrone, C. Lamberti, A. Zecchina, C. O. Arean, V. B. Kazansky and L. M. Kustov, *J. Chem. Soc. Faraday Trans.*, 1994, **90**, 3367-3372.
- 170. S. Kieger, G. Delahay, B. Coq and B. Neveu, *J. Catal.*, 1999, **183**, 267-280.
- 171. J. Yan, G.-D. Lei, W. Sachtler and H. H. Kung, *J. Catal.*, 1996, **161**, 43-54.
- 172. J.-H. Park, H. J. Park, J. H. Baik, I.-S. Nam, C.-H. Shin, J.-H. Lee, B. K. Cho and S. H. Oh, *J. Catal.*, 2006, **240**, 47-57.
- 173. J. H. Kwak, D. Tran, S. D. Burton, J. Szanyi, J. H. Lee and C. H. Peden, *J. Catal.*, 2012, **287**, 203-209.
- 174. P. Chen, V. Rizzotto, A. Khetan, K. Xie, R. Moos, H. Pitsch, D. Ye and U. Simon, *ACS Appl. Mater. Interfaces*, 2019, **11**, 8097-8105.
- 175. M. Moliner, C. Martinez and A. Corma, *Chem. Mater.*, 2013, **26**, 246-258.
- 176. M. Moliner, C. Franch, E. Palomares, M. Grill and A. Corma, *Chem. Commun.*, 2012, **48**, 8264-8266.
- 177. F. Gao, M. Kollár, R. K. Kukkadapu, N. M. Washton, Y. Wang, J. Szanyi and C. H. Peden, *Appl. Catal.*, *B-Environ.*, 2015, **164**, 407-419.
- 178. J. Kielland, J. Am. Chem. Soc., 1937, **59**, 1675-1678.
- 179. N. Martín, P. N. Vennestrøm, J. R. Thøgersen, M. Moliner and A. Corma, *Chem.: Eur. J.*, 2017, **23**, 13404-13414.
- 180. M. P. Ruggeri, I. Nova, E. Tronconi, V. Schmeißer and M. Weibel, *Chem. Ing. Tech.*, 2018, **90**, 803-815.
- 181. S. Han, Q. Ye, S. Cheng, T. Kang and H. Dai, *Catalysis Science & Technology*, 2017, 7, 703-717.
- 182. T. Usui, Z. Liu, S. Ibe, J. Zhu, C. Anand, H. Igarashi, N. Onaya, Y. Sasaki, Y. Shiramata and T. Kusamoto, *ACS Catalysis*, 2018, **8**, 9165-9173.
- 183. Y. Wang, X. Shi, Y. Shan, J. Du, K. Liu and H. He, *Industrial & Engineering Chemistry Research*, 2020, **59**, 6416-6423.
- 184. Y. Shan, J. Du, Y. Yu, W. Shan, X. Shi and H. He, *Applied Catalysis B: Environmental*, 2020, **266**, 118655.
- 185. Y. J. Kim, J. K. Lee, K. M. Min, S. B. Hong, I.-S. Nam and B. K. Cho, *J. Catal.*, 2014, **311**, 447-457.
- 186. J. Song, Y. Wang, E. D. Walter, N. M. Washton, D. Mei, L. Kovarik, M. H. Engelhard, S. Prodinger, Y. Wang and C. H. Peden, *ACS Catal.*, 2017, **7**, 8214-8227.
- 187. J. Luo, F. Gao, K. Kamasamudram, N. Currier, C. H. Peden and A. Yezerets, *J. Catal.*, 2017, **348**, 291-299.
- 188. J. Wang, H. Zhao, G. Haller and Y. Li, *Applied Catalysis B: Environmental*, 2017, **202**, 346-354.
- 189. J. H. Lee, Y. J. Kim, T. Ryu, P. S. Kim, C. H. Kim and S. B. Hong, *Applied Catalysis B: Environmental*, 2017, **200**, 428-438.

- 190. J. H. Kwak, D. Tran, S. D. Burton, J. Szanyi, J. H. Lee and C. H. Peden, *Journal of Catalysis*, 2012, **289**, 272.
- 191. T. Ryu, N. H. Ahn, S. Seo, J. Cho, H. Kim, D. Jo, G. T. Park, P. S. Kim, C. H. Kim and E. L. Bruce, *Angewandte Chemie*, 2017, **129**, 3304-3308.
- 192. T. Ryu, Y. Kang, I.-S. Nam and S. B. Hong, *Reaction Chemistry & Engineering*, 2019, 4, 1050-1058.
- 193. J. H. Kwak, D. Tran, J. Szanyi, C. H. Peden and J. H. Lee, *Catalysis letters*, 2012, **142**, 295-301.
- 194. F. Gao, E. D. Walter, M. Kollar, Y. Wang, J. Szanyi and C. H. Peden, *Journal of catalysis*, 2014, **319**, 1-14.
- 195. K. A. Lomachenko, E. Borfecchia, C. Negri, G. Berlier, C. Lamberti, P. Beato, H. Falsig and S. Bordiga, *Journal of the American Chemical Society*, 2016, **138**, 12025-12028.
- 196. T. Yu, T. Hao, D. Fan, J. Wang, M. Shen and W. Li, *The Journal of Physical Chemistry C*, 2014, **118**, 6565-6575.
- 197. W. Su, H. Chang, Y. Peng, C. Zhang and J. Li, *Environmental science & technology*, 2015, **49**, 467-473.
- 198. J. Li and S. Li, *Phys. Chem. Chem. Phys.*, 2007, **9**, 3304-3311.
- 199. T. C. Brüggemann and F. J. Keil, *J. Phys. Chem. C* 2008, **112**, 17378-17387.
- 200. T. C. Brüggemann and F. J. Keil, *J. Phys. Chem. C*, 2011, **115**, 2114-2133.
- 201. M.-L. Tsai, R. G. Hadt, P. Vanelderen, B. F. Sels, R. A. Schoonheydt and E. I. Solomon, *J. Am. Chem. Soc.*, 2014, **136**, 3522-3529.
- 202. A. Heyden, N. Hansen, A. T. Bell and F. J. Keil, *J. Phys. Chem. B*, 2006, **110**, 17096-17114.
- 203. T. Usui, Z. Liu, H. Igarashi, Y. Sasaki, Y. Shiramata, H. Yamada, K. Ohara, T. Kusamoto and T. Wakihara, *ACS Omega*, 2019, **4**, 3653-3659.
- 204. F. Maugé, P. Gallezot, J.-C. Courcelle, P. Engelhard and J. Grosmangin, *Zeolites*, 1986, **6**, 261-266.
- 205. D. W. Fickel and R. F. Lobo, J. Phys. Chem. C, 2009, 114, 1633-1640.
- 206. F. Gao, E. D. Walter, M. Kollar, Y. Wang, J. Szanyi and C. H. Peden, *J. Catal.*, 2014, **319**, 1-14.
- 207. M. Cheng, B. Jiang, S. Yao, J. Han, S. Zhao, X. Tang, J. Zhang and T. Wang, *J. Phys. Chem. C*, 2017, **122**, 455-464.
- 208. J. L. Sorrels, D. D. Randall, K. S. Schaffner and C. R. Fry, *EPA air pollution control cost manual*, 2019, **7**.
- 209. M. V. Twigg, Applied Catalysis B: Environmental, 2007, 70, 2-15.
- 210. J. Abdul Nasir, J. Guan, T. W. Keal, A. W. Desmoutier, Y. Lu, A. M. Beale, C. R. A. Catlow and A. A. Sokol, *Journal of the American Chemical Society*, 2022.
- 211. J. Neugebauer and T. Hickel, Wiley Interdisciplinary Reviews: Computational Molecular Science, 2013, **3**, 438-448.
- 212. Y. Elbaz, D. Furman and M. Caspary Toroker, *Advanced Functional Materials*, 2020, **30**, 1900778.
- 213. H. M. Senn and W. Thiel, *Angewandte Chemie International Edition*, 2009, **48**, 1198-1229.
- 214. S. Metz, J. Kästner, A. A. Sokol, T. W. Keal and P. Sherwood, *Wiley Interdisciplinary Reviews: Computational Molecular Science*, 2014, **4**, 101-110.
- 215. U. N. Morzan, D. J. Alonso de Armino, N. O. Foglia, F. Ramirez, M. C. Gonzalez Lebrero, D. A. Scherlis and D. A. Estrin, *Chemical reviews*, 2018, **118**, 4071-4113.

- 216. Y. Lu, M. R. Farrow, P. Fayon, A. J. Logsdail, A. A. Sokol, C. R. A. Catlow, P. Sherwood and T. W. Keal, *Journal of chemical theory and computation*, 2018, **15**, 1317-1328.
- 217. P. Sherwood, A. H. de Vries, M. F. Guest, G. Schreckenbach, C. R. A. Catlow, S. A. French, A. A. Sokol, S. T. Bromley, W. Thiel and A. J. Turner, *Journal of Molecular Structure: THEOCHEM*, 2003, **632**, 1-28.
- 218. B. Nagy and F. Jensen, Reviews in Computational Chemistry, 2017, 30, 93-149.
- 219. F. Weigend and R. Ahlrichs, *Physical Chemistry Chemical Physics*, 2005, **7**, 3297-3305.
- 220. A. K. Rappé, C. J. Casewit, K. Colwell, W. A. Goddard III and W. M. Skiff, *Journal of the American chemical society*, 1992, **114**, 10024-10035.
- 221. A. D. MacKerell Jr, Journal of computational chemistry, 2004, 25, 1584-1604.
- 222. G. Lewis and C. Catlow, Journal of Physics C: Solid State Physics, 1985, 18, 1149.
- 223. R. Salomon-Ferrer, D. A. Case and R. C. Walker, *Wiley Interdisciplinary Reviews: Computational Molecular Science*, 2013, **3**, 198-210.
- 224. X. Zhu, P. E. Lopes and A. D. MacKerell Jr, *Wiley Interdisciplinary Reviews: Computational Molecular Science*, 2012, **2**, 167-185.
- 225. M. Sanders, M. Leslie and C. Catlow, *Journal of the Chemical Society, Chemical Communications*, 1984, 1271-1273.
- 226. J. R. Hill and J. Sauer, *The Journal of Physical Chemistry*, 1994, **98**, 1238-1244.
- 227. T. P. Senftle, S. Hong, M. M. Islam, S. B. Kylasa, Y. Zheng, Y. K. Shin, C. Junkermeier, R. Engel-Herbert, M. J. Janik and H. M. Aktulga, *npj Computational Materials*, 2016, **2**, 1-14.
- 228. R. H. Swendsen and J.-S. Wang, *Physical review letters*, 1987, **58**, 86.
- 229. I. Bahar and A. Rader, Current opinion in structural biology, 2005, 15, 586-592.
- 230. J. C. Boeyens and P. Comba, Coordination Chemistry Reviews, 2001, 212, 3-10.
- 231. J. D. Gale and A. L. Rohl, *Molecular Simulation*, 2003, **29**, 291-341.
- 232. W. Smith, C. Yong and P. Rodger, Molecular Simulation, 2002, 28, 385-471.
- 233. H. Lin and D. G. Truhlar, Theoretical Chemistry Accounts, 2007, 117, 185-199.
- 234. G. Piccini, M. Alessio, J. Sauer, Y. Zhi, Y. Liu, R. Kolvenbach, A. Jentys and J. A. Lercher, *The Journal of Physical Chemistry C*, 2015, **119**, 6128-6137.
- 235. S. P. Greatbanks, P. Sherwood and I. H. Hillier, *J. Phys. Chem. C*, 1994, **98**, 8134-8139.
- 236. L. Dent and J. Smith, *Nature*, 1958, **181**, 1794-1796.
- 237. P. Sherwood, A. H. de Vries, S. J. Collins, S. P. Greatbanks, N. A. Burton, M. A. Vincent and I. H. Hillier, *Faraday Discuss.*, 1997, **106**, 79-92.
- 238. P. J. Wilson, T. J. Bradley and D. J. Tozer, *The Journal of Chemical Physics*, 2001, **115**, 9233-9242.
- 239. Y. Zhao, B. J. Lynch and D. G. Truhlar, *The Journal of Physical Chemistry A*, 2004, **108**, 2715-2719.
- 240. J. Smith, F. Rinaldi and L. Dent Glasser, Acta Crystallographica, 1963, 16, 45-53.
- 241. S. A. Bates, A. A. Verma, C. Paolucci, A. A. Parekh, T. Anggara, A. Yezerets, W. F. Schneider, J. T. Miller, W. N. Delgass and F. H. Ribeiro, *J. catal.*, 2014, **312**, 87-97.
- 242. E. A. Eilertsen, B. Arstad, S. Svelle and K. P. Lillerud, *Micropor. Mesopor. Mat.*, 2012, **153**, 94-99.
- 243. I. Chorkendorff and J. W. Niemantsverdriet, *Concepts of modern catalysis and kinetics*, John Wiley & Sons, 2017.
- 244. R. Olsen, G. Kroes, G. Henkelman, A. Arnaldsson and H. Jónsson, *The Journal of chemical physics*, 2004, **121**, 9776-9792.

- 245. W. Koch and M. C. Holthausen, *A chemist's guide to density functional theory*, John Wiley & Sons, 2015.
- 246. C. R. Jacob and M. Reiher, *The Journal of chemical physics*, 2009, **130**, 084106.
- 247. X. Cheng and R. P. Steele, *The Journal of Chemical Physics*, 2014, **141**, 104105.
- 248. M. F. Guest*, I. J. Bush, H. J. Van Dam, P. Sherwood, J. M. Thomas, J. H. Van Lenthe, R. W. Havenith and J. Kendrick, *Molecular physics*, 2005, **103**, 719-747.
- 249. L. Ma, Y. Cheng, G. Cavataio, R. W. McCabe, L. Fu and J. Li, *Chemical Engineering Journal*, 2013, **225**, 323-330.
- 250. R. Millan, P. Cnudde, V. Van Speybroeck and M. Boronat, *JACS Au*, 2021, **1**, 1778-1787.
- 251. C. R. A. Catlow, J. Buckeridge, M. R. Farrow, A. J. Logsdail and A. A. Sokol, Wiley-VCH, 2017.
- 252. P. Sherwood, A. H. De Vries, S. J. Collins, S. P. Greatbanks, N. A. Burton, M. A. Vincent and I. H. Hillier, *Faraday Discussions*, 1997, **106**, 79-92.
- 253. R. Haszeldine and J. Jander, *The Journal of Chemical Physics*, 1955, **23**, 979-980.
- 254. M. Piskorz and T. Urbanski, Bull. Acad. Pol. Sci., Ser. Sci. Chim, 1963, 11.
- 255. P. Tarte, Bulletin des Sociétés Chimiques Belges, 1954, 63, 525-541.
- 256. T. Kedrova, R. Gafurov, E. Sogomonyan and L. Eremenko, *Bulletin of the Academy of Sciences of the USSR, Division of chemical science*, 1979, **28**, 944-947.
- 257. F. Zapata and C. García-Ruiz, Spectrochimica Acta Part A: Molecular and Biomolecular Spectroscopy, 2018, **189**, 535-542.
- 258. L. Volod'Ko and L. T. Huoah, Journal of Applied Spectroscopy, 1968, 9, 1100-1104.
- 259. S. Bordiga, C. Lamberti, F. Bonino, A. Travert and F. Thibault-Starzyk, *Chemical Society Reviews*, 2015, **44**, 7262-7341.
- 260. C. Negri, P. S. Hammershøi, T. V. Janssens, P. Beato, G. Berlier and S. Bordiga, *Chemistry–A European Journal*, 2018, **24**, 12044-12053.
- 261. K. I. Hadjiivanov, *Catalysis Reviews*, 2000, **42**, 71-144.
- 262. X. Yao, K. Ma, W. Zou, S. He, J. An, F. Yang and L. Dong, *Chinese Journal of Catalysis*, 2017, **38**, 146-159.
- 263. A. G. Greenaway, A. Marberger, A. Thetford, I. Lezcano-González, M. Agote-Arán, M. Nachtegaal, D. Ferri, O. Kröcher, C. R. A. Catlow and A. M. Beale, *Chemical science*, 2020, 11, 447-455.
- 264. I. Lezcano-Gonzalez, U. Deka, B. Arstad, A. Van Yperen-De Deyne, K. Hemelsoet, M. Waroquier, V. Van Speybroeck, B. M. Weckhuysen and A. M. Beale, *Physical Chemistry Chemical Physics*, 2014, **16**, 1639-1650.
- 265. M. Moreno-González, R. Millán, P. Concepción, T. Blasco and M. Boronat, *ACS Catalysis*, 2019, **9**, 2725-2738.
- 266. N. Wilken, K. Kamasamudram, N. W. Currier, J. Li, A. Yezerets and L. Olsson, *Catalysis Today*, 2010, **151**, 237-243.
- 267. L. Olsson, K. Wijayanti, K. Leistner, A. Kumar, S. Y. Joshi, K. Kamasamudram, N. W. Currier and A. Yezerets, *Applied Catalysis B: Environmental*, 2015, **174**, 212-224.
- 268. M. Krossner and J. Sauer, The Journal of Physical Chemistry, 1996, 100, 6199-6211.
- 269. H. Jobic, A. Tuel, M. Krossner and J. Sauer, *The Journal of physical chemistry*, 1996, **100**, 19545-19550.
- 270. D. Parrillo, C. Lee and R. Gorte, Applied Catalysis A: General, 1994, 110, 67-74.
- 271. R. Millan, P. Cnudde, A. E. Hoffman, C. W. Lopes, P. Concepción, V. Van Speybroeck and M. Boronat, *The journal of physical chemistry letters*, 2020, **11**, 10060-10066.
- 272. D. Mei and J. A. Lercher, *AIChE Journal*, 2017, **63**, 172-184.
- 273. C. Tuma and J. Sauer, *Chemical physics letters*, 2004, **387**, 388-394.

- 274. F. Gao, J. H. Kwak, J. Szanyi and C. H. Peden, *Topics in Catalysis*, 2013, **56**, 1441-1459.
- 275. T. W. Keal and D. J. Tozer, *The Journal of chemical physics*, 2005, **123**, 121103.
- 276. J. Zheng, X. Xu and D. G. Truhlar, *Theoretical Chemistry Accounts*, 2011, **128**, 295-305.
- 277. A. J. O'Malley, I. Hitchcock, M. Sarwar, I. P. Silverwood, S. Hindocha, C. R. A. Catlow, A. P. York and P. Collier, *Physical Chemistry Chemical Physics*, 2016, **18**, 17159-17168.
- 278. W. Hu, T. Selleri, F. Gramigni, E. Fenes, K. R. Rout, S. Liu, I. Nova, D. Chen, X. Gao and E. Tronconi, *Angewandte Chemie*, 2021, **133**, 7273-7280.
- 279. M. P. Ruggeri, I. Nova and E. Tronconi, *Topics in Catalysis*, 2013, **56**, 109-113.
- 280. M. Bendrich, A. Scheuer, R. Hayes and M. Votsmeier, *Applied Catalysis B: Environmental*, 2018, **222**, 76-87.
- 281. L. Chen, H. Falsig, T. V. Janssens and H. Grönbeck, *Journal of catalysis*, 2018, **358**, 179-186.
- 282. M. Colombo, I. Nova and E. Tronconi, Catal. Today, 2010, 151, 223-230.
- 283. S. Soyer, A. Uzun, S. Senkan and I. Onal, *Catalysis today*, 2006, **118**, 268-278.
- 284. S. P. Walch, *The Journal of chemical physics*, 1993, **99**, 5295-5300.
- 285. D. Sun, W. F. Schneider, J. B. Adams and D. Sengupta, *The Journal of Physical Chemistry A*, 2004, **108**, 9365-9374.
- 286. M. Anstrom, N.-Y. Topsøe and J. Dumesic, Journal of Catalysis, 2003, 213, 115-125.
- 287. F. Gilardoni, A. T. Bell, A. Chakraborty and P. Boulet, *The Journal of Physical Chemistry B*, 2000, **104**, 12250-12255.
- 288. L. Chen, T. V. Janssens, P. N. Vennestrøm, J. Jansson, M. Skoglundh and H. Gronbeck, *ACS Catalysis*, 2020, **10**, 5646-5656.
- 289. Y. Mao, Z. Wang, H.-F. Wang and P. Hu, ACS Catalysis, 2016, 6, 7882-7891.
- 290. J. Li and S. Li, Physical Chemistry Chemical Physics, 2007, 9, 3304-3311.
- 291. T. C. Brüggemann and F. J. Keil, *The Journal of Physical Chemistry C*, 2008, **112**, 17378-17387.
- 292. N. Usberti, F. Gramigni, N. D. Nasello, U. Iacobone, T. Selleri, W. Hu, S. Liu, X. Gao, I. Nova and E. Tronconi, *Applied Catalysis B: Environmental*, 2020, **279**, 119397.
- 293. F. Gao, D. Mei, Y. Wang, J. Szanyi and C. H. Peden, *Journal of the American Chemical Society*, 2017, **139**, 4935-4942.
- 294. N. Akter, X. Chen, J. Parise, J. A. Boscoboinik and T. Kim, *Korean Journal of Chemical Engineering*, 2018, **35**, 89-98.
- 295. Y. Liu, W. Xue, S. Seo, X. Tan, D. Mei, C.-j. Liu, I.-S. Nam and S. B. Hong, *Applied Catalysis B: Environmental*, 2021, **294**, 120244.
- 296. T. Yu, J. Wang, M. Shen, J. Wang and W. Li, *Chemical Engineering Journal*, 2015, **264**, 845-855.
- 297. H. Lee, I. Song, S. W. Jeon and D. H. Kim, *The Journal of Physical Chemistry Letters*, 2021, **12**, 3210-3216.
- 298. Y. Wan, G. Yang, J. Xiang, X. Shen, D. Yang, Y. Chen, V. Rac, V. Rakic and X. Du, *Dalton Transactions*, 2020, **49**, 764-773.
- 299. C. Paolucci, I. Khurana, A. A. Parekh, S. Li, A. J. Shih, H. Li, J. R. Di Iorio, J. D. Albarracin-Caballero, A. Yezerets and J. T. Miller, *Science*, 2017, **357**, 898-903.
- 300. M. Wallin, C.-J. Karlsson, M. Skoglundh and A. Palmqvist, *Journal of Catalysis*, 2003, **218**, 354-364.
- 301. Y. Yue, B. Liu, P. Qin, N. Lv, T. Wang, X. Bi, H. Zhu, P. Yuan, Z. Bai and Q. Cui, *Chemical Engineering Journal*, 2020, **398**, 125515.

- 302. F. Gao, Catalysts, 2020, 10, 1324.
- 303. J. Pérez-Ramírez, G. Mul, F. Kapteijn, J. Moulijn, A. Overweg, A. Doménech, A. Ribera and I. Arends, *Journal of Catalysis*, 2002, **207**, 113-126.
- 304. L. Guimaraes, H. A. de Abreu and H. A. Duarte, *Chemical Physics*, 2007, **333**, 10-17.
- 305. D. Berger, A. J. Logsdail, H. Oberhofer, M. R. Farrow, C. R. A. Catlow, P. Sherwood, A. A. Sokol, V. Blum and K. Reuter, *The Journal of chemical physics*, 2014, **141**, 024105.
- 306. M. Brändle and J. Sauer, *Journal of the American Chemical Society*, 1998, **120**, 1556-1570.
- 307. U. Eichler, M. Brändle and J. Sauer, *The Journal of Physical Chemistry B*, 1997, **101**, 10035-10050.
- 308. J. Sauer, *Journal of molecular catalysis*, 1989, **54**, 312-323.
- 309. K. Suzuki, T. Noda, N. Katada and M. Niwa, *Journal of Catalysis*, 2007, **250**, 151-160.
- 310. C.-M. Wang, R. Y. Brogaard, B. M. Weckhuysen, J. K. Nørskov and F. Studt, *The journal of physical chemistry letters*, 2014, **5**, 1516-1521.
- 311. S. Li, Y. Wang, T. Wu and W. F. Schneider, ACS Catalysis, 2018, 8, 10119-10130.
- 312. C. Paolucci, A. A. Verma, S. A. Bates, V. F. Kispersky, J. T. Miller, R. Gounder, W. N. Delgass, F. H. Ribeiro and W. F. Schneider, *Angewandte Chemie International Edition*, 2014, **53**, 11828-11833.
- 313. Y. Zhang, Y. Wu, Y. Peng, J. Li, E. D. Walter, Y. Chen, N. M. Washton, J. Szanyi, Y. Wang and F. Gao, *The Journal of Physical Chemistry C*, 2020, **124**, 28061-28073.
- 314. C. Negri, E. Borfecchia, M. Cutini, K. A. Lomachenko, T. V. Janssens, G. Berlier and S. Bordiga, *ChemCatChem*, 2019, **11**, 3828-3838.
- 315. P. J. Smeets, R. G. Hadt, J. S. Woertink, P. Vanelderen, R. A. Schoonheydt, B. F. Sels and E. I. Solomon, *Journal of the American Chemical Society*, 2010, **132**, 14736-14738.
- 316. P. Vanelderen, B. E. Snyder, M.-L. Tsai, R. G. Hadt, J. Vancauwenbergh, O. Coussens, R. A. Schoonheydt, B. F. Sels and E. I. Solomon, *Journal of the American Chemical Society*, 2015, **137**, 6383-6392.
- 317. M. Metz and E. I. Solomon, *Journal of the American Chemical Society*, 2001, **123**, 4938-4950.
- 318. L. M. Mirica, M. Vance, D. J. Rudd, B. Hedman, K. O. Hodgson, E. I. Solomon and T. D. P. Stack, *Science*, 2005, **308**, 1890-1892.
- 319. E. I. Solomon, D. E. Heppner, E. M. Johnston, J. W. Ginsbach, J. Cirera, M. Qayyum, M. T. Kieber-Emmons, C. H. Kjaergaard, R. G. Hadt and L. Tian, *Chemical reviews*, 2014, **114**, 3659-3853.
- 320. S. T. Korhonen, D. W. Fickel, R. F. Lobo, B. M. Weckhuysen and A. M. Beale, *Chem. Commun.*, 2011, **47**, 800-802.
- 321. U. Deka, A. Juhin, E. A. Eilertsen, H. Emerich, M. A. Green, S. T. Korhonen, B. M. Weckhuysen and A. M. Beale, *J. Phys. Chem. C*, 2012, **116**, 4809-4818.
- 322. M. H. Groothaert, J. A. van Bokhoven, A. A. Battiston, B. M. Weckhuysen and R. A. Schoonheydt, *J. Am. Chem. Soc.*, 2003, **125**, 7629-7640.
- 323. W. Loewenstein, American Mineralogist: Journal of Earth and Planetary Materials, 1954, **39**, 92-96.
- 324. H. Lei, V. Rizzotto, A. Guo, D. Ye, U. Simon and P. Chen, *Catalysts*, 2021, **11**, 52.
- 325. W. Hu, T. Selleri, F. Gramigni, E. Fenes, K. R. Rout, S. Liu, I. Nova, D. Chen, X. Gao and E. Tronconi, *Angewandte Chemie International Edition*, 2021, **60**, 7197-7204.
- 326. C. Paolucci, A. A. Parekh, I. Khurana, J. R. Di Iorio, H. Li, J. D. Albarracin Caballero, A. J. Shih, T. Anggara, W. N. Delgass and J. T. Miller, *Journal of the American Chemical Society*, 2016, **138**, 6028-6048.

- 327. L. Chen, J. Jansson, M. Skoglundh and H. Gronbeck, *The Journal of Physical Chemistry C*, 2016, **120**, 29182-29189.
- 328. W. Hu, U. Iacobone, F. Gramigni, Y. Zhang, X. Wang, S. Liu, C. Zheng, I. Nova, X. Gao and E. Tronconi, *ACS Catalysis*, 2021, **11**, 11616-11625.
- 329. P. J. Smeets, B. F. Sels, R. M. van Teeffelen, H. Leeman, E. J. Hensen and R. A. Schoonheydt, *J. Catal.*, 2008, **256**, 183-191.
- 330. P. J. Smeets, M. H. Groothaert, R. M. van Teeffelen, H. Leeman, E. J. Hensen and R. A. Schoonheydt, *J. Catal.*, 2007, **245**, 358-368.
- 331. H. Falsig, P. N. Vennestrøm, P. G. Moses and T. V. Janssens, *Topics in Catalysis*, 2016, **59**, 861-865.

Appendices

In this section, the appendices are presented as a compilation of supplementary materials that enhance the comprehension and analysis of the main body of the thesis. These appendices encompass a range of supporting information, including resource requirements, job calculation details, experimental analysis, computational inputs, and other relevant materials.

A.1 Resource Requirements

Table A1. ARCHER2 CU calculated cost per job.

Job Type	No. of Nodes	Wallclock time	No. of jobs	CU per Job
		(hours)		
Single point	1	1	~40	1
Geom. Opt.	3	24	~50	72
Large Geom. Opt	6	48	~80 (NEB run)	288

Table A2. Estimated total ARCHER2 CU calculated cost.

Types of calculation	~CU	Materials	
Single point	40	CHA/BEA	
Commenter antimication	3600	CHA/DEA	
Geometry optimization	3000	CHA/BEA	
Vibrational analysis	6720	CHA/BEA	
J			
NEB analysis	23,040	CHA/BEA	
	T . 1		
Total active sites = 60			
Total $CU = 33,400$ on each platform			
1 star 2 25, 100 on each platform			

Table A3. Estimated total ARCHER2 MU calculated cost.

Types of calculation	~MAU	Materials
Nudged elastic band calculation	35	CHA/MFI
Further geometry optimization	15	CHA/MFI
Total MAU = \sim 50 (25 on each platform)		

Job Data

Table A4. Memory requirements for various jobs on ARCHER2 machine.

Description	Largest Job	Typical Job	Smallest Job
Total memory required (per job)	1536 GiB	768 GiB	256 GiB
Total time for these jobs (hours)	960	1200	40

The disk space is typically contained within ~ 1 GB per single job, and we expect to require about 1000 GB of the workspace. Gamess-UK with ChemShell has currently resulted in very large disk usage, meaning that large temporary space is required for work.

A.2 Experimental Study and Analysis

DRIFTS Operando ME Experiments

As noted the experimental data were obtained by Beale and co-workers using the facilities in the Catalysis Hub Centre on the Harwell Science and innovation Campus. Diffuse reflectance Fourier Transform spectroscopy (DRIFTS) spectra were recorded on a Bruker Vertex 70 spectrometer equipped with a liquid-N₂ cooled HgCdTe detector and a Praying Mantis mirror unit (Harrick). The spectroscopic cell connected to heated gas supply lines was equipped with a flat CaF₂ window (2 mm thick; d½ 25 mm). The outlet of the cell was coupled to a Fourier

transform infrared spectrometer (FTIR) equipped with a 70 mm path length gas cell heated to 150 °C (Bruker Alpha). The sample was dried in situ in 10 vol% O₂/N₂ (100 ml min⁻¹) at 400 °C for 2 h and was placed in the sample cup of the cell (*ca.* 30 mg, 57 mm³). DRIFTS spectra were collected by accumulating 10 interferograms under 80 kHz scanner velocity (0.9 s per spectrum) and at 4 cm⁻¹ resolution. Solenoid valves were used to repeatedly switch between gases during a concentration modulation excitation experiment which was functioned by the OPUS software (Bruker).

Catalyst Preparation

Synthesis of SSZ-13 zeolite (Si/Al=13) was performed, again by Beale and co-workers⁷ as following hydrothermal reported previously approach [1]. The N,N,Ntrimethyladamantammonium hydroxide was used as a structure-directing agent under fluoride media. The protonated zeolite is obtained by calcinating the sample in the air; first at 1 °C min⁻ ¹ to 120 °C for 2.5 h and then for 4 °C min⁻¹ to 550 °C for 10 h. By employing the wet ionexchange methodology, a typical amount of H-SSZ-13 is then mixed with a copper sulfate solution (50 mL of a 0.1 M solution of CuSO₄ per gram of zeolite) under constant heating (80 °C for 2 h) and stirring. The resultant product consists of a well-defined crystal of rhombohedral morphology (2.92 wt % Cu loading) which was washed with water and kept at 80 °C overnight. To perform operando spectroscopic analysis, the pellets of zeolite (8 mm bore, 1.5-tonne pressure) were prepared which is then crushed and sieved to retain a 250-450um fraction for experiments.

⁷ This work has been performed by Prof. Andrew Beale and coworkers using the facilities in the Catalysis Hub Centre on the Harwell Science and innovation Campus.

Catalyst Characterization

Powder X-ray Diffraction (PXRD) patterns were collected (performed by Beale and coworkers)⁸ to confirm phase purity and crystallinity on a Rigaku Miniflex diffractometer (Cu $K\alpha_1$, 1.54056 Å), samples were loaded onto a flat Teflon sample holder. The SSZ-13 samples obtained exhibit typical X-ray diffraction (XRD) patterns, which are associated with CHA structures (Figure A1) [2]. There was no obvious copper oxide (CuO_x) reflection in the XRD patterns of the Cu-exchange zeolite samples, indicating the absence of significant CuOx agglomerates. Diffraction patterns were collected between 5.0 and 50.0° in 0.02° steps. PXRD shows that a highly crystalline pure phase of Cu-SSZ-13 is present after calcination, subsequent ion exchange, and calcination steps. Energy Dispersive X-ray (EDX) analysis of Cu-SSZ-13 (see Table A5) shows that Cu-SSZ-13 has a composition of 2.92 wt % Cu with a Si/Al=13 which represents 75 % Cu ion-exchanged into available H⁺ sites. The Brunauer–Emmett–Teller (BET) method was used in the analysis of the total surface area, and the t–plot method was used in the micropore volume (Table A6).

-

⁸ This work has been performed by Prof. Andrew Beale and coworkers using the facilities in the Catalysis Hub Centre on the Harwell Science and innovation Campus

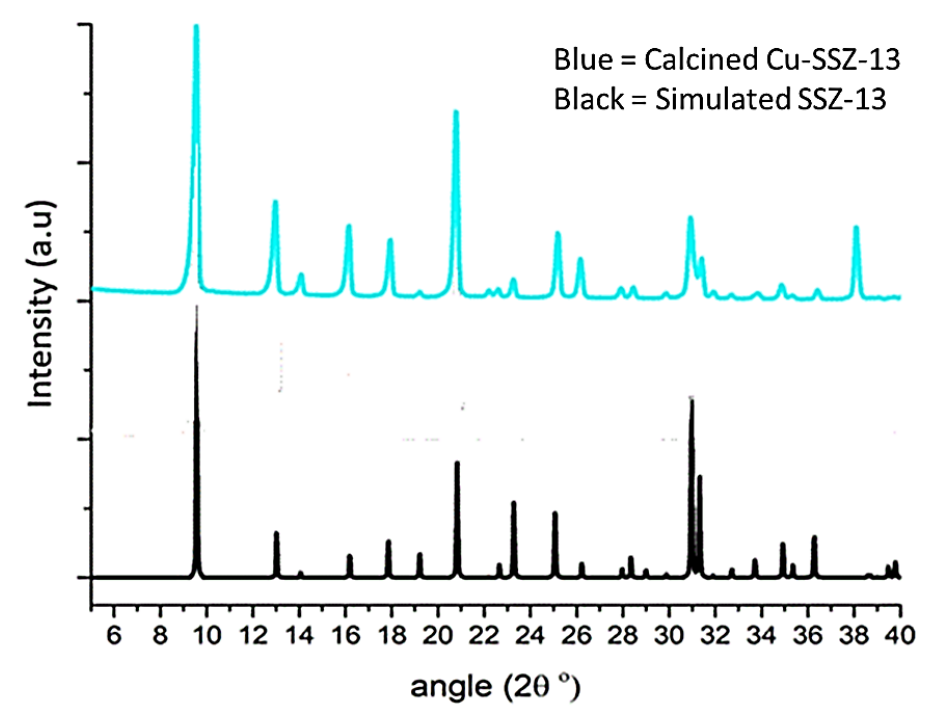


Figure A1. Diffraction patterns: Calcined Cu-SSZ-13 (blue), simulated PXRD (black), collected at room temperature in a hydrated state. Note reflection at 38 ° is due to the Teflon sample holder.

Table A5. XRF element composition of Cu-SSZ-13 sample.

Wt.%	Wt.% Sigma	
53.12	0.15	
3.19	0.04	
40.77	0.13	
2.92	0.10	
100.00		
	53.12 3.19 40.77 2.92	53.12 0.15 3.19 0.04 40.77 0.13 2.92 0.10

Table A6. Surface area and pore volume of Cu-SSZ-13 sample.

Sample	Micropore volume (cc/g)	Micropore area (m²/g)
Cu-SSZ-13	0.28	758

A.3 Computational Input files

Gulp input to optimize the BEA zeolite unitcell

optimise conp property phonon compare distance name silicate cell

```
12.66139 12.66139 26.40612 90.000 90.000 90.000
fractional 26
Si 0.33694 0.79277 0.05619
Si 0.33711 0.54031 0.05606
Si 0.71647 0.793 0.05872
O 0.33623 0.66652 0.06515
O 0.33454 0.81732 -0.00385
O 0.23433 0.84457 0.08279
O 0.44268 0.84276 0.08069
O 0.33456 0.51612 -0.00402
O 0.23464 0.48822 0.08264
O 0.44301 0.49038 0.08043
P 41 2 2
origin 2
species 2
Si 1.200000
O -0.600000
# The FF in this file was implemented by Sophia Proud and Samuel Watts, under the guidance of
Andrew Logsdail, in 2018.
# We are grateful to both the Cardiff University CUROP scheme and a CCP5 Summer Bursary for
their support
# The FF was taken from the work of Hill and Sauer, J. Phys. Chem. 99 (1995) 9536-9550
keyword molmec
element
covalent 9 0
rtol 1.1
harmonic k3 k4 bond kcal
# Two-body harmonic term. Input structure: k2 k3 k4 r0 coul rmin rmax
# k2 is calculated as: 459.0786*2
# k3 is calculated as:-672.4445*6
# k4 is calculated as: 443.3651*24
Si O 918.1572 -4034.6670 10640.7624 1.6104
three k3 k4 bond kcal
# Three-body term. Input structure: k2 k3 k4 theta0 rmax(1-2) rmax(1-3) rmax(2-3)
# k2(H2) is calculated as 81.9691*2
# k3(H3) is calculated as -36.5814*6
# k4 (H4) is calculated as 116.9558*24
Si O O 163.9382 -219.4884 2806.9392 112.0200
O Si Si 41.4030 165.3036 263.8320 173.7651
bacross bond kcal
# Bond-angle cross term. Input structure: k1 k2 r1 r2 theta0 rmax12 rmax13 rmax23 according to
online GULP help manual
```

```
# In the 1995 paper, and from DL Poly documentation, there are two constants, Fba and Fba'.
# As pointed out by Jingcheng Guan (UCL), these are to ensure environmental symmetry in the
bonding species
Si O O 78.1239 78.1239 1.6104 1.6104 112.0200
O Si Si 9.2390 9.2390 1.6104 1.6104 173.7651
bcross bond kcal
# Bond-bond cross term (3-body). Input structure: K r1 r2 rmax12 rmax13 rmax23
Si O O 0.0000 1.6104 1.6104
# assumed for K in above line of O-Si-O to be equal to zero as not mentioned in the 1995 paper
O Si Si 151.8742 1.6104 1.6104
uff4 bond kcal
# Torisonal UFF potential. Input structure: k n rmax(1-2) rmax(2-3) rmax(3-4) rmax(4-1)
# Whilst implemented in the original FF, this term seems to have no effect in DL POLY and
# so is disabled here for directly compatibility with the previous DL POLY implementation of FF.
## k calculated as: 2*0.0306(V1)
Si O Si O 0.0612 1.0000
## k calculated as: 2*-0.0105(V2)
Si O Si O -0.0210 2.0000
## k calculated as: 2*0.0804(V3)
Si O Si O 0.1608 3.0000
xangleangle bond kcal
# Angle-angle cross potential. Input structure A B C D k(213/4) k(312/4) k(412/3) theta0(213)
theta0(214) theta0(314) rmax(1-2) rmax(1-3) rmax(1-4)
Si O O O -6.3030 -6.3030 -6.3030 112.0200 112.0200 112.0200
torangle bond kcal
# Torsional-angle cross term. Input structure: A B C D K theta0 theta0' rmax(1-2) rmax(2-3) rmax(3-
4)
O Si O Si -4.5150 112.0200 173.7651
lennard 9 6 x13 kcal
# Lennard-Jones long-range VDW-type interaction. Input Structure: A B rmin rmax
# Represents second term in equation stated in the research paper
# A calculated as A(Si)*A(O): 432.3320*239.6090
Si O 103590.6 0.0 0.0000 15.0000
Si Si 186910.96 0.0 0.0000 15.0000
O O 57412.473 0.0 0.0000 15.0000
#
#
```

```
xtol 8
gtol 7
ftol 12
#
dump silicate.hillff.gin
output drv silicate.hillff.drv
output arc silicate.hillff.arc
output cif silicate.hillff.cif
output xyz silicate.xyz
```

Gamess-UK with DL-POLY (TCL-Chemshell)

Example of Fe framework-brønsted acid site

```
#write_xyz coords=mfi_QMMM_TCS.pun file=silica_sp_in.xyz
set conv {
{newscf}
{maxcyc 2000 }
{print full}
{Phase 1}
{ Level 10.0 10.0 }
{ DIIS }
{# Switch to phase 2}
{ next 2}
   Tester below 0.01 }
{Phase 2}
{ Level 0.5 0.5 }
{ DIIS }
{# Switch to phase 3}
{ next 3}
   Tester below 0.001 }
{Phase 3}
{ Level 0.0 0.0 }
{ DIIS }
{ next 0}
{# Converge calculation}
   Tester below 0.00001 }
{# Absolute energy change}
  dEabs below 0.0000001 }
{end}
set dl poly args " mm defs= zeolite.ff mxexcl=200 "
set gamess args "basisfile=basis \
             functional=b97-2 \
             ecpfile=Fe ecp \
             harmonic=yes \
             unique listing=no \
             scf keywords = [ list $conv ] \
             direct=yes \
             echo_input=no print_bqs=no \
             symmetry=off \
```

```
charge=0 \
              scftype=uhf \
             mult=6 \
             memory=99000000 "
#
               restart=yes "
#
               guessfile=guess.txt "
              scf thresh=5 \
set hybrid args "qm region={ atoms list } \
            mm theory = dl poly : [list $dl poly args] \
            qm theory = gamess : [ list $gamess args ] \
            coupling=shift \
            dipole adjust=yes "
#eandg energy=e \
#
     coords=bea cluster.pun \
#
     theory=hybrid: [list $hybrid args]
dl-find coords=mfi.T1.pun \
   maxcycle=500 \
   theory=hybrid: [list $hybrid args] \
   dump=1 \
   result=mfi.T1 opt.pun \
   tolerance=0.001 \
   active atoms= { atoms list }
    restart=yes
#write xyz coords=silica sp.pun file=silica sp out.xyz
```

NWCHEM with GULP (PY-Chemshell)

Example of Fe framework-brønsted acid site

```
from chemsh import *
from chemsh.utils import testutils
HEAP=1000
STACK=1000
GLOBAL=2000
inputfrag = Fragment(coords='mfi.T1.pun', connect_mode='covalent')
silicate_modifiers = {('Si','O1'):0.3, ('Si','O11'):0.3}
active_atoms = inputfrag.getRegion()
print("Active Atoms: ", active_atoms)
radius_active = 36
origin = [1.60549696682064e+01, 2.49184929790030e+00, 1.77433165897056e+01]
active_region = inputfrag.selectByRadius(radius_active,centre=origin)
qm_region = inputfrag.getRegion(1)
print("QM region is: ", qm_region)
```

```
qm charge = int(inputfrag.totalcharge)
print("QM charge is: ", qm charge)
qm theory = NWChem(method = 'dft',
           functional = 'becke97-2',
           memory = 99000000,
                 = 'basis.nwchem',
          basis
           еср
                  = 'Fe ecp',
          mult
                  = 6,
          scftype = 'uhf',
          charge = qm_charge,
          harmonic = True,
          direct = True,
          maxiter = 999,
          tol energy = 1.E-6,
           tol density = 1.E-5,
           tol gradient = 1.E-5,
          restart=True)
mm_theory = GULP(ff ='zeolite_gulp.ff',
         molecule = True)
qmmm = QMMM(qm=qm theory,
      mm=mm theory,
      frag=inputfrag,
      coupling='covalent',
      embedding='electrostatic',
#
       bond modifiers=silicate modifiers,
      dipole adjust=True,
      qm region=qm region)
opt = Opt(theory=qmmm,
     algorithm="lbfgs",
     maxcycle=300,
     maxene=300,
     dump=1,
     active=active region,
     tolerance=0.001,
     restart=True)
opt.run()
#sp = SP(theory=qmmm, gradients=True)
#sp.run()
#ecalc = sp.result.energy
inputfrag.save('mfi t1 opt Feohl.pun', 'pun')
```

NWCHEM with GULP (PY-Chemshell)

Example of Fe framework-brønsted acid site

QM/MM basis set

The dual basis set is based on the Def2-TZVP and Def2-SVP basis sets. The outermost diffuse orbitals are removed (see Chapter 2).

```
#BASIS "ao basis" PRINT
# def2-tzvp
\#BASIS SET: (4s,1p) \rightarrow [2s,1p]
H S
  13.0107010
                    0.19682158E-01
   1.9622572
                    0.13796524
   0.44453796
                    0.47831935
H S
   0.12194962
                    1.0000000
H P
   0.8000000
                    1.0000000
# def2-tzvp
H11 S
  34.0613410
                    0.60251978E-02
   5.1235746
                    0.45021094E-01
   1.1646626
                    0.20189726
H11 S
   0.32723041
                    1.0000000
H11 S
   0.10307241
                    1.0000000
H11 P
   0.8000000
                    1.0000000
#BASIS SET: (11s,6p,2d,1f) -> [5s,3p,2d,1f]
O11 S
 27032.3826310
                      0.21726302465E-03
 4052.3871392
                     0.16838662199E-02
  922.32722710
                     0.87395616265E-02
  261.24070989
                     0.35239968808E-01
  85.354641351
                     0.11153519115
  31.035035245
                     0.25588953961
O11 S
  12.260860728
                     0.39768730901
   4.9987076005
                     0.24627849430
O11 S
   1.1703108158
                     1.0000000
O11 S
   0.46474740994
                      1.0000000
O11 S
   0.18504536357
                      1.0000000
O11 P
  63.274954801
                     0.60685103418E-02
  14.627049379
                     0.41912575824E-01
   4.4501223456
                     0.16153841088
   1.5275799647
                     0.35706951311
```

```
O11 P
   0.52935117943
                      .44794207502
O11 P
   0.17478421270
                      .24446069663
O11 D
   2.31400000
                    1.0000000
O11 D
   0.64500000
                    1.0000000
#O F
                     1.0000000
    1.42800000
# def2-svp
#BASIS SET: (7s,4p,1d) \rightarrow [3s,2p,1d]
O1 S
 2266.1767785
                     -0.53431809926E-02
  340.87010191
                     -0.39890039230E-01
  77.363135167
                     -0.17853911985
  21.479644940
                     -0.46427684959
   6.6589433124
                     -0.44309745172
O1 S
   0.80975975668
                      1.0000000
O1 S
                      1.0000000
   0.25530772234
O1 P
  17.721504317
                     0.43394573193E-01
   3.8635505440
                     0.23094120765
   1.0480920883
                     0.51375311064
O1 P
   0.27641544411
                      1.0000000
O1 D
   1.2000000
                    1.0000000
# def2-tzvp
\#BASIS SET: (14s,9p,3d,1f) \rightarrow [5s,5p,2d,1f]
Sill S
 44773.3580780
                      0.55914765868E-03
 6717.1992104
                     0.43206040189E-02
 1528.8960325
                     0.22187096460E-01
  432.54746585
                     0.86489249116E-01
  140.61505226
                     0.24939889716
  49.857636724
                     0.46017197366
  18.434974885
                     0.34250236575
Si11 S
  86.533886111
                     0.21300063007E-01
                     0.94676139318E-01
  26.624606846
   4.4953057159
                     -0.32616264859
Sill S
   2.1035045710
                     1.3980803850
Sill S
   1.0106094922
                     0.63865786699
Sill S
   0.23701751489
                      1.0000000
#Si1 S
    0.85703405362E-01
                         1.0000000
Sill P
  394.47503628
                     0.26285693959E-02
```

```
93.137683104
                      0.20556257749E-01
  29.519608742
                      0.92070262801E-01
  10.781663791
                      0.25565889739
Si11 P
   4.1626574778
                      0.42111707185
Sill P
   1.6247972989
                       .34401746318
Sill P
   0.54306660493
                       1.0000000
Sill P
   0.20582073956
                       1.0000000
#Si1 P
    0.70053487306E-01
                          1.0000000
Sill D
   2.30300000
                     0.20000000
Sill D
   0.476000000
                      1.00000000
Sill D
   0.160000000
                      1.0000000
#Si1 F
    0.336000000
                       1.0000000
# def2-svp
\#BASIS SET: (10s,7p,1d) \rightarrow [4s,3p,1d]
Si<sub>1</sub> S
 6903.7118686
                      0.13373962995E-02
 1038.4346419
                      0.99966546241E-02
  235.87581480
                      0.44910165101E-01
  66.069385169
                      0.11463638540
  20.247945761
                      0.10280063858
Si<sub>1</sub> S
  34.353481730
                      0.70837285010E-01
   3.6370788192
                      -0.43028836252
   1.4002048599
                      -0.41382774969
Si<sub>1</sub> S
   0.20484414805
                       1.0000000
Sil S
   0.77994095468E-01
                         1.0000000
Si<sub>1</sub> P
  179.83907373
                      0.61916656462E-02
  41.907258846
                      0.43399431982E-01
  12.955294367
                      0.15632019351
                      0.29419996982
   4.4383267393
   1.5462247904
                      0.23536823814
Si<sub>1</sub> P
   0.35607612302
                       1.0000000
Sil P
   0.10008513762
                       1.0000000
Si<sub>1</sub> D
   0.3500000
                     1.0000000
# Fe def2-tzvp
Fe11 S
300784.8463700
                        0.22806273096E-03
 45088.9705570
                       0.17681788761E-02
                       0.91927083490E-02
 10262.5163170
```

```
2905.2897293
                     0.37355495807E-01
  946.11487137
                     0.12151108426
  339.87832894
                     0.28818881468
  131.94425588
                     0.41126612677
  52.111494077
                     0.21518583573
Fe11 S
  329.48839267
                    -0.24745216477E-01
  101.92332739
                    -0.11683089050
  16.240462745
                     0.55293621136
   6.8840675801
                     0.53601640182
Fe11 S
  10.470693782
                    -0.22912708577
   1.7360039648
                     0.71159319984
Fe11 S
   0.72577288979
                     1.0000000
Fe11 S
   0.11595528203
                     1.0000000
#Fe11 S
    0.41968227746E-01
                        1.0000000
Fe11 P
 1585.3959970
                     0.23793960179E-02
                     0.19253154755E-01
  375.38006499
  120.31816501
                     0.90021836536E-01
  44.788749031
                     0.25798172356
  17.829278584
                     0.41492649744
                     0.24207474784
   7.2247153786
Fe11 P
  28.143219756
                    -0.29041755152E-01
   3.8743241412
                     0.55312260343
   1.5410752281
                     0.96771136842
Fe11 P
   0.58285615250
                     1.0000000
#Fe11 P
                    1.0000000
#
    0.1349150
Fe11 D
  61.996675034
                     0.11971972255E-01
  17.873732552
                     0.73210135410E-01
   6.2744782934
                     0.23103094314
   2.3552337175
                     0.39910706494
Fe11 D
   0.85432239901
                      .41391589765
Fe11 D
   0.27869254413
                      .21909269782
#Fe11 D
    0.0910000
                    1.0000000
#Fe11 F
   1.5980000
                    1.0000000
END
QM/MM ECP (Fe)
ECP
```

ECP Fe11 nelec 10 Fe11 ul

2 1.000000000 0.000000000

Fe11 S 2 20.930000000 253.749588000 2 9.445000000 37.922845000 Fe11 P 2 21.760000000 161.036812000 9.178000000 2 27.651298000 Fe11 D 25.900000000 -24.431276000 2 8.835000000 -1.434251000 **END**

References

- 1. Greenaway, A.G., et al., Operando Spectroscopic Studies of Cu–SSZ-13 for NH3–SCR deNOx Investigates the Role of NH3 in Observed Cu (II) Reduction at High NO Conversions. Topics in catalysis, 2018. **61**(3): p. 175-182.
- 2. Treacy, M.M., J.B. Higgins, and R. von Ballmoos, *Collection of simulated XRD powder patterns for zeolites*. Vol. 552. 1996: Elsevier New York.